

Dissertation

submitted to the
Combined Faculty of Natural Sciences and Mathematics
of the Ruperto Carola University Heidelberg, Germany
for the degree of
Doctor of Natural Sciences

Presented by

Eva Riechert, M.Sc.
born in Munich, Germany

Oral examination: May 4th 2021

Post-transcriptional and translational mechanisms of cardiac growth

1. Identification of dynamic RNA-binding proteins in primary cardiomyocytes uncovers Cpeb4 as a regulator of cardiac growth

&

2. mTOR-proteasomal dysfunction following deletion of Pras40 inhibits cardiac growth but results in cardiac failure

Referees:

Prof. Dr. Georg Stoecklin, 1st referee

Dr. Mirko Völkers, 2nd referee

I. LIST OF FIGURES & TABLES	11
II. ABBREVIATIONS	15
III. ABSTRACT	21
IV. ZUSAMMENFASSUNG	23
1. INTRODUCTION	25
1.1 General Introduction	26
1.1.1 Cardiovascular disease and heart failure - background	26
1.1.2 The anatomy of the heart	26
1.1.3 Cardiac hypertrophy and remodeling	27
1.1.4 Molecular mechanisms of cardiac growth and remodeling	29
1.1.5 Model systems for cardiac hypertrophy	30
1.1.5.1 Pathological hypertrophy	30
1.1.5.2 Physiological hypertrophy	31
1.1.5.3 Phenotypic characterization of cardiac hypertrophy	32
1.2 Molecular levels of stress regulation post transcription	33
1.2.1 Post-transcriptional regulation	35
1.2.1.1 Interactome capture as a systemic approach to measure RBPs	35
1.2.1.2 RIC discovers atypical RBPs	36
1.2.1.3 Dynamic interactome capture - state of the art	37
1.2.1.4 Post-transcriptional regulation in disease	37
1.2.1.5 Aims	38
1.2.2 Proteostatic regulation	39
1.2.2.1 mTOR as main regulator of cell growth during cardiac hypertrophy	39
1.2.2.1.1 MTOR promotes anabolic processes	40
1.2.2.1.2 MTOR inhibits catabolic processes	41
1.2.2.2 The interplay of mTORC1 and the ubiquitin-proteasome system (UPS)	42
1.2.2.3 Selective inhibition of mTOR by Pras40 - a gene therapeutic option?	43
1.2.2.4 Aims	45
2. MATERIALS	47
2.1 Reagents	47
2.2 Antibodies and staining	50
2.2.1 Western blot analysis	50
2.2.2 Immunofluorescence staining/ Immunohistochemistry	52
2.2.3 Other staining reagents	52
2.3 Enzymes	52

2.4 Kits.....	53
2.5 Nucleic acids.....	54
2.5.1 Primers.....	54
2.5.1.1 Mouse.....	54
2.5.1.2 Rat.....	55
2.5.2 siRNA.....	55
2.5.3 Plasmids.....	55
2.6 Consumables.....	56
2.7 Lab equipment.....	58
2.8 Buffer and solutions.....	59
2.8.1 Buffers for general use.....	59
2.8.2 Cell culture media and solutions.....	59
2.8.2.1 NRVCM preparation and culture.....	59
2.8.2.2 Adult cardiomyocyte preparation and culture.....	61
2.8.2.3 Murine embryonic fibroblast preparation and culture.....	61
2.8.3 Buffers and solutions for molecular biological and biochemical methods.....	62
2.8.3.1 Buffers for protein analysis.....	62
2.8.3.2 RIP-Seq buffers.....	63
2.8.3.3 Ribosome profiling/ RiboSeq buffers.....	63
2.8.3.4 Interactome capture buffers.....	63
2.8.3.5 Buffer and solutions for histology.....	64
2.8.3.6 Agarose gel electrophoresis buffers.....	65
2.9 Software.....	65
3. METHODS.....	67
3.1 Animal procedures.....	67
3.1.1 Pas40 KO mice.....	67
3.1.2 RiboTag mouse.....	67
3.1.3 Cpeb4 KO mice.....	67
3.1.4 Genotyping of mice.....	67
3.1.5 Transverse aortic constriction (TAC) surgery.....	69
3.1.6 Swimming regime.....	69
3.1.7 Echocardiography.....	70
3.1.8 Puromycin incorporation assay.....	70
3.1.9 Organ isolation for lysis.....	70
3.1.10 Isolation of hearts for histology.....	71

3.1.11 Histological methods	71
3.1.11.1. Preparation of histological sections	71
3.1.11.2 Hematoxylin-Eosin staining	71
3.1.11.3 Masson trichrome staining	72
3.1.11.4 Immunohistochemistry	72
3.1.12 Isolation of primary cells	73
3.1.12.1 Isolation of murine adult cardiomyocytes.....	73
3.1.12.2 Isolation of ventricular cardiomyocytes of neonatal rats	74
3.1.12.3 Isolation of murine embryonic fibroblasts (MEFs).....	75
3.2 Cell culture methods	76
3.2.1 Thawing of cells	76
3.2.2 Trypsinizing/ Singularizing of cells.....	76
3.2.3 Counting of cells.....	76
3.2.4 Freezing of cells.....	77
3.2.5 Transfection with HiPerfect to induce knock-down in vitro	77
3.2.6 Viral transduction.....	77
3.2.7 Phenylephrine treatment	77
3.2.8 Actinomycin D assay	78
3.2.9 Cell size in vitro and in vivo.....	78
3.3 Molecular biological methods	78
3.3.1 RNA isolation from eukaryotic cells	78
3.3.1.1 Qiagen RNeasy Kit	78
3.3.1.2 Zymo RNA isolation kit.....	78
3.3.1.3 Phenol-Chloroform-extraction	79
3.3.2 Reverse transcription of RNA	79
3.3.3 Relative quantification of cDNA by real-time PCR	79
3.3.4 Protein isolation and quantification	80
3.3.5 Western blotting	81
3.3.6 Ponceau staining	82
3.3.7 Silver stain	82
3.3.8 Immunofluorescence staining	83
3.3.9 Proximity ligation assay	83
3.3.10 Proteasome activity assay	83
3.3.11 Immunoprecipitation.....	84
3.3.12 mRNA interactome capture (RIC).....	85

3.3.13 RNA-Immunoprecipitation.....	85
3.3.14 RIP-Seq analysis.....	86
3.3.15 Isolation of monosomes for RiboSeq of NRVCM samples.....	86
3.3.16 Precipitation of ribosomes for RiboSeq of in vivo RiboTag samples.....	87
3.3.17 Library generation for RiboSeq.....	87
3.3.18 Proteomic analysis.....	87
3.3.18.1 Sample preparation and TMT labeling.....	87
3.3.18.2 Mass spectrometry data acquisition.....	88
3.3.18.3 Mass spectrometry analysis.....	89
3.4 Functional analysis.....	90
3.5 Statistics.....	90
4. RESULTS I.....	91
4.1 mRNA interactome capture in primary cardiomyocytes.....	91
4.2 The cardiac RBPome.....	93
4.3 The dynamic cardiac RBPome during cardiac growth and homeostasis.....	96
4.4 Dynamic binding of RBPs during cardiac growth.....	98
4.5 Analysis of Cpeb4 as dynamically regulated RBP during pathological hypertrophy.....	100
4.5.1 Validation of Cpeb4 as dynamic binder.....	100
4.5.2 Cpeb4 during pathological cardiac growth in vitro in NRVCM.....	101
4.5.3 Cardiac phenotype of Cpeb4-depleted mice.....	102
4.6 Identification of Cpeb4 target mRNAs during growth and homeostasis.....	103
4.7 Identification of translationally regulated Cpeb4 target mRNAs in vitro and in vivo.....	104
4.8 Validation of differentially translated Cpeb4- bound target genes.....	107
5. DISCUSSION I.....	111
5.1 First compendium of RBPs in primary cardiomyocytes.....	112
5.2 First cardiac, dynamically regulated RBPome in homeostasis versus pathological cardiac hypertrophy.....	113
5.3 Cpeb4 is dynamically regulated during pathological hypertrophy and is critically involved in the adaptation to cardiac stress.....	114
5.4 Cpeb4 binding to mRNA of transcription factors suppresses their translation and inhibits onset of pathological gene expression.....	115
5.5 During pathological growth, Cpeb4 releases Zeb1 to activate expression of growth-related regulatory cascade.....	116
5.6 Conclusion and outlook.....	116
6. RESULTS II.....	119

6.1 Phenotyping of novel Pras40 KO for cardiac growth and function during cardiac hypertrophy	119
6.1.1 Validation of Pras40 knock-out in two novel mouse models	120
6.1.2 Phenotype of Pras40 KO during pathological and physiological hypertrophy	121
6.1.2.1 Phenotype of global Pras40 KO after TAC	122
6.1.2.2 Phenotype of global Pras40 KO after swimming	124
6.1.2.3 Phenotype of cardiomyocyte- specific Pras40 KO after TAC	125
6.1.2.4 Phenotype of cardiomyocyte-specific Pras40 KO after swimming	127
6.2 mTOR signaling upon depletion of Pras40 during pathological hypertrophy	128
6.2.1 mTOR activity upon Pras40 KO basally and during pathological growth	128
6.2.2 Upstream activation of mTOR to rescue signaling after deletion of Pras40	130
6.3 Effects of Pras40 deletion on translation	132
6.3.1 Overall translation upon depletion of Pras40 during pathological hypertrophy	132
6.3.2 System-wide analysis of differentially translated RNAs in Pras40 KO mice	133
6.3.3 Functional analysis of differentially translated genes in Pras40-depleted hearts	135
6.3.4 Validation of differentially translated UPS-related genes after Pras40 KO	137
6.4 Effects of Pras40 KO on proteasomal function	138
6.4.1 Analysis of 26S proteasomal activity and function in vitro and in vivo	138
6.4.2 Analysis of ubiquitination, protein aggregation and proteasomal activity in vitro ...	139
6.4.3 Re-activation of proteasome activity after TAC in Pras40 KO	140
6.5 Analysis of mTOR-Pras40 interaction during pathological hypertrophy	142
6.5.1 Effects of mTOR-released Pras40 on mTOR signaling and UPS abundance	143
6.5.2 Effects of mTOR-bound versus -released Pras40 to 26S proteasomal function	145
6.5.3 Heart function upon overexpression of mTOR-released Pras40 after TAC	145
7. DISCUSSION II	148
7.1 Pras40- the role in cardiac hypertrophy and state of the art	149
7.2 Loss of Pras40 leads to unexpected inhibition of cardiac growth and loss of cardiac function upon hypertrophic stimuli	151
7.3 Lack of Pras40 in the heart leads to attenuated mTOR activity and translation	152
7.4 Possible causes for mitigated mTOR activity in Pras40 KO	154
7.5 Pras40 critically affects proteasomal function when released from mTOR, and re-activation of the proteasome restores function in Pras40 KO mice	156
7.6 The interplay between mTORC1 and the proteasome	158
7.8 Conclusion and outlook	160
V. BIBLIOGRAPHY	163
VI. SUPPLEMENTAL FIGURES	179

VII. PUBLICATIONS185
VIII. CONTRIBUTIONS189
IX. ACKNOWLEDGMENTS191

I. LIST OF FIGURES & TABLES

Figure 1.1:	Scheme of cardiac hypertrophy.....	28
Figure 1.2:	Transverse aortic constriction method.....	30
Figure 1.3:	Levels of gene expression regulation and their relative contribution.....	33
Figure 1.4:	Overview of RIC method.....	36
Figure 1.5:	The mTORC1 during physiological or pathological growth.....	41
Figure 1.6:	The interplay between mTOR and Pras40 during starvation and growth....	44
Figure 2.1:	PCR products of genotyping PCRs.	68
Figure 4.1:	mRNA interactome capture in primary cardiomyocytes.....	92
Figure 4.2:	The RBPome and total proteome of NRVCMs.....	93
Figure 4.3:	The cardiac RBPome in comparison to other RBPomes.....	94
Figure 4.4:	Scheme of cardiomyocyte-specific RBPs and their localization within cardiomyocytes.....	96
Figure 4.5:	RIC analysis of RBPs during cardiac growth and homeostasis.....	97
Figure 4.6:	The dynamic cardiac RBPome during cardiac growth and homeostasis...	98
Figure 4.7:	Dynamic binding capacities of RBPs during cardiac growth.....	99
Figure 4.8:	Validation of Cpeb4 as a Class IV “dynamic binder“.....	100
Figure 4.9:	Cpeb4 controls cell growth <i>in vitro</i>	101
Figure 4.10:	Cpeb4 controls cell growth <i>in vivo</i>	102
Figure 4.11:	RIP-Seq reveals target mRNAs of Cpeb4 during homeostasis and pathological growth.....	104
Figure 4.12:	RiboSeq of Cpeb4-depleted versus control NRVCMs.....	105
Figure 4.13:	Translationally regulated target mRNAs of Cpeb4	106
Figure 4.14:	Validation of Cpeb4-binding DEGs and their transcriptional and translational regulation.....	107
Figure 4.15:	Cpeb4 shows repressive effect on the translation of transcription factors..	109
Figure 4.16:	Cpeb4 binds and represses translation of Zeb1 to inhibit pathological gene expression.....	110
Figure 6.1:	Knock-out models for Pras40-depleted mice.....	121
Figure 6.2:	Pathological hypertrophy induction in a global Pras40 KO model.....	123
Figure 6.3:	Physiological hypertrophy induction in a global Pras40 KO model.....	124

Figure 6.4:	Pathological hypertrophy induction in a conditional, Tamoxifen-inducible, cardiomyocyte-specific Pras40 KO model.....	126
Figure 6.5:	Physiological hypertrophy induction in a conditional, Tamoxifen-inducible, cardiomyocyte-specific Pras40 KO model.....	128
Figure 6.6:	mTOR activation and overall translation are blunted basally and after TAC surgery in Pras40 KO.....	129
Figure 6.7:	mTOR activation can be rescued by KD of TSC2 upstream of mTOR.....	131
Figure 6.8:	Overall translation is blunted after TAC surgery in Pras40 KO.....	133
Figure 6.9:	RiboSeq of Pras40-depleted to determine actively translating RNAs.....	134
Figure 6.10:	Quality control and preprocessing of RiboSeq library.....	135
Figure 6.11:	Functional analysis of translationally regulated, Pras40-dependent genes...	136
Figure 6.12:	List of DEGs and validation of translationally regulated, Pras40-dependent genes.....	137
Figure 6.13:	Pras40 KO blunts 26S proteasomal activity <i>in vivo</i> after TAC and <i>in vitro</i> and leads to protein aggregation.....	138
Figure 6.14:	Pras40 KO leads to poly-ubiquitination and aggregation of proteins <i>in vivo</i> and significantly deteriorated proteasomal activity <i>in vitro</i>	139
Figure 6.15:	Reactivation of proteasomal activity rescues severe phenotype of TAC-subjected Pras40 KO mice.....	141
Figure 6.16:	Pras40 binds mTOR in homeostasis but is released from mTOR during pathological growth <i>in vivo</i> and <i>in vitro</i>	143
Figure 6.17:	Mutant Pras40 without mTOR-interacting FRB domain is released from mTOR and does not inhibit mTOR downstream signaling.....	144
Figure 6.18:	Reactivation of proteasomal activity by delivery of Pras40-FRB rescues severe phenotype of TAC-subjected Pras40 KO mice.....	146

Figure S1:	PE treatment of NRVCMs for dynamic RBPome.....	179
Figure S2:	RIP-Seq of PE-treated versus control (mock) NRVCMs.....	179
Figure S3:	Ribo-Seq of Cpeb4 KD versus control NRVCMs.....	180
Figure S4:	Cpeb4 target Zeb1.....	181
Figure S5:	Enzymes and metabolic enzymes in the basal RBPome.....	181
Figure S6:	Quality control of RiboSeq of Pras40 KO versus WT hearts.....	182
Figure S7:	Overview and first analysis of RiboSeq and RNASeq libraries.....	183
Figure S8:	Signaling in FRB-overexpressing WT and Pras40 KO mice after TAC.....	184
Table 1:	Antibodies with supplier and order number, that were used for Western blot analysis.....	51
Table 2:	Antibodies with supplier and order number, that were used for Immunofluorescence staining/ Immunohistochemistry.....	52
Table 3:	Mouse Primers used for qRT-PCR, sequences are shown 5'-3'	54
Table 4:	Mouse Primers used for genotyping PCRs, sequences are shown 5'-3'	54
Table 5:	Rat Primers used for qRT-PCR, sequences are shown 5'-3'	55
Table 6:	Inhibitors and substrates to measure chymotrypsin-like, trypsin-like and caspase-like 26S proteasomal activities.....	84

II. ABBREVIATIONS

ACM	Adult primary cardiomyocyte
AdCtrl.	Adenovirus control, without coding insert
AdFRB	Adenovirus encoding for Pras40 mutant, lacking the FRB-interacting domain
AdPA28 α	Adenovirus encoding for proteasomal activator PA28 α
AdWT	Adenovirus encoding for WT Pras40
aMHC	alpha-myosin heavy chain
ATP	Adenosine triphosphate
AV	Adenovirus
AAV	Adeno-associated virus
BSA	Bovine serum albumine
cDNA	complementary DNA
CHX	Cycloheximide
cKO	conditional Pras40 KO
clip	cross-linked
cm	Centimeter
Col1a1	Collagen type I alpha 1 chain
CPE	Cytoplasmic polyadenylation element
Cpeb4	Cytoplasmic polyadenylation element binding protein
CreER ^{t2}	Cre recombinase (Cre) fused to a mutant estrogen ligand-binding domain (ER ^{t2})
Ct	cycle threshold
DAPI	4',6-Diamidino-2- phenylindole
DEG	Differentially expressed gene
DEPC	Diethyl pyrocarbonate
Deptor	DEP domain-containing mTOR-interacting protein
DMEM	Dulbecco's Modified Eagle Medium

DMSO	Dimethyl sulfoxide
DNA	Deoxyribonucleic acid
DNase I	Deoxyribonuclease I
dNTP	Nucleoside triphosphate
dRFU	delta of relative fluorescent units
ECL	Enhanced Chemiluminescence
EF	Ejection fraction
EDTA	Ethylene diamine tetra- acetic acid
e.g.	exempli gratia (for example)
eIF4E	Eukaryotic translation initiation factor 4E
ER	Endoplasmic reticulum
Erk5	Mitogen-activated protein kinase 7
ES cells	embryonic stem cells
et al.	Et alii (and others)
FC	Fold change
FCS	Fetal calf serum
FDR	False discovery rate
FRB	FKBP-rapamycin-binding domain
FS	Fractional shortening
for	forward
g	Gram
Gapdh	Glyceraldehyde 3-phosphate dehydrogenase
GO	Gene ontology
h	Hour
HBSS	Hanks' balanced salt solution
HE	Hematoxilin Eosin
HEPES	4-(2-Hydroethyl)-1- piper-azineethane- sulfonic acid
HF	Heart failure
Hprt	Hypoxanthine phospho- ribosyltransferase 1

IgG	Immunoglobulin G
IP	Immunoprecipitation
JNK	c-Jun N-terminal kinase
kg	Kilogram
KD	Knock-down
KO	Knock-out
l	Liter
lc3b	Microtubule-associated proteins 1A/1B light chain 3B
LiDS	Lithium dodecyl sulfate
log2	Logarithm to the base 2
logFC	Logarithmic fold change
LV	Left ventricle
m	Meter
mm	Millimeter
M	Molar concentration
μ	Micro
Mapk	Mitogen associated protein kinase
MEF	Murine embryonic fibroblast
Mhc	Myosin heavy chain
Mio	Million
min	Minute
mol	Mole
mRNA	Messenger RNA
MsrB3	Methionine-R-sulfoxide reductase B2
mTOR	Mammalian target of Rapamycin
mTORC1	Mammalian target of Rapamycin complex 1
Myh7	Myosin heavy chain
n	Sample size
N ₂	Nitrogen

NaCl	Sodium chloride
NaOH	Sodium hydroxide
neg	negative
nm	Nanometer
nppa	Natriuretic precursor peptide a
nppb	Natriuretic precursor peptide b
Nrf1	Nuclear respiratory factor 1
NRVCM	Neonatal rat ventricular myocyte
nt	Nucleotide
p	p-value
PA28 α	Proteasome activator complex subunit 1, alias: PSME1
PAGE	Polyacrylamide gel electrophoresis
PBS	Phosphate-buffered Saline
PCR	Polymerase chain reaction
PE	Phenylephrine
PFA	Paraformaldehyde
PGC-1 α	Peroxisome proliferator-activated receptor gamma coactivator 1-alpha
PI3K	Phosphoinositide 3-kinase
Pras40	Proline-rich Akt-substrate of 40KDa/ Proline-rich Akt substrate 1
P/S	Penicillin/Streptavidin
PVDF	Polyvinylidene difluoride
Raptor	Regulatory-associated protein of mTOR
RBD	RNA-binding domain
RBP	RNA-binding protein
rev	reverse
ribS6	Ribosomal protein S6
Ribo-Seq	Ribosome sequencing
RIC	RNA-interactome capture
RIP	RNA- immunoprecipitation

RIP-Seq	RNA- immunoprecipitation sequencing
RNA	Ribonucleic acid
Rnase	Ribonuclease
RNA-Seq	RNA sequencing
Rpl22	60S ribosomal protein L22
rRNA	Ribosomal RNA
RT	Room temperature
RT-qPCR	Quantitative reverse transcription PCR
RV	Right ventricle
S6K	Ribosomal protein S6 kinase beta-1
SDS	Sodium dodecyl sulfate
sec	Second
Ser	Serine
siRNA	Small interfering RNA
TAC	Transverse aortic constriction
TAM	Tamoxifen
TBS	Tris-buffered saline
TBS-T	Tris-buffered saline-Tween
TE	Tris-EDTA
Thr	Threonine
TMT	Tandem mass tag
TNB	Tris-NaCl-blocking buffer
TOS	TOR signaling motif
TSC2	Tuberous Sclerosis complex subunit 2
U	Unit for enzymatic activity in $\mu\text{mol}/\text{min}$
Ubr	Ubiquitin-protein ligase E3 component n-recognin
Ulk1	Unc-51 like autophagy activating kinase
UPS	Ubiquitin-proteasome-system
UTR	Untranslated region

V	Volt
WGA	Wheat germ agglutinin
WT	Wild type
Ybx-1	Y box binding protein 1
YTHDF2	YTH domain family 2
Zbtb20	Zinc finger and BTB domain-containing protein 20
Zeb1	Zinc finger E-box-binding homeobox 1
2D	Two dimensional
4EBP1	Eukaryotic translation initiation factor 4E-binding protein 1
18S	18S ribosomal RNA

III. ABSTRACT

1. Identification of dynamic RNA-binding proteins in primary cardiomyocytes uncovers Cpeb4 as a regulator of cardiac growth

Mutations or decreased expression of mRNA-binding proteins (mRBPs) can lead to cardiomyopathies in humans. The present study defined the first compendium of dynamically binding mRBPs in healthy versus diseased primary cardiomyocytes at a system-wide level by RNA interactome capture. Among these mRBPs, Cytoplasmic polyadenylation element binding protein 4 (Cpeb4) was defined as a dynamic mRBP in diseased cardiomyocytes, and was found to regulate cardiac growth both *in vitro* and *in vivo*. To investigate the functions of Cpeb4 in cardiomyocytes, mRNAs bound to and regulated by Cpeb4 were identified. These data implicate that Cpeb4 regulates transcriptional activity by differential translation of transcription factors involved in cellular remodeling in response to pathological growth stimulation. Among Cpeb4 target RNAs, two Zinc finger transcription factors (Zeb1 and Zbtb20) were identified. The present study shows that Cpeb4 regulates the translation of these mRNAs and that Cpeb4 depletion increases their expression. Thus, Cpeb4 emerges as critical regulator of myocyte function by differential binding of specific mRNAs in response to pathological growth stimulation.

2. mTOR-proteasomal dysfunction following deletion of Pras40 inhibits cardiac growth but results in cardiac failure

The mammalian target of Rapamycin complex 1 (mTORC1) increases cell size by initiating translation as well as by inhibiting catabolic functions such as proteolysis and autophagy. A previous study from our lab proposed Proline-rich Akt substrate 1 (Pras40) as a cardioprotective, endogenous inhibitor of mTOR-dependent protein synthesis during pathological growth. Pras40 is released from mTORC1 during growth, but other interactions are largely unknown. The present study aims at understanding the molecular mechanism of Pras40 to cardiac growth and function. To test consequences of Pras40

deletion on cardiac function *in vivo*, two novel Pras40 knock-out mice were subjected to pathological and physiological hypertrophy (Transverse aortic constriction, swimming). Conversely to Pras40 overexpression, growth was significantly blunted in KO animals and function reduced. mTORC1 signaling as well as proteasomal function were severely disturbed in KO animals. Mechanistically, chymotrypsin-like 26S proteasomal activity was blunted in KO hearts as well as isolated cardiomyocytes from KO animals. Disturbed proteasomal function in KO mice lead to severe alterations in metabolic functions highlighting the importance of both intact mTORC1 signaling and proper proteasomal maintenance during cardiac stress. Reactivation of proteasomal activity *in vivo* in KO mice restored cardiac function to WT levels, and overexpression of mutant, mTOR-released Pras40 had a similar effect. The present study provides evidence that Pras40 links anabolic protein synthesis and catabolic proteolysis in the heart: At rest, Pras40 binds and inhibits mTOR, but when released during pathological growth, Pras40 directly interacts with the 26S proteasome and modulates its activity.

IV. ZUSAMMENFASSUNG

1. Identifizierung dynamischer RNA-bindender Proteine in primären Kardiomyozyten in Homöostase und pathologischem Herzwachstum

Mutationen oder verringerte Expression von mRNA-bindenden Proteinen (mRBPs) sind in der Lage Kardiomyopathien zu verursachen. In der vorliegenden Studie ist es gelungen durch „RNA Interactome Capture“ (RIC) ein Kompendium mRNA-bindender Proteine zu bestimmen, die im gesunden oder kranken Myokard dynamisch an mRNAs binden. Mit Hilfe von RIC wurde das Cytoplasmatische polyadenylation element binding protein 4 (Cpeb4) als dynamisch bindendes RBP in hypertrophen Kardiomyozyten detektiert, welches Herzwachstum *in vitro* und *in vivo* reguliert. Um die Funktion von Cpeb4 in Kardiomyozyten zu untersuchen, wurden mRNAs untersucht, die von Cpeb4 gebunden und durch das Protein reguliert werden. Wir konnten zeigen, dass Cpeb4 die Translation von Transkriptionsfaktoren beeinflusst, die in pathologischen Umbauprozessen im Herzen beteiligt sind. Unter diesen von Cpeb4 gebundenen mRNAs befanden sich zwei Zinkfinger-Transkriptionsfaktoren, Zeb1 und Zbtb20. Wir konnten zeigen, dass Cpeb4 die Translation dieser mRNAs reguliert und dass Depletion von Cpeb4 ihre Expression steigert. Cpeb4 wurde somit als essentieller Regulator der Kardiomyozytenfunktion etabliert, der als Reaktion auf Wachstumsstimuli im Herzen spezifische mRNAs differentiell bindet und deren Translation beeinflusst.

2. mTOR-Proteasomale Dysfunktion nach Deletion von Pras40 inhibiert kardiales Wachstum und führt zu Herzversagen

Der „Mammalian Target of Rapamycin“ (mTOR) induziert Zellwachstum, indem er Translation initiiert und katabolische Prozesse wie Autophagie inhibiert. In einer vorhergehenden Studie wurde das „Proline-rich Akt substrate 1“ (Pras40) als kardioprotektiver, endogener Inhibitor mTOR-abhängiger Proteinsynthese während pathologischer Herzhypertrophie vorgestellt. Pras40 wird unter Wachstumsbedingungen durch Phosphorylierung von mTOR gelöst, andere mTOR-unabhängige Interaktionen sind jedoch nicht bekannt. Im Zuge der vorliegenden Studie sollte daher der molekulare

Mechanismus, über den Pras40 Herzwachstum und -funktion reguliert, untersucht werden. Um die Auswirkung einer Depletion von Pras40 auf die Herzfunktion *in vivo* zu testen, wurden zwei neue Knockout Mausmodelle auf ihren kardialen Phänotyp untersucht und dafür pathologischer oder physiologischer Hypertrophie ausgesetzt. (Transverse Aortenkonstriktion oder Ausdauerschwimmen). Im Gegensatz zur vorhergehenden Überexpressionsstudie war das Herzwachstum ohne Pras40 signifikant verringert, die Herzfunktion jedoch verschlechtert und pathologische Umbauprozesse erhöht. Die mTORC1 Signalkaskade, die sowohl Translation als auch Autophagie reguliert, sowie die Funktion des Proteasoms waren in Pras40 KO Tieren empfindlich gestört. Chymotrypsin-artige, 26S proteasomale Aktivität war sowohl in KO Herzen also auch in isolierten Kardiomyozyten aus KO Mäusen stark verringert. Überexpression einer mutanten Variante von Pras40, die nicht an mTOR bindet, führte zur Steigerung der proteasomalen Aktivität in Kardiomyozyten. Gestörte proteasomale Funktion führte in KO Mäusen zu schweren Störungen metabolischer Funktionen und verdeutlichte die Bedeutung einer intakt koordinierten mTOR Signalkaskade sowie proteasomaler Balance im gestressten Herzen. Die Reaktivierung proteasomaler Aktivität *in vivo* war in der Lage die Herzfunktion erheblich zu steigern. Dies ist als Hinweis zu sehen, dass dieser Mechanismus kausal für den erheblich veränderten Phänotyp im Pras40 KO Herzen ist. Überexpression von mutantem, mTOR-unabhängigem Pras40 hatte einen ähnlich förderlichen Effekt. In dieser Studie konnte zusammenfassend gezeigt werden, dass Pras40 anabole und katabole Prozesse im Herzen koordiniert: In Homöostase bindet Pras40 an mTOR und inhibiert seine Aktivität, während pathologischem Herzwachstum reguliert es das 26S Proteasom and moduliert seine Aktivität.

1. INTRODUCTION

Despite their diverse etiologies, pathological stimuli to the heart in many cases lead to a compensatory attempt to balance elevated stress levels and in the following to growth of the heart (cardiac hypertrophy, further described in 1.1.3). The activated molecular pathways are mostly ubiquitously expressed and therefore hard to manipulate pharmacologically due to severe side- and off-target effects. Tailored, genetically modifying treatment options that tackle critical nodal points in these pathways are therefore needed to generate genuinely disease-modifying drugs. Research has to date been to a vast majority focussed on genetic mutations that lead to inheritable cardiac diseases or on transcriptional changes that are linked to the onset of disease. Levels beyond transcription, such as post-transcriptional control and gene expression regulation controlled by levels of protein turnover have largely been disregarded, partly due to a lack of appropriate methodology.

This work is built up by two major pillars. The **first part** aims at understanding how post-transcriptional control can regulate the outcome of cardiac disease. A systemwide approach to detect RNA-binding proteins, the major driving forces of post-transcriptional control, is applied in conditions of homeostasis and cardiac growth and will help to understand networks of dynamic, post-transcriptional control. The **second part** of the thesis tries to understand regulation of gene expression in cardiac disease post transcription, namely from protein translation to decay. The focus will lie on one major pathway involved in the regulation of translational control in the onset of cardiac growth, the mammalian Target of Rapamycin. We will investigate a molecular partner, Pras40, which has previously been linked to a beneficial outcome of cardiac failure. As a potential gene therapy option, we aim at understanding the molecular mechanism by which Pras40 intervenes in the onset and progression of cardiac failure.

A specific introduction, results section and discussion for the first part of the thesis can be found in 1.2.1, 4. and 5. respectively. Part two is described in 1.2.2 (specific introduction), 6. (results) and 7 (discussion).

1.1 General Introduction

The following paragraphs will give a general background to understand the mechanisms of cardiac disease, the molecular mechanisms that lead to cardiac failure, as well as the mechanisms that are commonly applied to study cardiac hypertrophy.

1.1.1 Cardiovascular disease and heart failure - background

Cardiovascular diseases and above all heart failure (HF) are the number one cause of hospitalization and death worldwide with 17,9 Million deaths per year (2016), displaying around 30% of all deaths (WHO, 2019). Prevalence increases with age, reaching 8.4% in those aged 75 years or older compared with 0.7% in those patients that are 45 to 54 years of age (Redfield et al., 2003). 23 Million patients world-wide live with heart failure.

HF is a disease with manifold etiologies. Main causes to develop cardiovascular diseases, above all raised blood pressure, blood glucose and blood lipids, as well as overweight and obesity are caused by lifestyle factors such as unhealthy diet, physical inactivity, tobacco use and harmful use of alcohol. To date, therapy options mainly include simultaneous administration of vasodilating, dialysing, and heart rate slowing drugs that alleviate symptoms such as shortness of breath, edema, dizziness, and nausea and decrease the morbidity of heart failure. Still, there are no 'disease modifying' treatment options that erase the primary causes of cardiac failure (Breckenridge, 2010). Given these limited treatment choices, HF stays a life threatening clinical syndrome with a 30-day mortality around 10% and 5-year mortality of 45–75%, after diagnosis of HF (Bleumink et al., 2004; Goldberg et al., 2007; Levy et al., 2002).

1.1.2 The anatomy of the heart

The main task of the cardiovascular system - namely heart, blood and vessels - is the transport of oxygen, nutrients, neurotransmitters and hormones to their distal destinations in the body, but also the regulation of body temperature, blood pH and clearance of virus. The heart works as an autonomous muscular pump, maintaining the flow of blood into the periphery and back. The heart is a hollow organ, being built up by four cavities: Left

atrium and ventricle supply blood through the aorta to the systemic circuit, whereas right atrium and ventricle provide blood to the smaller lung circuit (Piper et al., 2010; Opie LH, et al. 2012).

The walls of the heart are built up from three different layers, the epicardium (external layer), the myocardium (middle layer) and the endocardium (inner layer). The epicardium, a thin layer of connective tissue makes up the outer layer of the heart walls. The endocardium, composed of endothelium, lines the inside of the chambers of the heart and covers the valves. Between these two outer layers lies the myocardium, comprised of cardiac muscle tissue. The heart muscle cells or cardiomyocytes account for the majority of the cardiac wall and are responsible for its pump function. Cardiomyocytes are large cells, making up around 80% of the heart mass but only 25-35% of the heart cells (Bergmann et al., 2015). The cardiovascular system is dynamically regulated through its cardiomyocytes, to be able to react to changes in acute and chronic demands.

1.1.3 Cardiac hypertrophy and remodeling

Cardiomyocytes are highly specialized cells that are responsible for maintaining cardiac function. As terminally differentiated cells, they are unable to divide and have a very limited regenerative potential. Long-term changes in work load of the heart are typically compensated by hypertrophic enlargement, which is characterized by an increase in the size of individual cardiomyocytes. Independent of the etiology, initially, cardiac hypertrophy induces a state of ‘compensated hypertrophy’ that counteracts elevated needs by increasing cardiac pump function and decreasing ventricular wall tension (Berenji et al., 2005). Depending on the origin of the growth stimulus, there are two major forms of cardiac hypertrophy:

As part of a pathological process, chronic pressure or volume overload in a disease setting, such as hypertension and valvular disease, myocardial infarction or inherited genetic mutations lead to pathological cardiomyocyte growth, going along with cardiomyocyte death, increased fibrosis and loss of cardiac output (Fig. 1.1). With time, pathological growth leads to weakening of cardiac muscle cells and dilation of the

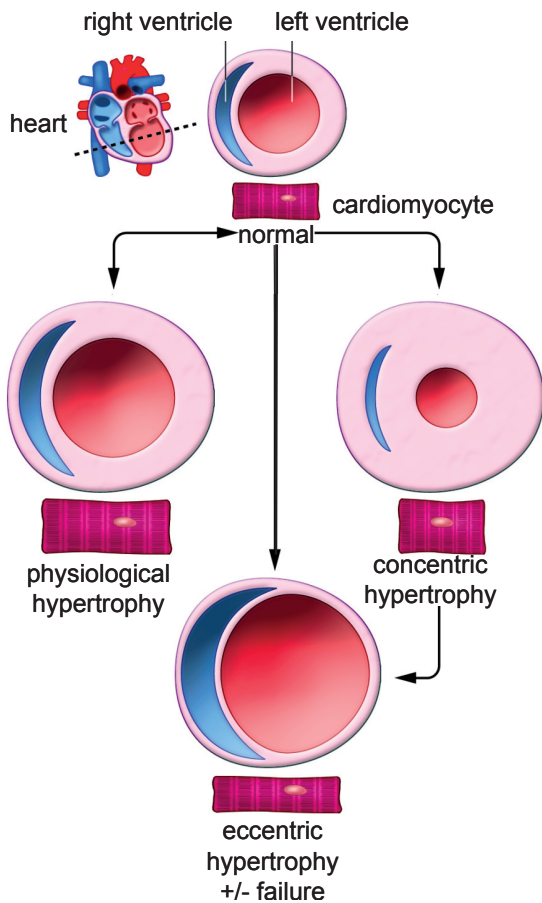


Figure 1.1: Scheme of cardiac hypertrophy. Depending on the etiology of the stimulus, the heart chamber compensates elevated work load by hypertrophy. Physiologic hypertrophy goes along with proportional chamber and wall enlargement, whereas pathological hypertrophy can be concentric, following pressure overload, leading to elevated wall thickness and smaller chamber diameter, or eccentric, following volume overload, leading to thinning of the ventricular walls and elevated chamber diameter. From Van Berlo et al., (2013).

ventricular walls. Terminally, dilated cardiac hypertrophy leads to heart failure and cardiac death. Pathological hypertrophy is an irreversible process (Heineke and Molkentin, 2006).

Depending on the etiology of the stimulus, pathological hypertrophy can be divided into concentric or eccentric hypertrophy (Shimizu and Minamino, 2016): Concentric hypertrophy is induced by pressure overload (e.g. hypertension or aortic stenosis) that generates an increase in systolic wall stress. It is defined by an increase in relative wall thickness and cardiac mass, leading to a small reduction or no change in chamber volume.

Sarcomeres are added in parallel and lead to an increase in myocyte cell width. Eccentric hypertrophy is induced by volume- rather than pressure overload (e.g. aortic regurgitation, aortic fistulas), leading to an increase in diastolic wall stress. Eccentric hypertrophy is linked to an increase in cardiac mass with increased chamber

volume, whereas relative wall thickness can be unchanged, decreased, or increased. During eccentric hypertrophy, sarcomeres are added in series and lead to an increase in cardiomyocyte length. In these settings of disease, chronic eccentric hypertrophy is typically associated with thinning of the ventricular walls.

As a physiological process, cardiac growth can be observed during development, in endurance athletes or during pregnancy, being mild and/or reversible. Physiological hypertrophy leads to maintained or elevated function and cardiac output and does not go along with scar formation (Dickhuth et al., 2004). Physiological growth can as well be induced by volume or pressure overload, e.g. by pregnancy or development, versus weight lifting or static strength training, but growth is correlated with a more proportional change in wall thickness. Physiological hypertrophy is a reversible process. The cardiac morphological changes in cavity diameter, heart mass and wall thickness as well as scar tissue formation are commonly referred to as cardiac remodeling (Cohn et al., 2000).

1.1.4 Molecular mechanisms of cardiac growth and remodeling

Molecularly, two major forms of initiating stimuli lead to the onset of cardiac hypertrophy: Biomechanical and stretch-sensitive mechanisms, or neurohumoral mechanisms that are closely linked to the release of hormones, cytokines, chemokines and peptide growth factors (Heineke and Molkentin, 2006). Whereas biomechanical stimuli are sensed by internal stretch-sensitive receptors, ligands are sensed by the cells through G-protein coupled receptors, receptors with intracellular tyrosine-kinase domains or serine/threonine kinase domains as well as gp130-linked receptors. Both molecular interplays lead to the activation of a relatively small number of molecular pathways that result in the onset of the remodeling process. Among these are the IGF1 - phosphoinositide 3-kinase [PI3K, (p110 α)]-Akt pathway and G α q signaling (downstream of G protein-coupled receptors (GPCR). Physiological hypertrophy has been linked to the gp130/JAK/STAT pathway, whereas pathological hypertrophy has been associated with abnormalities leading to enhanced PI3K(p110 γ), mitogen activated protein kinases (MAPKs), protein kinase C (PKC) and D (PKD) (Heineke and Molkentin, 2006). A more detailed description of pathways involved in cardiac hypertrophy will also be given in 1.2.2.1.

Remodeling of the heart walls goes along with differential expression of genes that are under homeostatic conditions only expressed during embryonic development. These genes include the genes for natriuretic precursor peptides a and b (Nppa and Nppb) and fetal contractile protein Myosin heavy chain (MHC), which undergoes an isoform switch from the adult α to the fetal β form during cardiac remodeling (Chien et al., 1993). The so called fetal gene program becomes re-activated only during pathological cardiac hypertrophy and serves as a prognostic marker system to predict clinical severity (Shepherd and Kahn, 1999).

1.1.5 Model systems for cardiac hypertrophy

Several *in vitro* and *in vivo* models are commonly used to study cardiac hypertrophy and its underlying molecular events.

1.1.5.1 Pathological hypertrophy

The experimental model to induce pathological cardiac hypertrophy *in vivo* used in this study is a surgical technique that mechanically elevates the work load in the heart. This technique, named transverse aortic constriction (TAC, Fig. 1.2), is based on a constriction of the aorta between brachiocephalic and left common carotid arteries to a

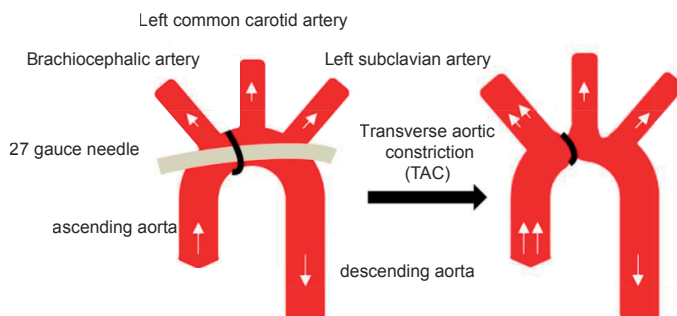


Figure 1.2: Transverse aortic constriction method (TAC). During TAC surgery, the aorta is occluded mechanically between brachiocephalic and left subclavian artery to induce pressure overload to the left ventricle of the heart. Adopted from Luo et al. (2015).

defined narrowed diameter, which induces a pressure overload to the left atrium and ventricle of the heart (Rockman et al., 1991). TAC acutely induces compensatory growth of the heart, accompanied by maintained or even enhanced contractile function. Chronically, the

hemodynamic overload induces a maladaptive cardiac hypertrophy, encompassed by cardiac fibrosis and ultimately leading to dilation of the heart walls and heart failure. TAC induces typical mechanical stimuli that induce pressure overload and pathological hypertrophy. Apart from TAC, another commonly used experimental model of heart failure is the complete occlusion of the left anterior descending (LAD) coronary artery, in contrast to which TAC provides a milder model of cardiac hypertrophy and a more gradual time course in the development of heart failure (deAlmeida et al., 2010). Surgical techniques closely replicate specific disease situations, still, a main limitation stays the more acutely induced pressure overload in a relatively young animal, compared to the human clinical situation, during which occlusion of arteries and thinning of the aorta is built up over a much longer time period and is often accompanied by comorbidities and age-related changes (Breckenridge, 2010).

Aside from surgical techniques, other options are the chronic delivery of pharmacological agents, to induce cardiac hypertrophy by neurohumoral stimuli. Commonly used agents are the catecholamines isoprenaline or angiotensin that are sensed through specific membrane-bound receptors on cardiomyocytes and on the downstream side lead to increased myocardial protein synthesis, and in turn elevated heart growth (Zimmer, 1997). The chronic delivery of these agents is typically conducted by the subcutaneous implantation of mini-osmotic pumps (Iaccarino et al, 1998). Pharmacological induction of hypertrophy has the major advantage of being technically less challenging, leading to lower mortality rates during the experimental procedures but they less closely resemble the clinical situation. Catecholamines or their derivatives, such as Phenylephrine, can also be applied *in vitro* to induce growth of cardiomyocytes. In the course of this work, Phenylephrine was applied to mimic pathological cardiac growth *in vitro*.

1.1.5.2 Physiological hypertrophy

To induce physiological hypertrophy, several mouse models of endurance exercise training have been established and are commonly used. These models include voluntary

running regimes (Allen et al., 2001), controlled treadmill running regimes (Kemi et al., 2002) or swimming (Evangelista et al., 2003). From these models, swimming results in biggest hypertrophic effects, with an increase of heart weight to body weight ratios of around 15-25% of cardiac weight and increased myocyte dimension of up to 20% (Evangelista et al., 2003). In this study, mice were therefore subjected to a swimming regime to induce physiological cardiac hypertrophy.

1.1.5.3 Phenotypic characterization of cardiac hypertrophy

Typically, animals subjected to hypertrophic stimuli are phenotypically analyzed by four main parameters that picture the distinct features of cardiac growth and remodeling (Bernardo et al., 2010):

I) Measuring **heart weight** to body weight ratios after sacrifice of the animal serves as a parameter to quantify hypertrophic growth.

II) Measuring amounts of **fibrosis** as a parameter to quantify remodeling and scar tissue formation, which is closely related only to pathological hypertrophy.

III) Determination of **cardiac function and contractility** by echocardiography. Important parameters are the fractional shortening (percent of ventricular diameter shortening between end systole and end diastole) and ejection fraction (percentage of ejected volume from end systole to end diastole) (Ram et al., 2011). Systolic function can be determined from two-dimensional (bright mode, B-mode) or one-dimensional (motion mode, M-mode) images, whereas the M-mode pictures a cross-section of the B-mode. Ventricular dimensions such as wall thickness or ventricular diameter can be determined as well from M-mode images.

IV) The determination of expression patterns of **fetal genes** such as *nppa*, *nppb*, *myh7* that are reactivated upon remodeling processes of the heart wall or undergo an isoform switch during the remodeling process (Taegtmeyer et al., 2010). For physiological hypertrophy, commonly used marker genes include *pgc-1a* and *gata4*.

1.2 Molecular levels of stress regulation post transcription

As described above, transcriptional changes during cardiac remodeling are well described and have been profoundly studied. The focus on transcriptional regulation

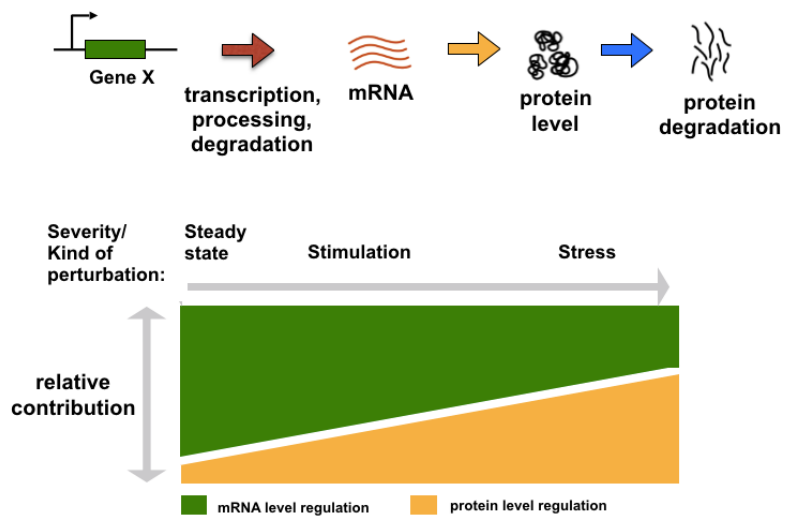


Figure 1.3: Levels of gene expression regulation and their relative contribution. The regulation of gene expression goes from transcription, to levels of protein synthesis and ultimately degradation. During homeostasis, gene expression regulation is mainly regulated through levels of transcription. This balance is shifted to protein level regulation during stress or disease. Increased stress leads to an increased shift of the balance towards protein level regulation. Modified from Jovanovic et al., (2015) and Liu and Aebersold, (2016).

stems from the classical concept of gene expression regulation, which was for a long time based on Watson's conception of the central dogma of molecular biology (Taubeneck, 1967): DNA is transcribed to RNA, which is the template for proteins to be synthesized. In this simplified concept, levels of proteins were thought to be directly responding to levels of mRNA, and transcript

levels were commonly used as proxies to estimate concentrations and activities of the corresponding proteins (Vogel and Marcotte, 2013). In the last years, technological advances were made on all levels of gene expression regulation and allow system-wide, quantitative measurements of transcription, translation and protein synthesis. The development of deep sequencing techniques now allows the detection of entire mRNA libraries of a model system to define “transcriptomes”. Additionally, the development of ribosome footprinting (Ingolia, 2010), a method that was developed to isolate translating, ribosome-protected mRNAs, in combination with deep sequencing, allows the measurement of “translatomes”. Advantages in mass spectrometry allow quantitative measurements of total “proteomes”.

Setting these levels of gene expression control into relation revealed complex dynamic regulation patterns that can be highly uncoupled, depending on the environmental condition of a cell. Recent studies have shown that by measuring transcription, translation and levels of protein, only 40% of protein abundance could be explained by levels of RNA, and abundance of proteins is importantly controlled at the level of translation (Schwanhüusser et al., 2011). Moreover, protein levels were shown to be more conserved between species than mRNA levels (Schrimpf et al., 2009; Weiss et al., 2010; Wilhelm et al., 2014), further highlighting the importance of post-transcriptional control.

Gene expression regulation was found to be highly depending on levels of mRNA in steady-state conditions, but was majorly regulated by levels of protein when cells were exposed to various stressors (Fig. 1.3). Two recent studies suggest that increasing stress leads to an increased shift towards protein level control: In a model system of Lipopolysaccharide treatment, which mainly induces specific changes in signaling, the shift was smaller than in a model of ER stress, which leads to the onset of anti-apoptotic programs and set the cell into a fundamental survival mode (Jovanovic et al.; Liu and Aebersold, 2016). In cardiomyocytes, recently published work as well as our own data suggest that short term adaption to cellular stress, as well as long term changes in gene expression are post-transcriptionally controlled by regulation of mRNA metabolism and translation (Doroudgar et al., 2019; van Heesch et al., 2019).

Given the importance of gene expression regulation at levels post transcription, the challenge now lies in understanding detailed molecular networks that are activated during states of cardiac hypertrophy. The main focus of this work is therefore to understand the mechanisms how post- transcriptional and translational gene expression regulation controls cardiac hypertrophy.

The following passages belong to the two major parts of this thesis:

- 1.2.1 will further describe post-transcriptional regulation via RNA-binding proteins and
- 1.2.2 translational regulation via mTOR in cardiac hypertrophy.

1.2.1 Post-transcriptional regulation

Post-transcriptional gene expression regulation is predominantly maintained by RNA-binding proteins (RBPs), as well as the binding of microRNAs that regulate an mRNA's fate. This regulation includes mRNA splicing, nuclear degradation, export, processing, sequestration in P-bodies for storage or degradation and ultimately translation (Day and Tuite, 1998).

microRNAs are short, non-coding, complementary RNA fragments that bind mRNA at its 3' untranslated region. Partial complementary binding leads to translational inhibition, whereas identical complementarity induces degradation of the target mRNA (Wienholds and Plasterk, 2005). RBPs have the potential to affect most post-transcriptional steps in gene expression and thereby control key elements of cellular function including cell growth and survival. Together with their target mRNA, RBPs form ribonucleoprotein complexes. Binding occurs at a RNA-binding domain, most notably the RNA Recognition Motif (RRM), K-homology domain (KH), RGG (Arg-Gly-Gly) box, zinc finger, double stranded RNA-binding domain (dsRBD), Pumilio/ PUF domain and Piwi/ Argonaute/ Zwiille (PAZ) domain (Finn et al., 2009; Oliveira et al., 2017). RBDs recognize short segments of RNA, typically 2–10 nucleotides in length. While single RBPs bind RBDs with low affinity, the specificity and affinity is increased by concerted function of multiple classical RBDs (Beckmann et al., 2016).

Over 850 RBPs have been discovered and investigated to date in model organisms. 380 of these have known RBDs (Baltz et al., 2012; Castello et al., 2012; McKee et al., 2005).

1.2.1.1 Interactome capture as a systemic approach to measure RBPs

The recently established RNA interactome capture (RIC) method has facilitated possibilities to understand proteome-wide networks of RBPs (Castello et al., 2013, Fig. 1.4). RNA interactome capture allows the generation of stable, covalent protein-RNA complexes by irradiating living cells with UV light at 254 nm, which crosslinks the photo-reactive nucleotide bases with amino acids such as Phenylalanine, Tryptophan, Tyrosine, Cysteine and Lysine. This crosslinking is highly specific to protein-RNA bonds

at „zero distance“. After lysis, mRNA-protein complexes are captured by precipitation of Poly(A) tails with magnetic Oligo d(T) beads and are purified through a series of stringent washes. mRNAs are lost by enzymatic digest and captured proteins can be detected by quantitative mass spectrometry.

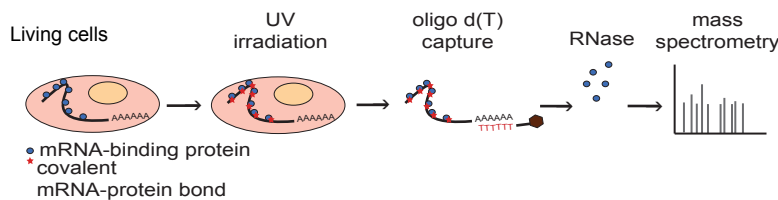


Figure 1.4: Overview of RIC method. Living cells are crosslinked *in vivo* with 254 nm ultraviolet light, resulting in covalent bonds between RNAs and directly bound proteins. Oligo d(T) beads capture Poly(A) tails of mRNA and co-precipitate mRNAs/protein complexes. RNase digest erases remaining RNAs bound to proteins and following quantitative mass spectrometry allows analysis of proteins.

RIC has been applied for the generation of RBP atlases in eukaryotic model systems such as mammalian cell lines, *Drosophila* embryos, yeast, and plant seedlings (Baltz et al., 2012; Beckmann et al., 2015;

Castello et al., 2012; Reichel et al., 2016; Sysoev et al., 2016). Primary cell lines have not been under much investigation so far.

1.2.1.2 RIC discovers atypical RBPs

The ability to perform system-wide analysis of RBPs in a model system, in contrast to previous *in silico* methods to predict binding behavior by structural entities of a protein, now also allows the detection of atypical RBPs with unknown binding domains. A high number of these unconventional RBPs has been identified to date, and more recent detailed insights into complex ribonucleoprotein complexes such as the ribosome or the spliceosome without canonical RBDs suggest that uncanonical RNA-binding might be a broad phenomenon. A high number of atypical RBPs was linked to metabolic functions, and more specifically, enzymatic activity. Unlike the classical view of RBPs affecting the bound mRNA, a mutual interplay of RBP and RNA has been suggested recently. RNA binding could control the localization or activity of an enzyme, and might lead to a switch between RNA binding and increased enzymatic activity when the RBP is released from the RNA-protein complex (Castello et al., 2015; Hentze et al., 2018).

1.2.1.3 Dynamic interactome capture - state of the art

There is very limited insight in how RBPs are dynamic in steady-state conditions versus stress, but the shift in mRNA to protein level balance from homeostasis to stress (see section 1.2 and fig. 1.3) raises the question whether dynamic RBP-RNA interactions fine-tune the stress response of a cell.

Few studies have aimed at understanding dynamic binding capacities in different conditions: A first dynamic study was performed by Sysoev et al. (Sysoev et al., 2016), comparing RBPs from early and late embryonic stages in drosophila. Further, comparative RIC was performed in a human lymphocyte cell line that treated cells with RNA demethylase inhibitor dimethylallylglycine and identifies RBPs responsive to N6-methyladenosine (m6A) (Perez-Perri et al., 2018). A recent comparative study detected a high number of RBPs being responsive to viral treatment and highlights how viral infection efficacy can be influenced by dynamic RBPs (Garcia-Moreno et al., 2019). These studies highlight the dynamic behavior of RBPs to external stimuli.

1.2.1.4 Post-transcriptional regulation in disease

Post-transcriptional regulation is known to be involved in the onset of many diseases and several microRNAs have been linked to cardiac development and disease (Humphreys et al., 2012). Dysfunction of RBPs has been linked to multiple pathologies, mainly to neurological diseases, muscular atrophies, metabolic disorders, and cancer (Lukong et al., 2008; Zhou et al., 2014). Several RBPs were found to be involved in preserving heart function and during the development of the post-natal heart, were in most cases differential expression of RBPs affects alternative splicing. The role of single RBPs, such as Quaking, HuR, Muscleblind, and SRSF1 have been shown to be crucial regulators in the cardiovascular system by guiding a wide-ranging number of post-transcriptional events that dramatically impact RNA fate. Homozygous knock out of these RBPs is commonly associated with cardiac - and/or vascular complications (De Bruin et al., 2017; Justice and Bode, 1988).

Importantly, a first systemic compendium of RNA-binding proteins in cardiomyocyte-like HL-1 cells was recently reported, which identified hundreds of new RBPs. This study highlights Sarcoplasmic/endoplasmic reticulum calcium ATPase (SERCA), a crucial protein for the maintenance of contractile function as an RBP. The authors suggest a moonlighting role of mRNA-binding to influence the contractile function of SERCA (Liao et al., 2016). Moreover it has been shown that targets of specific RBPs are enriched in translationally regulated genes in activated cardiac fibroblasts which contributed to fibrotic remodeling of diseased hearts, but the role of RBPs in cardiomyocytes during stress response and remodeling remains poorly understood (Chothani et al., 2019). However, the specific role of RBPs for cardiac remodeling during heart failure remain poorly understood.

1.2.1.5 Aims

The first chapter of this work has the following aims:

- Generating the **first RBPome in primary cardiomyocytes**. As mentioned above, a compendium of RBPs in primary cardiomyocytes has not been determined to date. We therefore want to provide the cardiac RBPome by performing RNA-interactome capture in neonatal rat ventricular cardiomyocytes (NRVCMs). The first aim is to generate the RBPome under basal conditions.
- For a more detailed picture of dynamics of post-transcriptional control during cardiac hypertrophy we would like to compare homeostatic NRVCMs to those treated by the hypertrophic agent Phenylephrine and generate an atlas of **RBPs during pathological cardiac hypertrophy**.
- Furthermore we would like to understand **dynamics in binding capacities of RBPs** as a response to the hypertrophic stimulus. For this purpose we will compare the RBPome from both conditions. Additionally we would like specifically determine RBPs that specifically change their binding capacities in demarcation to the overall abundance.
- We will further analyze the molecular role of dynamic RBPs and their role during pathological cardiac hypertrophy.

1.2.2 Proteostatic regulation

Aside from post-transcriptional control, proteostasis, namely the balance between synthesis, proper folding and degradation of proteins, crucially regulates levels of protein and has a major impact onto the health status of a cell.

Cardiac hypertrophy is closely linked to increased amounts of translation, providing proteins for cardiomyocyte growth. Overshooting anabolic processes severely disrupt the balance between folding capacity and folding requirements of cells. Chronic perturbation of the proteostatic balance activates the cellular stress response but leaves cells unable to clear aggregated proteins and cytotoxic species (Klaips et al., 2018; Lamech and Haynes, 2015). Such maladaptive stress response makes cells vulnerable because of the persisting aggregates, but also because the cells are unable to remove disease-associated proteins (Roth et al., 2014). Chronic imbalance of proteostasis is highly detrimental to the outcome of pathologic cardiac hypertrophy. Therefore, targeting protein quality control mechanisms to restore cardiac proteostasis is a novel therapeutic option in cardiac diseases (Henning and Brundel, 2017).

1.2.2.1 mTOR as main regulator of cell growth during cardiac hypertrophy

One major pathway that promotes both anabolic processes and inhibits catabolic process during cardiac hypertrophy is the mammalian target of Rapamycin (mTOR) that is activated by biomechanical stressors as well as growth factors. mTOR is a serine/threonine kinase and member of the phosphatidylinositol 3-kinase-related kinase family of protein kinases. The mTOR kinase interacts with several proteins and serves as core component of two different protein complexes, determined as mTOR complex (mTORC) 1 and 2. Both complexes consist of the mTOR kinase and mLST8 (mammalian lethal with SEC13 protein 8), which associates with the mTOR catalytic domain. mTORC1 is additionally built up by regulatory-associated protein of mTOR (Raptor), which facilitates substrate recruitment to mTORC1 through binding to the TOR signaling (TOS) motif found on several canonical mTORC1 substrates. The two non-core components DEP domain-containing mTOR-interacting protein (Deptor) and Proline-rich Akt

substrate 1 (Pras40) both have an inhibitory function to mTORC1. In mTORC2, the mTOR kinase and mLST8 are accompanied by Rictor (rapamycin insensitive companion of mTOR), which takes over a similar role as Raptor in mTORC1, as well as Deptor, and the regulatory subunits mSin and Protor1/2 (Kim et al., 2017; Saxton and Sabatini, 2017). Both complexes exert different molecular functions: While mTORC2 is involved in cell survival, mTORC1 is a critical regulator of cell growth and proliferation, and is activated during cardiac hypertrophy.

mTORC1 serves as nutrient/energy sensor and crucially controls protein synthesis and degradation. Activation of mTORC1 promotes a shift towards anabolic versus catabolic processes, which is highly dependent on the presence of endocrine signals, energy and molecular building blocks for protein synthesis. In mammals, the activity of mTORC1 is critically controlled by the availability of nutrients. During starvation, mTORC1 is inactive but becomes activated with increased amounts of growth factors, amino acids but also energy and oxygen (Saxton and Sabatini, 2017).

During cardiac hypertrophy, both physiological and pathological growth signals induce the activation of mTORC1, but the signaling pathways upstream of mTORC1 vary between these conditions (Figure 1.5). Physiological cardiac growth is predominantly regulated through the growth hormone/IGF axis via signaling through the PI3K/Akt pathway. During pathological cardiac growth, mechano-sensitive stretch receptors lead to a release of autocrine and paracrine neurohormonal factors that lead to strong recruitment of stress-activated MAPKs, p38 MAPKs and JNKs (Dorn and Force, 2005). Both pathways upstream of mTOR are thought to be partly interconnected but their influence is highly variable between physiological and pathological growth.

1.2.2.1.1 MTOR promotes anabolic processes

Once mTOR is activated, the promotion of protein synthesis is induced by direct phosphorylation of p70S6 Kinase 1 (S6K) and eIF4E Binding Protein (4EBP) downstream of mTOR. Phosphorylation of S6K leads to the phosphorylation of several downstream targets that aid the initiation of translation, such as eIF4B, a positive

regulator of the 5'cap binding eIF4F complex (Holz et al., 2005). Phosphorylation of 4EBP1 independently of S6K initiates translation initiation by dissociation from eIF4E at the Cap structure of mRNAs. Release of 4EBP1 then subsequently allows assembly of the eIF4F complex and translation initiation.

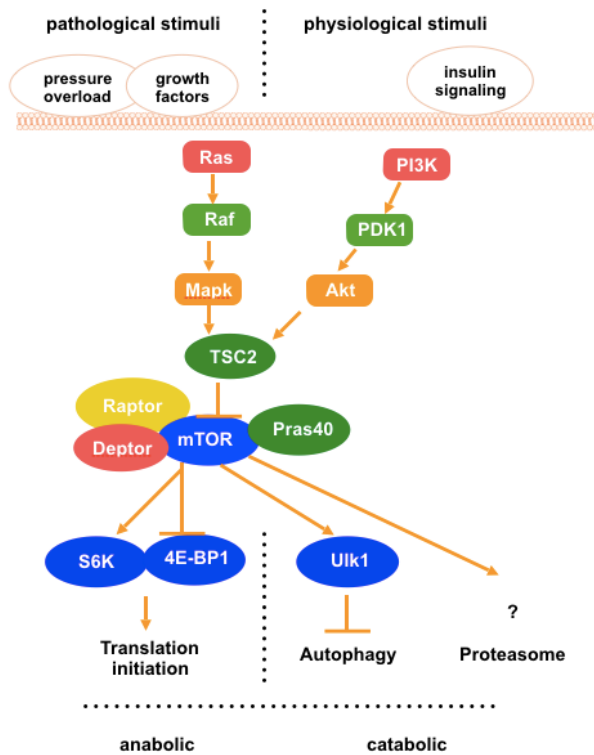


Figure 1.5: The mTORC1 during physiological or pathological growth. Pathological or physiological growth stimuli by mechanical stimuli or Insulin-like growth factors, respectively, lead to the onset of specific signaling cascades, that induce mTOR kinase activity. Downstream of mTOR, this leads to activation of the S6 kinase, 4E Binding protein 1 (induction of translation) or activation of Unc-51 like autophagy activating kinase (Ulk1), leading to inhibition of autophagy. The interplay between mTORC1 and the proteasome remains unclear. Pathological stimuli induce Mapk (Mitogen activated protein kinase) signaling. Physiological stimuli lead to PI3K (Phosphoinositide 3-kinase) signaling. Representative pathway nodal points depicted: PDK1: Phosphoinositide-dependent kinase-1. Akt: RAC-alpha serine/threonine-protein kinase. TSC2: Tuberlin.

1.2.2.1.2 MTOR inhibits catabolic processes

Additionally to directly promoting translation, activated mTORC1 supports anabolic processes by inhibition of protein degradation. The majority of aggregated, long-lived proteins is degraded by autophagy, a process that is relatively unspecific and can erase bulk proteins in response to cellular stress. It is well understood that mTORC1 inhibits autophagy by inhibiting Unc-51 like autophagy activating kinase (Ulk1).

Ulk1 importantly modulates the onset of autophagy by forming a complex with several interaction partners to induce autophagosome formation. Phosphorylation of Ulk1 by mTORC1 prevents the formation of the ULK1-containing pro-autophagic complex, which induces the formation of autophagosomes (Rabanal-Ruiz et al., 2017).

1.2.2.2 The interplay of mTORC1 and the ubiquitin-proteasome system (UPS)

Aside from the well-understood interplay between mTORC1 and the formation of autophagosomes, a connection between mTORC1 and the second main protein degradation machinery, the ubiquitin-proteasome-system (UPS), has been recently suggested by a number of studies.

The UPS degrades many regulated, short-lived, or damaged proteins and is responsible for about 80% of protein degradation. Degradation of proteins by the UPS is much more specific than lysosomal degradation/autophagy due to a two-step mechanism: Proteins are first labelled by covalent linking of multiple ubiquitin molecules, and are then recognized and degraded in the proteasomal complex. The first step of this degradation process, the labeling of proteins, happens through the coordinated action of ubiquitin enzymes E1 (ubiquitin-activating enzyme), E2 (ubiquitin-conjugating enzymes) and E3 (ubiquitin ligases). Poly-ubiquitin chains are then recognized by the proteasome and the labeled proteins is degraded into poly-peptides, whereas ubiquitin molecules are freed and can be reused for labeling of degradable proteins (Mearini et al., 2008).

The mammalian 26S proteasome is a large 2000 kDa multicatalytic structure composed of a 20S catalytic core and two 19S regulatory particles that serve as “caps” of the 20S core unit. The 19S regulatory particles recognize, bind, deubiquitinate and unfold the poly-ubiquitinated proteins, but also regulate the opening of the 20S core to channel the unfolded proteins into the 20S. These processing steps are energy-consuming and ATP-dependent. The 19S therefore contains six different ATPase subunits, which are located in the base subcomplex. The 20S catalytic core is composed of four stacked rings, two outer α -rings and two inner β -rings with each seven subunits. The catalytically active β -subunits β 1, β 2 and β 5 are specific for caspase-, trypsin-, and chymotrypsin-like substrate activities, respectively, meaning they cleave peptides at different amino acids. (Ciechanover, 2005). Apart from protein degradation, the UPS has also been shown to be involved in intracellular signaling, transcriptional control or regulation of cell death (Zolk et al., 2006)

Both degradation machineries were for a long time thought to be independent from each other, but recent reports have highlighted a concerted interplay of both systems (Lilienbaum, 2013).

A number of studies have linked mTOR to the ubiquitin-proteasome system, with an unclear link between mTOR and proteasomal function. Acute mTORC1 inhibition was shown to rapidly increase proteolysis by the UPS (Zhang et al., 2014). In contrast, two other studies see a concerted activation of autophagic and proteasomal protein degradation in states of active mTORC1 signaling. (Rousseau and Bertolotti, 2016; Zhao et al., 2015). It is thought that acute response to mTORC1 inhibition promotes proteolysis to restore free amino acid pools, prolonged mTORC1 activation leads to a compensatory increase in protein turnover to balance the increased rate of protein synthesis (Saxton and Sabatini, 2017). Full mechanistic understanding of the interplay between mTOR, autophagy and the UPS is still lacking.

1.2.2.3 Selective inhibition of mTOR by Pras40 - a gene therapeutic option?

Two members of the mTORC1 exert inhibitory functions to the mTOR kinase, Deptor and Pras40. Pras40 was initially found to be a 13-4-4 binding protein and substrate of Akt. Pras40 binds to mTOR during starvation, resulting in mTOR inhibition by competitive binding of the mTORC1 site where substrates 4E-BP1 and p70S6K are bound (Sancak et al., 2007; Wang et al., 2007). In energy-rich conditions, Pras40 is phosphorylated by mTOR or Akt on two distinct phosphorylation sites, S186 or T246, respectively. Phosphorylated Pras40 is released from mTOR and loses its inhibitory function.

Previous studies from our lab show that overexpression of Pras40 ameliorates the outcome of pathological cardiac hypertrophy by inhibiting mTOR (Volkers et al., 2013). Alternative signaling pathways prevent pathological growth by overexpression of Pras40, but allow physiological growth: During physiological growth, Akt is activated upstream of Pras40 and phosphorylates it at Threonine 246, resulting in release of Pras40 from mTOR and activation of the mTORC1 downstream pathway. During pathological

growth, an alternative pathway, which does not lead to activation of Akt prevents this phosphorylation at Threonine 246. Phosphorylation of Pras40 by mTOR at Serine 183 happens, but does not lead to full release from mTORC1. During pathological hypertrophy, Pras40 therefore binds and inhibits mTORC1.

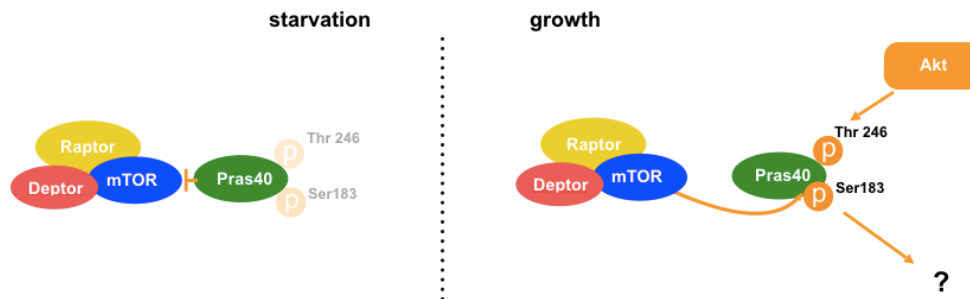


Figure 1.6: The interplay between mTOR and Pras40 during starvation and growth. During starvation, when mTOR is inactive, Pras40 is bound to mTOR and inhibits its downstream function. During growth, Pras40 is phosphorylated by mTOR and Akt at Serine 183 and Threonine 246, respectively. It is then released from mTORC1, losing its inhibitory effect.

The inhibitory role of Pras40 onto mTOR has been profoundly studied in different cellular environments, but its role independent of mTOR and its function when phosphorylated and mTOR-released remains unclear. Several studies document that deletion of Pras40 - in contrast to mTORC1 inhibition after overexpression - does not result in mirrored signaling cascades and activation of mTOR. Knock-down of Pras40 in primary human skeletal muscle cells decreased, rather than increased, phosphorylation of p70S6k and reduced the phosphorylation of AKT and mTORC1-regulated proteins (Wiza et al., 2013, 2014). Moreover, silencing of Pras40 in murine tumor models reduced tumorigenesis in different malignant cancer types (Huang et al., 2012; Madhunapantula et al., 2007). These observations have raised the question whether Pras40 has a yet unknown role that is independent from mTORC1 and has been completely overlooked so far.

With mTOR promoting anabolic cellular processes and inhibiting overshooting protein synthesis, activation of mTOR has been linked to worsening of pathological hypertrophy and worsening of cardiac function. Pharmacological inhibition of mTOR is known to

restore cardiac function after after pressure overload, myocardial infarction, and in genetic hypertrophic cardiomyopathies (McMullen et al., 2004; Shioi et al., 2003). Still, there are currently no heart-specific mTOR inhibitory treatment options and the ubiquitous role of mTOR in the body leads to severe side - and off-target effects when delivered systemically. The advancing of adeno-associated virus technologies have opened a new field of gene therapeutic treatment options (Daya and Berns, 2008; Pacak and Byrne, 2011) and Pras40 as a genetic inhibitor of mTOR would be a promising candidate to test as a gene therapy option to selectively and heart-specifically inhibit mTOR. For this, a full understanding of its molecular action during cardiac hypertrophy is indispensable.

1.2.2.4 Aims

The aim of this chapter of the project therefore is

- to study the molecular function of Pras40 in the context of cardiac hypertrophy and to elucidate how lack of Pras40 affects cardiac growth and function. More specifically, we aim
- to **phenotype the effects of Pras40 deletion onto cardiac growth, function, fibrosis and marker gene expression**. For this, we will determine cardiac growth, remodeling, and functional changes in two novel Pras40 knock-out mouse models that we will subject to pathological (TAC surgery) and physiological (swimming) hypertrophy.
- to understand the molecular singularities underlying this phenotype, especially the **effect to mTOR signaling and the activity of the mTOR downstream signaling cascade**.
- to understand the **role of mTOR-released Pras40** in the cardiac context. For this, we will investigate the effects of a Pras40 mutant that does not bind mTOR, in order to break down mTOR dependent and independent effects of Pras40 on growth and mTOR activity.

2. MATERIALS

2.1 Reagents

Reagent	Brand	Catalog-Number
4-(2-Hydroethyl)-1-piperazineethanesulfonic acid (HEPES)	Thermo Fisher Scientific	15630056
Acetic acid	Honeywell	64-19-7
Aceton	Carl Roth	T906.1
Agarose	Jena Bioscience	AC-001S
Ammonium hydroxide solution	Honeywell	05002
Aniline blue solution	Sigma-Aldrich/Merck	HT154
B-Mercaptopethanol	Sigma-Aldrich/Merck	M6250
Bieberich Scarlet solution	Sigma-Aldrich/Merck	HT151
Bouin's solution	Sigma-Aldrich/Merck	HT10132
Bovine serum albumin (BSA)	Sigma-Aldrich/Merck	A6003
BZ-VGR-AMC	Enzo Life Sciences	BML-BW9375-0005
Cadmium chloride (CdCl ₂)	Honeywell	20899
Chloroform	Merck	32211
Cycloheximide (CHX)	Sigma-Aldrich/Merck	C1988
DC™ Protein Assay	Bio-Rad	5000111
Dialized serum	Gibco™ Thermo Fisher Scientific	A3382001
Diethyl pyrocarbonate (DEPC)	BioChemica	A0881,0100
Dithiothreitol (DTT)	Sigma-Aldrich/Merck	43819
DNA loading dye	Thermo Fisher Scientific	R0611
dNTP mix	Promega	U1511
Dulbecco's Modified Eagle Medium (DMEM)	Sigma-Aldrich/Merck	D5796-24X
DMEM, glucose-free	Thermo Fisher Scientific	A1443001
DMEM/F-12, HEPES	Thermo Fisher Scientific	11330057
Dimethyl sulfoxide (DMSO)	Sigma-Aldrich/Merck	D8418
Enhanced Chemiluminescence (ECL) Western Lightning Plus substrate	PerkinElmer	NEL104001EA
Eosine Y	Sigma-Aldrich/Merck	E4009

Epoxomicin	Santa Cruz Biotechnology	sc-201298A
Ethylene diamine tetra acetic acid-(EDTA)-disodium salt	Honeywell	6381-92-6
Ethanol	Sigma-Aldrich/Merck	51976
Ethidium bromide	Sigma-Aldrich/Merck	E1510
Fetal bovine serum (FBS), superior	Biochrom/Merck	S0615
FBS	Gibco™/Thermo Fisher Scientific	10270
Fibronectin from bovine plasma	Sigma-Aldrich/Merck	F1141
Formaldehyde (35 %, v/v)	Carl-Roth	50-00-0
Gelatine	Sigma-Aldrich/Merck	G9391-100G
GeneRuler 50 bp DNA ladder	Thermo Fisher	SM0373
GeneRuler 1 kb DNA ladder	Thermo Fisher	SM0313
D-Glucose	Sigma-Aldrich	50-99-7
Hank's buffer salt solution, Ca ²⁺ and Mg ²⁺ free (HBSS)	Thermo Fisher	14170088
Heparin-Natrium-25000- ratiopharm®	Ratiopharm	N648542.04
HiPerFect Transfection Reagent	Qiagen	301704
Hydrochloric acid (HCl, [37%])	Honeywell	30721
Isoflurane Baxter	Baxter	HDG9623
Isopropanol	Sigma-ALdrich/Merck	I9516
iTaq™ Universal SYBR® Green Supermix	Bio-Rad	1725124
Laemmli buffer	Bio-Rad	161-0747
Lithiumchloride (LiCl)	Sigma-Aldrich	62476-500GF
Lithium dodecyl sulfate (LiDS)	Sigma-Aldrich	L9781
Methanol	VWR Chemicals	20847.307
Magnesium chloride (MgCl ₂)	Sigma-Aldrich	P9333-1KG
Magnesium sulfate (MgSO ₄)	Sigma-Aldrich	M2643-500g
5X Mammalian Polysome Buffer	Epicentre/Illumina	ASBHMR1212
MOPS (3-(N- Morpholino)propansulfonic acid)	Bio-Rad	161-0788
Nonidet® P-40 Substitute (NP-40)	Sigma-Aldrich/Merck	74385-1L
Oligo(dT25) magentic beads	New England BioLabs	S1419S
Paraffin (Surgipath Paraplast)	Leica Biosystems	39602012

Paraformaldehyde (PFA) 20% aqueous solution	Electron Microscopy Sciences	15713
PEI MAX	Polysciences	24765
Penicillin-Streptomycin	Gibco™/Thermo Fisher Scientific	15140122
Penicillin-Streptomycin-Glutamine	Gibco™/Thermo Fisher Scientific	10378016
Percoll	GE Healthcare	17-0891-02
Phenol:Chloroform:IAA 25:24:1	Thermo Fisher Scientific	AM9730
Phenol Red	Sigma-Aldrich/Merck	P3532
(R)-(-)-Phenylephrine hydrochloride	Sigma-Aldrich/Merck	P6126
Phloxine B	Sigma-Aldrich/Merck	P3532
Phospho-buffered Saline (PBS)	Sigma-Aldrich/Merck	D8537
Phosphomolybdic acid solution	Sigma-Aldrich/Merck	HT153
Phosphotungstic acid solution	Sigma-Aldrich/Merck	HT152
PhosSTOP	Sigma-Aldrich/Merck	4906837001
Pierce™ protein A/G magnetic beads	Thermo Fisher Scientific	88802
Ponceau S	Sigma-Aldrich/Merck	P3504
Potassium chloride (KCl)	Sigma-Aldrich/Merck	P9333
Precision Plus Protein™ Dual Color	Bio-Rad	1610374
Protease inhibitor cocktail tablets	Sigma-Aldrich/Merck	11873580001
Puromycin	Millipore	540411
Qiazol	Qiagen	79306
RNaseZap™ RNase Decontamination Solution	Thermo Fisher Scientific	AM9780
RNasin® Ribonuclease Inhibitor	Promega	N2611
RPMI-1640	Sigma-Aldrich/Merck	R8758
Skim milk powder	Carl Roth	T145.2
Sodium Acetate (C ₂ H ₃ NaO ₂)	Merck	1.01539.0500
Sodium Citrate (C ₆ H ₅ Na ₃ O ₇)	AppliChem	A1531.0025
Sodium Chloride (NaCl)	Carl Roth	9265.2
Sodium Dihydrogen Phosphate (H ₂ NaPO ₄)	Sigma-Aldrich/Merck	S5011-500G
Sodium deoxycholate	AppliChem GmbH	A1531.0025
Sodium dodecyl sulfate (SDS)	Serva	20765.03
Sodium Hydroxid (NaOH)	Sigma-Aldrich/Merck	30620

Suc-LLVY-AMC	Enzo Life Sciences	BML-P802-0005
Sucrose	Sigma-Aldrich/Merck	84100
SUPERase•In RNase Inhibitor	Thermo Fisher Scientific	AM2696
Tamoxifen	Sigma-Aldrich	T5648-5G
Transfer Buffer: Invitrogen Novex NuPAGE (20X)	Thermo Fisher Scientific	NP00061
Tris	Carl Roth	4855.1
Tris hydrochloride (Tris-HCl)	Carl Roth	9090.2
Triton X-100	Sigma-Aldrich/Merck	X100
Trypsin	Thermo Fisher Scientific	15090046
Trypsin-EDTA	Thermo Fisher Scientific	25200056
Tween® 20	Carl Roth	25300-120
Vectashield® antifade mounting media	Vector Laboratories	H-1000
Water, nuclease-free	Thermo Fisher Scientific	AM9937
Weigert's iron hematoxin solution set	Sigma aldrich	HT1079
Western Lightning Plus-Enhanced Chemiluminescence Substrate	PerkinElmer	NEL104001EA
Xylol	Carl Roth	9713.5
Zinc chloride (ZnCl ₂)	Sigma-Aldrich/Merck	Z0152
Z-LLE-AMC	Enzo Life Sciences	BML-ZW9345-0005

2.2 Antibodies and staining

2.2.1 Western blot analysis

antibody	brand	order number	dilution
a-tubulin	Sigma-Aldrich	T4026	1:5000
b-actin	Santa Cruz	sc-47778	1:1000
cpeb4	Atlas	HPA038394	1:1000
eif4a3	Cell signaling techn.	A302-980-A	1:1000
Erk5	Cell signaling techn.	#12950	1:1000
Flag	Sigma-Aldrich	F3165	1:5000
gapdh	Santa Cruz	sc-365062	1:1000

antibody	brand	order number	dilution
lamin	Santa Cruz	sc-374015	1:1000
lc3b	Cell signaling techn.	#3868	1:1000
mTOR	Cell signaling techn.	#2983	1:5000
Msrb3	Santa Cruz	sc-514897	1:1000
Pras40	Cell signaling techn.	#2691	1:5000
PA28 α / Psme1	proteintech	10543-1-AP	1:1000
Puromycin	Merck Millipore	MABE343	1:10 000
Raptor	Cell signaling techn.	#2280	1:1000
ribS6	Cell signaling techn.	#2317	1:1000
p-ribS6	Cell signaling techn.	#4858	1:500
S6K	Cell signaling techn.	#2708	1:1000
p-S6K ^{Thr421/Ser424}	Cell signaling techn.	#9204	1:500
p-Ulk1 ^{Ser757}	Cell signaling techn.	#14202	1:1000
4EBP1	Cell signaling techn.	#9664	1:1000
p-4EBP1 ^{Thr37/46}	Cell signaling techn.	#2855	1:1000
Ubiquitin	Cell signaling techn.	#3936	1:1000
Ubr1	Santa Cruz	sc-515753	1:500
Ubr2	Santa Cruz	sc-135594	1:500
Ubr5	Santa Cruz	sc-515494	1:500
Ybx-1	Cell signaling techn.	#9744	1:1000
Ythdf-2	Proteintech	24744-1-AP	1:1000
Zeb1	Proteintech	21544-1-AP	1:1000
Zbtb20	Proteintech	23987-1-AP	1:1000
Peroxidase-Anti-Mouse	Jackson Immuno Research	715035151	1:5000
Peroxidase-Anti-Rabbit	Jackson Immuno Research	111035144	1:5000

Table 1: Antibodies with supplier and order number, that were used for Western blot analysis.

2.2.2 Immunofluorescence staining/ Immunohistochemistry

antibody	brand	order number	dilution
Actin	Santa Cruz Biotechnology	sc-8432	1:200
Sarcomeric Actin	Sigma-Aldrich/Merck	A2172	1:200
Cpeb4	Atlas	HPA038394	1:100
Flag	Cell Signaling Technology	2044S	1:100
Tnt	Abcam	ab209813	1:100
Zeb1	Proteintech	21544-1-AP	1:100
Anti-rabbit IgG-FITC	Jackson Immuno Research	711-095-152	1:200
Anti-mouse IgG-C3	GE healthcare	29038275	1:200

Table 2: Antibodies with supplier and order number, that were used for Immunofluorescence staining/ Immunohistochemistry.

2.2.3 Other staining reagents

Wheat Germ Agglutinin: Oregon Green™ conjugate	Thermo Fisher Scientific	W6748
DAPI:FluoroPure™	Thermo Fisher Scientific	D21490

2.3 Enzymes

Item	Supplier	Catalog-Nr.
DNase I	Sigma-Aldrich/Merck	10104159001
DNase I	Thermo Fisher Scientific	EN0525
Proteinase K	Thermo Fisher Scientific	10259184
RNase A	Sigma-Aldrich	R4642

2.4 Kits

Kit	Supplier	Catalog-Nr.
Agilent RNA 6000 Nano kit	Agilent	5067-1511
DC™ protein assay	Bio-Rad	5000112
iScript™ cDNA Synthesis Kit	Bio-Rad	1708891
Masson Trichrome Staining set	Bio-Rad	HT15-1KT
Pierce Silver Stain kit	Thermo Fisher Scientific	24612
Plasmid Miniprep Kit: Gen Elute™	Sigma-Aldrich/Merck	PLN70
Plasmid Plus Maxi Kit	Qiagen	12965
Proteostat® Protein aggregation assay	Enzo Life Sciences	ENZ-51023
Quick RNA™ Miniprep	Zymo Research	R1055
Ribo-zero™ magnetic gold	Epicentre	MRZG12324
RNA Clean & Concentrator	Zymo Research	R1013
RNeasy	Quiagen	74106
SuperScript™ III First-Strand Synthesis Super Mix	Thermo Fisher Scientific	18080400
TruSeq Ribo Profile (Mammalian) Library Prep Kit	Illumina	ASLPA1212
Weigert's iron hematoxylin kit	Sigma-Aldrich/Merck	HT1079- 1SET

2.5 Nucleic acids

2.5.1 Primers

Primers were ordered at Thermo Fisher Scientific.

2.5.1.1 Mouse

target	primer for	primer rev
<i>β-Actin</i>	ACTGTTCGAGTCGCGTCCA	ATCCATGGCGAACTGGTGG
<i>Coll1a1</i>	GCTCCTCTTAGGGGCCACT	CCACGTCTCACCATGGGGG
<i>Hprt</i>	CTTCCTCCTCAGACCGCTTT	TCGCTAATCACGACGCTGG
<i>Msrb3</i>	ATGCACAGGGTGGAAACCAGCT	CTTTGATGCCGCTTCCTTCTGC
<i>Myh7</i>	AGGGCGACCTCAACGAGAT	CAGCAGACTCTGGAGGCTCTT
<i>Nppa</i>	TTGTGGTGTGTACGCAGCT	TGTTCAACCACGCCACAGTG
<i>Nppb</i>	TTTGGGCTGTAACGCACTG	CACTTCAAAGGTGGTCCCAGA
<i>PGC1a</i>	TGCATGAGTGTGTGCTGTGTGTC	CACCAACCAGAGCAGCACACT
<i>Pa28α</i>	TGCAGTGAATAAGCAGCCA	CACAGCATAAGCATTGCGGA
<i>Ubr1</i>	CTTTGAGCGGGCAGTGGACAT	CTTTGAGCGGGCAGTGGACAT
<i>Ubr2</i>	GTCGTGGCTGGGAAGTGTTA	ACGCTCATAGTTTTTAGCAAATCG
<i>Ubr5</i>	AGCAGCTGGTTTGGGTAGAC	CAGTCGCTGCTGTGGTAAGA
<i>Zeb1</i>	ATTCAGCTACTGTCAGCCCTGC	CATTCTGGTCCTCCACAGTGGGA
<i>Zbtb20</i>	CCTCATCCACTCGACACATTCAC	GAAGGTTGATGCTGTGAATGCGC
<i>18s</i>	CGAGCCGCCTGGATAACC	CATGGCCTCAGTTCCGAAAA

Table 3: Mouse Primers used for qRT-PCR, sequences are shown 5'-3'.

target	primer for	primer rev
Pras40	GGAGATGGTTACAAGTACACATCTCC	TCCTGGAGGGTGGCATCCTCATCC
Cre	ATGACAGACAGATCCCTCCTATCTCC	CTCATCACTCGTTGCATCATCGAC

Table 4: Mouse Primers used for genotyping PCRs, sequences are shown 5'-3'.

2.5.1.2 Rat

target	primer for	primer rev
<i>Cpeb4</i>	CGTCTGCTATGCTGGAATCG	GGCTTAACCCCTCCACCCGTTT
<i>Hprt</i>	TCAGACCGCTTTTCCCGCGA	TCACTAATCACGACGCTGGGACTGAG
<i>Nppa</i>	TACAGTGCGGTGTCCAACACAGAT	TGGGCTCAATCCTGTCAATCCTA
<i>Nppb</i>	GAACAATCCATGATGCAGAAGC	TACAGTGCGGTGTCCAACACAGAT
<i>Msrb3</i>	GCTGTTCTCAGTGTGGTGCT	GACAGTGGTGAGGCGGAA
<i>Zeb1</i>	GCGGCGCAATAACGTTACAAA	CACTGTCTGGTCTGTTGGCA
<i>Zbtb20</i>	GAAACAGGTGCCTCCTCTCC	CAATGGCTGCCCGATTGATG
<i>18s</i>	CGAGCCGCCTGGATAACC	CATGGCCTCAGTTCGAAAA

Table 5: Rat Primers used for qRT-PCR, sequences are shown 5'-3'.

2.5.2 siRNA

Target	Supplier	Catalog-Nr.
siCpepb4 (ms)	Thermo Fisher Scientific	s154777
siPras40 (rt)	Ambion	4390771
siTSC2 (ms, rt)	Thermo Fisher Scientific	s75509
Silencer™ Select Negative Control #1(siRNA)	Thermo Fisher Scientific	4390844

2.5.3 Plasmids

Name	Supplier	Catalogue-No.
hu Cpeb4-pDonr221	Biocat	GS3000-GBS
pENTR	Invitrogen™/ Thermo Fisher Scientific	
pENTR_Mettl3	provided by Verena Kamuf-Schenk	
pENTR_Mettl3_Mut	provided by Verena Kamuf-Schenk	
pAD (Adenovirus, Control)	provided by Verena Kamuf-Schenk	

pAD_Pras40_WT (Adenovirus, Pras40)	provided by Verena Kamuf-Schenk
pAD_Pras40_FRB (Adenovirus, Pras40 mTOR-released)	provided by Verena Kamuf-Schenk
pAD_PA28 α	provided by Verena Kamuf-Schenk
pAD_LacZ	provided by Verena Kamuf-Schenk
pSSV9_CVM	provided by Verena Kamuf-Schenk
pSSV9_CVM_Pras40_WT (AAV9, Pras40)	provided by Verena Kamuf-Schenk
pSSV9_CVM_Pras40_FRB (AAV9, Pras40 mTOR-released)	provided by Verena Kamuf-Schenk
pSSV9_CVM_PA28 α	provided by Verena Kamuf-Schenk

2.6 Consumables

Item	Supplier	Catalogue-No.
Amicon Ultra centrifugal filters (50 ml, 10 kDa cutoff)	Millipore	UFC901024
Amicon Ultra centrifugal filters (0,5 ml, 3 kDa cutoff)	Millipore	UFC500396
Aspiration Pipettes, sterile 2 ml	Greiner bio-one	710183
Cell Scraper	Greiner bio-one	341070
CL-XPosure™ Film, 20 x 25 cm	Thermo Fisher	34091
Conical Centrifuge Tubes 15 ml	Greiner bio-one	188271
Conical Centrifuge Tubes 50 ml	Greiner bio-one	352070
Cover slips (24 x 60 mm)	Marienfeld GmbH	0101242
Dynabeads sheep anti rabbit IgG	Invitrogen	11203D
Filter Tip 10 μ l	Neptune Scientific	976-010
Filter Tip 20 μ l	Neptune Scientific	976-020
Filter Tip 200 μ l	Neptune Scientific	976-200
Filter Tip 1000 μ l	Neptune Scientific	976-1250
Gel loading Tips: Gel-Saver	Kisker, Steinfurt	GSII054R

MicroAmp™ Fast Optical 96-Well Reaction Plate, 0.1 ml	Applied Biosystems™	4346907
Nunc™ Lab-Tek™ Chamber Slide	Thermo Fisher	177429PK
Nunc™ Cell Culture dish, 15cm	Thermo Scientific	168381
Nunc™ Cell Culture dish, 10 cm	Merck	Z755923-150EA
Novex™ NuPAGE™ 4-12 % Bis-Tris Protein-Gel, 18 well	Bio-Rad	3450124
Novex™ NuPAGE™ 4-12 % Bis-Tris Protein-Gel, 26 well	Bio-Rad	3450113
Parafilm	Sigma-Aldrich/Merck	P7793
PCR plate, 96-well	Steinbrenner	SL-PP96-3L
Pipette Tips 10 µl	StarLab	S1111-3700
Pipette Tips 20 µl	StarLab	S1111-070
Pipette Tips 200 µl	StarLab	S1111-0706
Pipette Tips 1000 µl	StarLab	S1111-6810-C
Prolene monofil USP 7/0	Ethicon	EH7970H
Prolene monofil USP 6/0	Ethicon	EH7235H
PVDF-Membrane Immobilon-P	Millipore/Merck	IPVH00010
RNA 6000 Nano Bioanalyzer chip	Agilent Technologies	5067-1511
RNA 6000 Nano Bioanalyzer reagents	Agilent Technologies	5067-1512
Scalpel	Feather	02.001.30.010
Serological Pipette, 5 ml	Sarstedt	356543
Serological Pipette, 10 ml	Sarstedt	356551
Serological Pipette, 25 ml	Sarstedt	861.685.001
Syringe needle, 27 gauge	BD Microlance	3086999
Vetbond tissue adhesive	Fisher Scientific	10430774
Well Plates 6-wells	Greiner bio-one	657160
Well Plates 12-wells	Greiner bio-one	665180

2.7 Lab equipment

Devices	Supplier
Agilent 2100 Bioanalyzer	Agilent
Axio Observer Z1 fluorescence microscope	Zeiss
Cell Incubator: Hera Cell® 240i	Thermo Fisher Scientific
Criterion Cell System	Bio-Rad
Enspire Multimode Plate Reader	Perkin Elmer
Gel Imaging System, UV Transilluminator	Biostep
Gradient Station	BioComp
Harvard volume-cycled rodent ventilator	Harvard Apparatus Bio-Rad
Horizontal electrophoresis system	Bio-Rad
Laminar Flow Hood: Herasafe 2030i	Thermo Fisher Scientific
Laser Scanning Microscope: Cell observer SD	Zeiss
Multi Shaker, Plattform 409 x 297 mm	NeoLab
Magnetic stirrer: neo Mag® 1500 UpM	NeoLab
Mini Trans-Blot Cell	Bio-Rad
Nanodrop™ spectrometer	Thermo Fisher Scientific
Optima XPN-80 Ultracentrifuge	Beckman Coulter
Power Pac™ HC	Bio-Rad
Real-time PCR system: Viiia 7	Thermo Fisher Scientific
Stratalinker 2400 UV Crosslinker	Stratagene/Agilent
Thermal Cycler: C1000 Touch™	Bio-Rad
Tissue homogenizer, Bullet Blender	Next Advance
Vevo 2100 Imaging System	Visualsonics

2.8 Buffer and solutions

2.8.1 Buffers for general use

if not stated otherwise, buffers were prepared in ddH₂O

10 x PBS pH 7.4

1,37 M NaCl
26,8 mM KCl
14,7 mM KH₂PO₄
63,3 mM Na₂HPO₄ x 2 H₂O

10 x TBS

0.2 M Tris
1.5 M NaCl
Adjusted to pH 7.6

1 x TBST

1 x TBS
0,05% (V/V) Tween

TE-Buffer

100 mM TrisHCl pH 8
1 mM EDTA pH 8

2.8.2 Cell culture media and solutions

2.8.2.1 NRVCM preparation and culture

Digestion solution

In HBSS
0.25% (v/v) Trypsin
300 U/ ml DNase II
0.4 M HEPES
0.0016 M NaOH
2% (v/v) Penicillin-Streptomycin

ADS, 10 x

1.16 M NaCl
180 mM HEPES
8.45 mM NaHPO₄
55.5 mM Glucose
53.7 mM KCl
8.31 mM MgSO₄
Adjusted to pH 7.35±0.5

Stock Percoll

90% (v/v) Percoll
10% ADS, 10x

Top Percoll (density= 1.059 g/ml)

83% (v/v) Stock Percoll
17% ADS, 1x

Bottom Percoll (density 1.082 g/ml)

65% (v/v) Stock Percoll
35% (v/v) red ADS

Percoll gradient

4 ml Top Percoll (pipetted first)
3 ml Bottom Percoll (pipetted underneath)

Stop solution

4% (v/v) FBS
300 U/ ml DNase II
2% (v/v) Penicillin-Streptomycin

red ADS buffer

116 mM NaCl
18 mM HEPES
845 μ M NaHPO₄
5.55 mM Glucose
5.37 mM KCl
831 μ M MgSO₄
0.002% Phenol Red
Adjusted to pH 7.35 \pm 0.5

NRVCM Culture media

In DMEM/F-12 medium
10% (v/v) FBS
1% Penicillin-Streptomycin-Glutamine

NRVCM treatment media

In DMEM/F-12 medium
0.5% (v/v) FBS
1% Penicillin-Streptomycin-Glutamine

2.8.2.2 Adult cardiomyocyte preparation and culture

Perfusion buffer

113 mM NaCl
4,7 mM KCl
0,6 mM KH₂PO₄
0,6 mM Na₂HPO₄
1,2 mM MgSO₄
12 mM NaHCO₃
10 mM KHCO₃
10 mM HEPES
30 mM Taurin
5,5 mM Glucose
10 mM BDM (2,3-butanedione Monoxime)

Adult cardiomyocyte culture media

In MEM-Medium (MEM, Hanks' Balanced Salts)
0,2% BSA
50 U/ml Penicillin-Streptomycin
2 mM Glutamin/GlutaMAX
5 mM Taurin
10 mM BDM (2,3-butanedione Monoxime)
10 mM HEPES
1% ITS-Supplement

2.8.2.3 Murine embryonic fibroblast preparation and culture

MEF culture media

In DMEM
10% FBS
1% PSG
0.55 mM β-Mercaptoethanol

MEF freezing media

MEF culture media
+10% DMSO

2.8.3 Buffers and solutions for molecular biological and biochemical methods

2.8.3.1 Buffers for protein analysis

Ripa buffer

150 mM NaCl
1% (v/v) NP-40
0.5% (v/v) Na-Deoxycholate
0.1% (v/v) SDS
50 mM Tris-HCl pH 8

Mammalian polysome lysis buffer

in mammalian polysome buffer
20 mM Tris pH 7.4
10 mM MgCl
200 mM KCl
2 mM DTT
100 µg/ml CHX
1% Triton X-100
1U DNase/µl

Transfer buffer for Western blot analysis

192 mM Glycine
25 mM Tris
20% (V/V) Methanol
Adjusted to pH 8.3

RIP wash buffer

in mammalian polysome buffer
10% Triton,
1U DNase/µl

Ponceau S staining solution

0.1% (w/v) Ponceau S
5%(v/v) acetic acid

Homogenization buffer

20 mM HEPES
1 mM MgCl₂
150 mM NaCl
0.5 mM EDTA

processed Homogenization buffer

Homogenization buffer
+ 1mM DTT (added freshly)
+ PhosSTOP

2.8.3.2 RIP-Seq buffers

RIP high salt buffer

in mammalian polysome buffer

1M KCl

10% Triton

1U DNase/ μ l

2.8.3.3 Ribosome profiling/ RiboSeq buffers

Sucrose gradient (Polysome Profiling)

2x Sucrose buffer

In DEPC water

20 mM Tris-HCl pH 8.0

200 mM KCl

10 mM MgCl₂

0.2 mg/ml CHX

1 x Protease inhibitor cocktail

10 % Sucrose solution

In DEPC water

10 % (m/g) sucrose

50 % (v/v) 2x Sucrose buffer

50 % Sucrose solution

In DEPC water

50 % (m/g) sucrose

50 % (v/v) 2x Sucrose buffer

High salt buffer

20 mM Tris pH 7.4

10 mM MgCl

300 mM KCl

2 mM DTT

1% Triton X-100

2.8.3.4 Interactome capture buffers

Lysis buffer

20 mM Tris-HCl (pH 7.5)

500 mM LiCl

0.5% LiDS (wt/vol, stock 10%)

1 mM EDTA

5 mM DTT

0,05% Tween

store for up to 3 months at 4 °C.

Buffer 1

20 mM Tris-HCl (pH 7.5)
500 mM LiCl
0.1% LiDS (wt/vol, stock 10%)
1 mM EDTA
5 mM DTT
0,05% Tween
store for up to 3 months at 4 °C.

Buffer 2

20 mM Tris-HCl (pH 7.5)
500 mM LiCl
1 mM EDTA
5 mM DTT
0,05% Tween
store for up to 3 months at 4 °C.

Buffer 3

20 mM Tris-HCl (pH 7.5)
200 mM LiCl
1 mM EDTA
5 mM DTT
store for up to 3 months at 4 °C.

Elution buffer

20 mM HEPES
1 mM EDTA

Proteinase K buffer 5×

50 mM Tris-HCl (pH 7.5)
750 mM NaCl
1% (wt/vol) SDS
50 mM EDTA,
2.5 mM DTT and
25 mM CaCl₂

2.8.3.5 Buffer and solutions for histology**TN buffer (TNB)**

100mM Tris
150mM NaCl

Ammonia water solution

0.2 % (v/v) Ammonium hydroxide

Eosine stock solution

1 % (m/v) Eosin Y

Phloxine stock solution

1 % (m/v) Phloxine B

Eosine-phloxine solution

In Ethanol (95 %)

1 % (v/v) Eosine stock solution

0.1 % (v/v) Phloxine stock solution

0.4 % Acetic Acid

Phosphotungstic/phosphodic solution

In dionized water

25 % (v/v) Phosphotungstic Acid solution

25 % (v/v) Phosphomolybdic Acid solution

2.8.3.6 Agarose gel electrophoresis buffers**50x TAE buffer**

50 mM EDTA disodium salt

2 M Tris

1 M Acetic Acid

Agarose gel 1.5 %

in 1x TAE buffer

1.5% (m/v) Agarose

0.2 µg/ml ethidium bromide

2.9 Software

Adobe illustrator

Blast

Database for Annotation, Visualization and Integrated Discovery (DAVID) v6.8

Image J (Fiji) Microsoft Office

Primer-Blast Prism

R Studio

3. METHODS

3.1 Animal procedures

All experiments were performed in 9-12 week-old male mice. Institutional Animal Care and Use Committee approval was obtained for all animal studies.

3.1.1 Pas40 KO mice

Pras40 KO mice had been generated prior to this work. Pras40 KO embryonic stem cells were ordered from the European knock-out consortium (EuComm).

3.1.2 RiboTag mouse

The Ribo-tag mice were purchased from Jackson Laboratory (JAX ID 011029). The Ribo-tag mouse was bred to the α MHC- Cre mice to obtain cardiac myocyte Rpl22HA homozygous mice, respectively, as described before (Doroudgar et al., 2019).

3.1.3 Cpeb4 KO mice

Mice carrying a global deletion of Cpeb4 have been described previously (Calderone et al., 2016). Samples of mice were kindly provided by Raúl Méndez (IRB Barcelona).

3.1.4 Genotyping of mice

To determine the genotype of KO mice, a piece of tail tip was taken from living animals and used for isolation of genomic DNA, PCR and gel electrophoresis. Tail tips were digested in 95 μ l Buffer A for 35 min at 70 °C before 75 μ l of Buffer B were added. The samples were vortexed and after this step can be stored at 4 °C.

Polymerase chain reaction was performed with reagents from the REDEExtract-N-Amp™ Tissue PCR Kit according to the manufacturers protocol:

5 μ L	REDExtract-N-Amp PCR Reaction Mix
1 μ L	Forward Primer
1 μ L	Reverse Primer
2 μ L	Tissue Extract
ad 10 μ L	

The PCR reaction was run according to the manufacturers protocol and bands were visualized on a 1.5% agarose gel.

Global *Pras40* mice were randomly tested for the deleted locus, which instead of the WT band (530-550 bp) leads to a lower band (250-300 bp, Fig. 2.1A).

Conditional *Pras40* KO and Ribotag-HA mice were detected by their *Cre* locus. Sample of *Cre* negativ animals lead to one single PCR product, whereas *Cre* positiv animals show an additional, slightly higher band (Fig. 2.1B).

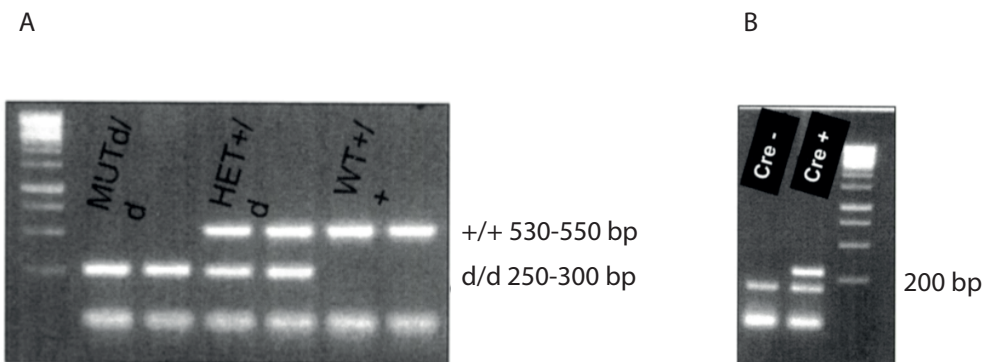


Figure 2.1: PCR products of genotyping PCRs. (A) PCR products of PCR for phenotyping of global *Pras40* KO mice. d/d represents deleted allele, +/+ WT allele. (B) PCR products of PCR for phenotyping of conditional mice, that are transgenic when *Cre* positive. PCR of *Cre* positive (*Cre*⁺) animals generates two PCR products, whereas *Cre* negative (*Cre*⁻) animals only show one band.

3.1.5 Transverse aortic constriction (TAC) surgery

For transverse aortic constriction, mice were anesthetized with 2.5 vol% Isoflurane and 1.5 l/min 100% O₂, and intubated by opening the skin as well as muscle and connective tissue around the trachea to enable vision of the tubus in the trachea. After closing up the wound, the mouse was placed in a supine position onto a heat pad at 37 °C to ensure stable body temperature. The intubation was connected to a Harvard volume-cycled rodent ventilator cycling at 200 breaths/minute, maintaining anesthesia at 2% isoflurane with 1.5 l/min 100% O₂. The aorta was reached by a micro invasive technique. Skin was opened above the sternum and muscle tissue is opened between the first and second rib on the left side of the mouse. Muscle tissue was held open with four clips from each side. The thymus was removed carefully with the clips to ensure clear vision of the aorta. Connective tissue around the aorta was cleared and a 7.0 gauge prolene threat was pulled under the aortic arch between both carotids. With a 27 gauge needle as a spacer, a defined aortic construction was defined: Two double knots around aorta and spacer were tied and the spacer was quickly removed to enable proper blood flow. Muscle tissue was sewed with 6.0 gauge Prolene threat and the skin was glued with tissue vet bond.

Mice were treated with 0,3 mg/kg Buprenorphine intra-peritoneally pre and post surgery and one day post TAC.

3.1.6 Swimming regime

To induce physiological cardiac hypertrophy, mice were subjected to an endurance swimming regime. Swimming was performed in a pre-heated pool with bubble-induced buoyancy, to avoid floating of the animals.

Swimming was performed twice daily, with increasing endurance, starting with 10 min/session and increasing by 10 min/day. Mice were subjected to the regime for a total of 4 weeks.

3.1.7 Echocardiography

Echocardiography was performed by the Visual Sonics Vevo 2100 Imaging System baseline before treatments and at specific timepoints after the treatments to define heart anatomy and function. Images were taken with the MS-M550D transducer from parasternal long and short axis of the heart to define anterior and posterior wall thickness and function. Images were taken in B-mode, followed by a time-dependent cross-section was taken in M-mode.

Before measurements were recorded, animals were shaved to enable better picture quality with less background. Animals were then anesthetized with 2.5 vol% Isoflurane and fixed in a supine position onto the four electrodes of the heated plate (37 °C). Electrode gel allowed proper transmission of heart and breathing rates. Pictures were recorded at a heart rate between 400 and 450 beats per minute to allow comparability between images and to avoid bias in heart function measurements.

Analysis was performed using the standard 2D quantification software. Ejection fraction and fractional shortening were analyzed from M-mode images of the short axis, anterior left ventricular wall thickness from M-mode images of the long axis.

3.1.8 Puromycin incorporation assay

To detect newly synthesized proteins, we injected antibiotic protein synthesis inhibitor Puromycin, which is incorporated into the nascent polypeptide chain and therefore labels newly synthesized proteins. Puromycin was injected intraperitoneally at a concentration of 50 mg/kg for a chase period of 30 min before sacrifice and organs were then isolated in the standard procedure.

3.1.9 Organ isolation for lysis

Hearts, lung, liver, tibia and skeletal muscle were typically isolated for analysis of protein and RNA of the experimental animals. Mice were sacrificed by cervical dislocation and quickly opened above the diaphragm.

Hearts were taken first, washed in ice cold PBS and atria were removed. Left and right ventricles were weighed and shock frozen in the liquid phase of N₂. Other organs were then removed after and stored in N₂ as well.

3.1.10 Isolation of hearts for histology

Mice were sacrificed by cervical dislocation and the chest was opened to expose the heart. 2 ml of 100 mM CdCl₂ were slowly injected into the left ventricle to stop beating in diastole *in situ*. The right ventricle was cut open for drainage and then 5 ml 100 U/ml Heparin/PBS were gradually injected into the right ventricle to wash out the blood from the vessel. Then 10 ml of 10% formaldehyde solution were gently infused from the right ventricle into the left ventricle. Next, the heart was excised, cleaned from connective tissue and fixed in 4% formaldehyde/PBS for 24 h at RT and then transferred into 70% ethanol for > 24 h.

3.1.11 Histological methods

3.1.11.1. Preparation of histological sections

After fixation, hearts were dehydrated in a series of ethanol dilutions (80%, 96%, 2 x 100%) for 2 hours each. Dehydrated hearts were then embedded in paraffin, sectioned and placed on slides. Mounted sections were deparaffinized in xylol for 2 x 5 min, then rehydrated by decreasing amounts of ethanol (2 x 100%, 96%, 70%) 5 min each. Slides were washed in PBS and used for stainings.

3.1.11.2 Hematoxylin-Eosin staining

Slides were incubated in hematoxylin for 5 minutes, followed by washing in water for 5 minutes and differentiating in 1% acid alcohol for 30 seconds. Slides were then rinsed in water for 1 min, and blued in 0.2% ammonia solution for 30-60 seconds. The slides were washed in running tap water for min, then rinsed in 95% alcohol and counterstained in eosine-phloxine solution for 30-60 sec. Stained slides were dehydrated by 5 minutes in

by an ethanol series (2 x 95%, 3 x 100%), followed by 2 x 5 minutes washes in Xylol. Slides were covered with coverslip by Vectashield® antifade mounting media.

3.1.11.3 Masson trichrome staining

Slides were incubated in Bouin's solution for 1 h at 60 °C, then washed with running tap water for 5 minutes, followed by incubation in Weigert's iron hematoxylin solution for 10 minutes. Slides were then washed with running tap water and placed in Bieberich Scarlet solution for 5 minutes, followed by 3 cycles of rinsing in distilled water. Next, slides were incubated in phosphotungstic/ phosphomolybdic solution and then directly transferred to aniline blue for 10 min. Slides were rinsed in 1% acetic acid 3 times, then incubated in 1% acetic acid and rinsed in distilled water. Slides were dehydrated again in an ethanol series (70, 90, 100) and then in Xylol, each for 1 minutes. Slides were then covered with coverslip using Vectashield® antifade mounting media.

3.1.11.4 Immunohistochemistry

Antigen retrieval was achieved by boiling the slides in 10 mM citrate (pH 6.0) for 12 minutes, after which the slides were washed several times with distilled water, and once with PBS. Slides were blocked with 5% BSA in TN buffer (TNB). Primary antibodies were diluted in 5% BSA in TNB and added to slides which were incubated at 4 °C ON. The samples were then washed 5 x with TNB and incubated with secondary antibodies in TNB at RT in the dark for 2 h. Slides were covered with coverslip using Vectashield® antifade mounting media. Images were obtained using a Zeiss Observer. Z1 fluorescence microscope. Images were obtained with a 10, 20 and 40 x objective.

3.1.12 Isolation of primary cells

3.1.12.1 Isolation of murine adult cardiomyocytes

Adult cardiomyocytes were isolated by a Langendorff perfusion set-up, as described before (Döring, 1990).

Before starting, 90 ml of perfusion buffer (PB) per mouse was thawed and pre-heated to 37°C, the water bath of the Langendorff perfusion system was pre-heated to 37 °C and the flow rate was set to 3,5 ml/min. The apparatus was washed with 100 ml of distilled water, then for 5 minutes with PBS, making sure to get rid of bubbles. The syringe of the Langendorff system was filled with 20 ml PB and put into its position.

100 IU Heparin was injected intraperitoneally before the procedure. The mouse was sacrificed by cervical dislocation, and the heart was isolated including 1-1,5 mm of aorta, and transferred into 25 ml of ice-cold PBS. The aorta was placed onto the cannula of the Langendorff system, tightened and placed in the system. The heart was then washed with PB for 2-3 minutes. The setup was then changed to digestion buffer (DB), and the heart was washed with DG for 13 minutes. The heart was then removed from the apparatus, transferred to 2.5 ml DB, and cut to small pieces for around 30 seconds. Immediately after, 2.5 ml stop buffer were added. The solution was then filtered through gauze tissue into a 15 ml conical tube and the cells were then allowed to settle for 11 minutes. The supernatant, containing dead cells and erythrocytes, was removed and the remaining cells were mixed with 5 ml stop buffer II.

Calcium was restored according to the following scheme, with incubation times of 4 minutes per cycle:

after 4 minutes: 25 µl Ca²⁺ 10 µM

after 8 minutes: 25 µl Ca²⁺ 10 µM

after 12 minutes: 50 µl Ca²⁺ 10 µM

after 16 minutes: 20 µl Ca²⁺ 100 µM

after 20 minutes: 30 µl Ca²⁺ 100 µM

After the last step, stop buffer II was removed to 1 ml and the cells were mixed with ACM medium and seeded onto laminin coated dishes or chamber slides.

3.1.12.2 Isolation of ventricular cardiomyocytes of neonatal rats

Neonatal ventricular cardiomyocytes (NRVCMs) were isolated from hearts of 1-2 days old Sprague-Dawley rats. Isolated hearts were kept in HBSS with 0,5% Penicillin and Streptomycin (P/S) on ice and cleared from both atria. Ventricles were washed in HBSS+P/S to remove blood and blood clots and were then cut into 1 mm pieces to allow efficient digest.

Crushed ventricles were taken up in 5 ml digestion solution, transferred into a 50 ml centrifugation tube and supernatant was discarded. Another 10 ml digestion solution were added, and once cardiomyocytes were settled removed again. Cardiomyocytes were then digested in 10 ml digestion solution for 10 minutes at 37 °C. Trypsin-dependent digestion was stopped by the addition of stop solution containing FCS. Undigested material will settle at the ground of the tube, whereas digested cells will be part of the supernatant. Digestion was repeated for 8 times with the remaining pellet, pooled supernatant was then centrifuged at 4 °C and 500 G for 15 minutes. Supernatant was discarded and cells were resuspended in DMEM/F12, sterile filtered and centrifuged at 250 G for 5 minutes, to separate cells from the supernatant. Cells were then resuspended in 1-1.5 ml ADS. To ensure a clear cardiomyocyte population, a Percoll gradient was performed. For this purpose, two Percoll solutions with different densities were prepared, that will form the „top“ and „bottom“ of the gradient. To prepare the gradient, 4 ml of top solution were added to a 15 ml centrifugation tube and 3ml of bottom solution were carefully added to the bottom of the tube. 2 ml of cell solution were then added to the top of both solutions, the gradient was centrifuged for 30 minutes at 15000 G and RT. To ensure separation of both gradient phases the centrifuge was accelerated at intensity 5 and brake intensity 0. After centrifugation, cell populations are separated between phases.

The upper phase contains the ADS, the second yellow phase the fibroblasts, the white middle phase the ADS, the bottom yellow phase the cardiomyocytes, the two bottom phases ADS and dead cells respectively. Cardiomyocytes were collected carefully, transferred in a 50 ml centrifugation tube, filled up to 50 ml with ADS and centrifuged for 5 minutes at 250 G. The supernatant was discarded and centrifugation repeated with another 50 ml of ADS. Pelleted cardiomyocytes were resuspended in NRVCM culture medium. For plating of the NRVCMs, plastic petri dishes were coated with fibronectin from bovine serum, prediluted in DMEM/F12 Medium 1:200 and incubated at 37 °C for 1 h to ensure attachment of NRVCMs onto the plastic surface. After removal of fibronectin, NRVCMs were seeded in NRVCM culture media. After 24 h of culture, cells were washed with and cultured in NRVCM treatment media.

3.1.12.3 Isolation of murine embryonic fibroblasts (MEFs)

Murine embryonic fibroblasts (MEFs) were isolated from embryos between E12 and E14. To isolate embryos, the yolk sac was opened and fetuses were dissected and transferred to a dish containing 10 ml of sterile PBS. Hearts and livers were removed, as well as brains (by removing upper part of the head). Remaining parts were washed in PBS to remove as much blood as possible and transferred to a new dish. 2-3 ml of ice-cold 0.25% trypsin-EDTA were added to the dish and fetuses were dissected into small pieces. Fetuses were transferred to a 50 ml conical tube, and after sedimentation of the tissue, PBS was removed. 0.25% Trypsin-EDTA were added to a total amount of 3 ml/fetus. The tube was let stand ON at 4 °C. On the next morning, without suturing the tissue, the solution was aspirated, leaving around twice the amount of volume of the tissue. The tube was then incubated at 37 °C in the water bath for 30 minutes. 25 ml of MEF culture media were then added and the mixture was pipetted rigorously to break up the digested tissue. A 1 minute incubation period was then performed to blow sedimentation of the cell suspension, the supernatant was transferred to a new tube. The pellet was again mixed with ME culture media, pipetted up and down. After another sedimentation period of 1 minute, both supernatant batches were mixed and cells were.

Cells were incubated ON, then washed with sterile PBS to discard non adherent cells, and then cultured to confluence before freezing in MEF freezing media.

3.2 Cell culture methods

All cells were grown in adherent cultures in the incubator at 37 °C and 5% CO₂ in a H₂O saturated atmosphere. Cell culture work was performed in a laminar-flow hood under sterile conditions. NRVCMs and ACMs as primary cells can be cultured for few days after isolation, MEFs can be further frozen and passaged.

3.2.1 Thawing of cells

To clear the cells from the DMSO-containing freezing medium as fast as possible, cells were thawed in the 37 °C water bath and diluted with fresh growth medium. After centrifugation for 3 minutes at 1000 rpm in a conical tube, the cell pellet was resuspended in an appropriate amount of medium and cells were seeded. To distribute the cells equally, the plate can be moved horizontally in eight-shaped circles.

3.2.2 Trypsinizing/ Singularizing of cells

Cells were washed with PBS twice before trypsinization. The detaching of the cells was then induced by adding 1x trypsin for an incubation time of at least 3 but no longer than 5 minutes in the incubator. The trypsin was then inactivated by two volumes of 10% serum containing medium. The cells were singularized by pipetting up and down the mixture several times. After centrifugation in a conical tube for 3 minutes at 1000 rpm, the pellet was resuspended in fresh medium.

3.2.3 Counting of cells

10 µl of cell suspension were pipetted into a Neubauer chamber. The known volume of the chamber allows calculating the number of cells per milliliter of suspension. The cell number per milliliter was determined by the number of one main square multiplied by 10⁴.

3.2.4 Freezing of cells

Cells were washed twice with PBS and trypsinized as described above. After adding fresh medium, the cells were pelleted (10 °C, 1000 rpm, 3 minutes) and resuspended in FCS containing 10% sterile DMSO. Cells were stored at -80 °C or in the gas phase of N₂.

3.2.5 Transfection with HiPerfect to induce knock-down *in vitro*

To knock down a protein of interest *in vitro*, NRVCMs or MEFs were transfected with small interfering RNA (siRNA). 24 h after plating, NRVMs or MEFs were transfected with either 25 nM scrambled siRNA or siRNA targeting the gene of interest using the transfection agent HiPerfect according the manufacturer's protocol. The transfection reaction was set up in media containing 0.5% FCS. Media containing the transfection solution was replaced by fresh media after an incubation ON.

3.2.6 Viral transduction

Adenovirus or AAV6 was added to cell culture media 24 h after plating of NRVCMs or at 70% confluence for MEFs. For NRVCMs, virus was added into 0.5% culture medium, for MEFs to standard culture medium. After 24 h of culture, cells were harvested in RIPA buffer or Trizol/ RNA Lysis buffer for RNA isolation.

3.2.7 Phenylephrine treatment

To mimick pathological cardiac hypertrophy, NRVCMs were treated with the α 1 receptor agonist Phenylephrine (PE), which induces pathological cell growth in cardiomyocytes *in vitro* (Simpson, 1985). After 24 h of culture in NRVCM culture media, and a starvation period of another 24 h in NRVCM treatment media, Phenylephrine was freshly dissolved in cell culture grade H₂O and diluted in NRVCM treatment media to a final concentration of 50 μ M. Cells were PE-treated for 24 h and then directly harvested.

3.2.8 Actinomycin D assay

To inhibit transcription, NRVMs were treated with 2 μ M Actinomycin D in NRVM culture media for 1, 2 and 4 hours. Cells were harvested for RNA isolation and RT-qPCR of Cpeb4 target gene transcripts. Fold changes of Δ Ct from Ct of each time point and time point 0 h of Actinomycin D treatment were calculated and non-linear regression curves using GraphPad Prism were modeled in order to determine transcript stability over time.

3.2.9 Cell size *in vitro* and *in vivo*

For cardiomyocyte cell size measurements, only strictly cross-sectional cells were analyzed. At least 50 cells were analyzed from every heart/ chamber slide. Cell size determination was performed blinded to the experimental group when scanning the slides and analyzing the data.

3.3 Molecular biological methods

3.3.1 RNA isolation from eukaryotic cells

RNA was isolated from cell or organ lysates as described in the following section. Typically, RNA from organ lysates was isolated by Phenol-chloroform extraction, whereas RNA from *in vitro* samples was isolated by the Qiagen RNeasy or the Zymo RNA isolation kit, as available.

3.3.1.1 Qiagen RNeasy Kit

RNA was isolated according to the protocol; the lysis step was performed by directly adding Buffer RLP to the PBS-washed cells. RNA was eluted in 20 μ l nuclease-free H₂O.

3.3.1.2 Zymo RNA isolation kit

RNA was isolated according to the protocol; the lysis step was performed by directly adding lysis Buffer to the PBS-washed cells. RNA was eluted in 20 μ l nuclease-free H₂O.

3.3.1.3 Phenol-Chloroform-extraction

The cells were washed with PBS at least once before adding Quiazol reagent (1 ml/ 6-well). After three minutes at RT, the samples were centrifuges for 15 minutes at 12000 g at 4 °C to bring the RNA to the aqueous phase, which was then transferred into a new reaction tube. The mixture was vortexed with 500 µl Isopropanol and kept for 10 minutes at RT before centrifuging at 12000 g and 4 °C. The pellet was washed with 75% Ethanol and subsequently dried for 5 minutes. The dry pellet was resuspended in 20 µl RNase free ddH₂O and solved in the heat block for 5 minutes at 55 °C.

3.3.2 Reverse transcription of RNA

Isolated mRNA was transcribed into cDNA with the cDNA Synthese Kit iScript™ from Bio Rad by reverse transcription according to the manual:

500 ng mRNA
4 µl reaction mix
1 µl reverse transcriptase
ad 20 µl nuclease-free H ₂ O

were mixed in an autoclaved, DNase/ RNase free reaction tube. The reaction mix was incubated according to the manufacturers protocol: 5 minutes/ 25 °C preheating; 30 minutes/ 42 °C reverse transcription; 5 minutes/ 85 °C transcription stopping. cDNA was diluted 1:10 in nuclease-free water and stored at -20 °C.

3.3.3 Relative quantification of cDNA by real-time PCR

To quantify amounts of cDNA, quantitative real-time PCR was performed. The amount of target cDNA was normalized to two house keeping genes, that have stable in expression levels. For qPCR, iTaq™ Universal SYBR Green Supermix from Bio-Rad

was applied. This kit consists of Taq-DNA-polymerase, dNTPs, MgCl₂, SYBR[®]-green I, enhancers and stabilizers. The following components were mixed in a reaction tube:

3 µl cDNA (1 ng/ul)
5 µl of iTaq™ Universal SYBR Green Supermix
1 µl of forward primer
1 µl of reverse primer

The reaction was run in a PCR machine according to the manufacturers protocol.

Primer sequences are listed in materials section 2.5.1.

3.3.4 Protein isolation and quantification

Lysis of cells was performed in protein lysis (RIPA) buffer with freshly added Phosphatase – inhibitor and Protease – inhibitor after washing once in ice-cold PBS. Cells were scraped with a cell scraper in lysis buffer, transferred into a reaction tube and stored at -20 °C. For protein determination, the lysate was centrifuged for 10 minutes at 14000 rpm and 4 °C.

Protein determination was performed by the Bio-Rad DC Protein Assay kit according to the manufacturer's protocol. This protocol is based on the Lowry method for protein determination, which is a colorimetric approach based on the reaction between protein, copper and Folin-reagent in alkaline medium, that results in a blue color change with maximum extinction at 750 nm.

As standard, a dilution series with BSA in the same buffer as the samples was prepared in the following concentrations: 0 mg/ml, 0,15625 mg/ml, 0,3125 mg/ml, 0,625 mg/ml, 1,25 mg/ml, 2,5 mg/ml, 5 mg/ml and 10 mg/ml.

From measured extinctions and known BSA concentrations a standard curve was calculated, that was used to determine concentrations in the lysate samples.

3.3.5 Western blotting

To prepare the samples for gel electrophoresis, 10-30 µg protein were mixed with RIPA buffer and 1/4 Laemmli containing 10% β-Mercaptoethanol. Samples were then heated for 10 minutes at 75 °C in a heating block and loaded into a Sodiumdodecylsulfate Polyacrylamide gel.

During gel electrophoresis, proteins are separated according to their molecular mass in an electrical field (Burnette, 1981; Towbin et al., 1992). SDS, an anionic tensid, is used to negatively charge proteins, making them run towards the anode of the electrical field.

For all shown experiments, commercially available gels in BisTris buffer (pH = 6.4) with an Acrylamide gradient of 4-12% were used (BioRad).

Electrophoresis was performed in BioRad appliances in a 3-(*N*-Morpholino)propanesulfonic acid (=MOPS) SDS running buffer. To allow proper running of samples, runs were started at 100V and then increased to 180V. Following separation of proteins, proteins were blotted onto a Polyvinylidene difluoride- (PVDF-) membrane by a wet transfer method: For this purpose, the PVDF-membrane was activated in methanol and layed onto the gel with the gel facing the cathode. One layer of Whatman[®] filter paper and sponge were added on both the cathode and anode side, the stack was fixed in a holder and placed in the transfer appliance. The transfer was run for 35 minutes at 100 V in 1000 ml transfer buffer.

The membrane was blocked for unspecific binding sites in 5% milk in TBST for 1 hour at RT and proteins were then incubated with appropriate antibodies over night at 4 °C on a shaker. Antibodies were diluted in 5% milk in TBST. Membranes were then washed three times in TBST for 10 minutes and then incubated in the appropriate horseradish peroxidase-conjugated secondary antibody matching the species of the primary antibody. After three rounds of washing in TBST, detection was performed using Western Lightning Plus-Enhanced Chemiluminescence (ECL) substrate.

Primary antibodies were used as shown in the table 2.2.1.

3.3.6 Ponceau staining

To visualize protein bands on PVDF membranes, membranes were stained with ponceau staining solution for 5 minutes. To remove pink background stain, membranes were then washed in ultra pure H₂O in three rounds of 5 minutes.

3.3.7 Silver stain

Silver staining to visualize proteins separated on SDS Polyacrylamide gels were performed with the Pierce Silver stain kit according to the manufacturers protocol.

In addition to the protocol, the following solutions were prepared:

Fixing Solution: 30% ethanol, 10% acetic acid

Stop Solution: 5% acetic acid

Ethanol Wash: 10% ethanol

To prepare the samples for gel electrophoresis, 10-30 µg protein were mixed with RIPA buffer and 1/4 Laemmli containing 10% β-Mercaptoethanol. Samples were then heated for 10 minutes at 75 °C in a heating block and loaded into a Sodiumdodecylsulfate Polyacrylamide gel.

The gel was transferred into a clean dish and washed in ultrapure water for 5 minutes twice. The gel was then incubated for 15 minutes at RT in fixing solution twice. The gel can remain in fixing solution overnight without affecting stain performance. In the following, the gel was washed in ethanol wash for 5 minutes twice and then ultrapure water for 5 minutes twice. Sensitizer solution was then freshly prepared from 1 part Silver Stain Sensitizer with 500 parts ultrapure water and the gel was incubated in sensitizer solution for exactly 1 min, followed by 2 x 1 minute wash steps. Stain enhancer solution was mixed from 1 part Silver Stain Enhancer with 100 parts Silver Stain and used to incubate the gel for 5 minutes. Developer working solution was prepared by mixing 1 part Silver Stain Enhancer with 100 parts Silver Stain Developer. The gel was quickly washed twice with two changes of ultra pure water for 20 seconds

each and then developed by developer working solution until protein bands appeared (2-3 minutes). The developing was then stopped quickly by adding two charges of stop solution.

3.3.8 Immunofluorescence staining

To visualize the expression of transgenes on protein level, cells were stained by a primary antibody, and a binding secondary antibody with a fluorescent label.

NRVCMs were grown on glass chamber slides (gelatin-coated). Cells were fixed by 4% PFA for 20 minutes at room temperature, washed three times with PBS, and permeabilized in PBS with 0.1% Triton-X for 10 minutes, then blocked in PBS with 10% horse serum for 1 h. Primary antibodies diluted in blocking solution (PBS with 10% horse serum) were applied overnight at 4 °C. The next day, cells were washed with PBS and incubated for 1 h at RT with secondary antibody diluted in blocking solution. After three washing steps in PBS, cells were mounted using Vectashield® antifade mounting media and cover slips with 1:1000 DAPI as nuclear staining.

A list of antibodies used for immunofluorescence stainings can be found in section 2.2.2.

3.3.9 Proximity ligation assay

The proximity ligation assay was performed prior to this project as described before (Volkers et al. 2013).

3.3.10 Proteasome activity assay

Proteasomal activities were determined by a previously established enzymatic assay (Drewe et al., 2007, 2010).

To assess proteasomal activity *in vivo* or *in vitro*, hearts or cells were lysed in processed homogenization buffer, that keeps proteasomes intact. Before harvest, cells were washed with PBS; hearts were used shock-frozen in N₂. Lysates were homogenized by needling with a 25 G syringe 8-10 times and centrifuged in an ultracentrifuge at 45 000 rpm for 1 h at 4 °C. The supernatant containing the cytosolic fraction of the lysate was transferred

into a new 1.5 ml tube and used for the further procedure of the experiment. To quantify protein amounts, 1/10 of the sample was diluted 1:1 in 2 x RIPA buffer and protein determination was performed as described above.

For the actual measurement, 26S buffer was prepared from homogenization buffer, ATP (final concentration of 50 μ M per well) and proteasome inhibitor for one of the 26S proteasomal activities or DMSO as vehicle. Inhibitors for all three activities were added as shown in table 6. 25 μ g protein were used per well and filled up to 90 μ l with 26S buffer. The plate was incubated in the dark for 30 minutes at RT and 15 minutes on ice. The respective peptide substrate was then added in 10 μ l of homogenization buffer to a final concentration of 100 μ M per well. The reaction was then placed into the pre-heated (37 $^{\circ}$ C) plate reader and fluorescence was measured at an excitation wavelength of 390 nm and an emission wavelength of 460 nm every 5 minutes for 90 minutes.

Activities were calculated from the net difference of activities without and with inhibitor, and from the slope of each sample in the linear phase of the protein degradation, defining $d(t) = t(55 \text{ min}) - t(20 \text{ min})$.

	reagent	concentration/well	activity
inhibitor	Epoxomicin	10 μ M	chymotrypsin
	Epoxomicin	20 μ M	trypsin
	MG132	50 μ M	caspase
substrate	Suc-LLVY-AMC	100 μ M	chymotrypsin
	BZ-VGR—AMC	100 μ M	trypsin
	Z-LLE-AMC	100 μ M	caspase

Table 6: Inhibitors and substrates to measure chymotrypsin-like, trypsin-like and caspase-like 26S proteasomal activities.

3.3.11 Immunoprecipitation

Cells were harvested in IP lysis buffer needed for complete lysis. Equal amounts of lysate per sample were filled to 1 ml in a reaction tube and incubated with primary AB overnight at 4 $^{\circ}$ C on a rotator, then for 1 h at RT with prepared dynabeads sheep anti

rabbit IgG. Coprecipitate was washed 5 times with IP wash buffer, by collecting the beads on a magnetic rack and discarding the supernatant. After a following wash step in PBS the supernatant was transferred to a clean reaction tube, and the supernatant was discarded. The beads were then dissolved in 20 μ l RIPA and 20 μ l Laemmli containing 10% β -Mercaptoethanol and heated for 10 minutes at 70 °C. The eluate was then separated from the beads on the magnetic rack and used for Western blot analysis.

3.3.12 mRNA interactome capture (RIC)

Interactome was performed according to Castello et al. (Castello et al., 2013), with minor changes to the protocol. Lysis and wash buffers 1-2 additionally contained 0.02% Tween. For the elution buffer, Tris was replaced by the same concentration of HEPES. For one biological replicate, 18 Mio. cells were seeded onto 3 x 15 cm dishes and dishes were then pooled for one oligo d(T) capture sample. Cells were harvested in 3 x 3 ml lysis buffer for Poly(A)-precipitation. 300 μ l were kept for analysis of total proteome (TP). 2.5 ml Oligo d(T) beads were washed according to the manufacturers protocol, added to the cell lysate and incubated together for 1h at 4°C. Beads were then collected at a magnet, the supernatant removed and the beads were washed in several steps, including 5 min incubation for each wash step on a rotator at 4°C: Three wash steps in buffer 1 and buffer 2, respectively were followed by two wash steps in buffer 3. After these wash steps, the beads were dissolved in 1ml buffer 3 and transferred to a 1.5ml reaction tube. The supernatant was removed at the magnet, and the RBPs were removed from the beads in 1ml elution buffer by heating the mixture at 70°C for 3 minutes. The eluted sample was concentrated on a Amicon device according to the manufacturers protocol.

3.3.13 RNA-Immunoprecipitation

RNA-Immunoprecipitation was performed by Eshita Varma. NRVCMs were harvested in mammalian polysome buffer (10% Triton, DNase, RNase inhibitor added freshly) and sonicated for complete lysis. Lysate was incubated with Cpeb4 AB overnight at 4 °C, then for 1h at RT with prepared dynabeads sheep anti rabbit IgG. Coprecipitate was

washed once with wash buffer (mammalian polysome buffer, 10% Triton, DNase I added freshly), three times with high salt buffer (mammalian polysome buffer + 1M KCl, 10% Triton, DNase I) and once with wash buffer. RNA was eluted by addition of Trizol and following RNA clean-up. Lexogen Quant-Seq kit was used for library generation following the manufactures instruction. Libraries were multiplexed and sequenced on a NextSeq550 sequencer.

For RIP-PCR, eluted RNA was reverse-transcribed and used for qRT-PCR analysis.

3.3.14 RIP-Seq analysis

RIP-Seq analysis was performed by Thileepan Sekaran, EMBL Heidelberg. Reads were trimmed with Cutadapt (v2.5) and mapped to rat genome (Rnor_6.0) with STAR (v2.7) and summarized with featureCounts (v1.6.4). DESeq2 (Love et al., 2014) with IHW (Ignatiadis et al., 2016) for multiple hypothesis correction was used to determine significantly enriched RNAs in IP samples vs corresponding input controls (adjusted p-value < 0.1; log₂ fold-change > 0.5).

3.3.15 Isolation of monosomes for RiboSeq of NRVCM samples

Ribosome footprints (RPF) were generated after isolation of Polyribosomes from NRVMC lysates and RNase I digestion (ribonuclease I) as previously published (Kmietczyk et al., 2019). Briefly, 15 Million NRVMs were lysed in 500 µl polysome buffer containing 100 µg/ml CHX. The lysate was used for RPF generation using polysome profiles after RNase I digestion. For complete lysis, the samples were kept on ice for 10 minutes and subsequently centrifuged for 10 minutes at 20,000 g to dispose cell debris. Sucrose solutions were prepared in polysome gradient buffer and 20 U/mL SUPERase-In. Sucrose density gradients (10–50% wt/vol) were freshly made in SW40 ultracentrifuge tubes using a BioComp Gradient Master (BioComp). Ribosome footprints were generated after treating the lysate with RNase I. Cell lysates were loaded onto sucrose gradients, followed by centrifugation for 250 minutes at 220000 g, 4 °C, in an SW40 rotor. Separated samples were fractionated at 0.375 ml/min by using a

fractionation system BioComp Gradient Station that continually monitors OD254 values. Monosomal fractions were collected into tubes at 0.3 mm intervals.

3.3.16 Precipitation of ribosomes for RiboSeq of *in vivo* RiboTag samples

Mice were sacrificed, and hearts were excised and washed in PBS containing 100 $\mu\text{g/ml}$ cycloheximide (CHX). For storage, hearts were snap frozen in liquid nitrogen. Left ventricular tissue was homogenized in a tissue homogenizer after adding 5 volumes of ice-cold polysome buffer containing 100 $\mu\text{g/ml}$ CHX. To completely lyse the ventricular tissue, samples were incubated on ice for 10 minutes followed by 10 minutes centrifugation at 20,000 $\times g$ to precipitate cell debris. 100 μL of lysate were kept as input. All other lysate was used for anti-HA Immunoprecipitation of polysomes. 100 μl anti-HA magnetic beads per heart were washed with 1000 μL polysome lysis buffer three times. The lysate was then added to anti-HA magnetic beads and incubated on a rotator at 4 $^{\circ}\text{C}$ overnight. The beads were then washed three times with 500 μL of high salt buffer. The washed beads were subjected to RNA extraction for library generation.

3.3.17 Library generation for RiboSeq

Libraries were generated according to the mammalian Ribo-seq kit (Illumina) and sequenced on a NextSeq 550.

3.3.18 Proteomic analysis

3.3.18.1 Sample preparation and TMT labeling

Mass spectrometry analysis was performed by Mandy Rettel, Proteomics facility EMBL Heidelberg. Reduction of disulphide bridges in cysteine containing proteins was performed with dithiothreitol (56 $^{\circ}\text{C}$, 30 minutes, 10 mM in 50 mM HEPES, pH 8.5). Reduced cysteines were alkylated with 2-chloroacetamide (room temperature, in the dark, 30 minutes, 20 mM in 50 mM HEPES, pH 8.5). Samples were prepared using the SP3 protocol (Hughes et al., 2014, 2019) and trypsin (sequencing grade, Promega) was

added in an enzyme to protein ratio 1:50 for overnight digestion at 37 °C. Peptides were labelled with TMT10plex (Werner et al., 2014). Isobaric Label Reagent (ThermoFisher) according the manufacturer's instructions. For further sample clean up an OASIS® HLB μ Elution Plate (Waters) was used. Offline high pH reverse phase fractionation was carried out on an Agilent 1200 Infinity high-performance liquid chromatography system, equipped with a Gemini C18 column (3 μ m, 110 Å, 100 x 1.0 mm, Phenomenex), resulting in 5 fractions for interactome samples and 12 fractions for full proteome analysis (Reichel et al., 2016).

3.3.18.2 Mass spectrometry data acquisition

Mass spectrometry data acquisition was performed by Mandy Rettel, Proteomics facility EMBL Heidelberg. An UltiMate 3000 RSLC nano LC system (Dionex) fitted with a trapping cartridge (μ -Precolumn C18 PepMap 100, 5 μ m, 300 μ m i.d. x 5 mm, 100 Å) and an analytical column (nanoEase™ M/Z HSS T3 column 75 μ m x 250 mm C18, 1.8 μ m, 100 Å, Waters). Trapping was carried out with a constant flow of solvent A (0.1% formic acid in water) at 30 μ L/min onto the trapping column for 6 minutes. Subsequently, peptides were eluted via the analytical column with a constant flow of 0.3 μ L/min with increasing percentage of solvent B (0.1% formic acid in acetonitrile) from 2% to 4% in 4 minutes, from 4% to 8% in 2 minutes, then 8% to 28% for a further 96 minutes, and finally from 28% to 40% in another 10 minutes. The outlet of the analytical column was coupled directly to a QExactive plus (Thermo) mass spectrometer using the proxeon nanoflow source in positive ion mode. The peptides were introduced into the QExactive plus via a Pico-Tip Emitter 360 μ m OD x 20 μ m ID; 10 μ m tip (New Objective) and an applied spray voltage of 1.5 kV. The capillary temperature was set at 250 °C. Full mass scan was acquired with mass range 375-1200 m/z in profile mode in the FT with resolution of 70000. The filling time was set at maximum of 250 ms with a limitation of 3×10^6 ions. Data dependent acquisition (DDA) was performed with the resolution of the Orbitrap set to 35000, with a fill time of 120 ms and a limitation of 2×10^5 ions. A normalized collision energy of 32 was applied. A loop count of 10 with count

1 was used and a minimum AGC trigger of $2e^2$ was set. Dynamic exclusion time of 30 seconds was used. The peptide match algorithm was set to 'preferred' and charge exclusion 'unassigned', charge states 1, 5 - 8 were excluded. MS² data was acquired in profile mode.

3.3.18.3 Mass spectrometry analysis

Mass spectrometry analysis was performed by Frank Stein, Proteomics facility EMBL Heidelberg. IsobarQuant (Franken et al., 2015) and Mascot (v2.2.07) were used to process the acquired data, which was searched against the Uniprot *Rattus norvegicus* proteome database UP000002494. The following modifications were included into the search parameters: Carbamidomethyl (C) and TMT10 (K) (fixed modifications), Acetyl (N-term), Oxidation (M), and TMT10 (N-term) (variable modifications). A mass error tolerance of 10 ppm and 0.02 Da was set for the full scan (MS1) and the MS/MS spectra, respectively. A maximum of two missed cleavages were allowed and the minimal peptide length was set to seven amino acids. At least two unique peptides were required for protein identification. The FDR on peptide and protein level was set to 0.01. The R programming language (ISBN 3-900051-07-0) was used to analyze the protein.txt output files of IsobarQuant. Only proteins which were quantified with at least 2 unique peptides were allowed for the downstream analysis. Raw 'signal_sum' columns were used for the analysis. Potential batch effects were removed using the 'removeBatchEffect' function of the limma package (McAlister et al., 2014) and normalized using a variance stabilization normalization using the vsn package (Huber et al., 2002). Individual normalization coefficients were estimated for crosslinked and non-crosslinked conditions. Normalized data were tested for differential expression using the limma package. The replicate factor was included into the linear model. For comparisons between crosslinked versus non-cross-linked, the FDR calculated by limma was employed to annotate hits. When comparing PE and untreated conditions, the R package fdrtool (Strimmer, 2008) was employed to calculate FDRs using the t values from the limma output. Proteins were annotated as 'hits' with an FDR < 5 % and a fold-change

(FC) > 50 %. In PE/untreated comparative experiments, proteins were first tested for their enrichment over –UV controls, and the intensity of the proteins enriched in at least one condition were compared in the corresponding +UV samples. Proteins with an FDR < 5% and a consistent FC of at least 10% in each replicate were defined as hits. The ggplot2 R package (Ginestet, 2011) was used to generate the graphical representations.

3.4 Functional analysis

GO-term enrichment analysis was performed using DAVID (Database for Annotation, Visualization and Integrated Discovery) with the rat or mouse genome as background, according to the sample origin. Test: Fisher exact test. For comparison of RIC data with other RIC studies, the rat identifiers were mapped to mouse, and compared. Mapping by Thomas Schwarzl, EMBL Heidelberg. Novel RBPs are defined as those RIC hits that do not have a known RNA-binding domain (Hentze et al., 2018) and that lack known RNA-binding functions based on Gerstberger et al (Gerstberger et al., 2014). Overlaps with other RIC data sets were displayed in UpSet plots (Conway et al., 2017). Graphical display of GOs by Dot graph by Frank Stein, EMBL Heidelberg.

3.5 Statistics

Cell culture experiments were performed at least two times with n = at least two biological replicates for each treatment. Cell size measurements of NRVCs or heart sections were performed with at least two biological replicates and at least 50 cells measured per replicate. The investigators have been blinded to the sample group during the experiment and analysis of the data. Unless otherwise stated, values shown are mean ± SEM and statistical treatments are one-way ANOVA followed by Bonferroni's post hoc comparisons (three or more experimental groups) or unpaired t-test (two experimental groups) as indicated in the figure legends.

4. RESULTS I

The importance of post-transcriptional control has for a long time been overlooked, and appropriate methods to determine networks of post-transcriptionally controlled genes were not available. Recently established, system-wide approaches now allow the determination of post-transcriptional control in mammalian model systems and have in the past years been applied to identify over one thousand RNA-binding proteins (RBPs) in human cells (Castello et al., 2013) but also several other mammalian model organisms. Newer studies have performed comparative studies of RBPs in settings of stress or disease. A comparative study of primary cardiac cells under conditions of homeostasis versus pathological growth has not been made to date and was the primary focus of this study.

Parts of chapter 4 and 5 (Results I and Discussion I) have been published as Sneek Peak in Cell press during the revision process in Cell Reports (Riechert et al., 2020).

4.1 mRNA interactome capture in primary cardiomyocytes.

In order to generate an atlas of mRNA-binding proteins in neonatal rat ventricular cardiomyocytes (NRVCMs), I optimized the RNA interactome capture (RIC) method established by Castello et al. (2013) in these cells (Fig. 4.1A). RIC has initially been established in HeLa cells, a cell population that divides frequently and provides high amounts of mRNA and proteins. In contrast, NRVCMs are non-dividing, post-mitotic cells with low levels of RNA and their isolation and culture is by far more delicate and expensive. Amounts of input material were therefore optimized to lowest possible amounts. 18×10^6 NRVCMs per condition were shown to be successful for efficient pull-down of RBPs. Another peculiarity of NRVCMs is their large size and their high amounts of sarcomeric structures, that have to be permeated by the UV light to enable efficient cross-linking. Irradiation dosage was therefore raised from 0.15 to 0.2 J cm⁻².

Due to lower amounts of starting material, Oligo d(T) capture was optimized to elute maximum amounts of mRNA-protein complexes. To reduce loss of mRNA-bead complexes during washing procedures, all lysis and wash buffers were mixed with 0.02% TritonX.

I subjected RIC eluates as well as input controls to downstream analysis to test the specificity and yield of the method in NRVCMs (Fig. 4.1B). Sodium dodecyl sulfate-polyacrylamide gel electrophoresis (SDS- PAGE) and silver staining of eluted proteins showed differential patterns between RIC and input samples. RIC-specific bands were absent in the non-irradiated controls, indicating the enrichment of specific RBPs only after UV cross-linking (Fig. 4.1C). To test for the enrichment of mRNA during Oligo d(T) capture, I isolated RNA from RIC eluates after removal of proteins by Proteinase K digest and transcribed it into cDNA.

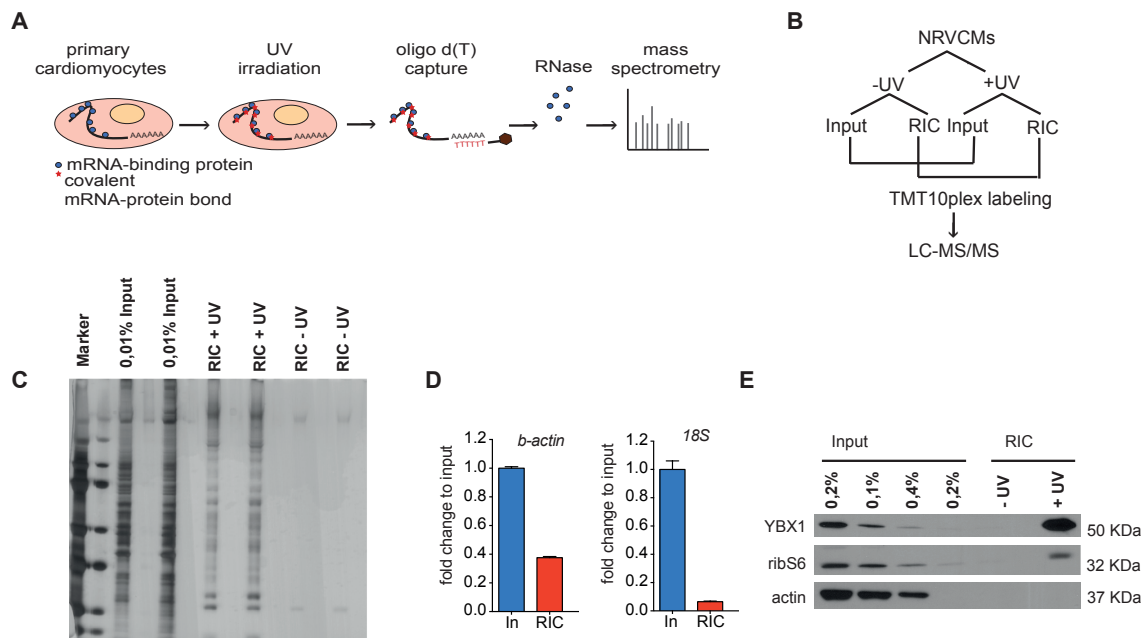


Figure 4.1: mRNA interactome capture in primary cardiomyocytes. (A) Overview of RIC method. Primary cardiomyocytes are cross-linked *in vivo* with 254 nm ultraviolet light, resulting in covalent bonds between RNAs and directly bound proteins. Oligo d(T) beads capture Poly(A) tails of mRNA and co-precipitate mRNAs/protein complexes. RNase digest erases remaining RNAs bound to proteins and following quantitative mass spectrometry allows analysis of proteins. (B) Schematic overview of experimental setup to measure UV-crosslinked input samples and RIC eluates versus non cross linked “UV-” controls. (C) Silver stain of input and RIC samples with/without UV-irradiation. (D) Quantitative real-time PCR of Input and RIC mRNA (*b-actin*) and rRNA (18S). (E) Western blot analysis of input and RIC samples +/-UV of known RNA-binding proteins YBX1 and ribS6P and negative control actin. Western blot by Eshita Varma.

mRNA enrichment was detected by quantitative real-time PCR of mRNA-specific b-actin and rRNA-specific 18S. In RIC-eluted samples, amounts of rRNA were depleted to a much higher extent than amounts of mRNA (Fig.4.1D). The capture of RBPs was validated by Western blot analysis of RIC eluates and detected known RBPs Y-box binding protein 1 (Ybx-1) and ribosomal S6 protein (ribS6) in the UV-irradiated RIC samples but not in non cross-linked controls, as expected. Actin as a negative control was not detected in eluate samples (Fig. 4.1E).

4.2 The cardiac RBPome

I first aimed at determining the RNA-binding proteome (RBPome) in NRVCMs under basal conditions. Together with the eluate from the Oligo-d(T)-bound fraction (RIC), input samples were measured to define the total proteome (TP, Fig. 4.1B). Protein eluates from two independent biological experiments were labeled by 10-plex tandem mass tag (TMT) and subjected to quantitative mass spectrometry (LC-MS/MS). Proteomic data acquisition was performed by Mandy Rettel (Proteomics core facility, EMBL Heidelberg) and data analysis was performed in collaboration with Frank Stein and Thomas Schwarzl (Proteomics core facility and Hentze lab, EMBL Heidelberg). Proteins that were significantly enriched in the crosslinked samples compared to the un-crosslinked control samples (false discovery rate (FDR) 0.05 (moderated t-test) and fold change (FC) ≥ 1.5) were considered as “hits”.

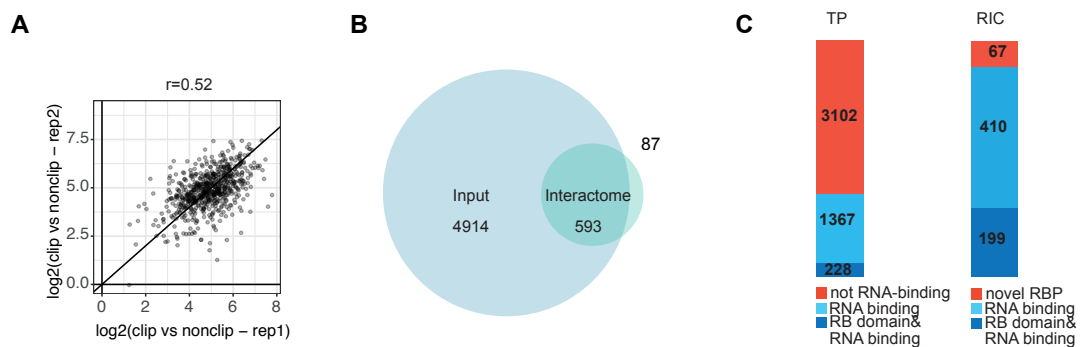


Figure 4.2: The cardiac RBPome and total proteome. (A) Scatter plot showing the enrichment ratios (clips versus non-clip) of biological replicates from two experimental runs. (B) Venn diagram of total proteome and RBPome in NRVCMs. (C) Distribution of proteins with known RNA-binding domain (Beckmann et al., 2015) or RNA-related function (from GO “biological process”) in total proteome and RBPome according to Hentze et al. (2018) and Gerstberger et al. (2014). Data analysis in collaboration with Frank Stein and Thomas Schwarzl, EMBL Heidelberg.

Biological replicates were compared and show a strong correlation (Fig 4.2A). 680 proteins were enriched in our RIC (Figure 4.2B) versus 5507 proteins in the total proteome/ input. 87 proteins were under the detection limit before Poly(A)-capture and are only detected after RIC. Clear enrichments of RNA-related proteins were found after RIC compared to the TP, with 199 proteins that harbor a known RNA binding domain (RBD) and 410 proteins with an unknown RBD but a known RNA-related role (Figure 4.2C). 67 proteins in the RIC fraction had no known RBD and have not been linked to any RNA-related function before. These proteins I refer to as novel, cardiac-specific RBPs.

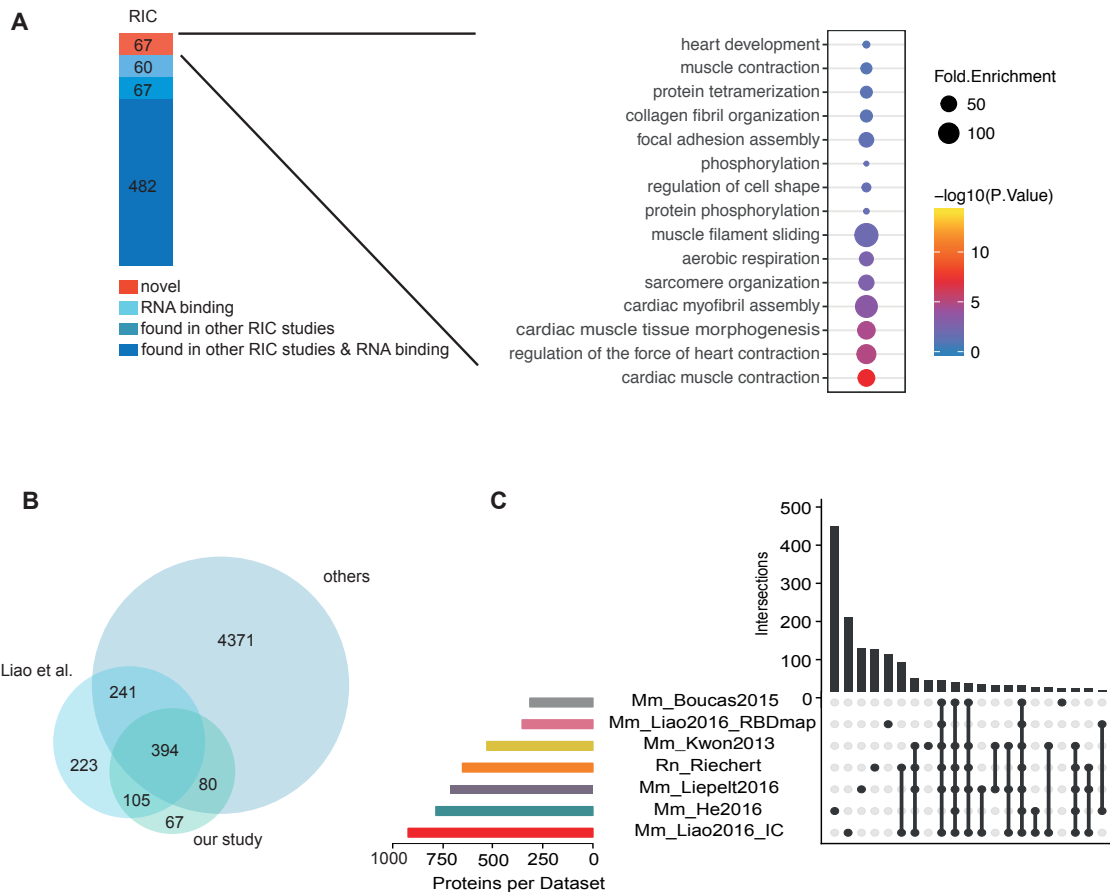


Figure 4.3: The cardiac RBPome in comparison to other RBPomes. (A) left: Comparison of RBP data set with previously found RBPs from RIC experiments, current rat RBPome mapped to mouse Right: Gene ontology of novel cardiac RBPs. **(B)** Venn diagramm of overlaps between our RBP set and previous RIC studies. **(C)** Upset plot of other RIC studies and our data, according to Conway et al. (2017). Mapping of data and upset blot in collaboration with Thomas Schwarzl, EMBL Heidelberg.

To closer evaluate the novelty of our dataset and compare our identified RBPs with other datasets, I looked for overlaps with previously published RIC studies (Boucas et al., 2015; He et al., 2016; Kwon et al., 2013; Liao et al., 2016; Liepelt et al., 2016) and compared the present RBP set with these studies. 482 of our RBPs had been detected by RIC in previous studies (Fig. 4.3A, Left panel). 67 of the present hits had been associated with an RNA-related GO term, 60 where detected in previous RIC studies but are unconventional RBPs without a known RNA-related function, the remaining 67 RBPs were not found in any other RIC study and are novel. I performed unsupervised clustering and posterior Gene Ontology (GO) analysis of all novel cardiac RBPs, which revealed a high enrichment for terms associated with cardiac structure and function, such as “heart development,” “muscle contraction”, and “sarcomere organization” (Fig. 4.3A, right panel).

Biggest overlaps of the current RBPome existed with the previously mentioned study from Liao et al. (2016), who performed RIC in cardiomyocyte-like HL-1 cells, with 487 RBPs overlapping in both studies. 93 RBPs are uniquely overlapping in the present data and the data of Liao et al. (Fig. 4.3B) but were not found in any of the other studies. A more detailed overview of intersections between the current RBP data set and previous studies is displayed in the upset plot in Figure 4.3C.

I then searched all RBPs for known cardiomyocyte-specific functions and found 19 RBPs with a known cardiac function (GO molecular function, biological process). Interestingly, most of the cardiac-specific RBPs are localized at the Z-disc, which is both an important structural entity of a cardiomyocyte but also one of its specific central signaling hubs. Cardiac-specific RBPs with their location in cardiomyocytes are depicted in the scheme in Figure 4.4. I also searched the data of Liao et al. (2016) for RBPs with a known cardiac function, and searched for overlaps with our cardiac RBPs. 6 cardiac-specific RBPs overlapped in both studies, namely *Serca2*, *Flnc*, *Ldb3*, *Mhy7*, *Myh6* and *Mybpc3*. All other cardiac-specific RBPs were only found in one of both studies. 13 RBPs that I found in NRVCMs were not detected in HL-1 cells by Liao et al., whereas in their data they find only 4 RBPs with a cardiac localization and function, that were not

detected by the present study. This difference most likely comes from the different character of both studies, which was in the present case performed from primary rat cells, whereas Liao et al. used a human cell line.

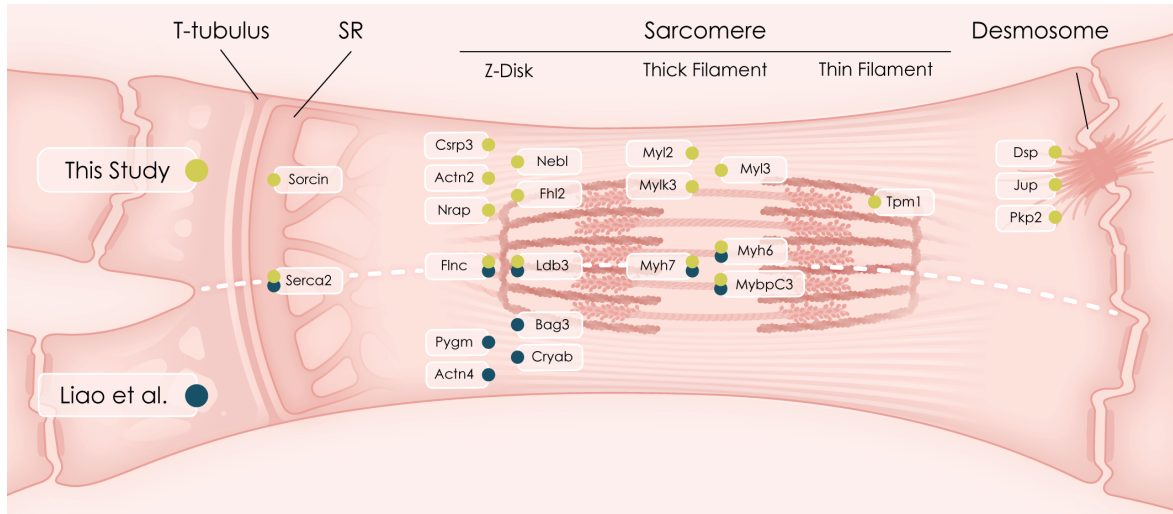


Figure 4.4: Scheme of cardiomyocyte-specific RBPs and their localization within cardiomyocytes. Localization of cardiac-specific RBPs from our study (yellow) and of HL-1 RBPs (Liao et al., 2016) (blue). Graphical design by Philipp Jordan, Jordangraphics

4.3 The dynamic cardiac RBPome during cardiac growth and homeostasis

To generate a dynamic atlas of RBPs in the heart, I mimicked pathological heart growth by treating NRVCMs with the $\alpha 1$ receptor agonist Phenylephrine (PE), which induces pathological cell growth in cardiomyocytes *in vitro* (Simpson, 1985). Again, input samples were measured to determine the total proteome in parallel to RIC eluates. PE-treated samples were compared to mock (DMSO) treated cells (Fig. 4.5A). The induction of pathological growth by treatment with PE was validated by increased cell size (1.3-fold after PE-treatment, Fig. 4.5B) and the expression of pathological marker genes *nppa* and *nppb*, that are linked to cardiac growth and were significantly increased upon treatment with PE. (Fig. 4.5C). Biological replicates strongly correlated (Fig. 4.5D), and overall gene expression patterns as well as the expression of *myh7*, a known remodeling marker, in the TP varied significantly in treated versus untreated samples, whereas they remained similar between replicates (Fig. 4.5E).

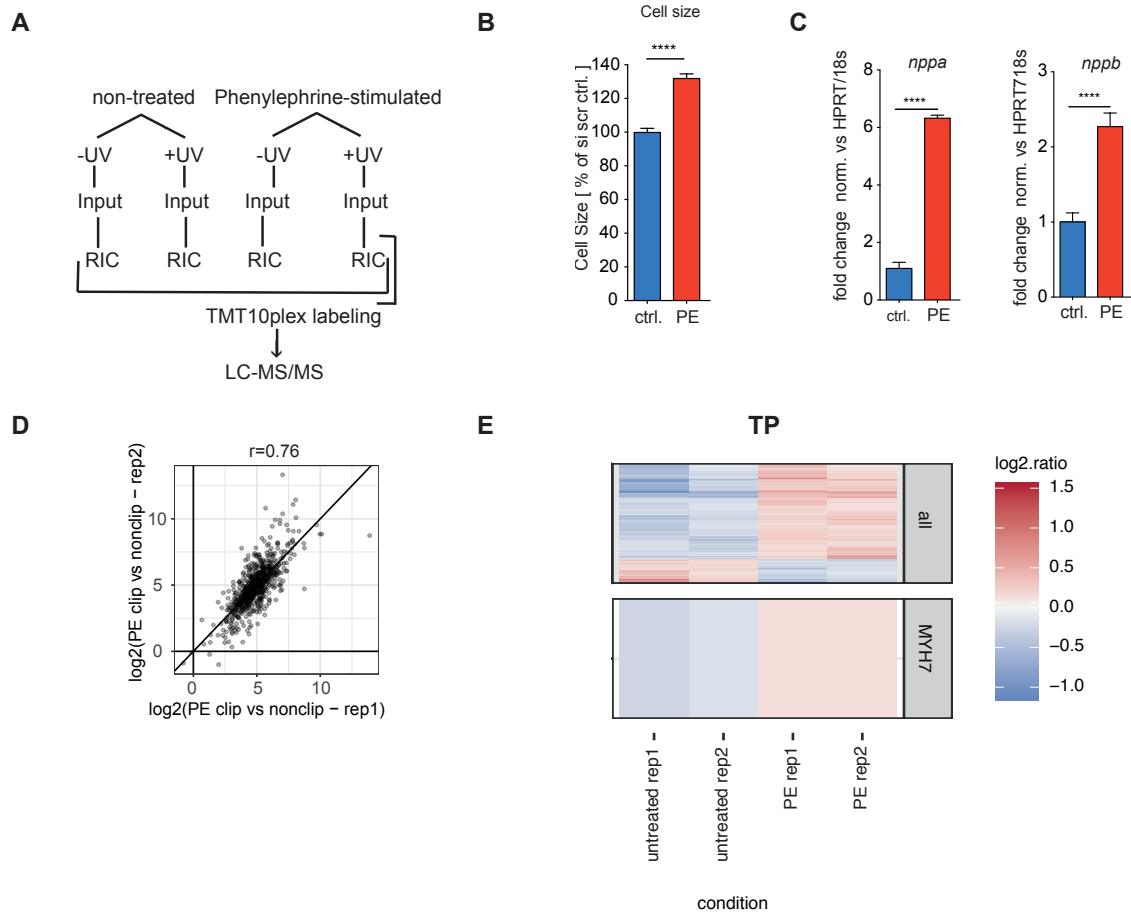


Figure 4.5: RIC analysis of RBPs during cardiac growth and homeostasis. (A) Schematic overview of experimental setup to measure UV-crosslinked input and RIC eluates versus non cross-linked „UV-“ controls from both untreated and Phenylephrine (PE) treated NRVCMs. (B) Cell size measurements of PE-treated versus non treated control NRVCMs to validate PE treatment. **** $P < 0.0001$ by unpaired t-test. (C) Fetal remodeling marker genes *nppa* and *nppb* in PE versus untreated NRVCMs. **** $P < 0.0001$ by unpaired t-test. (D) Scatter plot showing the enrichment ratios from PE versus untreated condition of two biological replicates (E) Heat map of TP of biological replicates (color gradient displays the \log_2 ratio against the average abundance over all four conditions) and representative pathological marker *myh7*. B and C: by Christoph Hofmann; D and E: in collaboration with Frank Stein, EMBL Heidelberg.

All RBPs with a fold change of at least 25% between treatments were defined as PE-responsive. RIC recovered a specific group of 35 RBPs with increased and of 49 RBPs with decreased abundance after PE treatment, whereas 593 RBPs show unchanged abundance after RIC (Fig. 4.6A). Unsupervised clustering and posterior GO analysis of PE-responsive RBPs revealed clear differences between proteins with lower versus higher abundance after PE treatment (Fig. 4.6B). Proteins with lower abundance mainly belong to metabolic processes such as “Succinyl-CoA-metabolic process”, “isocitrate

metabolic process” or “succinate metabolic process”, whereas proteins with higher abundance regulate translation (e.g. “regulation of translational initiation”, “formation of translation preinitiation complex”).

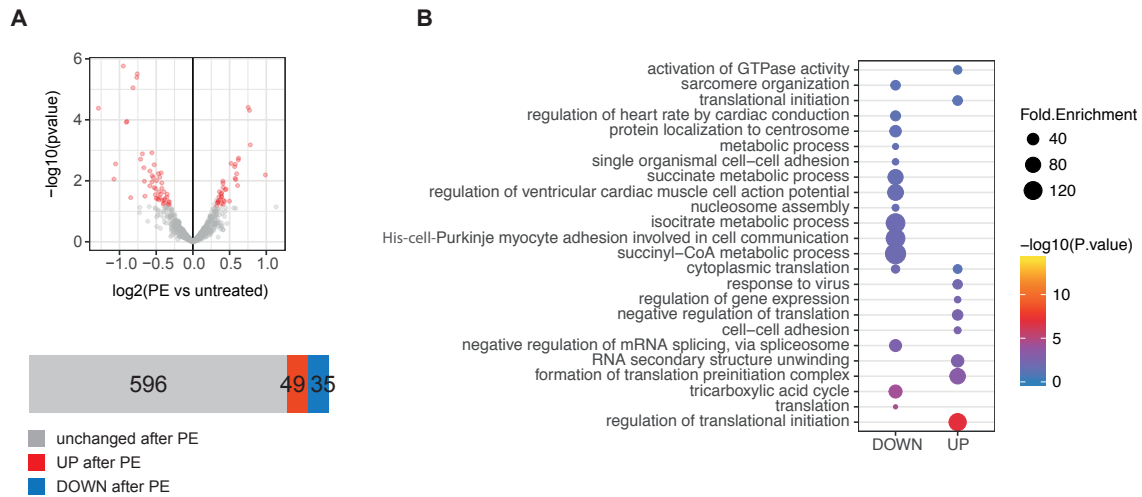


Figure 4.6: The dynamic cardiac RBPome during cardiac growth and homeostasis. (A) Volcano plot and bar graph of PE-treated versus untreated RBPs. ‘Hits’ with an FDR < 5 % (moderated t-test using limma) and a fold-change (FC) >25% when comparing conditions, marked in red in volcano plot. Data analysis in collaboration with Frank Stein. **(B)** Gene ontology of PE-responsive RBPs.

4.4 Dynamic binding of RBPs during cardiac growth

Next, I integrated overall abundance of proteins with changes in binding in response to PE treatment. Setting both measurements into relation allows measuring dynamic changes in mRNA-binding behavior (by RIC) normalized to overall abundances (TP) of proteins (Fig. 4.7A). Four different scenarios for binding over abundance are possible, that were classified for clarification: Class I RBPs (grey) remain unchanged in abundance after PE treatment in RIC (mRNA binding) and total proteome (TP, displaying overall abundance). Class II RBPs (red) change their binding capacities consistent with their abundance in the TP, meaning no dynamic binding changes occur between treatments. Class III RBPs (blue) change their abundance only in the TP but not the RBPome. Class IV RBPs (green) change their binding capacity as a reaction to PE treatment, while their overall abundance in the TP remains unchanged. This class I determined as „dynamic binders“.

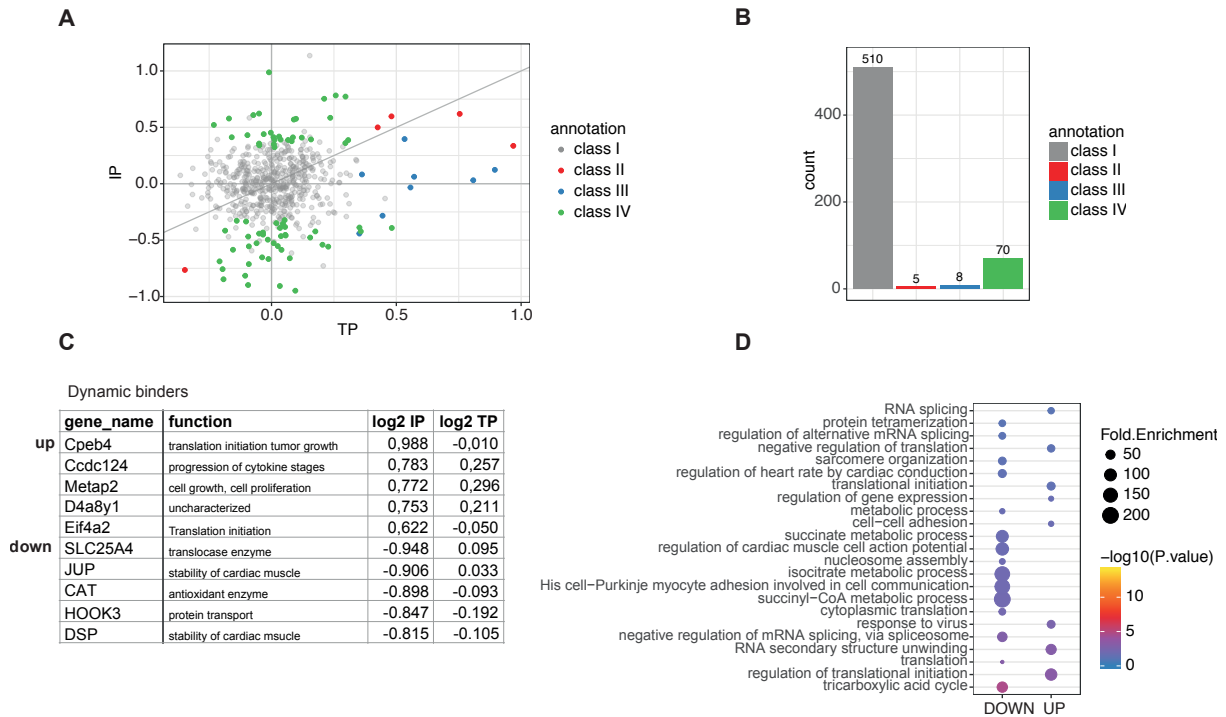


Figure 4.7: Dynamic binding capacities of RBPs during cardiac growth. (A) Scatter plot of average protein abundance PE-treated/untreated in RNA-bound fractions (ordinate) and total protein lysates (abscissa). Grey: proteins whose abundance does not significantly change neither in the RNA-bound fraction, nor in the total proteome. Red: proteins whose abundance change in the RNA-bound fractions follows the change in the total proteome. Blue: proteins whose overall abundance changes only in the total proteome. Green: proteins whose abundance in the RNA-bound fraction significantly changes, and is inconsistent with their abundance change in the total protein lysate, suggesting active regulation of their RNA-binding capacity ('dynamic binders'). 'Hits' with a fold-change (FC) >25% when comparing conditions. In collaboration with Frank Stein, EMBL Heidelberg (B) Bar graph of (A) with frequencies. (C) List of Top dynamic binders with log2 fold change of IP and TP. (D) Gene ontology of class IV 'dynamic binders'.

70 dynamic binders were found in the PE- treated samples, compared to the untreated condition (Fig. 4.7B). 8 RBPs belonged to class III, 5 to class II, while the remaining 510 RBPs did not respond to the treatment neither in abundance or binding capacities. Representative significant dynamic binders ranked by their change in binding capacity upon treatment with PE are depicted in Figure 4.7C. Unsupervised clustering and posterior GO analysis that I performed of PE-responsive dynamic binders showed a clear difference for RBPs with lower versus higher binding capacity after PE treatment. Dynamic binders with weaker binding behavior after PE were enriched for terms

associated with metabolism, whereas stronger binders were enriched for translational-related functions (Figure 4.7D).

4.5 Analysis of Cpeb4 as dynamically regulated RBP during pathological hypertrophy

Among the group of dynamic binders, the most significant changes in mRNA binding capacity after PE treatment were observed for Cytoplasmic polyadenylation element binding protein 4 (Cpeb4), a protein that has formerly been related to translational activation during tumor growth and specifically to activation of silenced mRNAs during tumorigenesis (Ortiz-Zapater et al., 2012). Cpeb4 showed enhanced binding after treatment with PE but no changes in overall abundance (\log_2 IP 0.98, \log_2 TP -0.01, Fig. 4.7A, C). Since no reports existed about the role of Cpeb4 in cardiomyocytes, I aimed to characterize the role of Cpeb4 in regulating cell growth.

4.5.1 Validation of Cpeb4 as dynamic binder

To validate Cpeb4 as a dynamic binder, Western blot analysis was performed from lysates of PE- or untreated NRVCMs, which validated that levels of Cpeb4 were unchanged after treatment, as expected (Fig. 4.8A). Western blot analysis of RIC eluates from PE- versus untreated NRVCMs validated higher amounts of Cpeb4 after PE treatment, and unchanged levels of class I proteins, Ythdf2 and Ybx-1 (Fig. 4.8B, marked in grey), which reflects higher binding capacities of Cpeb4 to mRNA after PE treatment.

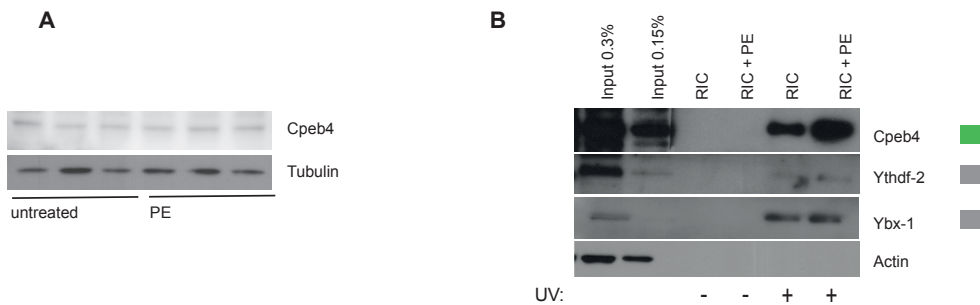


Figure 4.8: Validation of Cpeb4 as a Class IV “dynamic binder“. (A) Western blot of *dynamic binder* Cpeb4 with and without PE treatment. (B) Western blot of eluates after RIC, representing RNA-bound, Oligo d(T)-captured proteins. *class IV* Cpeb4 (green) and *class I* RBPs Ythdf-2, and Ybx-1 (in grey).

In contrast, levels of Cpeb4 protein after treatment with PE were elevated after Oligo d(T) capture in eluates. Together with unchanged overall abundance (Fig. 4.8A), this validated Cpeb4 as dynamically binding RBP (Figure 4.8B).

4.5.2 Cpeb4 during pathological cardiac growth *in vitro* in NRVCs

To perform further analysis on the function of Cpeb4 on cardiac growth, I depleted Cpeb4 in NRVCs by siRNA transfection and treated these cells with PE. Knockdown (KD) of Cpeb4 was validated by qPCR and Western blot analysis. Amounts of Cpeb4 transcript (Fig. 4.9A) and protein (Fig. 4.9B) were clearly reduced after siRNA treatment. Successful PE treatment was validated by significantly increased levels of *nppb* (Fig. 4.9A, right panel). As expected, I did not observe Cpeb4 transcript or protein levels elevated after PE treatment, confirming that differences in mRNA binding are not caused by increased total abundance of Cpeb4 protein (Fig. 4.9A,B).

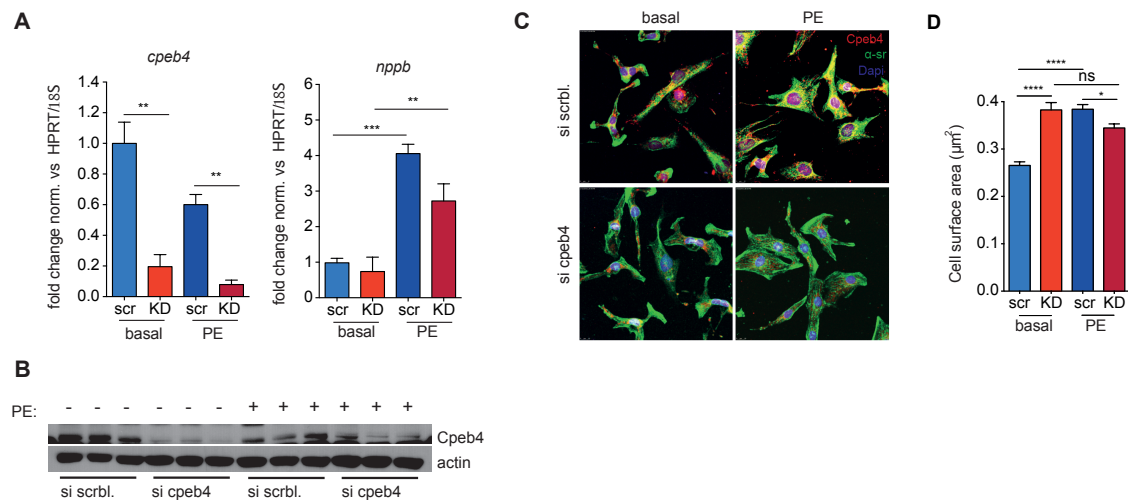


Figure 4.9: Cpeb4 controls cell growth *in vitro*. (A) siRNA-induced knock-down of both untreated and Phenylephrine (PE) treated NRVCs with cpeb4 siRNA (KD) or scrambled control siRNA (scr) left: qPCR of *cpeb4* levels, right: levels of *nppb*. **P < 0.01 ***P < 0.001 by one-way ANOVA followed by Bonferroni's post-hoc comparisons. (B) Levels of Cpeb4 protein after siRNA KD and PE-treatment. (C) Immunofluorescence staining of NRVCs after siRNA KD and PE treatment. Staining for Cpeb4 (red), Dapi (nucleus, blue) and α -sarcomeric actin (cytoskeleton, a-sr, green) *P < 0.05 ****P < 0.0001 by one-way ANOVA followed by Bonferroni's post-hoc comparisons. (D) Cell size quantification of Cpeb4 KD, PE-treated NRVCs, as stained in C.

Effects of Cpeb4 to cell growth were evaluated by immunostaining of NRVCMs after Cpeb4 KD and PE treatment with antibodies detecting Cpeb4, DAPI (nuclei) and α -sarcomeric actin (cytoskeleton) (Fig. 4.9C). Cell size was measured from three replicates of each condition, and for at least 60 cells per replicate. As, expected, cell size was increased after PE treatment in the control group. Cpeb4 KD led to basal increase of cell size in untreated cells, comparable to the induction of cell growth after PE treatment in control cells (Fig. 4.9D), suggesting that binding of Cpeb4 to mRNA critically effects the adaptation process to pathological heart growth. PE treatment of Cpeb4-depleted NRVCMs did not result in any additional cell growth.

4.5.3 Cardiac phenotype of Cpeb4-depleted mice

The effect of Cpeb4 onto heart and cardiomyocyte size was additionally tested *in vivo* in a mouse model carrying a global deletion of the Cpeb4 gene (Calderone et al., 2016, Fig. 4.10A), that was kindly provided by Raúl Méndez from IRB Barcelona. Cpeb4 knock-out (KO) mice showed clear increase in left ventricular anterior mass, as shown in Masson-Trichrome-stained heart sections in Fig. 4.10B.

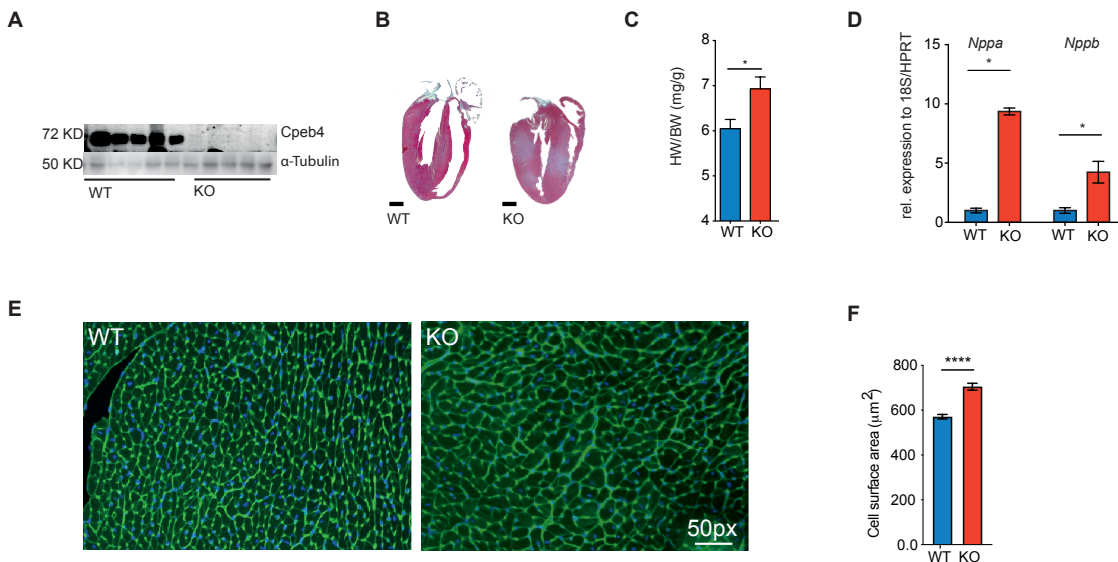


Figure 4.10: Cpeb4 controls cell growth *in vivo*. (A) Levels of Cpeb4 protein in WT and Cpeb4 KO mice, all samples from laboratory of Raul Mendez, Barcelona. (B) Masson-Trichrome staining of WT and Cpeb4 KO heart. (C) Heart weight to body weight ratios of WT versus Cpeb4 KO mice. * $P < 0.05$ by unpaired t-test, Data from Raul Mendez. (D) levels of *nppa* and *nppb* in WT and Cpeb4 KO mice. * $P < 0.05$ by unpaired t-test (E) Representative image of Wheat germ agglutinin (WGA) staining of heart sections of WT and Cpeb4 KO mouse. (F) Cell size quantification of E. **** $P < 0.0001$ by unpaired t-test.

Heart weight to body weight ratios were measured from KO versus wild type (WT) mice and were found to be significantly increased in the KO group (Figure 4.10C). Together with increased hearts, marker genes for pathological heart growth *nppa* and *nppb* were significantly increased in lysates of Cpeb4 KO versus WT hearts, indicating that increased heart size is part of a pathological process (Figure 4.10D). To specifically test that this effect is induced by the size of cardiomyocytes and not by other cardiac cell populations, cardiomyocyte size was determined from wheat germ agglutinin stained heart sections. Cell size was measured from at least two replicates of each condition, and for at least 60 cells per replicate. Cardiomyocyte size was significantly increased in Cpeb4 KO hearts (Figure 4.10E, Quantification in F). All together, these data show an unknown role of Cpeb4 for cell growth *in vitro* and *in vivo*.

4.6 Identification of Cpeb4 target mRNAs during growth and homeostasis

To systemically identify target mRNAs that are bound by Cpeb4, RNA-immunoprecipitation was performed, and followed by high-throughput sequencing of the immunopurified RNAs (RIP-Seq). RIP-Seq was performed from PE-treated versus untreated NRVCs to specifically identify binding of Cpeb4 during growth versus homeostasis. (Fig. 4.11A). In parallel, RNA from all input samples was isolated and sequenced (Fig 4.11B). RIP-Seq was performed in biological triplicates. All libraries showed high amounts of aligned reads, and clustering of replicates when performing principal component analysis (Fig. S2, supplements). RIPSeq libraries were generated by Eshita Varma and were analyzed in collaboration with Thileepan Sekaran at EMBL Heidelberg. Specific precipitation of Cpeb4 was validated by Western blot analysis (Fig. 4.11C).

9783 transcripts were detected in the input samples, representing the total transcriptome. Of these 9783, 2.7% were found to bind to Cpeb4 under homeostatic conditions (mock), 6.6% during growth (PE treatment) and 2.3% bind commonly for both treatments (Fig. 4.11D). Among Cpeb4-bound RNAs from both treatments, a significant number of transcripts encoded for a Cytoplasmic polyadenylation element (Cpe), that has previously

been shown to be a reliable predictor of Cpeb protein binding (Piqué et al., 2008) (Fig. 4.11E). I performed unsupervised clustering and posterior GO analysis for “biological processes” of Cpeb4 binders from mock and PE-treated conditions, which showed high enrichment for mRNA processing and transcriptional processes (Fig. 4.11F).

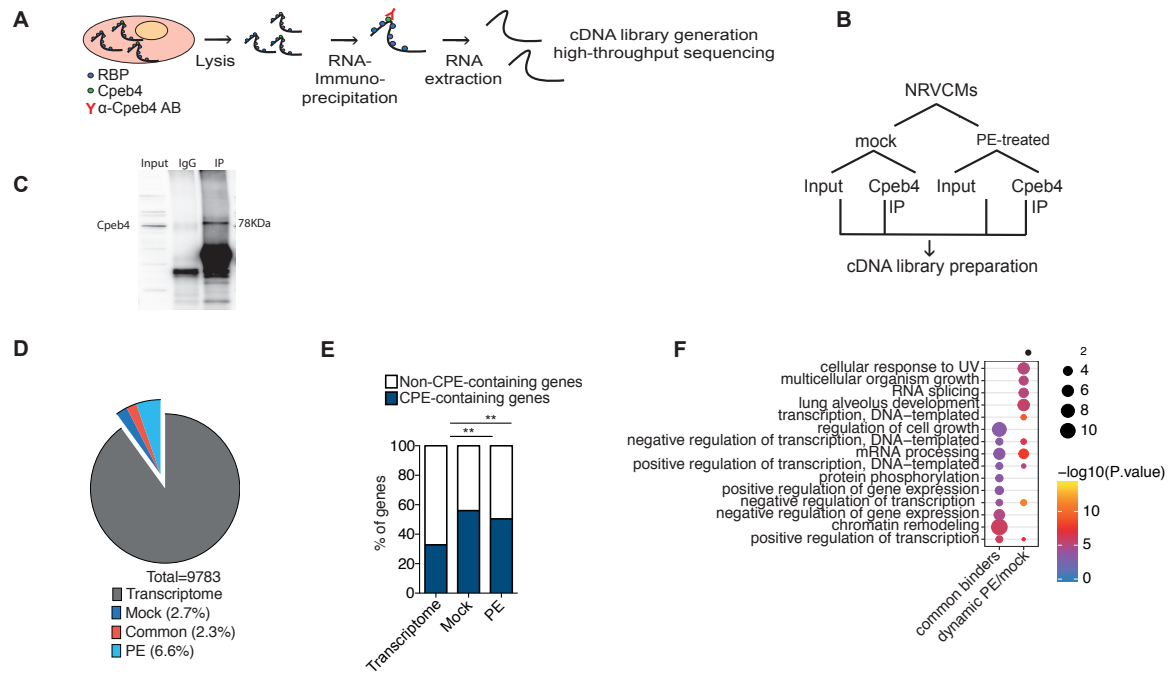


Figure 4.11: RIP-Seq reveals target mRNAs of Cpeb4 during homeostasis and pathological growth. (A) Schematic overview of RIP-Seq method to precipitate Cpeb4-bound RNAs from both untreated and Phenylephrine (PE) treated NRVCMs and detect target RNAs by deep sequencing. (B) Experimental setup to prepare RIP-Seq deep sequencing libraries and input controls (RNA-Seq). (C) Representative blot of Input and eluate from Cpeb4 and control IP. (D) Pie chart of transcripts measured in input samples (Transcriptome) and RIP-Seq samples from mock versus PE-treated NRVCMs. (E) Relative distribution (%) of CPE-containing transcripts from transcriptome and RIP-Seq. $**P < 0.01$ by one-way ANOVA. (F) Gene ontology (Biological process) of Cpeb4-binders from mock and PE-treated NRVCMs. RIP-Seq performed by Eshita Varma; RIPSeq analysis performed in collaboration with Thileepan Sekaran, EMBL Heidelberg; Analysis of CPE-containing RNAs by Mirko Völkers.

4.7 Identification of translationally regulated Cpeb4 target mRNAs *in vitro* and *in vivo*

I further aimed to identify the effects of Cpeb4 binding to target mRNAs and to study translational changes induced by Cpeb4. For this purpose, RiboSeq analysis was performed from control and Cpeb4 KD NRVCMs (Fig. 4.610A, suppl. fig. 3). This

technique specifically isolates RNAs that are occupied by ribosomes and therefore protected from nuclease digest (Ingolia, 2010). Isolated ribosomal fragments, so called footprints, can be used to generate deep sequencing libraries and then represent all actively translating RNAs (Fig. 4.12A). From sequencing reads, only periodic fragment lengths were kept that showed a distinctive triplet periodicity and were specifically aligned. These reads were used for downstream analysis, as we have described it in a previous study (Fig. 4.12B, Doroudgar et al., 2019). Libraries yielded around 5 million usable (periodic) reads. Ribo-seq libraries had a distinct read-length distribution, which peaked at 29 nt, the typical length of a ribosomal footprint (Fig. 4.12C) and Pearson correlation values were consistently high between replicates (4.12D). A detailed quality control for every sample can be found in supplementary figure 3.

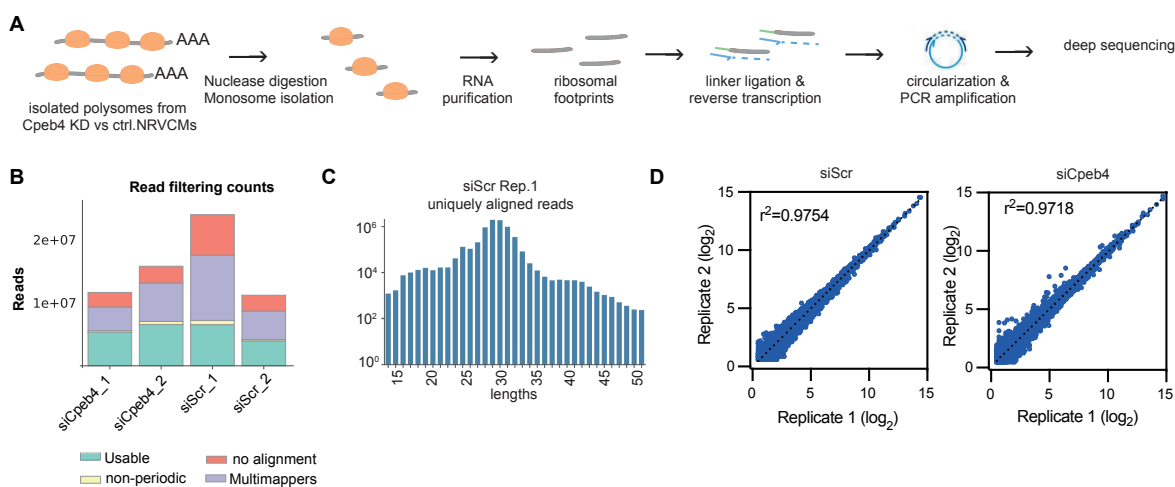


Figure 4.12: RiboSeq of Cpeb4-depleted versus control NRVCMs. (A) Schematic overview of RiboSeq method to precipitate translating RNAs from both Cpeb4-depleted versus control NRVCMs for deep sequencing. (B) Read filtering for preprocessing of sequencing reads. (C) Representative example of read length distribution of RiboSeq reads of scr. control sample. (D) Pearson's correlation of duplicates of both conditions. Preprocessing and quality control by Etienne Boileau, Heidelberg.

I identified 362 differentially expressed genes (DEGs), 208 of these being down-regulated and 154 being up-regulated after KD of Cpeb4 (Fig 4.13A). To discover which classes of mRNAs displayed altered translation patterns in Cpeb4-depleted cells, I performed unsupervised clustering and GO analysis for genes whose translation level was changed (log₂ fold change > 0.5) in Cpeb4 KD cells compared to controls. In line

with the results from the RIP-Seq, GO analysis for “biological processes” showed that differentially translated genes after Cpeb4 KD in cardiomyocytes are enriched for processes such as transcriptional regulation or signaling cascades (Fig. 4.13B). To identify all genes, that are both differentially translated upon KD and bound by Cpeb4, I compared RiboSeq DEGs with CPE-containing Cpeb4-binders from the RIP Seq data (Section 4.6). From 261 Cpe-containing Cpeb4-binders and 362 DEGs, I found 15 genes, that overlapped in both datasets (Fig. 4.13C). These 15 include several genes, that belong to the GO-enriched functional class “transcriptional regulation”. The heat map in Figure 4.13D shows the differential regulation of highly regulated DEGs bound by Cpeb4 between mock and PE-treated cells and the high reproducibility between replicates.

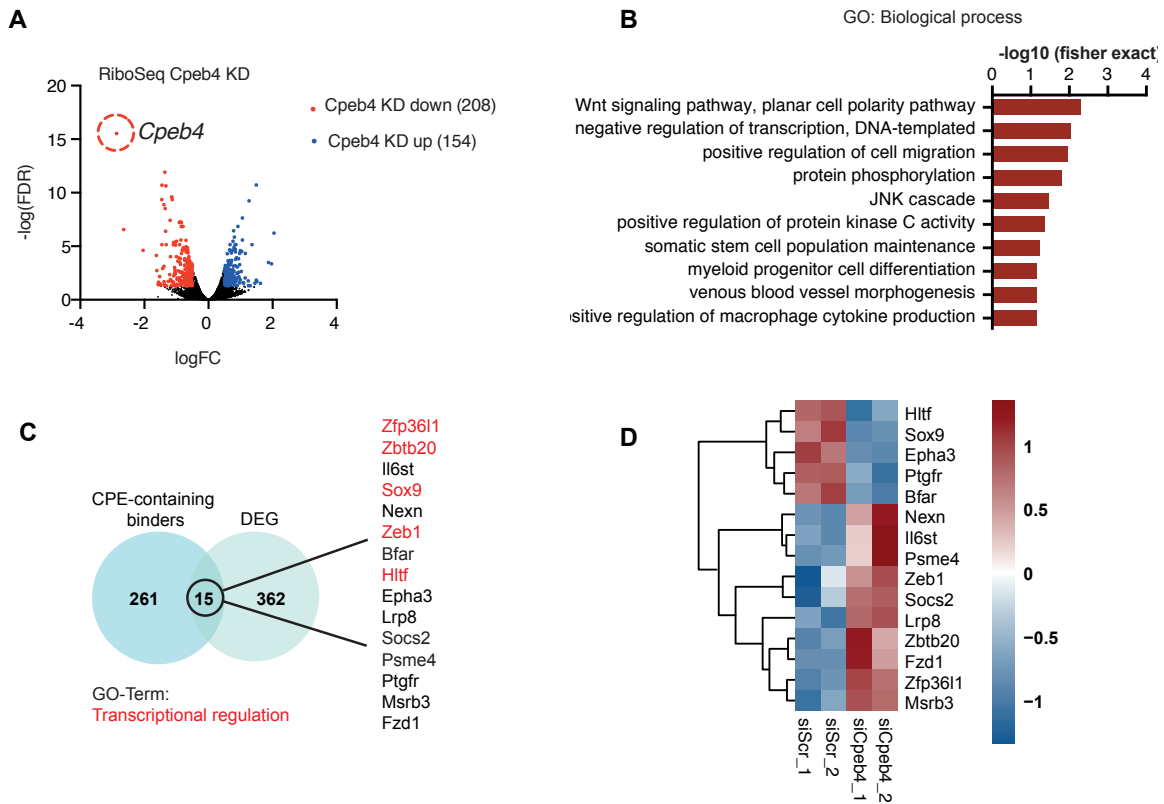


Fig. 4.13: Translationally regulated Cpeb4 binding transcripts. (A) Scatter plot of differentially expressed genes (DEGs) from RiboSeq of Cpeb4 KD and control NRVCMs. (B) Unsupervised clustering and GO analysis for „biological process“ of RiboSeq hits. (\log_2 fold change > 0.5) (C) Venn diagram of Cpeb4 target mRNAs with CPE and DEGs from RiboSeq and list of overlapping genes. (D) Heat map of highly regulated DEGS that are bound by Cpeb4, heat map by Mirko Völkers.

4.8 Validation of differentially translated Cpeb4- bound target genes

Among these Cpe-containing DEGs, two interesting zinc finger transcription factors, Zinc Finger E-Box Binding Homeobox 1 (*Zeb1*) and Zinc Finger and BTB Domain Containing 20 (*Zbtb20*), were bound by Cpeb4 and differentially translated upon KD of Cpeb4. I measured the expression of these potential Cpeb4-binding targets in Cpeb4-depleted, as well as PE-treated NRVCMS and found basal levels of *Zeb1* protein increased after KD of Cpeb4 (Fig. 4.14A, Quantification in B), whereas *Zbtb20* and *Mrsb3* were unaltered. Enhanced expression of *Zeb1* after KD suggested that Cpeb4 has a repressive effect on the expression of this transcription factor. In line, treatment of cardiomyocytes with PE, which like Cpeb4 KD increases cell size, increased *Zeb1* levels as well. Levels of *Zeb1* and *Mrsb3* cDNA were not regulated, whereas *Zbtb20* was slightly increased for after Cpeb4 KD (Fig. 4.14C). Since Cpeb4 has been suggested to control mRNA stability of target transcripts, I evaluated the mRNA half-lives after inhibiting transcription in NRVCMS with actinomycin D (Figure 4.14D). *Zeb1*, as well as *Mrsb3*, displayed similar half-lives in control and Cpeb4 KD cells, whereas Cpeb4 depletion significantly changed the mRNA half-life of *Zbtb20*.

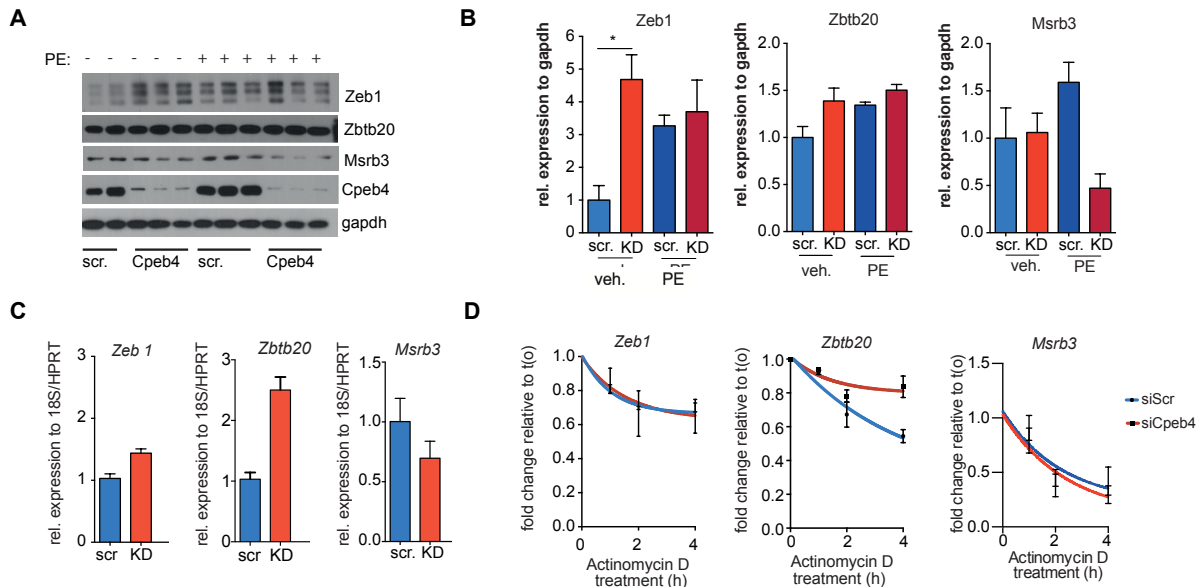


Figure 4.14: Validation of Cpeb4-binding DEGs and their transcriptional and translational regulation. (A) Western blot of CPE-containing DEGs from Cpeb4-depleted NRVCMS after mock or PE treatment. (B) Quantification of A. *P < 0.05 by one-way ANOVA followed by Bonferroni's post-hoc comparisons. (C) Transcript levels of CPE-containing DEGs measured by qRT-PCR. (D) RNA stability over time of CPE-containing DEGs.

To investigate the effect of Cpeb4 on translational control *in vivo*, a previously published RiboSeq data set (Doroudgar et al., 2019) was used to analyze Cpeb4 target mRNAs from the present study. Briefly, in this previous study, I had generated RiboSeq libraries from cardiomyocytes, that were isolated from hearts after acute pressure overload. For this purpose, I had subjected mice to transverse aortic constriction (TAC) surgery, which is an accepted model for pathological hypertrophy of the left ventricle. By the use of the Ribo-tag mouse (Sanz et al., 2019), that carries an HA-tagged variant of Ribosomal protein RPL22, we were able to purify tagged cardiomyocyte ribosomes from cardiac lysates and subjected the ribosome-protected mRNA fragments to deep sequencing. Cpeb4 target transcripts from the present RIP-Seq data set (4.7) were searched in this *in vivo* data set and were found to be highly translated in response to TAC surgery compared to the overall transcript levels (Figure 4.15A, left panel). Cpeb4 target transcript levels measured in a parallel RNA-seq data set were unchanged after TAC compared to overall transcripts (Figure 4.15A, right panel). This suggested that Cpeb4 targets were post-transcriptionally regulated during pathological growth.

Since Zeb1 protein levels increased *in vitro* in NRVCs after pathological growth induction by PE treatment, I aimed to confirm this effect *in vivo* and determined levels of Cpeb4 targets Zeb1 as well as Zbtb20 and Mrs3b in heart lysates of TAC or sham operated animals. All three, Zeb1, Zbtb20 and Mrs3b were upregulated during pathological growth induction by TAC surgery (Fig. 4.15B, Quantification in C). Transcripts levels measured by qRT-PCR were unchanged and suggested post-transcriptional regulation of our identified Cpeb4 mRNA targets (Figure 4.15D). Since Cpeb4 represses expression of Zeb1 and Zbtb20, RNA-immunoprecipitation was performed against Cpeb4 from heart lysates of mice after TAC or sham surgeries and amounts of bound Zeb1 and Zbtb20 were measured by qRT-PCR. Indeed, levels of Zeb1 and Zbtb20 decreased after TAC in RIP-PCRs, suggesting that a repressive effect of Cpeb4 on specific target RNAs is released during pathological growth induction (Figure 4.15E). This is in line with the location and number of several CPE elements in the

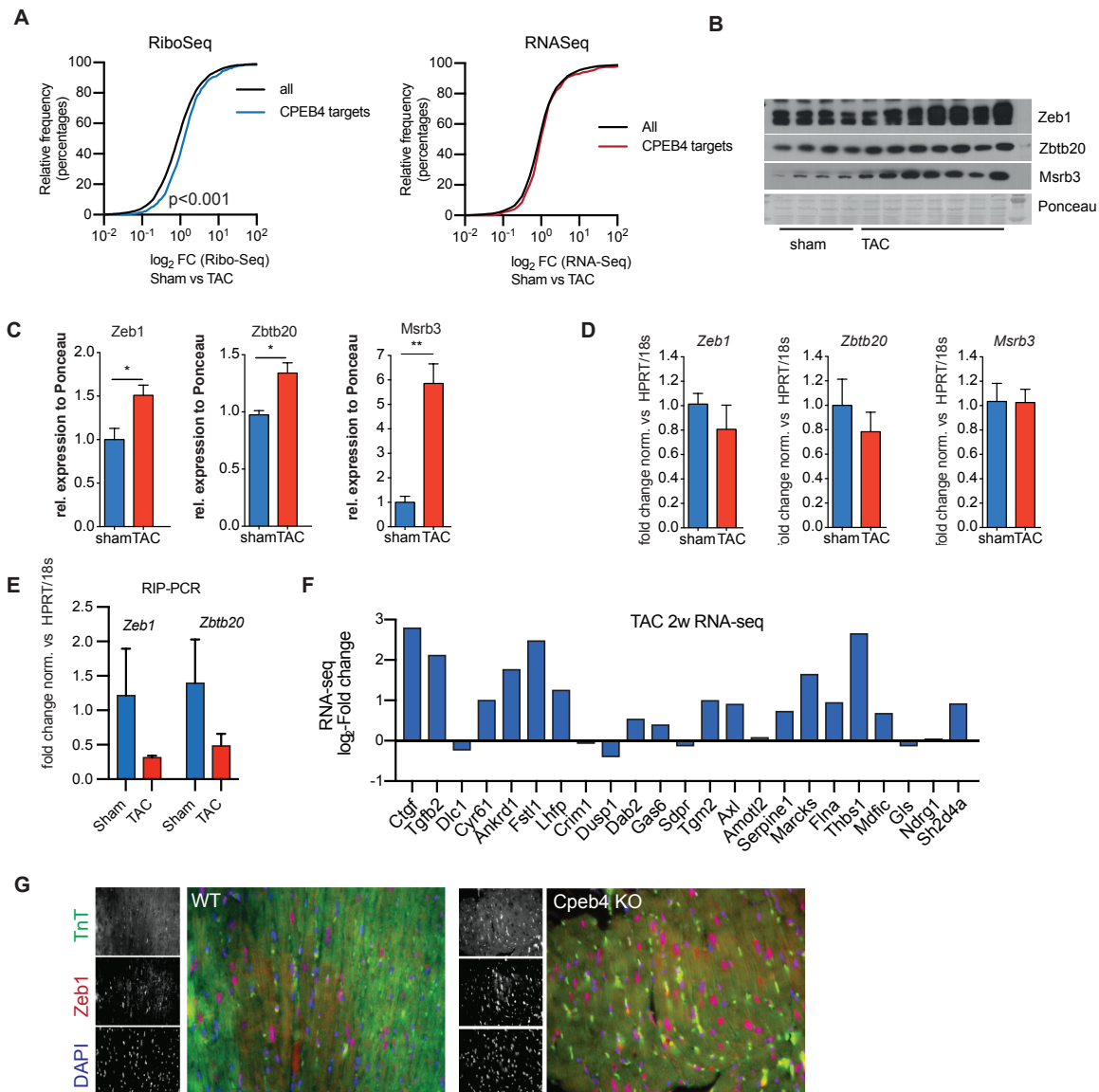


Figure 4.15: Cpeb4 shows repressive effect on the translation of transcription factors. (A) Cumulative fraction of Cpeb4 target transcripts and total transcripts TAC versus sham (2d post surgery) for DEGs from RiboSeq (blue) or RNASeq (red). (B) Protein levels of Cpeb4 targets from TAC or sham operated mice (4wks post surgery). (C) Quantification of B. *P < 0.05 **P < 0.01 by unpaired t-test (D) Transcript levels of Cpeb4 targets in TAC versus sham operated mice (4wks post surgery) (E) Transcript levels of Zeb1 and Zbtb20 after Cpeb4-targeted RIP and qRT-PCR. (F) Differentially expressed transcripts after TAC from RNA Seq that are related to Zeb1 (G) Immunofluorescence staining of WT and Cpeb4 KO heart sections. TnT: Troponin T (cell structure). Cumulative fraction analysis and RNA Seq analysis by Mirko Völkers.

3'UTR, that predict a suppressive function of Cpeb4 onto Zeb1 (Piqué et al., 2008) (Suppl. fig 4).

To determine whether increased levels of Zeb1 in pathological hypertrophied mouse hearts are associated with transcriptional activity of Zeb1, the expression of genes that

are known to be depending on Zeb1 (Lehmann et al., 2016) was analyzed in the RNA-Seq data of TAC and sham treated hearts (Doroudgar et al., 2019, Figure 4.15F). Most known Zeb1 targets were strongly upregulated after TAC surgery. Several of these Zeb1-dependent DEGs belonged to pathways that are known to be involved in cell growth and proliferation, such as the Hippo pathway (Ctgf, Serpin, Tgfb2) or the Mapk/Erk pathway (Dusp1, Flna, Tgfb2). Finally, the expression and subcellular localization of Zeb1 was analyzed in Cpeb4 KO hearts. Immunofluorescence confirmed increased Zeb1 localization in the nucleus in myocardial sections from Cpeb4 KO mice compared to WT mice (Figure 4.15G).

All together, I was able to find a dynamic mechanism, by which Cpeb4 regulates translation of Zeb1: In homeostatic conditions, Cpeb4 represses the translation of *Zeb1* mRNA. After a pathological stimulus, Cpeb4 is released from *Zeb1* mRNA, loosing its repressive effect and leading to increased Zeb1 synthesis. Zeb1 as a transcription factor binds to DNA of genes involved in the onset of pathological gene programs, and promotes their transcription (Fig. 4.16).

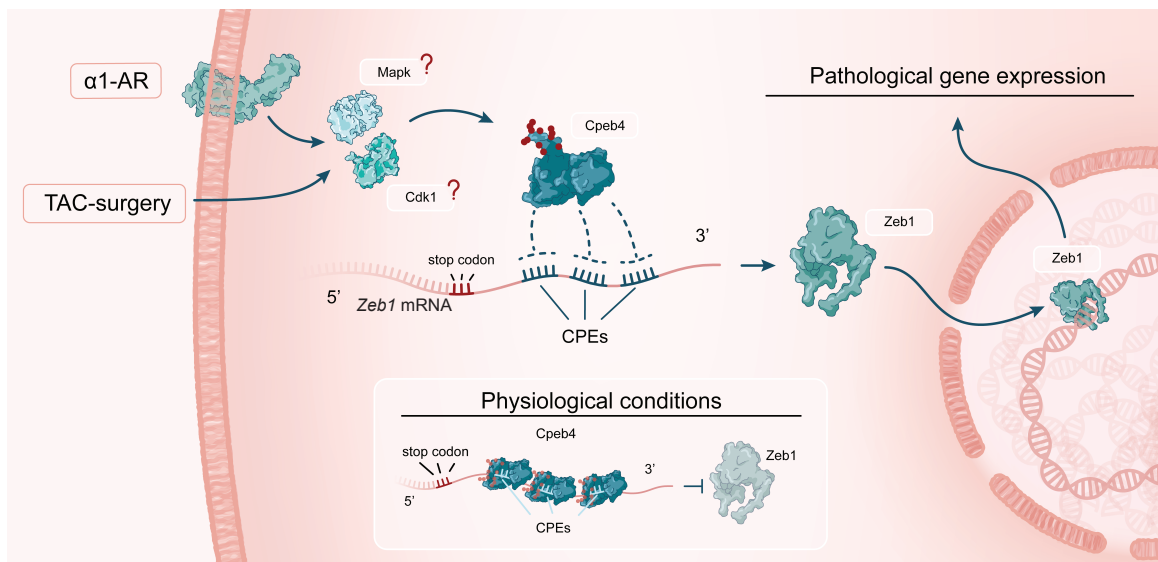


Figure 4.16: Cpeb4 binds and represses translation of Zeb1 to inhibit pathological gene expression. Graphical scheme of Cpeb4-Zeb1 axis: In homeostatic conditions, Cpeb4 represses the translation of *Zeb1* mRNA. After pathological stimulus, Cpeb4 is released from *Zeb1* mRNA, leading to increased Zeb1 synthesis. Zeb1 as a transcription factor binds to DNA of genes involved in the onset of pathological gene programs, and promotes their transcription. Graphical design by Philipp Jordan, jordangraphics.

5. DISCUSSION I

The aim of this project was the generation of a detailed compendium of RNA-binding proteins (RBPs) in primary cardiomyocytes. Furthermore, the dynamics in binding behavior of RBPs during a hypertrophic treatment were measured to shed light on RBPs that play a role in the adaptation to pathological cardiac hypertrophy.

Gene expression regulation was for a long time thought to be regulated mainly by levels of transcription. The unraveling of methods that allow system-wide analysis of all levels of gene expression regulation, from transcription, post-transcriptional regulation, translation and protein synthesis and decay, has highlighted the role of post-transcriptional regulation especially in stressed and diseased cells (Liu and Aebersold, 2016). Several studies have unravelled networks of post-transcriptional control in diverse cell types and organisms from mammalian cell lines, drosophila, yeast, and plant cells (Baltz et al., 2012; Beckmann et al., 2015; Castello et al., 2012; Reichel et al., 2016; Sysoev et al., 2016). A large number of these RNA-binding proteins has been mechanistically described in detail, among those a number of cardiac RBPs, such as Quaking, HuR, Muscleblind, and SRSF1 (De Bruin et al., 2017; Justice and Bode, 1988). Deletion of these cardiac RBPs has been linked to cardiac malfunctions. The complete network of RBPs in the heart has been addressed in a single previous study, that performed RNA-Interactome capture in a cardiac cell line. The cardiac RBPome in primary cardiac cells had not been described to date, and there were no comparative studies to shed light on dynamic changes in RNA binding in conditions of cardiac disease versus homeostasis.

In this study I present the first comprehensive compendium of RBPs in primary cardiomyocytes. Additionally, I performed the first comparative study in cardiac cells, by comparing RBPs in homeostasis versus pathological cardiac growth. The analysis of the dynamically regulated RBP Cpeb4 during pathological hypertrophy revealed a novel role of Cpeb4 to cardiac growth: Cpeb4 regulates transcriptional activity by differential

translation of transcription factors that are involved in cellular remodeling during pathological growth stimulation.

5.1 First compendium of RBPs in primary cardiomyocytes.

In this study, I applied the RNA interactome capture technique (RIC) (Castello et al., 2013) to primary neonatal rat cardiomyocytes (NRVCMs). Isolation of RBPs was achieved through UV-crosslinking of living NRVCMs and isolation of poly(A) mRNA. Like this, I identified 680 proteins as high confidence cardiac RBPs. As expected, the data show high enrichment of proteins with RNA-related function or with known RNA binding domains compared to the total proteome. Apart from these known RNA-binders I found 67 novel RBPs that have not been linked to any RNA-related function before. Several of these novel RBPs exert a cardiac-specific function, and are involved in biological processes such as heart development, contractile function or sarcomere organization. This functional specificity might explain why these RBPs have not been found in other studies before but are specific to the heart. These novel RBPS were also specific to our primary model, and had not been found in HL-1 cells, a human heart cell line from a previous study (Liao et al., 2016). Apart from the set of novel RBPS, a detailed analysis of the cardiomyocyte RBPome revealed a number of RBPs that exert cardiac-specific functions, and a number of these RBPs where also found by Liao et al.. Still, the majority of cardiac-specific RBPs from the present study was not found in HL-1 cells. One main reason might be the different cellular model system, which in the present case is a primary cell model, whereas Liao et al. (2016) have used a human cardiac cell line.

The cardiac RBPs that I determined in our study showed a high overrepresentation of RBPs, that are specifically linked to the Z-disc of cardiomyocytes. Several of the RBPs in HL-1 cells (Liao et al., 2016) were connected to the Z-disc as well, underlining a possible functional importance of these RBPs. While the Z-disc was for a long time thought to be a structural entity connecting the thin filaments of a sarcomere and a transmitter of contractile force, it is now understood as central hub to sense and transfer

biomechanical stimuli. As such it is an important signaling interface involved in cardiac function and disease (Frank et al., 2006). Several Z-disc proteins have been proven as indispensable to the adaptation to increased cardiac stress and mutations in Z-disc proteins have been shown to lead to the onset of cardiomyopathies (Frank and Frey, 2011). The finding of several Z-disc proteins being mRNA-binding evokes the question whether their interaction with specific mRNAs plays a role in the adaptation to cardiac stress. Conceptually, not only RBPs affect the fate of bound mRNAs but also vice versa, the RNA could regulate the structure and function of the binding RBP (Beckmann et al., 2016). It would be interesting to evaluate whether RNA-binding to Z-disc related, contractile proteins and other myocyte-specific proteins affects their contractile function, rather than focussing only on the effect of the RBP to the target mRNA. A detailed evaluation of cardiac-specific RBPs in models of cardiac hypertrophy and the mutual role of the RBP-RNA complex is therefore of special interest to understand the molecular events that lie at the onset of cardiac hypertrophy and loss of cardiac function.

5.2 First cardiac, dynamically regulated RBPome in homeostasis versus pathological cardiac hypertrophy.

Only few studies have addressed the dynamic behavior of RBPs to external stimuli and the dynamic binding capacities of RBPs in diseased primary cells (Garcia-Moreno et al., 2019; Perez-Perri et al., 2018; Sysoev et al., 2016). In the current study, I identified distinct RBPs with increased or decreased mRNA binding behavior upon pathological growth treatment, that mimics pathological heart growth *in vivo*. Increased RNA binding behavior during pathological growth was closely linked to GO terms that are associated with translation, the formation of the translation pre-initiation complex and the regulation of gene expression. As cardiac hypertrophy is very closely linked to enhanced synthesis of proteins, these RBPs might act as positive regulators of anabolic processes. On the other hand, RBPs that respond negatively to the PE-treatment are closely linked to metabolic processes. A novel role of RBPs as players in intermediary and protein metabolism has been highlighted before and suggests that many metabolic enzymes are

“moonlighting“ as RBPs. A number of enzymatic RBPs have been found that are competitively either binding RNA or exerting their enzymatic activity (Castello et al., 2015). Metabolic RBPs in the present study are therefore of special interest to follow up on. A first screening of the basal RBPome in this study revealed 96 enzymes, and 1 metabolic enzyme, Ndufa9 (NADH:Ubiquinone Oxidoreductase Subunit A9, supplementary Fig.5). Ndufa9 has been found in two previous studies that performed interactome capture in embryonic stem cells and HL-1 cells (He et al., 2016; Liao et al. 2016). As a member of the mitochondrial respiratory complex I, which has been shown to be indispensable to prevent cardiac failure (Gadicherla et al., 2012). Ndufa9 would therefore be of interest for a follow-up study.

5.3 Cpeb4 is dynamically regulated during pathological hypertrophy and is critically involved in the adaptation to cardiac stress

One focus of the study was the detailed analysis of RBPs, which change their binding capacities depending on a specific stimulus independently of protein abundance. The comparison of mRNA-binding determined by RIC to total RBP abundance can specifically evaluate binding efficiencies. A similar method had been applied in a previous study to compare RBPs in different stages of drosophila development by Sysoev et al. (2016). To evaluate the impact of such dynamic RNA binding for regulating gene expression and pathological phenotypes of stressed cardiomyocytes, I performed follow up experiments on the RBP with highest binding dynamics in homeostasis versus cardiac hypertrophy, Cpeb4. Expression of Cpeb4 remains unchanged during pathological cell growth, but its binding capacity is doubled. I found that depletion of Cpeb4 leads to pathological cellular growth both *in vitro* and *in vivo* in cardiomyocytes, suggesting that Cpeb4 is critically involved in the adaptation to cardiac stress. Cpeb4 belongs to a family of proteins that share similar RBDs, by which they control the translation of cytoplasmic polyadenylation element (CPE)-containing mRNAs (Guillén-Boixet et al., 2016) in the 3' UTR of mRNAs. Cpebs are known to have dual functions as translational repressors or activators depending on the composition and location of the CPE within the target

sequence (Piqué et al., 2008). In cardiac hypertrophy, which is closely connected to elevated levels of translation, Cpeb4 might importantly influence cellular growth.

5.4 Cpeb4 binding to mRNA of transcription factors suppresses their translation and inhibits onset of pathological gene expression

When analyzing co-precipitated mRNAs bound to Cpeb4, I find several transcription factors being bound and regulated by Cpeb4, and among these zinc finger transcription factors *Zeb1* and *Zbtb20*. Expression of *Zeb1* increased upon Cpeb4 depletion. This repressive effect of Cpeb4 is in line with a previous study that designed a prediction tool of Cpeb4-bound targets, allowing to estimate a repressive or activating effect of Cpeb4. According to the composition and position of functional groups of *Zeb1*, a suppressive effect of Cpeb4 binding was predicted (Supplementary fig. 4).

In line, I found that pathological growth conditions caused decreased binding of Cpeb4 to *Zeb1*. This suggests that the decreased binding of Cpeb4 to *Zeb1* removes the inhibitory effect of Cpeb4 on *Zeb1* translation, leading to increased *Zeb1* expression. Exact mechanisms about differential binding of Cpeb4 to its target mRNAs in cardiomyocytes are still unknown, but it has been suggested that the activity of Cpeb4 can be regulated through post-translational modifications by phosphorylation of Cpeb4 through Erk or Cdk1 signaling pathways, which keeps Cpeb4 in a monomeric and active state. Vice versa, unphosphorylated Cpeb4 sequesters CPE-containing mRNAs into inactive, liquid-like droplets (Guillén-Boixet et al., 2016). Specifically, Erk signaling has been shown to regulate pathological cardiac cell growth in several studies (Bueno et al., 2000). Similar to these data, the analysis of RNASeq data from mice that underwent cardiac hypertrophy in our own lab revealed differential regulation of Erk and Cdk1 signaling -related RNAs during cardiac failure. Thus, (in)-activation of Cpeb4 by intracellular signaling events such as Erk signaling might activate specific RBPs by phosphorylation, linking signaling cascades to post-transcriptional regulation of gene expression.

5.5 During pathological growth, Cbeb4 releases Zeb1 to activate expression of growth-related regulatory cascade.

Zeb1 is best known for its role in epithelial-mesenchymal transition (EMT) (Xue et al., 2019) and the onset and progression of various tumors (Han et al., 2016; Liu and Lin, 2016; Liu et al., 2014). In skeletal muscle, Zeb1 deficiency has been linked to poorer regeneration potential (Siles et al., 2019). Mechanistically, Zeb1 promotes cancer progression and MET onset by activating the Wnt5 pathway (Xue et al., 2019). Both activation and repression of gene expression by DNA binding of Zeb1 has been suggested. While transcriptional repression requires direct DNA binding of Zeb1, indirect recruitment to regulatory regions by the Wnt pathway effector Lef1 results in gene activation. Moreover, a direct interaction of Zeb1 with the Hippo pathway through YAP has been suggested, causing increasing transcriptional activity of a common Zeb1/Hippo target gene set (Lehmann et al., 2016).

The present results show that Zeb1 expression is increased after loss of Cbeb4 in cardiomyocytes both *in vitro* and *in vivo* and several Zeb1 target genes are differentially expressed in failing myocardium. This suggests a functional role of the Cbeb4-Zeb1 axis in the diseased myocardium. These DEGs belong to pathways that are known to be involved in cell growth and proliferation, such as the Hippo pathway (Ctgf, Serpin, Tgfb2) or the Mapk/Erk pathway (Dusp1, Flna, Tgfb2).

5.6 Conclusion and outlook

In conclusion, in this project I have generated the first compendium of RNA-binding proteins in primary cardiomyocytes and the first dynamic RBPome in homeostatic versus pathological hypertrophic conditions. RNA-interactome capture in primary cardiomyocytes now open a whole field of interesting possibilities to study dynamic binding of RBPs in settings of cardiac diseases. Since our lab is interested in the activation of the mammalian target of Rapamycin (mTOR) in the onset and progression of cardiac hypertrophy, one interesting study would be a compendium of mTOR-dependent RBPs in NRVCMs by modulating mTOR pharmacologically. Other than that,

RBPomes *in vitro* from other cardiac cell types, or from *ex vivo* isolated adult cardiomyocytes from diseased hearts would be interesting to study.

I found that the dynamically regulated RBP Cpeb4, in addition to its established role in the brain and liver (Calderone et al., 2016; Kan et al., 2010), directly controls pathological cell growth in cardiomyocytes, potentially by increasing expression of specific transcription factors such as Zeb1 and Zbtb20. Expression of Zeb1 target genes is dysregulated in diseased myocardium and this might contribute to the pathological hypertrophy and decreased cardiac function. I found a direct molecular connection of Cpeb4 and Zeb1, which might be an important target to intervene with the outcome of cardiac hypertrophy. Further research needs to be done for better understanding how differential RNA binding behavior of Cpeb4 is regulated and how Cpeb4 regulates translation or stability of specific target mRNAs in response to stress in cardiomyocytes. While the present study has given first evidence how Cpeb4 controls Zeb1 to repress the onset of pathological signaling cascades, functional studies using mouse models with Zeb1 deficient cardiomyocytes are needed to fully characterize the role of Zeb1 in cardiac remodeling. For a detailed mechanistic analysis, Zeb1 should be overexpressed or depleted (e.g. siRNA knockdown), and the effect on myocyte growth should be studied. *In vivo*, Zeb1 transgenic mice could be subjected to cardiac hypertrophy by TAC and subjected to detailed analysis of heart growth and function.

6. RESULTS II

The mTOR pathway has previously been studied in the heart because of its central role in the onset and progression of cardiac hypertrophy. Völkers et al. (2013) have previously shown that genetic inhibition of mTORC1 by overexpression of Pras40 ameliorated the outcome of pathological cardiac hypertrophy, reducing growth and remodeling and restoring function. In this previous study, the role of Pras40 was studied *in vivo* by cardiomyocyte-specific overexpression of Pras40 by AAV9 delivery. The phenotypic effects of a Pras40 deletion *in vivo* in cardiomyocytes are unknown to date, as well as the molecular events following Pras40 depletion. Mechanistic insight in the heart has partly been made for mTOR-bound Pras40, its function once it has been released from mTOR remains largely unclear.

The aim of this study is therefore:

- 1) to study the phenotypic effects after depletion of Pras40 with a focus to cardiac function and growth.
- 2) to understand the molecular peculiarities that underlie the Pras40 KO phenotype, with a focus on mTOR activity and levels of translation.
- 3) to understand the role of mTORC1-released Pras40 during cardiac growth.

6.1 Phenotyping of novel Pras40 KO for cardiac growth and function during cardiac hypertrophy

The focus of the first part of this project lied on the phenotypic analysis of heart growth and function in Pras40-depleted mice during pathological or physiological hypertrophy. Unlike the cardiac phenotype after overexpression of Pras40, which has been published before (Völkers et al., 2013), this phenotype is unknown and prevents therapeutic use of Pras40 as an anti-hypertrophic gene therapy option.

6.1.1 Validation of Pras40 knock-out in two novel mouse models

To gain mechanistic insight into the role of Pras40 during cardiac hypertrophy, two novel Pras40 knock-out (KO) mouse models had been generated prior to this work. For both models, genetically modified embryonic stem (ES) cells had been ordered from the European Conditional Mouse Mutagenesis (EUCOMM) Programme and had been used for the generation of genetically modified mice. Both models had been prepared by Dr. Mirko Völkers in the laboratory of Prof. Mark Sussmann at San Diego State University and were kindly provided for use in this project. KO mice were generated from ES cells, that carry a mutated Akt1S1 (Pras40 gene) locus. This mutated Akt1S1 locus encodes for three loxP sites between exons 2 and 5 of the Akt1S1 gene (Fig. 6.1A), as well as two Flp recombination sites flanking a lacZ reporter site. LoxP sites can be recombined by Cre protein (from „causing recombination“), whereas Flp sites can be recombined by Flippase recombinase. For the global deletion model, the Akt1S1 locus was recombined by Cre, leading to loss of exons 3 and 4. After in vitro fertilization of early stage embryos and transfer into a foster mothers, offspring will be chimeric for a deleted Akt1S1 locus, and from the first daughter generation, parts of the offspring carry the deleted Akt1S1 locus (fullKO), lacking exons 3 and 4. For the second model, (Fig. 6.1B), mice generated from the same ES cells were bred with animals encoding for a Tamoxifen-inducible form of Cre (CreER^{t2}) under the control of the cardiomyocyte-specific α MHC promotor. Expression of CreER^{t2} and delivery of Tamoxifen leads to transfer of the Cre-Tamoxifen complex into the nucleus and recombination of the loxP sites, which leads to deletion of exons 3 and 4 (Fig. 6.1B). In this model, deletion of Pras40 is conditional and cardiomyocyte-specific (cKO). To validate the KO in both models, I tested amounts of Pras40 protein by Western blot analysis of left ventricle and liver lysates of both KO models and wild-type (WT) mice. Pras40 was undetectable in full KO animals and significantly decreased in left ventricles but not livers of cKO mice (fig. 6.1A,B, bottom panel). Blots were made from whole organ lysates, and expression of Pras40 in left ventricles of cPras40 mice resulted from other cardiac cell types that lack the expression of the cardiomyocyte-specific α MHC promotor and were therefore not Pras40-depleted.

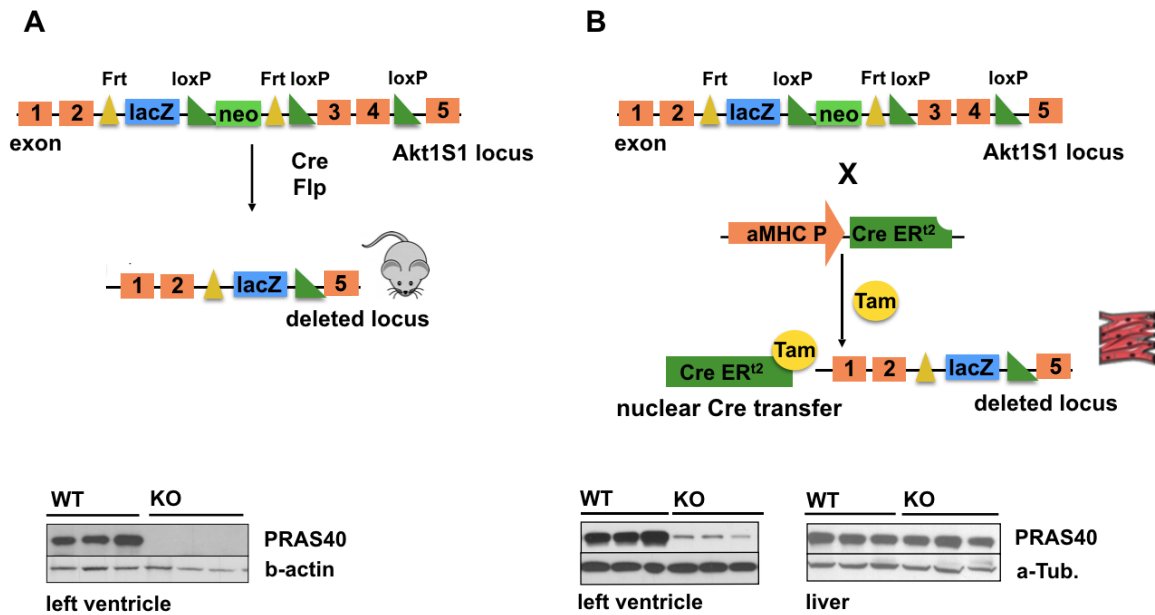


Figure 6.1: Knock-out models for Pras40-depleted mice. (A) Global deletion of Pras40, scheme (upper panel) and western blot of left ventricle lysates (bottom panel). Embryonic stem cell with mutated Akt1S1 locus can be recombined by Cre and/or Flippase (Flp) recombinases, which leads to a globally deleted Akt1S1 locus. These ES cells are then used to generate mice carrying the deleted Akt1S1 locus globally. Western blot analysis of left ventricular lysates (bottom panel) validated the knock-out of Pras40. Mouse symbol in A will indicate global KO in the following figures. (B) Tamoxifen-inducible, cardiomyocyte-specific deletion of Pras40, scheme (upper panel) and western blot of left ventricle and liver lysates (bottom panel). Mice with mutated Akt1S1 locus are crossed to mice which encode for a cardiomyocyte-specific Cre recombinase under the control of cardiomyocyte-specific a-MHC promoter. The Akt1S1 locus is deleted only after delivery of Tamoxifen, which translocates the Cre protein to the nucleus and leads to recombination. The Pras40 protein is only depleted in left ventricles (cardiomyocyte population), but not in other organs (representative liver lysates), as shown in the western blot of organ lysates (bottom panel). The cardiomyocyte symbol will indicate inducible, cardiomyocyte-specific KO in the following figures.

6.1.2 Phenotype of Pras40 KO during pathological and physiological hypertrophy

To analyze phenotypic changes in hearts of Pras40-depleted mice during cardiac hypertrophy, I subjected both mouse models to either pathological or physiological cardiac hypertrophy. To induce pathological hypertrophy, I constricted the aorta between brachiocephalic and left common carotid artery (transverse aortic constriction surgery, TAC, see 1.1.5.1) to a defined width of 27 gauge, generating a pressure overload to the left ventricle of the heart (deAlmeida et al., 2010). TAC surgery typically leads to increased left ventricular wall diameter, and after a compensatory phase, in which the heart grows and adapts to the raised pressure overload, to loss of cardiac function. I

determined the phenotype of WT and KO mice after TAC surgery by analyzing four major parameters, heart weight, cardiac function, fibrosis and expression of fetal markers (compare 1.1.5.3).

To evaluate how KO hearts respond to a physiological stimulus, I subjected mice to a swimming regime (also see 1.1.5.2). Endurance swimming induces physiological cardiac hypertrophy, as an adaptive, reversible response to the elevated work load, which is typically linked to sustained or elevated function (Evangelista et al., 2003). Mice were subjected to swimming for 2 weeks (fullKO) or 4 weeks (cKO), with increasing durations of swimming twice per day (start: 10min/twice per day, increasing by 10min/day up to 90min/twice daily). As for the pathological model, during and after the regime I measured heart growth, cardiac function, fibrosis and fetal marker gene expression.

6.1.2.1 Phenotype of global Pras40 KO after TAC

First phenotyping experiments were performed in the full KO model. I subjected WT and full KO mice to TAC for a time span of two weeks before performing echocardiography and sacrifice (Fig. 6.2A). As expected, heart weight/body weight ratios were significantly increased by 47% after TAC in the WT group, compared to WT sham animals. Surprisingly, this growth response was significantly blunted in the KO group. While basal heart weights were comparable between both sham groups, increase in heart size after TAC was reduced by half in KO animals, resulting in only 22% increase in heart size compared to KO sham animals (Fig. 6.2B). I aimed to confirm this effect to cell size on cardiomyocyte level in adult cardiomyocytes from full KO and WT mice, that I had subjected to TAC surgery. I saw cardiomyocyte size increased by 25% after TAC in WT animals, KO cardiomyocytes were 20% smaller basally as well as after TAC surgery (Fig. 6.2C, D). Echocardiography two weeks after TAC/sham surgery showed no significant difference in EF and FS between both sham groups. In WT TAC animals, contractility (ejection fraction and fractional shortening; EF and FS) was declined at non-significant levels compared to their sham controls, whereas it was significantly

deteriorated in the KO TAC group (-23%) (Fig. 6.2E). Loss of function after TAC in KO animals therefore happens earlier than in WT animals.

In line with this, the expression of fetal markers *nppa*, *nppb* and *myh7* that I measured by qRT-PCR of left ventricular lysates was increased in WT animals after TAC, but this effect was enhanced in KO animals (Fig. 6.2F). This indicates elevated remodeling in the KO TAC group. Amounts of *Colla1*, representing cardiac fibrosis, were elevated in both TAC groups compared to their sham controls. *Colla1* levels were also slightly elevated in sham-operated KO animals compared to the WT sham group, but not significantly higher in KO versus WT TAC animals (Fig. 6.2F).

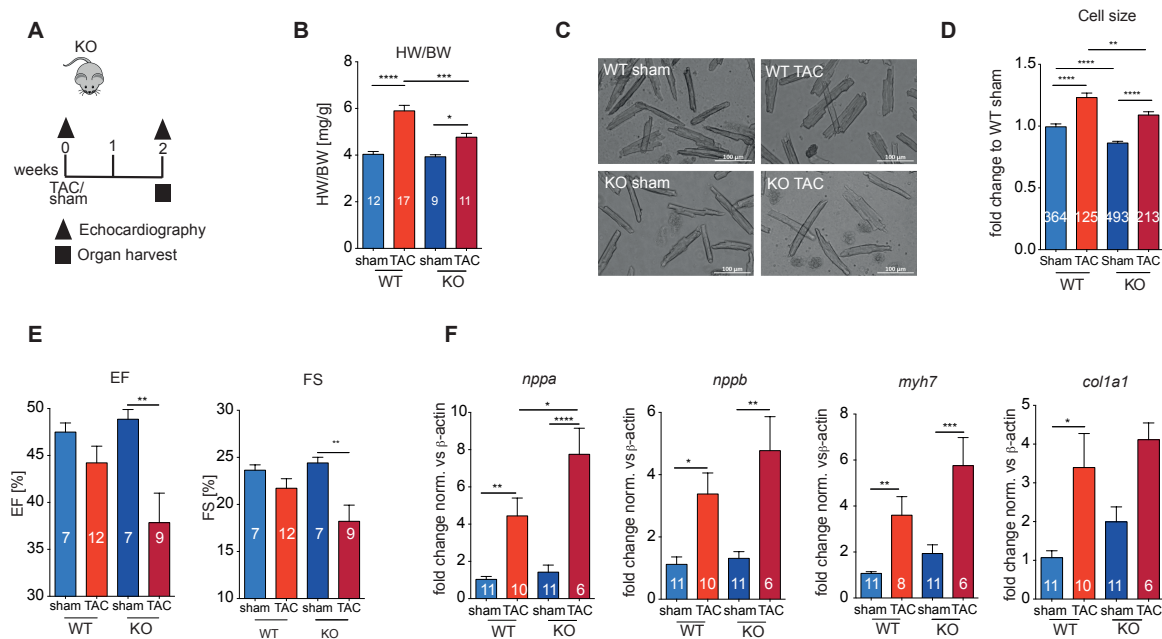


Figure 6.2: Pathological hypertrophy induction in a global Pras40 KO model. (A) Scheme of experimental setup for transverse aortic constriction (TAC) surgery. (B) Heart weight to body weight ratios (HW/BW) of TAC subjected animals 2 weeks post TAC/sham. * $P < 0.05$, *** $P < 0.001$, **** $P < 0.0001$ by one-way ANOVA followed by Bonferroni's post-hoc comparisons. (C) Representative images of isolated adult cardiomyocytes of WT and KO TAC mice 4 weeks post TAC/sham. (D) Cell size quantification of isolated adult cardiomyocytes as shown in (C). ** $P < 0.01$, *** $P < 0.001$, **** $P < 0.0001$ by one-way ANOVA followed by Bonferroni's post-hoc comparisons. (E) Cardiac function, shown by measures of ejection fraction (EF) and fractional shortening (FS) two weeks post TAC/sham. ** $P < 0.01$ by one-way ANOVA followed by Bonferroni's post-hoc comparisons. (F) qRT-PCR measurements of fetal markers natriuretic peptide form a (*nppa*) and b (*nppb*), myosin heavy chain (*myh7*) and collagen (*col1a1*) from left ventricles two weeks post TAC. * $P < 0.05$, ** $P < 0.01$, *** $P < 0.001$, **** $P < 0.0001$ by one-way ANOVA followed by Bonferroni's post-hoc comparisons. Isolation of adult cardiomyocytes by Moritz Kern.

All together I saw KO animals showing less pathological hypertrophy, but together with deteriorated function and elevated levels of fetal markers this did not reflect an ameliorative effect, but rather an inability to compensate the elevated haemodynamic load. I therefore hypothesized that an adaptation to the pathological stimulus is not possible without Pras40.

6.1.2.2 Phenotype of global Pras40 KO after swimming

To test whether the inability to adopt to elevated stress was unique to pathological stimuli, I subjected full KO versus WT mice to a physiological swimming regime for 2 weeks with increasing amounts of swimming twice per day (start: 15min/twice daily, increase of 10min/day, up to 90min/twice daily) (Fig. 6.3A). I performed Echocardiography basally and after two weeks of swimming, before sacrifice of the animals. Functional data are shown after two weeks of swimming.

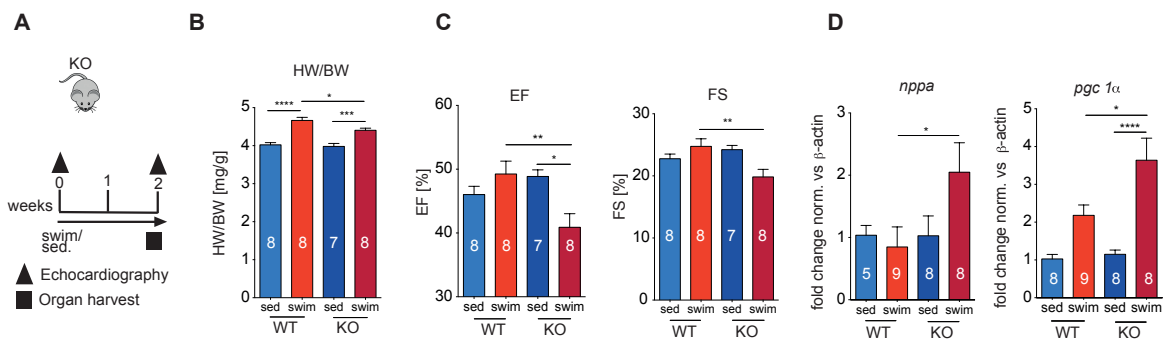


Figure 6.3: Physiological hypertrophy induction in a global Pras40 KO model. (A) Experimental setup of swimming model to induce physiological cardiac hypertrophy (B) Heart weight to body weight ratios (HW/BW) after two weeks of swimming/sedentary control regime. *P < 0.05, ***P < 0.001, ****P < 0.0001 by one-way ANOVA followed by Bonferroni's post-hoc comparisons. (C) Cardiac function, shown by measures of ejection fraction (EF) and fractional shortening (FS) after two weeks of swimming/sedentary control regime. *P < 0.05, **P < 0.01 by one-way ANOVA followed by Bonferroni's post-hoc comparisons. (D) qRT-PCR measurements of fetal markers from left ventricles after two weeks of swimming/sedentary control regime. *P < 0.05, ****P < 0.0001 by one-way ANOVA followed by Bonferroni's post-hoc comparisons.

After two weeks of swimming, heart weight to body weight ratios in WT swimmers were significantly increased by 21%, as expected. Similar to the pathological regime, full KO mice showed a significantly attenuated growth response (+12% HW/BW) after

swimming compared to the WT group (Fig. 6.3B). As expected, heart function (EF, FS) was slightly elevated in the WT swim group. In the KO swim group, heart function was significantly reduced compared to KO sedentary animals (-18% EF, -20% FS), and also significantly lower than in WT swimmers (Fig. 6.3C). In line with loss of function, levels of *nppa* were increased only in the KO swim group, but not in WT swimmers. Swimming as a physiological regime classically does not lead to increased fetal genes. *Pgc1 α* , a marker typically induced by exercise, was elevated in both swim groups, but at a significantly higher extent in KO swimmers (Fig.6.3D).

All together, full KO mice seem to be unable to adapt to a physiological growth regime, which in WT animals is not linked to remodeling or loss of function. This strengthens the hypothesis, that Pras40 is crucial for the adaptation to hemodynamic overload. Strikingly, Pras40 seems to be inevitable to respond to growth stimuli, independent of their etiology.

6.1.2.3 Phenotype of cardiomyocyte- specific Pras40 KO after TAC

To confirm that this phenotype is cardiomyocyte-related, I repeated phenotypic characterization in the Tamoxifen-inducible cKO mouse model. I subjected mice to TAC or sham surgery and sacrificed 2 days or 6 weeks post surgery (Fig. 6.4A). Echocardiography was performed after weeks 1, 3, 5 and 6, to follow heart function. Data are shown for the 6 weeks time point, when function was clearly decreased. The early time point for organ harvest (2d) represents an acute response to the pathological stimulus, that allows measuring of acute transcriptional changes, whereas the 6 weeks time point reflects a chronic hypertrophic setting were hearts have typically begun to undergo cardiac failure.

When I sacrificed animals 6 weeks post TAC/sham treatment, WT hearts were significantly enlarged compared to their sham control group (+45% HW/BW). KO TAC hearts grew significantly less (+25% HW/BW). Left ventricle anterior wall thickness, calculated from parasternal long axis M-mode echocardiographic images was significantly smaller (-15%) in KO TAC animals compared to the WT TAC group. Significant basal differences in HW/BW ratios and left ventricular anterior wall thickness

in sham-operated animals were not observed (Fig. 6.4B). Contractile function (EF) was diminished in both WT and KO TAC animals, but was deteriorated more severely in TAC-operated KO animals (-7% in KO versus WT TAC, Fig. 6.4C).

I determined survival of both WT and KO TAC animals by the Kaplan-Meier estimator (Kaplan and Meier, 1958) and in line with deteriorated function saw significantly lower survival rates in the KO TAC group (Fig. 6.4D).

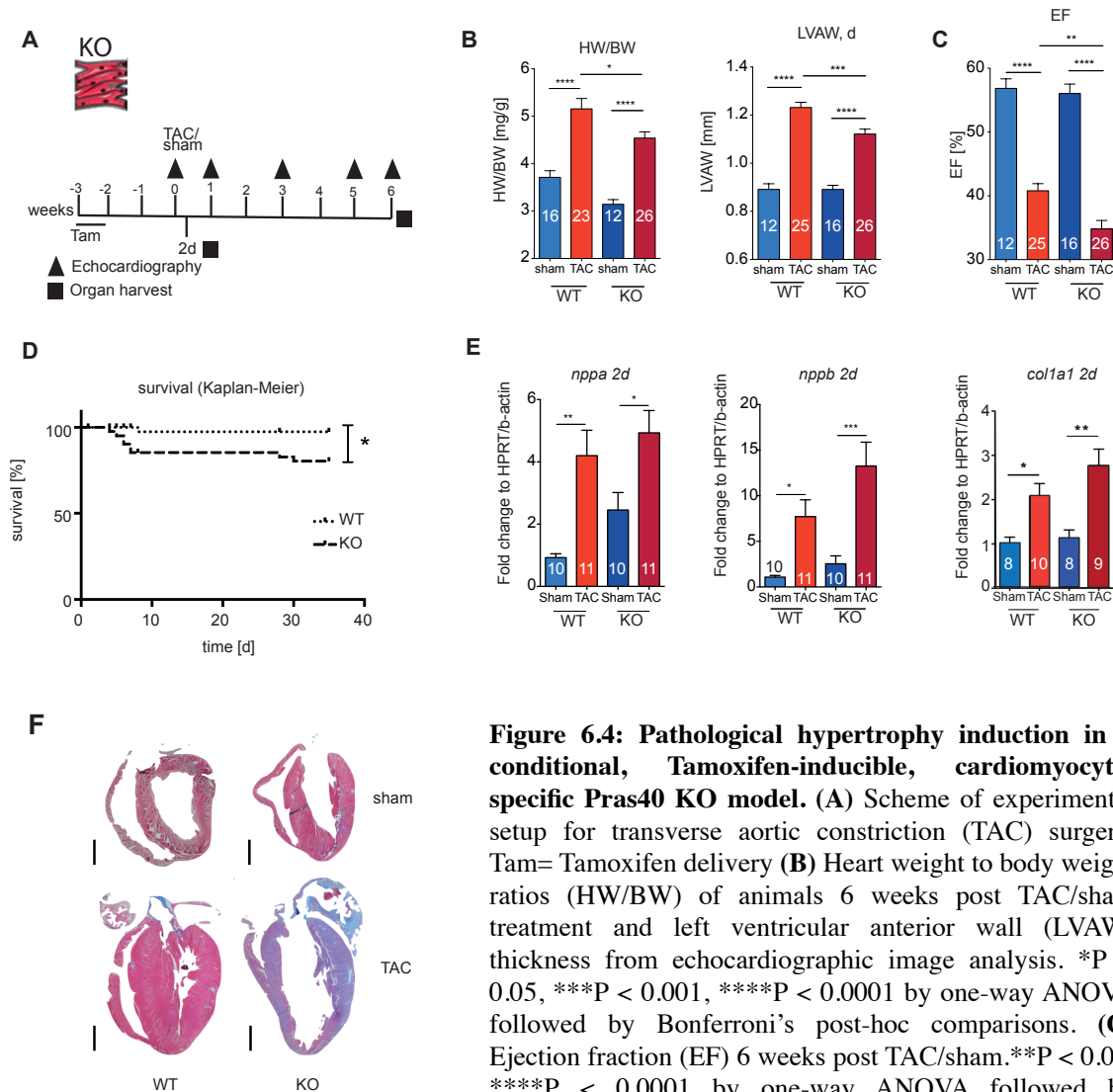


Figure 6.4: Pathological hypertrophy induction in a conditional, Tamoxifen-inducible, cardiomyocyte-specific Pras40 KO model. (A) Scheme of experimental setup for transverse aortic constriction (TAC) surgery. Tam= Tamoxifen delivery (B) Heart weight to body weight ratios (HW/BW) of animals 6 weeks post TAC/sham treatment and left ventricular anterior wall (LVAW) thickness from echocardiographic image analysis. *P < 0.05, ***P < 0.001, ****P < 0.0001 by one-way ANOVA followed by Bonferroni's post-hoc comparisons. (C) Ejection fraction (EF) 6 weeks post TAC/sham. **P < 0.01, ****P < 0.0001 by one-way ANOVA followed by Bonferroni's post-hoc comparisons. (D) Kaplan-Meier estimator plot of survival after TAC surgery (E) qRT-PCR measurements of fetal markers nppa and nppb and collagen from left ventricle lysates 2 days post TAC. *P < 0.05, **P < 0.01, ***P < 0.001 by one-way ANOVA followed by Bonferroni's post-hoc comparisons. (F) Masson trichrome staining of longitudinal heart sections.

2 days post TAC, fetal marker genes *nppa* and *nppb* were increased after TAC in both groups but the response was slightly elevated in KO animals. Amounts of fibrosis that I measured by levels of *Colla1* were slightly elevated in the cKO TAC versus the WT TAC group (Fig. 6.4E). Representative longitudinal heart sections stained by Masson-Trichrome validated significantly smaller left ventricular wall diameters and elevated amounts of fibrosis (Fig. 6.4F, fibrosis in purple color).

All together, depletion of Pras40 in cardiomyocytes is sufficient to induce the inability of KO hearts to adapt to the pathological stimulus, resulting in blunted heart growth, deteriorated function and elevated levels of pathological markers and fibrosis. I therefore suggest an indispensable role of Pras40 in cardiomyocytes for the adaptation to pressure overload.

6.1.2.4 Phenotype of cardiomyocyte-specific Pras40 KO after swimming

I next aimed at understanding the response of cKO mice to a physiological growth stimulus and subjected mice to swimming for a duration of 4 weeks with increasing amounts of swimming twice per day (start: 15min/twice daily, increase 10min/day, up to 90min/twice daily). I performed echocardiography every other week and at the end of the swimming treatment and isolated organs at the end of the 4 weeks treatment period (Fig. 6.5A). Functional data are shown after 4 weeks of swimming.

Similar to the full KO animals, cKO mice showed no significant growth response to the swimming regime compared to the sedentary KO group, whereas WT swimmers grew significantly. (+36%). (Fig. 6.5B). As for the sham animals in the TAC experiment, basal left ventricular to tibia (LV/TL) ratios were similar for WT and cKO animals. Heart function was sustained in the WT swim group, as expected, but was slightly decreased in KO swimmers (Fig. 6.5C). Levels of fetal genes *nppa* and *nppb* remained unchanged in all groups (Fig. 6.5D). As for the full KO model, physiological growth was induced to a lower extent in KO animals compared to their WT controls, and cKO mice reacted to the physiological stimulus with slight functional perturbation, even though the effect was less severe than in the full KO model.

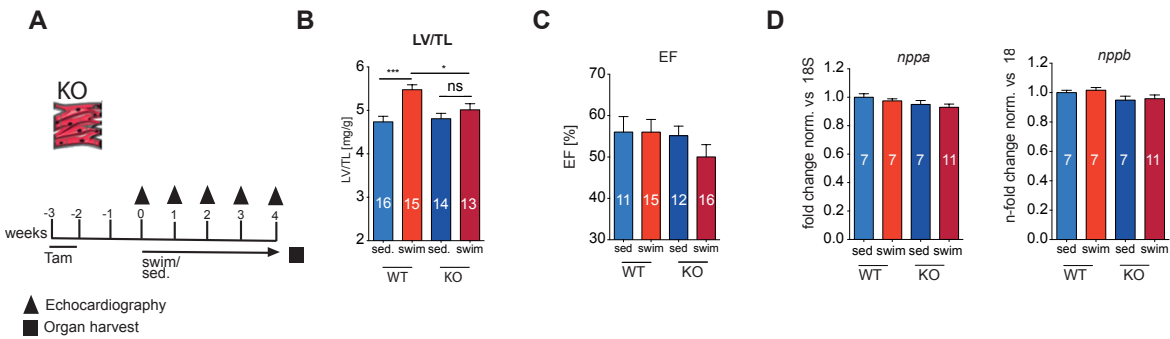


Figure 6.5: Physiological hypertrophy induction in a conditional, Tamoxifen-inducible, cardiomyocyte-specific Pras40 KO model. (A) Experimental setup of swimming model to induce physiological cardiac hypertrophy. Tam= Tamoxifen delivery (B) Left ventricle to tibia length ratios (LV/TL) after four weeks of swimming/sedentary control regime. * $P < 0.05$, *** $P < 0.001$ by one-way ANOVA followed by Bonferroni's post-hoc comparisons.(C) Ejection fraction (EF) after four weeks of swimming/sedentary control regime. (D) qRT-PCR measurements of fetal markers from left ventricles after four weeks of swimming/sedentary control regime.

All in all, the phenotype of hypertrophy-subjected Pras40 KO mice is unexpected concerning growth behavior, severeness of remodeling and contractile function. The previously published study showed that overexpression of Pras40 can rescue heart function before and even after TAC and blunts pathological growth (Volkers et al.; 2013). The Pras40 KO model does not reflect this phenotype, but I rather observed an unknown, crucial function of Pras40 in the adaptation to both physiological and pathological growth. A detailed analysis of molecular events following the hypertrophic regime was therefore of major interest.

6.2 mTOR signaling upon depletion of Pras40 during pathological hypertrophy

To understand the molecular mechanism underlying the KO phenotype, I aimed at determining the activity of the mTOR downstream cascade upon depletion of Pras40 basally and during cardiac hypertrophy.

6.2.1 mTOR activity upon Pras40 KO basally and during pathological growth

To determine basal levels of mTOR activity, I performed Western blot analysis from isolated adult full KO and WT cardiomyocyte lysates and measured mTORC1 activation

by amounts of phosphorylated downstream targets 4EBP1, S6K and ribS6P. Elevated amounts of phosphorylated downstream targets reflect activation of mTOR as described in detail in 1.2.2.1.1 (Fig.6.6A). Surprisingly, I saw that lack of Pras40 inhibited activation of mTORC1 in adult cardiomyocytes: Amounts of p-S6K, p-ribS6 and p-4EBP1 were reduced by 80%, 61% and 30% compared to WT levels, respectively (Fig. 6.6B, Quantification in D). Like the phenotypic data after TAC and swim, these data are not in line with the previous study (Volkers et al., 2013), which showed reduced mTOR activation following overexpression of Pras40. However, attenuated mTOR activation in KO cardiomyocytes could explain blunted cardiomyocyte and left ventricular growth in Pras40 KO animals. The expression of the mTOR kinase and mTORC1 component Raptor was slightly lower at non-significant levels in KO versus WT cardiomyocytes (Fig. 6.6B, Quantification in D).

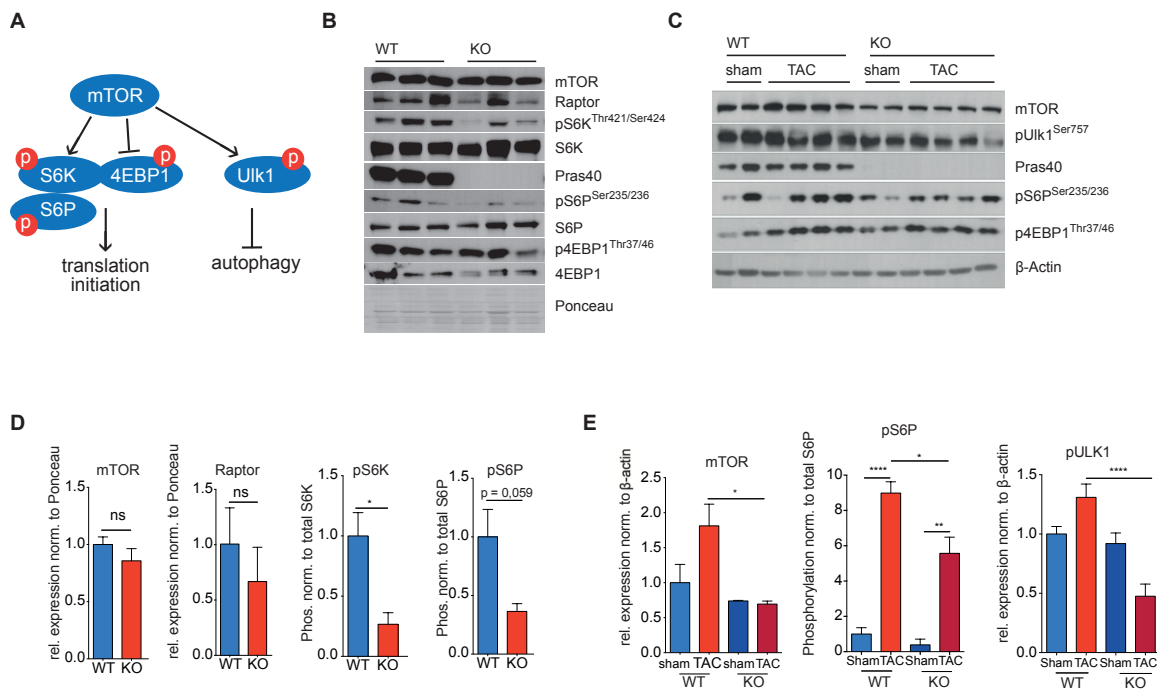


Figure 6.6: mTOR activation is blunted basally and after TAC surgery in Pras40 KO. (A) Scheme of mTOR downstream signaling cascade. mTOR downstream targets are activated by phosphorylation. Phosphorylation of S6K, S6P and 4EBP1 leads to translation initiation, whereas phosphorylation of Ulk1 inhibits autophagy. (B) Western blots of isolated adult cardiomyocytes from WT and full KO mice. Cell isolation by Albert von der Lieth. (C) Western blots from left ventricular lysates of TAC or sham treated WT or cKO mice 2 days post TAC (D)-(E): Quantifications of (B)-(C) *P < 0.05, **P < 0.01, ****P < 0.0001 by two-tailed student's t-test (D) or one-way ANOVA followed by Bonferroni's post-hoc comparisons (E).

To determine mTORC1 activation during pathological cardiac hypertrophy, I determined the phosphorylation of mTORC1 downstream targets in heart lysates from TAC- and sham-subjected WT and cKO mice 2 days post TAC (Fig. 6.6C, Quantification in E). I tested on amounts of p-ribS6 and p-4EBP1 like before, and on p-Ulk1, which indicates inhibition of autophagy when mTOR is activated. In line with the results in adult cardiomyocytes, I found levels of p-ribS6P reduced in KO sham lysates compared to their WT controls (-61%). After TAC, levels of p-S6P were elevated in both TAC groups compared to their sham controls. Still, this increase was significantly blunted in KO TAC animals (-38% in KO versus WT TAC), indicating reduced mTOR activity in KO mice after TAC. Levels of p-Ulk1 were similar in both sham groups. After TAC, levels of p-Ulk1 were increased by 30% in WT animals, as expected, indicating lower amounts of autophagy. In KO TAC animals, levels of p-Ulk1 were reduced compared to their sham control group (-48%) and to the WT TAC group (-64%). This decrease indicated higher levels of autophagy and less mTOR activity. Similar to the basal data in adult cardiomyocytes, the expression of the mTOR kinase was lower in sham treated KO versus WT lysates, at non-significant levels. After TAC, I observed increased levels of mTOR in WT mice. This increase was completely blocked in TAC-treated KO mice, that showed significantly reduced amounts of mTOR, compared to WT TAC lysates (-62%), and no increase of mTOR after TAC. (Fig. 6.6C, Quantification in E).

6.2.2 Upstream activation of mTOR to rescue signaling after deletion of Pras40

Blunted mTOR activation after deletion of Pras40 brought up the question whether this effect is depending on mTOR or whether Pras40 might regulate downstream targets independently of mTOR. To test whether the activity of mTOR downstream targets can be restored, even when Pras40 is depleted, I activated mTOR by blocking TSC2 upstream of the mTOR kinase. Knock-down of TSC2 in WT cells or animals leads to increased mTOR activity and to the phosphorylation of mTOR downstream targets (Fig. 6.7A), as also described in detail in Fig. 1.5.

I isolated mouse cardiomyocytes from neonatal WT or full Pras40 KO mice and knocked down TSC2 by siRNA transfection in both groups. Treatment with scrambled siRNA (scrbl.) served as control. After 24h of KD, I evaluated amounts of phosphorylated mTOR downstream targets by Western Blot analysis.

KD of TSC2 was successful and significantly decreased levels of TSC2 protein by 45% (WT) or 65% (KO) (Fig. 6.7B, Quantification in C). As shown in the previous experiment (Fig. 6.6B), levels of mTOR downstream target p-S6P were reduced in KO versus WT cardiomyocytes transfected with siRNA scrbl. (Fig. 6.7B, C) and levels of p-4EBP1 were decreased as well. Amounts of p-Ulk1 were again similar in KO versus WT scrbl. control cells. After KD of TSC2, phosphorylation levels of all three mTOR downstream targets Ulk1, S6P and 4EBP1 were increased in WT cardiomyocytes, as expected (+23%, +23%, +39%, respectively).

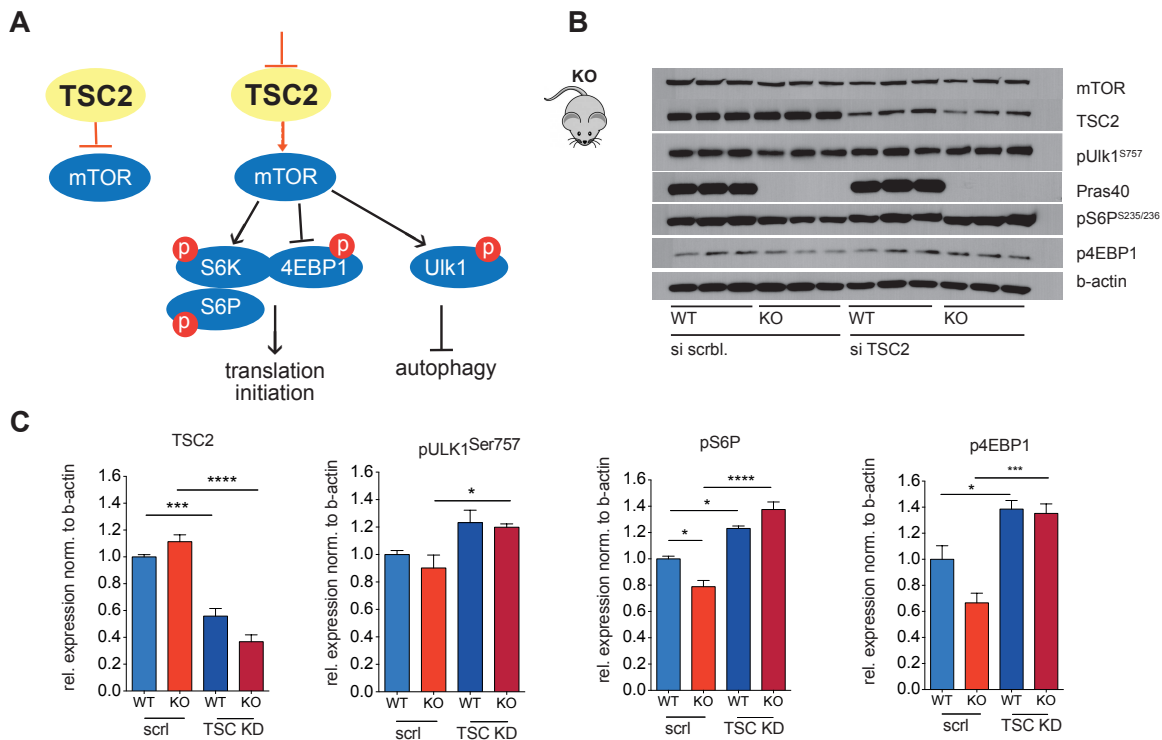


Figure 6.7: mTOR activation can be rescued by KD of TSC2 upstream of mTOR. (A) Scheme of mTOR inhibition by active TSC2 or mTOR activation by inhibition of TSC2. (B) Western blots of isolated neonatal mouse cardiomyocytes from WT and full KO mice, that were transfected with siRNA against TSC2 or scrambled control siRNA (scrbl.) (C) Quantification of Western blots from (B). *P < 0.05, ***P < 0.001, ****P < 0.0001 by one-way ANOVA followed by Bonferroni's post-hoc comparisons.

Interestingly, these target proteins were phosphorylated in TSC2 KD, Pras40 KO cells to a similar extent (+20%, +37%, +35%). Blunted mTOR signaling after KO of Pras40 can therefore be restored by reactivating mTOR upstream of the kinase. An mTOR-independent effect of Pras40 to mTOR downstream targets therefore seems unlikely.

6.3 Effects of Pras40 deletion on translation

Since lack of Pras40 mitigated the activity of mTOR, and mTOR in turn directly regulates several targets involved in translation initiation, I was interested in analyzing the effects of Pras40 on overall levels of translation. Additionally I aimed at testing which specific sets of RNAs are differentially translated, when Pras40 is deleted, and what biological functions these regulated RNAs share. As described in 6.2, mTOR downstream signaling was significantly mitigated after deletion of Pras40 both basally and during hypertrophic conditions. I therefore hypothesized that levels of overall translation might be lower after KO of Pras40.

6.3.1 Overall translation upon depletion of Pras40 during pathological hypertrophy

My first goal was the analysis of overall translation rates in KO and WT mice during pathological hypertrophy. I therefore labelled newly synthesized proteins by a Puromycin incorporation assay *in vivo* in KO versus WT mice after TAC or sham treatment. Puromycin is an antibiotic protein synthesis inhibitor, which is incorporated into the nascent polypeptide chain and prevents elongation. Amounts of incorporated Puromycin in newly synthesized proteins directly reflect the rate of overall mRNA translation (Nathans, 1964). Puromycin was delivered by intra peritoneal injection to KO and WT mice 2 days after TAC or sham surgery for 45 minutes before sacrifice (Fig. 6.8A). Incorporation rates were measured in left ventricular lysates by Western blot analysis with a Puromycin-specific antibody.

When comparing WT TAC operated animals to their sham control group, translation rates were increased by 3.5-fold after TAC surgery. This clear increase was expected, as

hypertrophy requires *de novo* synthesis of proteins (Heineke and Molkenin, 2006). Increase in translation after TAC was significantly weakened in KO animals, with translation rates being only increased by 1.4-fold compared to the KO sham group (Fig. 6.8B, Quantification in C). Reduced overall translation rates are in line with blunted mTOR activation in KO hearts after TAC (compare Fig. 6.6B, C) as well as with the mitigated growth response in KO animals in pathological or physiological growth conditions (compare 6.1.2).

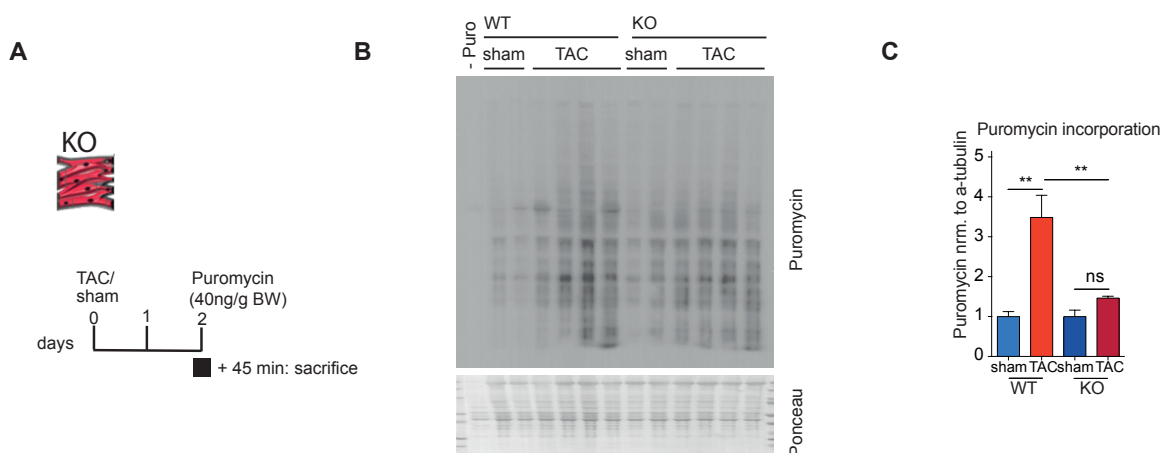


Figure 6.8: Overall translation is blunted after TAC surgery in Pras40 KO. (A) Experimental setup for in vivo Puromycin incorporation experiment. Conditional Pras40 KO versus WT mice were subjected to TAC surgery and after 2d to 45min Puromycin treatment, delivered intraperitoneally. (B) Puromycin incorporation rates measured by Western blot analysis of left ventricular lysates of WT or cKO mice 2d after TAC/sham. (C) Quantification of B. **P < 0.01, by one-way ANOVA followed by Bonferroni's post-hoc comparisons.

6.3.2 System-wide analysis of differentially translated RNAs in Pras40 KO mice

Having shown that depletion of Pras40 negatively affects global translation rates and the activation of the mTOR downstream signaling cascade, I further aimed at understanding which specific RNAs are differentially translated upon deletion of Pras40. For a system-wide approach, I combined the Ribo-tag system (Sanz et al., 2019) with Ribosome profiling (Ingolia et al., 2011) and Ribosome sequencing (RiboSeq). We had previously crossed the Ribo-tag mouse (Sanz et al., 2019), to be cardiomyocyte-specific and Pras40 depleted. The RiboTag mouse encodes for a variant of Ribosomal protein 22 (Rpl22, a

component of the large ribosomal subunit), which is flanked by recombination sites and followed by an identical C-terminal Rpl22 exon with 3 copies of the HA epitope (HA-Tag) before the stop codon (Sanz et al., 2019). We had crossed this mouse to a mouse line that encodes Cre recombinase protein under the control of the cardiomyocyte-specific, α -myosin heavy chain (α -MHC) promoter. Cardiomyocyte-specific recombination of the RPL22 locus leads to recombination and deletion of the untagged RPL22 locus with its stop codon, and expression of HA-tagged RPL22 in cardiomyocytes (aMHC-RiboTag). To compare actively translating RNAs in KO versus WT mice, I now crossed the aMHC-RiboTag mouse to the Pras40 full KO mouse (Fig. 6.9A).

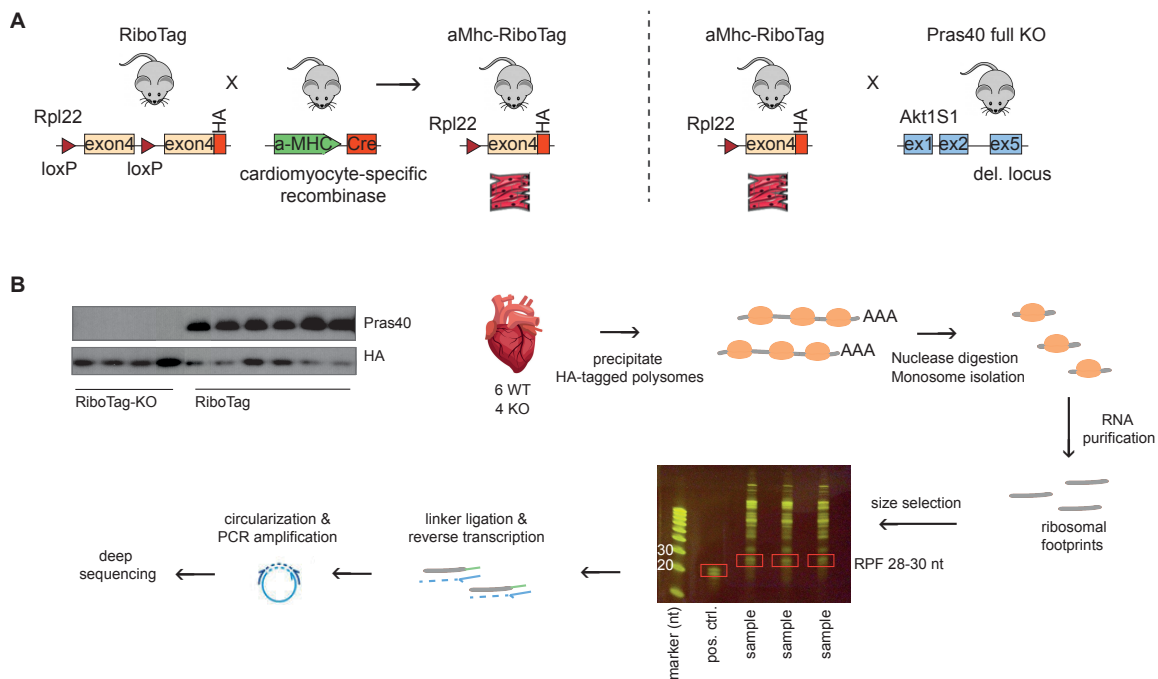


Figure 6.9: RiboSeq of Pras40-depleted hearts to determine actively translating RNAs. (A) Scheme of Pras40-depleted, cardiomyocyte-specific RiboTag mouse. Left panel: The cardiomyocyte-specific RiboTag mouse was crossed from the RiboTag mouse (Jackson lab), that carries a mutated Rpl22 locus with HA-tagged exon 4, and a mouse encoding for Cre recombinase under the control of cardiomyocyte-specific α Myosin heavy chain promoter (α -MHC). Cre recombination excises untagged exon 4 and its stop codon and leads to expression of HA-tagged RPL22. Right panel: The cardiomyocyte-specific α -MHC-RiboTag mouse was crossed to the full Pras40 KO to measure Pras40-dependent active translation. **(B)** Ribosome sequencing (RiboSeq) method. The genotype of Pras40 KO versus WT RiboTag mice, and the expression of HA-tagged Rpl22 was validated by Western blot. Polysomes from left ventricular lysates are precipitated with anti HA magnetic beads. Nuclease digest removes all RNAs, that are not protected by ribosomes, resulting in protected ribosome footprints. Footprints are isolated by size selection on a PAGE gel, made accessible for primers by appropriate linker ligation and are reversely transcribed, circularized and amplified by PCR. These libraries can then be used for deep sequencing.

Ribosomes were isolated by immunoprecipitation of HA-tagged Ribosomes from cardiac lysates, following nuclease digest and RNA isolation. I prepared cDNA libraries from the ribosome-protected mRNA fragments and performed deep sequencing (sequencing by BioQuant Sequencing facility, detailed scheme in Fig. 6.9B). Translational regulation was assessed in hearts of 4 fullKO/Ribotag versus 6WT/RiboTag mice. I validated HA-tagged Rpl22 and Pras40 deletion by Western blot analysis (Fig. 6.9B). Pre-processing of the sequencing data filtered reads for triplet periodicity and specific mapping, and removed ribosomal reads and reads without alignment or poor quality (Fig. 6.10A). Only periodic fragment lengths that showed a distinctive triplet periodicity (usable reads, Fig. 6.10A) were kept for downstream analysis, as we have published it previously (Doroudgar et al., 2019). Libraries yielded around 2 and 8 million usable reads and after trimming had the distinct read-length distribution of ribosomal footprints, which peaked around 29 nt (representative read length of WT 1 in Fig. 6.10B). Further quality control analysis can be found in supplementary figure 6.

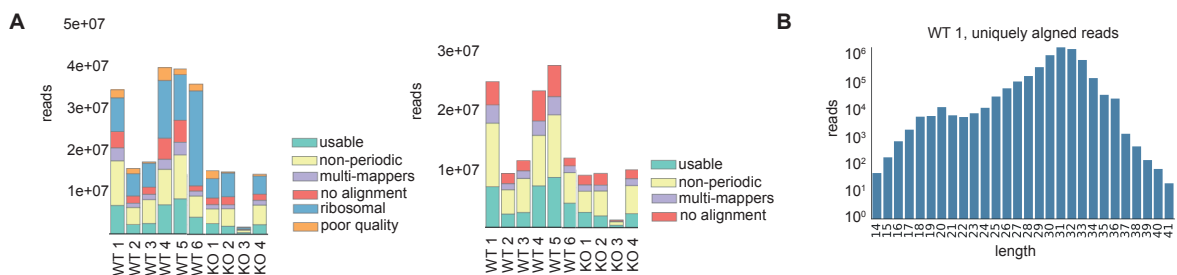


Figure 6.10: Quality control and preprocessing of RiboSeq library of Pras40-depleted versus WT hearts. (A) Sequencing data were preprocessed to filter only periodic, specifically aligned reads. Left panel shows distribution of reads of all 10 samples, with usable reads, in contrast to non-periodic reads, multi-mapped reads, reads without alignment, ribosomal reads and reads of poor quality. The right panel shows reads after filtering out the ribosomal reads, which is the first step in the pre-processing pipeline. (B) Representative read length distribution of preprocessed reads after trimming. Read length represents length of ribosomal footprints. Preprocessing and quality control by Etienne Boileau.

6.3.3 Functional analysis of differentially translated genes in Pras40-depleted hearts

In our RiboSeq data, I found 126 differentially expressed genes (DEGs) between KO and WT samples (log fold change > 0.5, FDR<0.1), 22 being upregulated in KO versus WT

mice and 104 being downregulated (Fig. 6.11A). Among those DEGs, Akt1S1 was found downregulated, as expected (Fig. 6.11A, marked in red). To discover which classes of mRNAs displayed altered translation patterns in Pras40 depleted hearts, I performed unsupervised clustering and gene ontology (GO) analysis for differentially expressed genes (log fold change>0.5, FDR<0.1) in KO compared to WT samples. GO analysis for “biological processes“ showed high enrichment of DEGs that are involved in ubiquitin-dependent catabolic processes and the ubiquitin-proteasome system (UPS) (Fig. 6.11B, red). Intriguingly, three of the top 10 enriched biological processes belonged to processes linked to proteolysis or ubiquitin-dependent degradation. Apart from protein degradation-involved DEGs, biological processes linked to mRNA processing and translation were most prominent, as well as functions involved in protein transport.

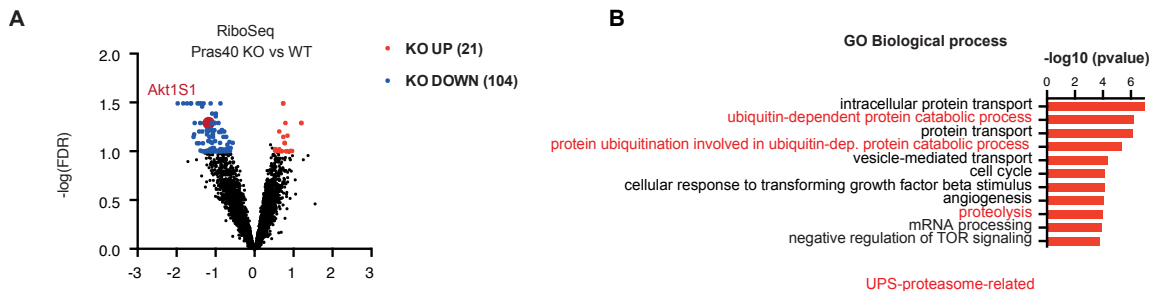


Figure 6.11: Functional analysis of translationally regulated, Pras40-dependent genes. (A) Translationally regulated genes from Pras40 KO versus WT KO cardiomyocytes. Significant hits were defined as genes that are enriched/depleted by at least FC of +/-0.5 and an FDR<0.1 (B) Gene ontology for “Biological process“ of genes with the same cut-off criteria as shown in (A).

I next screened the dataset for the genes that I found in the enriched GO terms for a more detailed analysis. Among the ubiquitin-proteasome-related, Pras40-dependent DEGs, I found several Ubiquitin-Ligases (Ube3c, Ubr1,2,5, Herc1-3, Fig. 6.12A). Cullin, which was also found to be differentially expressed, serves as scaffold protein which provides support to ubiquitin ligases. Interestingly, all of these transcripts down-regulated in Pras40-depleted hearts. Apart from DEGS that belonged to the most prominent “biological processes“, I also searched the list of DEGs for genes that are known to be

involved in the remodeling process during pathological cardiac hypertrophy. This might help understand the pathological phenotype of *Pras40* KO mice (Fig. 6.12B). I found both natriuretic peptides type A and B (*nppa*, *nppb*), as well as *myh7* significantly elevated in *Pras40* KO mice. Collagen 1 (*Col1a1*), a marker for fibrosis, was differentially expressed at higher levels in KO mice as well.

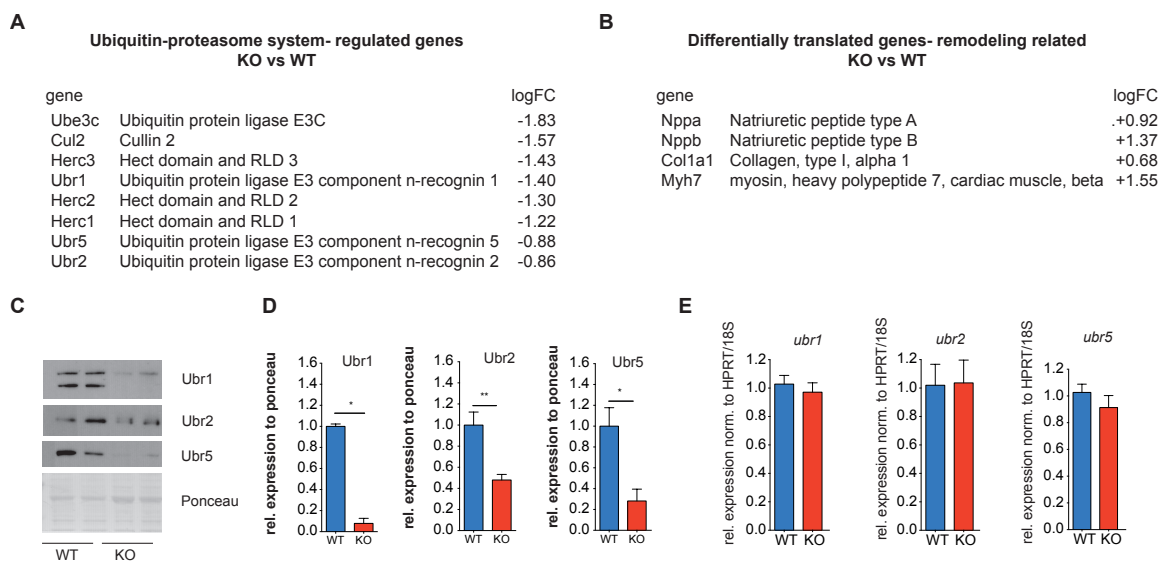


Figure 6.12: List of DEGs and validation of translationally regulated, *Pras40*-dependent genes. (A) List of DEGs that belong to enriched GO terms related to the UPS. (B) List of DEGs that are significantly regulated and are known to be involved in cardiac remodeling. (C) Validation of DEGs by Western blot analysis of murine embryonic fibroblast lysates of WT or fullKO mice. (D) Quantification of (C). *P < 0.05, **P < 0.01, two-tailed student's t-test (E) qRT-PCR from WT or fullKO MEF RNA from parallel experiment to (C). *P < 0.05, two-tailed student's t-test.

6.3.4 Validation of differentially translated UPS-related genes after *Pras40* KO

To validate the changed abundance of UPS-related genes on protein level, I performed Western blot analysis of KO and WT murine embryonic fibroblasts (MEFs) that were generated from the fullKO mouse line. In line with the RiboSeq data, levels of *Ubr1*, *Ubr2* and *Ubr5* protein were significantly reduced in KO versus WT MEFs (Fig. 6.12C, Quantification in D). Levels of *Ubr1*, *Ubr2* and *Ubr5* transcripts were measured by q-RT-PCR and did not significantly vary in KO versus WT MEFs (Fig. 6.12E). Downregulated levels of these Ubrs were also found *in vivo* in lysates of left ventricles (Suppl. Fig. 8).

6.4 Effects of Pras40 KO on proteasomal function

With UPS- related genes being differentially translated upon deletion of Pras40, I hypothesized that proteasomal activity might be altered in Pras40-depleted hearts or cells. To understand how the ubiquitin-proteasome is affected, I aimed at testing proteasomal function, as well as levels of poly-ubiquitination and protein aggregation, both markers for disturbed proteasomal function.

6.4.1 Analysis of 26S proteasomal activity and function *in vitro* and *in vivo*

I first measured 26S proteasomal activity in lysates of sham and TAC operated WT and full KO mice 2 days after the treatment. 26S proteasomal activity was measured by degradation rates of a fluorescently labelled substrate, which is specifically degraded by one of the three proteasomal activities, chymotrypsin-like, trypsin-like, and caspase-like, respectively. I followed degradation over 180 minutes and calculated proteasomal activities from the fluorescence difference between minutes 20 and 55 (delta of relative fluorescence units, dRFU, Fig. 6.13A, left panel). I saw an increase in 26S chymotrypsin-like activity in WT mice after TAC surgery (Fig. 6.13A, right panel), as it has been shown before (Depre et al., 2006). In KO mice, this increase was completely blocked. A similar effect could be observed for trypsin-like (Fig. 6.13B) 26S activity, even though the effect was slightly smaller. Caspase-like (Fig. 6.13C) activity remained unchanged.

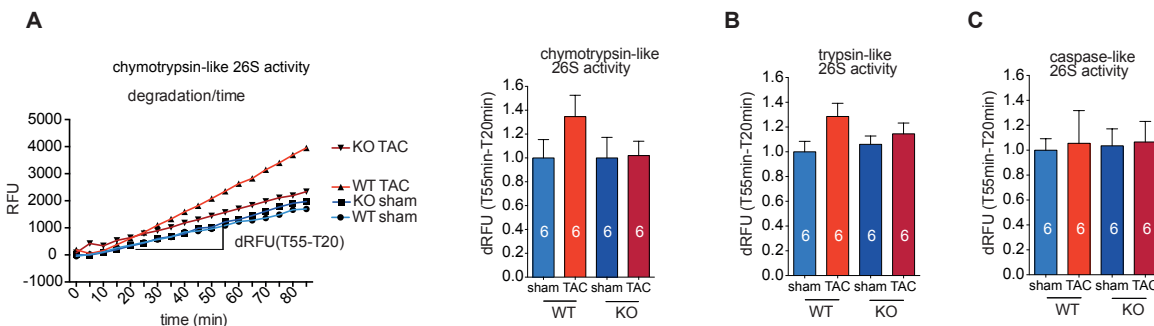


Figure 6.13: Pras40 KO blunts 26S proteasomal activity *in vivo* after TAC. (A) Chymotrypsin-like 26S proteasomal activity of left ventricular lysates of WT or cKO TAC versus sham mice (2d post surgery). Left panel: relative fluorescent units (RFU) over time and read-out of dRFU of linear phase between 20 minute and 55 minutes. (B) dRFU of trypsin-like activity from left ventricle lysates of WT or KO mice 2d post TAC/sham. (C) dRFU of caspase-like activity from left ventricle lysates of WT or KO mice 2d post TAC/sham.

I therefore hypothesized, that Pras40 holds a crucial function in the activation of the 26S proteasome. Since in the present data and previous studies (Depre et al., 2006), chymotrypsin-like 26S activity showed the biggest response after TAC, I focused on this activity in the following experiments.

6.4.2 Analysis of ubiquitination, protein aggregation and proteasomal activity *in vitro*

As the proteasomal response to the pathological stimulus is deteriorated in Pras40 KO mice after TAC, I aimed at analyzing the amounts of poly-ubiquitinated proteins in KO versus WT heart lysates 2 days after TAC. Accumulation of poly-ubiquitinated proteins has been linked to deteriorated proteasomal clearance. I saw an increase in levels of poly-ubiquitinated proteins after TAC in both WT and KO mice, which reflects a compensatory effect following the hypertrophic stimulus and overshooting anabolic state. Still, levels of poly-ubiquitination were elevated in KO mice both basally and after TAC when compared to the WT control groups (fig. 6.14A). This is in line with mitigated proteasome function described in 6.4.1.

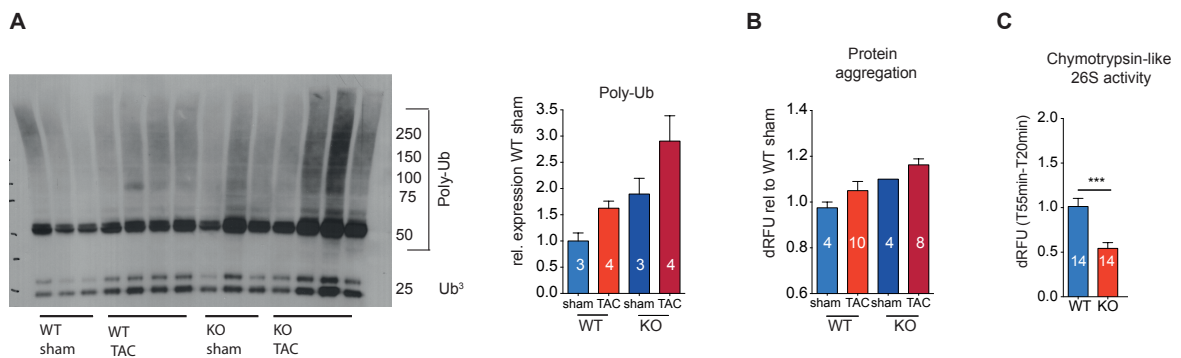


Figure 6.14: Pras40 KO leads to poly-ubiquitination and aggregation of proteins *in vivo* and significantly deteriorated proteasomal activity *in vitro*. (A) Western blot and quantification of left ventricular lysates of WT or cKO TAC versus sham mice (2d post surgery) to determine amounts of poly-ubiquitinated proteins. (B) Proteostat assay to detect amounts of aggregated protein from left ventricle lysates of WT or KO mice 2d post TAC/sham (C) Chymotrypsin-like 26S proteasomal activity of WT or fullKO MEF lysates. ***P < 0.001, two-tailed student's t-test. Proteostat assay by Mirko Völkers.

To test whether decreased proteasomal activity and elevated poly-ubiquitination goes along with aggregation of proteins, Mirko Völkers measured protein aggregation in heart lysates of KO versus WT mice 2d post TAC by performing the commercially available “Proteostat“ protein aggregation assay. He found slightly increased amounts of protein aggregates after TAC surgery in WT as well as KO samples, which is in line with deteriorated proteasomal activity. In KO mice, protein aggregation was higher in both sham and TAC animals compared to their WT controls (Fig. 6.14B).

To further evaluate the function and activity of the 26S proteasome in WT versus KO cells, I measured 26S Chymotrypsin-like proteasomal activity of KO and WT MEFs *in vitro*. Strikingly, I saw chymotrypsin-like activity significantly reduced by 50% in KO MEFs compared to their WT controls (Fig. 6.14C).

All together, I hypothesize that Pras40 is indispensable to maintain proper proteasomal function *in vivo* and *in vitro*.

6.4.3 Re-activation of proteasome activity after TAC in Pras40 KO

After finding the function of the 26S proteasome deteriorated upon deletion of Pras40, I aimed at testing whether re-activation of protein degradation by the UPS has beneficial effects on the cardiac phenotype of Pras40 KO mice after TAC.

To enhance proteasomal activity, I used virus encoding for the proteasomal activator PA28 α under the control of the cardiomyocyte-specific promotor α MHC, that was generated by Verena Kamuf-Schenk. PA28 α overexpression was found to specifically induce chymotrypsin-like 26S proteasomal activity in a previously published study (Li et al., 2011). I first tested the reactivation of chymotrypsin-like proteasomal function *in vitro* by transducing KO MEFs with adenovirus encoding for PA28 α or a control virus. I saw chymotrypsin-like 26S proteasomal activity enhanced by 1.7-fold after transducing KO MEFs with Adeno-PA28 α for 24h (Fig.6.15A). I then delivered cardiomyocyte-specific PA28 α adeno-associated virus serotype 9 (in the following named PA28 α) to Pras40 cKO mice by tail vein injection at the age of 8 weeks. Control AAV9-injected WT and KO mice served as control groups. Two weeks after virus delivery, I subjected

animals to TAC versus sham surgery and followed them for 4 weeks. Function was then measured by echocardiography and organs were isolated for protein and RNA isolation (Fig. 6.15B). I validated elevated expression of *Pa28α* transcript by qRT-PCR (Fig. 6.15C).

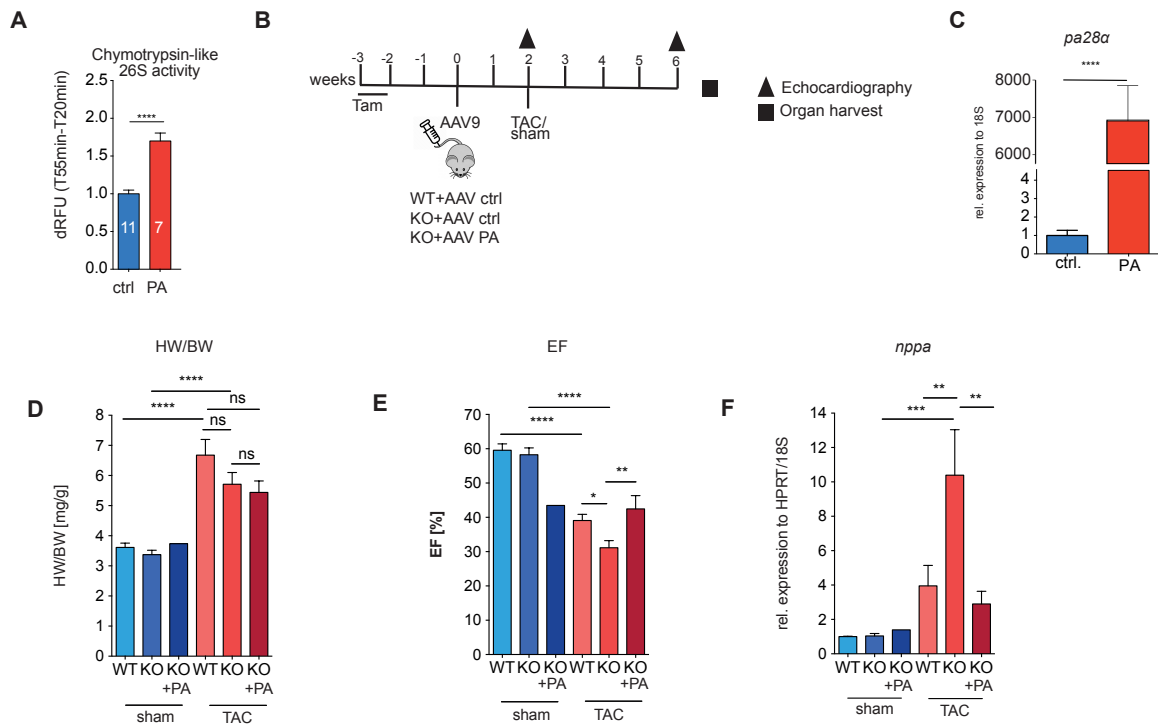


Figure 6.15: Reactivation of proteasomal activity rescues severe phenotype of TAC-subjected Pras40 KO mice. (A) Chymotrypsin-like 26S proteasomal activity of fullKO MEFs treated with Proteasomal activator PA28α adenovirus (PA) or control adenovirus. (ctrl.) ***P < 0.001, two-tailed student's t-test (B) Scheme of experimental setup for AAV9 delivery and TAC surgery. (C) Validation of PA28α transcript levels in PA28α/control treated left ventricle lysates by qRT-PCR. ***P < 0.001, two-tailed student's t-test. (D) Left ventricle to body weight ratios (LV/BW) of virus treated, TAC subjected animals 4 weeks post TAC. *P < 0.05, **P < 0.01, by one-way ANOVA followed by Bonferroni's post-hoc comparisons. (E) Ejection fraction (EF) of PA28α- or control AAV9 treated and TAC/sham subjected mice 4 weeks post TAC. *P < 0.05, by one-way ANOVA followed by Bonferroni's post-hoc comparisons. (F) qRT-PCR measurements of *nppa* from left ventricles 4 weeks post TAC/sham. *P < 0.05, by one-way ANOVA followed by Bonferroni's post-hoc comparisons. Analysis of echocardiographic measurements by Mirko Völkers.

HW/BW ratios 4 weeks after surgery revealed that PA28α does not affect the basal heart weight in PA28α cKO sham animals compared to ctrl. cKO sham animals or ctrl. WT sham animals. As observed before (compare section 6.2), ctrl. WT hearts had grown

significantly after TAC (+46% HW/BW, to WT sham), and growth was blunted in ctrl. cKO hearts (+ 41% HW/BW, to cKO sham). Increase in HW/BW ratios in PA28 α cKO TAC mice was smaller than in both control groups (HW/BW +32%, to PA28 α cKO sham) (Fig. 6.15D). This phenotype could either originate from the typical inability of Pras40 KO hearts to adapt to the pathological stimulus but could also be a beneficial effect of PA28 α overexpression.

Heart function was significantly decreased in WT mice after TAC, and this effect was even bigger in KO ctrl. mice, as expected. After delivery of PA28 α , I saw a significant rescue of heart function in cKO TAC mice, since EFs of PA28 α cKO TAC hearts were significantly higher than in ctrl. cKO TAC mice (42% to 31%, Fig. 6.15E), and even slightly higher than in WT mice (42% to 39%). This result indicates that re-activation of the proteasome can rescue heart function significantly and can counteract the inability of cKO mice to adapt to pathological stress. This finding was underlined by levels of the fetal marker gene *nppa*, that were significantly reduced in PA28 α cKO TAC mice compared to the ctrl. cKO TAC group (Fig. 6.15F): Levels of *nppa* in PA28 α cKO TAC mice were restored to levels in ctrl. WT TAC mice. The remodeling process in cKO mice therefore seems clearly reduced after reactivation of 26S proteasomal activity.

All in all, reactivation of 26S proteasomal activity has a beneficial effect to the outcome of cardiac hypertrophy in Pras40 KO mice, suggesting that perturbation of proteasomal function is causal for the severe phenotype in Pras40 KO hearts.

6.5 Analysis of mTOR-Pras40 interaction during pathological hypertrophy

The adverse effect of Pras40 deletion and overexpression in the present and the previous study (Volkers et al., 2013) raised the question if there are other unknown mechanisms that Pras40 is involved in. Most of the phenotypic effects that I observed in the experiments described above were strongest after the induction of hypertrophy: Heart weight as well as cardiac function but also proteasomal activity *in vivo* was most affected after TAC or swimming. During growth, when mTOR is activated, Pras40 is known to be

released from the mTORC1 (Sancak et al., 2007; Wang et al., 2007) an effect that has also been observed during cardiac hypertrophy (Volkers et al., 2013). I therefore aimed at specifically studying mTOR-released Pras40 and its effect on cardiac growth and function, as well as proteasomal function.

A previous test experiment in our lab performed by Mirko Völkers compared the interaction between mTOR and Pras40 in sections of sham versus TAC operated WT hearts. In a proximity ligation assay, binding of Pras40 to mTOR was only observed in sham treated animals, but not after TAC, as expected (Fig. 6.16A). An additional experiment by Christoph Hofmann tested the interaction *in vitro* by treating NRVCMs with Phenylephrine to induce a pathological stimulus. PE- versus untreated NRVCMs were used for immunoprecipitation of mTOR and Western blot analysis to quantify amounts of precipitated mTOR and co-precipitated Pras40. In line with the *in vivo* data, Pras40 was found to bind 35% less mTOR after PE treatment compared to the untreated condition (Fig. 6.16B).

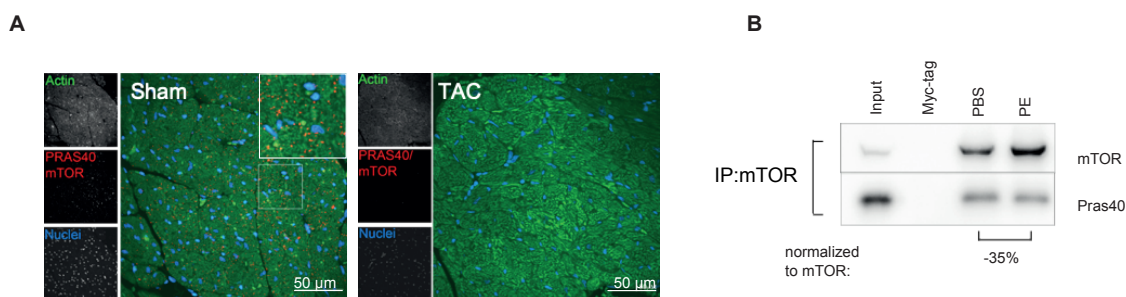


Figure 6.16: Pras40 binds mTOR in homeostasis but is released from mTOR during pathological growth *in vivo* and *in vitro*. (A) Proximity ligation assay to detect interaction between Pras40 and mTOR in histological sections of TAC or sham subjected WT heart. (B) Western blot of immunoprecipitation of mTOR and co-precipitation of Pras40 during homeostasis (PBS as vehicle) and growth (PE treatment) in NRVCMs. Myc-tag as negative control IP. Proximity ligation assay performed by Mirko Völkers, IP and blot performed by Christoph Hofmann.

6.5.1 Effects of mTOR-released Pras40 on mTOR signaling and UPS abundance

To further study the role of mTOR-released Pras40, adeno- and adeno-associated virus, that encodes for a mutant form of Pras40, was generated by Verena Kamuf-Schenk in our

laboratory. These viruses encode for a mutant form of Pras40 which carries 4 mutations (L215A, I218A, A219G, L225A) in the C-terminal region of the protein that interacts with the FKBP-rapamycin-binding (FRB) site of mTOR (Fig. 6.17A). Yang et al. (2017) have previously shown that these mutations lead to reduced inhibition of mTORC1 and an increase of 4EBP1 phosphorylation by a factor of ~50. To validate that Pras40-FRB (in the following abbreviated as FRB) is released from mTOR and does not inhibit mTORC1, I transduced Pras40 KO MEFs with Pras40 WT and FRB Adenovirus to precipitate both proteins by their flag tag. Mild lysis and washing conditions prevented the disintegration of the mTORC1. Co-precipitated mTOR was detected by Western blot and levels of mTOR were quantified normalized to the amounts of precipitated Pras40 (Fig. 6.17B). As expected, I saw 82% less mTOR binding for FRB compared to the WT protein.

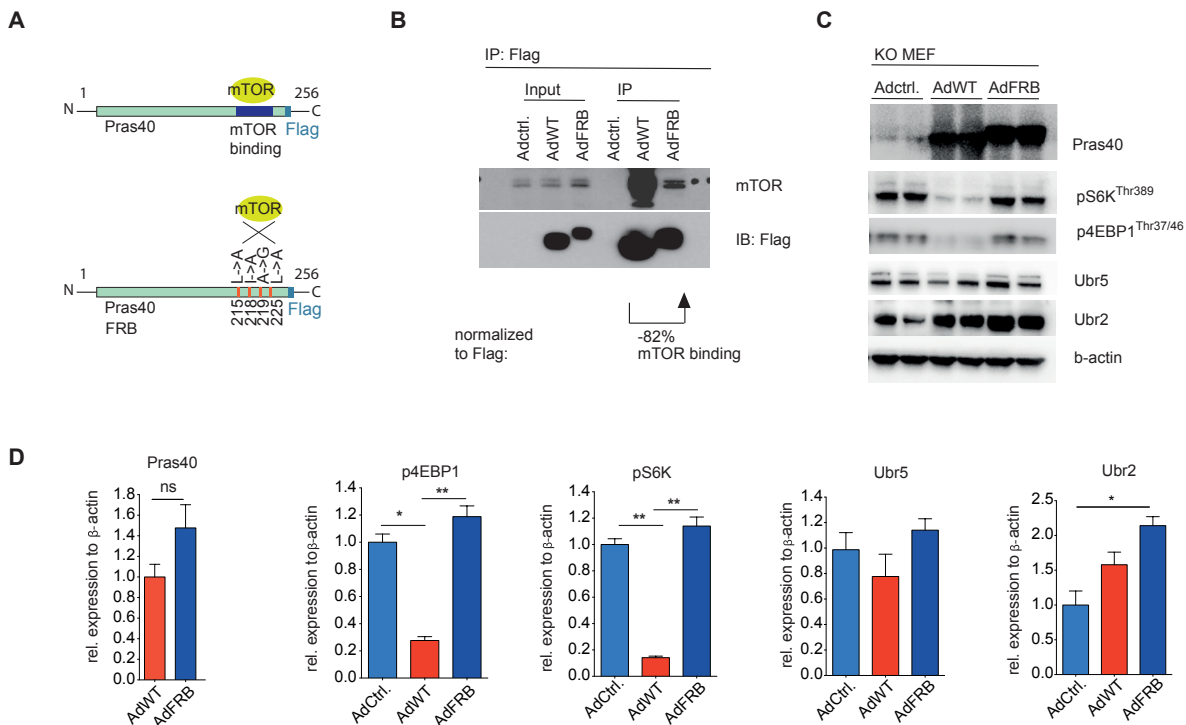


Figure 6.17: Mutant Pras40 without mTOR-interacting FRB domain is released from mTOR and does not inhibit mTOR downstream signaling. (A) Scheme of WT Pras40 and mutant, that lacks specific C-terminal region, which interacts with FRB domain of mTOR protein. (B) Western blot of immunoprecipitation of Flag (viral Pras40) and co-precipitation of mTOR in fullKO MEFs. (C) Western blot analysis of KO MEFs transduced with WT or FRB adenovirus for 24h. (D) Quantification of two biological replicates of the experiment shown in (C). *P < 0.05, **P < 0.01, by one-way ANOVA followed by Bonferroni's post-hoc comparisons.

I further determined the effects of FRB versus WT Pras40 to the mTOR signaling cascade by performing Western blot analysis of FRB or WT transduced KO MEFs. KO MEFs transduced with control virus served as control. Amounts of both Pras40 viruses had been adjusted for proper comparison and showed no significant difference in protein levels (Fig. 6.17D, left panel). Overexpression of WT Pras40 significantly inhibited the activation of mTOR and lead to significantly decreased levels of p-4EBP1 (-76%) and p-S6K (-86%), as expected. In FRB transduced MEFs, this inhibitory effect was completely lost, and levels of p-4EBP1 and p-S6K were not significantly different to those of ctrl. KO MEFs (Fig. 6.17C, Quantification in D). Interestingly, transduction with both WT or FRB virus was able to increase the amounts of Ubr2 and Ubr5 protein. Decreased mTOR binding and inhibition showed that FRB could be used for future experiments as a model of mTOR-independent Pras40.

6.5.2 Effects of mTOR-bound versus -released Pras40 to 26S proteasomal function

To dissect, whether there is a difference between mTOR-released or mTOR-bound Pras40 for restoring proteasomal function, I measured chymotrypsin-like 26S proteasomal activity in KO MEFs that had been transduced with FRB or WT Adenovirus versus a control virus. Transduction with FRB was able to raise the 26S chymotrypsin-like activity to 1.7-fold (Fig. 6.18A), compared to ctrl. transduced MEFs. Strikingly, WT virus did not change proteasomal activity compared to ctrl. transduced MEFs. An activation of proteasomal activity is therefore only possible with mTOR-released Pras40. I therefore hypothesized that Pras40 crucially effects the function of the 26S proteasome when released from mTORC1.

6.5.3 Heart function upon overexpression of mTOR-released Pras40 after TAC

After having shown that proteasomal activation had a beneficial effect on the outcome of the remodeling process in Pras40 KO mice, and that mTOR-released Pras40 can rescue proteasomal function, I hypothesized that FRB overexpression would be able to alleviate the severe phenotype of Pras40 KO mice after TAC. I therefore overexpressed Pras40-

FRB in cKO and WT mice by tail vein injection of AAV9 at 8 weeks of age. WT and cKO littermates injected with ctrl. AAV9 served as controls. I then subjected mice to TAC or sham surgery two weeks after AAV9 delivery. Echocardiography and organ isolation was performed 4 weeks after TAC/sham (Fig.6.18B). I validated the expression of FRB by qRT-PCR and by Western blot analysis (Fig. 6.18C).

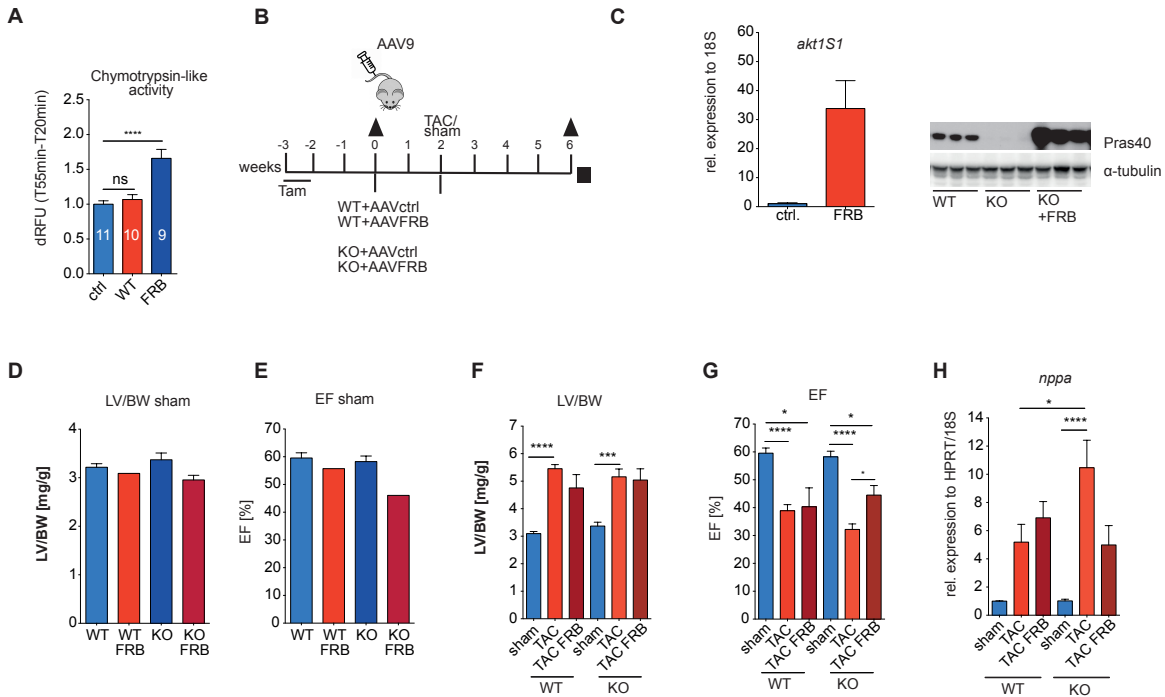


Figure 6.18: Reactivation of proteasomal activity by Pras40-FRB rescues severe phenotype of TAC-subjected Pras40 KO mice. (A) Chymotrypsin-like 26S proteasomal activity of fullKO MEFs treated with Pras40 WT, FRB or control adenovirus. ****P < 0.0001, by one-way ANOVA followed by Bonferroni's post-hoc comparisons. (B) Scheme of experimental setup for AAV9 delivery and TAC surgery. (C) Validation of FRB transcript and protein levels in FRB/control treated mice by qRT-PCR with *Akt1S1* (Pras40 gene) primers or Western blot (D) Left ventricle to body weight ratios (LV/BW) of sham treated WT or cKO mice with FRB- or control AAV9. (E) Ejection fraction (EF) of sham treated WT or cKO mice with FRB- or control AAV9 (F) Left ventricle to body weight ratios (LV/BW) of virus treated animals 4 weeks post TAC. (G) Ejection fraction (EF) of WT or cKO mice with FRB- or control AAV9 4 weeks post sham/TAC. (H) qRT-PCR of *nppb* from left ventricles 4 weeks post sham/TAC. Analysis of echocardiographic measurements by Mirko Völkers.

To evaluate an effect of FRB overexpression to heart size and function basally, I first compared FRB and ctrl. treated WT and cKO sham animals. LV/BW ratios did not differ in any of the sham groups (Fig. 6.18D). Heart function (EF) was not significantly

affected by FRB overexpression in both WT and cKO sham mice (Fig. 6.18E). 4 weeks after TAC surgery, HW/BW ratios had significantly increased in all TAC groups compared to their sham controls but there was no significant difference between FRB or ctrl. TAC groups, neither for WT or cKO mice. (Figure 6.18F, for all sham groups see Fig. 6.18D).

EF was decreased after TAC in both WT groups (FRB or ctrl virus) to a similar extent, a rescue of cardiac function after delivery of FRB in WT TAC mice was therefore not observed. In FRB cKO TAC mice compared to their respective ctrl TAC group, function was significantly elevated (Fig 6.18G for all sham groups see Fig. 6.18E). Heart function in FRB cKO mice TAC mice was even slightly higher than in FRB WT or ctrl. WT TAC mice. A functional rescue of cKO TAC mice by overexpression of mTOR-released Pras40 was therefore successful. In line with this, the fetal marker *nppb* was significantly reduced in FRB cKO TAC mice compared to ctrl. cKO TACs (Fig. 6.18H). Levels of *nppb* were decreased to levels similar to WT TAC mice. Interestingly, the most beneficial effect to heart function was observed by FRB alone in cKO mice, rather than in WT mice which also express endogenous Pras40. First Western blot data of left ventricular lysates of this experiment can be found in supplementary figure 8, and suggest that differences between WT and Ko animals in the activity of mTOR (measured by amounts of p-4EBP1) as well the expression of Ubrs, that are found in sham animals, are lost by the overexpression of FRB virus in WT versus KO TAC animals.

7. DISCUSSION II

While the role of mTOR on growth or proliferation has been well studied before, the role of Pras40 is not completely clear. mTOR-bound Pras40 is known to inhibit mTOR activity by competitive binding at mTOR downstream target sites (Sancak et al., 2007; Wang et al., 2007). Phosphorylation of Pras40 leads to release from mTOR and mTOR activation, a mechanism that was shown in different types of cells and organisms, mainly during cancer growth and progression (Lv et al., 2017). The role of Pras40 independent of mTOR has not been fully understood so far.

In the heart, it is known that mTOR is activated during both physiological and pathological cardiac hypertrophy (Sciarretta et al., 2014). Inhibition of mTORC1 has beneficial effects on the outcome of pathological cardiac hypertrophy and the pharmacological mTOR inhibitor Rapamycin improves cardiac function in murine cardiomyopathy models (McMullen et al., 2004). Chronic administration of Rapamycin leads to severe off-target and side effects and does not allow its use as anti-hypertrophic drug. Genetic inhibition of mTOR would therefore be a novel therapeutic option to selectively inhibit mTORC1 in the heart and ameliorate cardiac function. A previous study in the heart (Volkers et al., 2013) has suggested Pras40 as potential gene therapy approach. The authors were able to show that overexpression Pras40 is sufficient to bind to and inhibit mTOR and prevent the onset and progression of pathological cardiac hypertrophy. As in previous studies in other organisms and cell types, full understanding of mTOR-released Pras40 in the heart remains elusive, and prevents its clinical use as a tool for gene therapy.

In the current study, I characterized Pras40-depleted hearts and find cardiac function severely disturbed. Pras40 KO hearts are unable to grow and in line with this show mitigated mTOR activity and lower levels of overall translation. Together with differential abundance of UPS-related genes, proteasomal function of Pras40 deleted mice is deteriorated, an effect that is causal for the severe cardiac phenotype in Pras40-depleted mice. mTOR-released Pras40 is able to rescue function in Pras40 KO mice.

7.1 Pras40- the role in cardiac hypertrophy and state of the art

Pras40 has initially been identified as a substrate of Akt downstream of the phosphatidylinositol 3-kinase pathway (Kovacina et al., 2003), before immunoprecipitates of mTORC1 revealed Pras40 as component and substrate of mTORC1 (Oshiro et al., 2007). Binding of Pras40 to Raptor was then found to be inhibitory to the activity of mTORC1 and the phosphorylation of mTORC1 downstream targets *in vitro* (Sancak et al., 2007). An mTORC1-inhibiting role of Pras40 in the heart has been found *in vitro* and *in vivo* in a model of cardiac hypertrophy (Volkers et al., 2013). In the latter study, Pras40 was found highly expressed in cardiomyocytes. After insulin stimulation, the authors saw Pras40 phosphorylated at Thr²⁴⁷ and its binding affinity to Raptor and mTOR weakened. The inhibitory effect of Pras40 onto mTORC1 was shown to be lost by phosphorylation of Pras40 at Thr²⁴⁷ and Ser¹⁸³ by mTORC1 early after a hypertrophic stimulus (TAC surgery). Völkers et al. (2013) hypothesized that with its inhibitory effect onto mTOR, Pras40 overexpression might rescue the function and remodeling process after TAC. Indeed, in their study, tail vein delivery of Pras40 by adeno-associated virus before TAC surgery was able to significantly ameliorate the outcome of pathological growth and contractility. Even when delivered after TAC, Pras40 was able to stabilize the remodeling process and prevented heart failure. A similar inhibitory effect of Pras40 overexpression onto pathological growth was observed *in vitro* in NRVCs treated with Phenylephrine. In the same study, physiological growth was not affected by overexpression of Pras40 and this phenomenon was explained by an alternative signaling pathway, by which Akt phosphorylates Pras40 at Thr²⁴⁷, releasing Pras40 from mTORC1. Insulin-sensitive PI3K-Akt signaling has been shown to weaken the inhibitory effect of Pras40 by phosphorylation at Thr²⁴⁷ before (Sancak et al., 2007). Despite the insights made for cardiac phenotype after Pras40 overexpression, further understanding of the molecular mechanisms of Pras40 is needed to test it as a potential gene therapy option to prevent cardiac failure. For complete understanding of the mechanism of Pras40, the effects of Pras40 depletion have to be studied as well. The first *in vivo* study, which investigated the role of Pras40 by knocking down the protein was

performed in drosophila (Pallares-Cartes et al., 2012). Pallares-Cartes et al. (2012) surprisingly found Pras40 KO mutants to be viable and normal sized. This stands in contrast to mutants of other mTOR regulators, such as TSC1, TSC2 or Rheb, which are known to be lethal. In their study, the authors show that Pras40 KO does not affect growth during development, and in the fly, Pras40 KO positively affects the activity of mTOR and links insulin/IGF signaling and mTOR in the ovaries but not other body parts of the flies. A second *in vivo* study of Pras40 depletion was performed in a model of cerebral ischemia with global Pras40 KO mice (Xiong et al., 2014). The authors found increased infarct size in Pras40 depleted animals, going along with decreased mTOR activity and mTOR downstream signaling, but unaffected Akt signaling. These two studies (Pallares-Cartes et al., 2012; Xiong et al., 2014) highlight that the effect of Pras40 depletion to the activity of mTOR seems to be highly dependent on the model organism and is also tissue-specific. A previous study from our own laboratory has highlighted a beneficial role of Pras40 in the progression of arteriosclerosis in an endothelium-specific, tamoxifen-inducible PRAS40 deficiency mouse model, that was generated from stem cells with the same Pras40 deleted locus as in the current study (Zhang et al., 2019).

Cardiomyocyte-specific knock-out animal models were not at hand to date and prohibited complete understanding of the mechanism of Pras40 in the mammalian myocardium. The cardiac phenotype of Pras40 depleted mice was therefore unknown. The aim of the present study was therefore the detailed phenotypic analysis of the newly generated KO mouse model and a further mechanistic understanding how Pras40 regulates cardiac hypertrophy. The validation of two novel Pras40 KO mouse models- a global deletion (different to the model used by Xiong et al., 2013, which deletes exons 2-5) and an inducible and cardiomyocyte-specific depletion was successful. The present study is therefore the first one to study the role of Pras40 *in vivo* in a cardiomyocyte-specific, inducible KO model. Similar to the drosophila model (Pallares-Cartes et al., 2012), both mouse models were viable and did not show basal growth defects or affected body size. An observation that I made during breeding of the mice was a slightly reduced number of pregnancies, that I didn't follow up on. With the previous study from Pallares-Cartes et

al. (2012) it might be interesting to study whether similar to the fly, this comes from a role of Pras40 in the ovaries in the mouse as well.

7.2 Loss of Pras40 leads to unexpected inhibition of cardiac growth and loss of cardiac function upon hypertrophic stimuli

With the previous findings by Völkers et al. (2013) and knowing Pras40 as an inhibitor of cellular growth, I initially hypothesized that deletion of Pras40 might lead to strongly increased pathological growth and remodeling after TAC surgery. Decreased heart weight to body weight ratios and blunted cardiomyocyte and left ventricular growth in Pras40 KO mouse during both pathological and physiological hypertrophy challenged this assumption. Even though many studies have shown the inhibitory role of Pras40 to mTOR, parallel evidence to our growth phenotype has been made before: In models of tumor growth, depletion of Pras40 was linked to reduction of tumor growth and reduced development of malignant melanoma and Ewing sarcoma (Huang et al., 2012; Madhunapantula et al., 2007). The study by Huang et al. (2012) suggests that reduction of Pras40 makes cells more responsive to apoptosis signaling, and therefore slows down cancer progression. A similar link between downregulation of Pras40 and enhanced apoptosis was made by Wang and Huang (2009), who link decreased drosophila Pras40 homologue “Lobe“ to increased apoptosis signaling. Alongside my cell and heart size measurements, analysis of apoptosis levels in Pras40 KO mice should therefore be performed in future experiments. Loss of cells due to apoptosis might be one factor that through reduction of cardiomyocyte numbers leads to reduced heart weights in TAC-treated KO hearts. I found a first hint to altered apoptosis in Pras40 KO mice in RiboSeq data from Pras40 KO mice subjected to physiological hypertrophy (swimming): A first analysis and gene ontology of these data show an enrichment of apoptosis-related biological processes after swimming in Pras40 KO mice (Suppl. figure 7). As a state-of-the-art regime to induce physiological growth, swimming is typically not linked to remodeling of the ventricle, but to elevated or maintained cardiac function (Evangelista et al., 2003). In contrast, the phenotype of Pras40 KO mice subjected to swimming in the

present study was accompanied by increased fetal markers and loss of contractile function, resembling the phenotype after induction of pathological hypertrophy. This emphasized the inability of Pras40 KO mice to adapt to even milder forms of stress. Blunted growth is therefore clearly not linked to a beneficial effect, but reflects a severe liability to compensate elevated work loads in the heart. In both the physiological regime as well as after TAC, amounts of apoptosis should therefore be measured in detail in addition to contractility, growth and remodeling markers.

7.3 Lack of Pras40 in the heart leads to attenuated mTOR activity and translation

To understand the molecular peculiarities that go along with the severe phenotype of Pras40-depleted hearts and the mitigated growth response, I aimed at analyzing the activation of the mTOR signaling cascade. Elevated mTOR activity has been linked to cardiomyopathies but also to various diseases, above all cancer (Laplante and Sabatini, 2012). In turn, mTORC1 inhibition leads to a beneficial reduction of cardiac growth (Marin et al., 2011) and Pras40 has previously been linked to beneficial inhibition of mTORC1 and restored cardiac function (Volkers et al., 2013). Knowing Pras40 as a classical inhibitor of mTOR signaling, I had initially expected that deletion of Pras40 together with elevated growth would lead to increased mTOR activity. Instead, in Pras40-depleted KO cardiomyocytes and hearts I found levels of phosphorylated mTORC1 downstream targets (directly correlating with mTOR activity) being mitigated. Pras40 overexpression and deletion thus do not lead to mirrored signaling cascades in the myocardium. Together with the functional data, mitigation of mTOR activity in the present study does not have a beneficial effect, as it has been suggested before (Marin et al., 2011, Volkers et al., 2013). A completely unknown function of Pras40 apart from mTOR inhibition is therefore likely. An unclear interplay between levels of Pras40 and mTORC1 activation *in vitro* has been discussed before. Two first studies *in vitro* in HEK293T and HEK293E cells, respectively, showed that silencing of Pras40 leads to loss of Akt phosphorylation upstream of mTORC1, but enhanced phosphorylation of S6K and activity of mTORC1. These studies presented Pras40 as a member of mTORC1

and upstream negative regulator of the complex (Haar et al., 2007; Sancak et al., 2007). Enhanced phosphorylation of S6K is complementary to the present data. Two other studies in HEK293 cells are in line with the present data and showed that silencing of Pras40 leads to impairment of both the amino acid- and insulin-stimulated phosphorylation of 4E-BP1 and the phosphorylation of ribS6. In contrast to the earlier studies (Haar et al., 2007; Sancak et al., 2007), the authors did not see an effect on the phosphorylation of Akt (Fonseca et al., 2007; Oshiro et al., 2007) and therefore suggest that Pras40 acts downstream of mTORC1. Fonseca et al. (2007) argue that their model system, HEK293 cells, is more suitable to study mTOR signaling in homeostasis, since these cells in contrast to HEK293T cells don't show basal mTOR activation. Several studies that observed decreased phosphorylation of mTORC1 downstream target S6K after silencing Pras40 in skeletal muscle cells, malignant melanoma and Ewing sarcoma are in line with my present data as well (Wiza et al., 2013, Madhunapantula et al., 2007, Huang et al., 2012). *In vivo*, Xiong et al. (2014) observed decreased activity of mTOR when Pras40 is deleted, additionally supporting the phenotype that I observed. In that study, like Fonseca et al. (2007) and Oshiro et al. (2007), the authors observed no effect of Pras40 KO on Akt signaling. Also for the drosophila Pras40 homologue “Lobe“, decreased amounts of the protein were connected to hypoactivation of mTOR by Wang and Huang (2009), whereas Pallares-Cartes et al. (2012) observed increased mTOR activity after Pras40 KO, but only in ovaries. In the heart, mitigation of mTOR signaling after knock-out or knock-down of Pras40 was completely unknown before the current study.

All together it seems that the specific cellular model system, as well as the exact experimental setup can lead to drastic differences in the regulation of the mTOR signaling cascade. The study by Wiza et al. (2013) which was performed in skeletal muscle cells -the cellular model system that resembles cardiac muscle cells the closest- is in line with my results. In the present study as well as in theirs, the phosphorylation of S6K was effected to a higher extent by depleting Pras40, compared to phosphorylation of

4EBP1. Also, the temporal aspect of the Pras40 knock out or knock down (rather acute or chronic) might play a crucial role in the outcome of the signaling cascade.

In addition to studying the effects of Pras40 KO to the mTOR cascade and its downstream targets, a detailed analysis of the Akt pathway should be additionally performed, as it has been done previously in other cell types (Xiong et al., 2014; Fonseca et al. 2007, Oshiro et al., Haar et al., 2007; Sancak et al., 2007). While Xiong et al. (2014), Fonseca et al. (2007) and Oshiro et al. (2007) did not see an effect of Pras40 KO to Akt signaling, Haar et al. (2007) and Sancak et al. (2007) observed a reduction of Akt phosphorylation upon depletion of Pras40. Reduced Akt phosphorylation leads to suppression of the Akt signaling cascade, inhibition of TSC2 and higher mTORC1 activity. My data showed that inhibition of TSC2 restores the activity of mTOR in Pras40 KO cells to levels measured in WT cells. A possible upstream mechanism of Pras40 to the phosphorylation of Akt, and therefore to the activity of mTOR could explain why mTOR activity is mitigated in Pras40 depleted cells. The role of the different upstream pathways is therefore of major interest and should be addressed in future experiments.

7.4 Possible causes for mitigated mTOR activity in Pras40 KO

Several possible mechanisms are conceivable for the mitigated mTOR activity when Pras40 is depleted. As Pras40 binds to the mTOR kinase through the scaffolding protein Raptor and when released from mTOR binds to the scaffolding 14-3-3 protein, one possible explanation for deteriorated mTOR activity would be an indispensable role of Pras40 for the stability or assembly of the mTOR complex. Previous data (Fonseca et al., 2007) showed a small, but reproducible reduction of Raptor/mTOR ratios after Pras40 RNAi KD, when co-precipitating the complex, but the authors rated these data as minor effect. Still, measuring ratios of Raptor to mTOR in our Pras40 KO mice might bring new insight into a scaffolding role of Pras40 to the mTOR complex.

Another explanation for mitigated mTOR signaling would be an effect of Pras40 to the expression of the mTOR kinase, or its complex components, and therefore less activation of mTOR downstream targets. Indeed, I find levels of mTOR decreased in Pras40 KO

versus WT cells. A similar decrease of mTOR protein was found in KO mice after TAC surgery. Expressional changes of mTOR and Raptor in Pras40 KD HEK 293 cells have been investigated before and were unchanged in this cell type (Fonseca et al., 2007). Since in their study Pras40 KD also lead to higher mTOR activity, their overall results vary significantly from ours and might be cell-type specific. For a more detailed analysis of mTOR and Raptor expression levels apart from the Western blot analysis, I searched our RiboSeq data of Pras40 KO versus WT mice again and found amounts of mTOR and also Raptor decreased by -0.6 fold for both proteins. Downregulation of mTOR and Raptor was therefore reproducible by different methods. A connection between differential expression levels of these mTOR complex proteins and the activation of downstream targets could in future experiments be validated by modulating mTOR or Raptor levels in vitro and measuring the effects on mTOR downstream targets.

The present RiboSeq data revealed that several components of the Ubiquitin-proteasome system, as well as members of the translation initiation machinery are translated at lower levels after depletion of Pras40. When performing gene ontology analysis on the translationally regulated hits, interestingly, several ubiquitin ligases were overlapping for both biological processes “proteasome regulation“ as well as “regulation of mTOR“. A number of studies have linked ubiquitin ligases to negative regulation of mTOR before: Herc1, one of the DEGs found in the present RiboSeq data, is known to interact with TSC2, leading to destabilizing of the TSC1/TSC2 complex and therefore to loss of TSC2-mediated mTORC1 inhibition (Chong-Kopera et al., 2006). Lower levels of Herc1, as I see them in our Pras40 KO data, might therefore cause decreased activity of mTOR. Similar findings were made for the ubiquitin ligase Ubr5, that I also found translated at lower levels in Pras40 KO mice. Ubr5 was found to be an important player in skeletal muscle anabolism and hypertrophy, and RNAi mediated knock down of Ubr5 resulted in muscular atrophy (Hughes et al., 2020). A more detailed validation of the translational regulation of these proteasome-related genes, and in further experiments the modulation of these genes by overexpression or knock down would be of interest to study the causality between downregulation of UPS-related genes and decreased

activation of mTOR in Pras40 depleted hearts or cells. Interestingly, Herc1 and Ubr5, but also most other differentially translated UPS-related genes are E3 ubiquitin ligases. E3 ubiquitin ligases recruit E2 ubiquitin-conjugating enzymes and assist or catalyze the transfer of ubiquitin from the E2 to the protein substrate. This ubiquitination step has the highest impact on the specificity of the UPS (Adegoke et al., 2019), as proteins involved in ubiquitin are hierarchically organized: While there are only two E1 ubiquitin activating enzymes and 35 E2 ubiquitin conjugating enzymes in human, there are hundreds of E3 ubiquitin ligases responsible for ubiquitination of a diversity of specific substrates (Chaugule and Walden, 2016). Many E3 ligases, including Cullin-RING ligases, that I also find regulated after depletion of Pras40, recognize their substrate only after phosphorylation. In a review, that analyzed the interplay between the two “super complexes“ mTOR and the proteasome, a link between the two machineries has been theoretically suggested before. (Adegoke et al., 2019). The fact that I saw both higher amounts of poly-ubiquitination in Pras40 KO versus WT mice but also lower ribosomal occupancy of specific E3 ligase transcripts in the RiboSeq might result from the fact that only specific E3 ligases are regulated by KO of Pras40, and this specificity was not visible with the antibody used in this study.

Proteasomal activity has previously been known to be transcriptionally controlled (Radhakrishnan et al., 2010; Steffen et al., 2010), but a more recent study stated that the abundance of proteasome components is primarily regulated through mRNA translation (Rousseau and Bertolotti, 2016). Together with changed abundance of UPS-related genes in our RiboSeq data, these data suggest that Pras40 might affect UPS-dependent proteolysis by regulating the abundance of UPS components.

7.5 Pras40 critically affects proteasomal function when released from mTOR, and re-activation of the proteasome restores function in Pras40 KO mice

Additionally to the changed abundance of UPS-related proteins, I find 26S proteasomal function disturbed when Pras40 is depleted. During pathological hypertrophy *in vivo*, proteasomal function is typically elevated (Depre et al., 2006), but is completely

unchanged in Pras40 KO hearts after TAC. *In vitro*, proteasomal activity is attenuated by half without Pras40. I was therefore able to link Pras40 to the regulation of proteasome activity in the heart, a link that has not been made before. One previous study in HEK293 cells supports my finding of a connection between Pras40 and the proteasome, even though this study did not perform functional assays: In this study, Pras40 was found as an interaction partner of several subunits of the 26S immunoproteasome, a proteasome with alternative b-subunits (Yun et al., 2016). Yun et al. found Pras40 binding to precursors of proteasomal b-subunits in HEK 293 cells. They observed a switch between starvation conditions, when Pras40 is bound to and inhibited by mTOR (and vice versa) and growth conditions, when Pras40 is released from mTORC1. Only after release from mTORC1, Pras40 interacted with proteasomal precursor b5t to then bind proteasome maturation protein (Pomp). Their study thus showed that the formation of 26S immunoproteasomes was promoted by activity of mTORC1 and inhibition of mTORC1 suppressed their formation. Rather than the regulation of proteasomal abundance, that I see affected by KO of Pras40, the authors show an effect of Pras40 on the assembly of the proteasome. Still, parallel to my present study, Yun et al. (2016) found Pras40 affecting the proteasome when released from mTOR. In my study as well, the effect of Pras40 to proteasomal function *in vivo* was biggest during hypertrophy, when Pras40 is released from TOR, and I was only able to rescue proteasomal function with mTOR-released, mutant Pras40. Strikingly, overexpression of WT Pras40 was not able to rescue levels of proteasomal activity *in vitro*. In line with this, *in vivo*, overexpression of mTOR- released Pras40 alone restores function and growth in Pras40 KO mice. The proteasome-promoting role of Pras40 in the present as well as the previous study by Yun et al. (2016) therefore seems to be exerted once Pras40 is released from mTORC1. I therefore hypothesize that Pras40 acts as a molecular switch between mTORC1, which it inhibits in conditions of starvation or homeostasis, and the proteasome, which it regulates during hypertrophic conditions. Similar functional studies on the activity of the proteasome were not made by Yun et al., but the authors hypothesize that the assembly of the I-proteasome by Pras40 might help to maintain proteostasis during cellular growth. The

present study supports this assumption since I was able to show perturbed proteostasis and lower proteasomal activity without Pras40. I was also able to show that the perturbation of proteasomal activity after loss of Pras40 is causal for the severe inability to adapt to elevated stress in the heart.

7.6 The interplay between mTORC1 and the proteasome

Even though a functional link between Pras40 and both mTOR and the UPS has not been made before the current study, the UPS and mTOR as the two major complexes regulating proteostasis have been correlated in previous studies. The UPS is known to be activated under energy deprivation, when mTOR is inactive, whereas mTOR activation is closely correlated with high levels of growth factors or amino acids as well as insulin signaling. An opposite regulation of both complexes therefore seems likely, but according to several conflicting studies is an oversimplified assumption (Adegoke et al., 2019). Instead, conflicting reports have linked mTORC1 inhibition to increased degradation of long-lived proteins by the proteasome in combination with enhanced autophagy (Zhao et al., 2015) or a concerted action of mTORC1 and the UPS (Zhang et al., 2014). Zhang et al. performed a study in MEFs with genetically induced mTORC1 activation (TSC2 KD) or Rapamycin induced mTORC1 inhibition. Proteolysis by the UPS in their study was found to be enhanced when mTORC1 was activated. This study correlates with my results in a way that decreased activity of mTOR (in the present study after depletion of Pras40) is linked to decreased proteasomal abundance and activity. Increased proteasomal activity in their study (Zhang et al., 2014) has been correlated to higher proteasomal abundance and increased expression of proteasomal subunits and even though the UPS-related proteins in their and my study are not the same, an effect on the level of translation was found in both studies. Mechanistically, Zhang et al. (2014) explained proteasome subunit abundance by a transcriptional effect linked to NRF1. NRF1 has been demonstrated to induce the global expression of proteasomal subunit genes through direct binding of shared regulatory elements in their promoters. Levels of NRF1 were increased when mTORC1 was activated by TSC KD.

In contrast, Zhao et al. (2015) performed mTORC1 inhibition by both Torin or Rapamycin in HEK293 cells and saw it linked to an increased degradation of long-lived proteins. Unlike my present data, protein synthesis and degradation were not regulated in a concerted but rather an opposite manner. In their study, the proteasome and autophagy are activated in parallel and the UPS can independently of the lysosomal/autophagic proteolysis react to the inhibition of mTORC1. The authors also found enhanced proteolysis to be independent of mTORC1 downstream targets 4EBP1, S6K and Ulk1. Interestingly, control of proteolysis in their study was independent of changes in proteasomal activity but was regulated by enhanced ubiquitination of proteins after mTORC1 inhibition. Even though the correlation between mTOR and proteasomal activity in their study does not go along with the present findings, the regulation of ubiquitination also seems likely in our system, since the abundance of several E3 ubiquitin ligases is Pras40-dependent. In detail, Zhao et al. (2015) suggest the specific ubiquitination of growth related proteins, and even more specifically of a number of mTORC1 substrates. The fact that members of mTORC1 are targeted by the proteasome, has been shown before: Among these are the mTOR kinase itself, Deptor and Raptor (Bridges et al., 2017; Gao et al., 2011; Mao et al., 2008; Peterson et al., 2009; Zhao et al., 2011). Additionally, a number of upstream regulators of mTORC1 are regulated by ubiquitin-proteasomal degradation. (Adegoke et al., 2019). A study in Raptor depleted mice has shown decreased levels of mRNA expression of several E3 ubiquitin ligases (Bentzinger et al., 2008), which correlates closely with the present data.

Conceptually, Zhao et al. (2015) highlight the importance of proteolysis in energy-deprived conditions as necessary mechanism to provide amino acids for new protein synthesis and energy production. In contrast, Zhang et al. (2014) rather suggest that the activation of proteasomal abundance and activity as a quality control mechanism during enhanced levels of protein synthesis. Even though the results of the present study more closely resemble the results of Zhang et al. (2014), with concerted inhibition of mTORC1 and the proteasome, differential translation of genes involved in ubiquitination in our data conceptually resembles the study by Zhao et al. (2015). Some discrepancy in the

data might again originate from the different experimental set-up of experiments that either acutely induce mTORC1 inhibition or result in prolonged activation. The acute response to mTORC1 inhibition promotes proteolysis to restore free amino acid pools, prolonged mTORC1 activation leads to a compensatory increase in protein turnover to balance the increased rate of protein synthesis (Saxton and Sabatini, 2017).

7.8 Conclusion and outlook

The present study is the first to study the cardiac phenotype of a cardiomyocyte-specific Pras40 KO mouse model. In contrast to the phenotype after Pras40 overexpression (Volkers et al., 2013), cardiac growth is weakened upon deletion of Pras40, which was before known as a classical mTORC1 inhibitor. I was able to show that blunted hypertrophy is not an adaptive effect, but is clearly correlated to loss of function and enhanced pathological remodeling. This suggests a critical function of Pras40 to the adaptation of elevated stress in the heart, induced by either physiological or pathological stimuli. Deletion of Pras40 results in loss of 26S proteasomal function, suggesting a novel role of Pras40 for the regulation of the ubiquitin-proteasome system. I was able to show that this effect is causal for the severe phenotype of Pras40-depleted hearts, since reactivation of the proteasome rescued the severe phenotype. Moreover, I was able to specifically assign the activating effect to proteasomal function to mTOR-released Pras40, which was able to partially restore proteasomal function *in vitro* and *in vivo*. I therefore suggest a dual role for Pras40 as an inhibitor of mTOR during homeostasis or starvation and as an activator of proteasomal function during cardiac hypertrophy. This novel mechanism adds to the mechanistic understanding that is necessary to evaluate Pras40 as a potential gene therapy option.

Future experiments should be performed to understand how Pras40 and the proteasome are interconnected. A detailed analysis of regulated UPS genes upon deletion of Pras40, especially the translationally regulated E3 ubiquitin ligases, that are important regulators of substrate specificity during proteasomal degradation, should be performed. In addition to the current RiboSeq study, I have also prepared RiboSeq libraries for Pras40 KO

versus WT mice after TAC and swim. The analysis of these data will allow us a detailed picture of which RNAs are differentially translated during pathological and physiological hypertrophy. Since we observed the most significant differences in contractility and also proteasomal function *in vivo* during hypertrophy, these data will be of major interest. Adding to the Pras40 KO versus WT RiboSeq experiment, I prepared libraries from WT versus Pras40 overexpressing mice (by AAV9), that will add to the picture of which RNAs are differentially translated with or without Pras40 (Overview of all RiboSeq and the respective RNASeq analysis can be found in figure S7).

The analysis of mTOR-released Pras40 should be continued by an *in vivo* study, which directly compares WT and FRB AAV overexpression in Pras40 KO mice after TAC. Like this, a more accurate comparison of the rescuing effects of mTOR-released versus bound Pras40 will be possible. The generation of constitutively mTOR-binding Pras40 mutants in comparison to the currently used Pras40 mutant would also add more specificity to future experiments. Future *in vivo* studies should also include the detailed analysis of the mTOR downstream pathway after reactivation of the proteasome, as well as upstream signaling by Akt and levels of apoptosis. A first preliminary analysis of mTOR signaling after overexpression of FRB can be found in supplementary figure 8. Apart from the functional analysis of the proteasome and the abundance of actively translating UPS-related genes, a direct interaction between Pras40 and the proteasome has been suggested before (Yun et al., 2016). In a current study, that I have not included into this thesis, together with Moritz Kern I performed an interaction study by labeling proteins in close proximity to Pras40 (Apex2 method). Further validation and analysis of this study will give us more insight into direct interactions of Pras40 that have not been known before. We will specifically search our data for proteins of the UPS system, to see whether there are direct interactions with Pras40.

V. BIBLIOGRAPHY

- Adegoke, O.A.J., Beatty, B.E., Kimball, S.R., and Wing, S.S. (2019). Interactions of the super complexes: When mTORC1 meets the proteasome. *Int. J. Biochem. Cell Biol.* *117*, 105638.
- Allen, D.L., Harrison, B.C., Maass, A., Bell, M.L., Byrnes, W.C., and Leinwand, L.A. (2001). Cardiac and skeletal muscle adaptations to voluntary wheel running in the mouse. *J. Appl. Physiol.* *90*, 1900–1908.
- Baltz, A.G., Munschauer, M., Schwanhäusser, B., Vasile, A., Murakawa, Y., Schueler, M., Youngs, N., Penfold-Brown, D., Drew, K., Milek, M., et al. (2012). The mRNA-Bound Proteome and Its Global Occupancy Profile on Protein-Coding Transcripts. *Mol. Cell* *46*, 674–690.
- Beausoleil, S.A., Jedrychowski, M., Schwartz, D., Elias, J.E., Villén, J., Li, J., Cohn, M.A., Cantley, L.C., and Gygi, S.P. (2004). Large-scale characterization of HeLa cell nuclear phosphoproteins. *Proc. Natl. Acad. Sci. U. S. A.* *101*, 12130–12135.
- Beckmann, B.M., Horos, R., Fischer, B., Castello, A., Eichelbaum, K., Alleaume, A.M., Schwarzl, T., Curk, T., Foehr, S., Huber, W., et al. (2015). The RNA-binding proteomes from yeast to man harbour conserved enigmRBPs. *Nat. Commun.* *6*.
- Beckmann, B.M., Castello, A., and Medenbach, J. (2016). The expanding universe of ribonucleoproteins: of novel RNA-binding proteins and unconventional interactions. *Pflugers Arch. Eur. J. Physiol.* *468*, 1029–1040.
- Bentzinger, C.F., Romanino, K., Cloëtta, D., Lin, S., Mascarenhas, J.B., Oliveri, F., Xia, J., Casanova, E., Costa, C.F., Brink, M., et al. (2008). Skeletal Muscle-Specific Ablation of raptor, but Not of rictor, Causes Metabolic Changes and Results in Muscle Dystrophy. *Cell Metab.* *8*, 411–424.
- Berenji, K., Drazner, M.H., Rothermel, B.A., and Hill, J.A. (2005). Does load-induced ventricular hypertrophy progress to systolic heart failure? *Am. J. Physiol. - Hear. Circ. Physiol.* *289*, 8–16.
- Bergmann, O., Zdunek, S., Felker, A., Salehpour, M., Alkass, K., Bernard, S., Sjöström, S.L., Szewczykowska, M., Jackowska, T., Dos Remedios, C., et al. (2015). Dynamics of Cell Generation and Turnover in the Human Heart. *Cell* *161*, 1566–1575.

Bernardo, B.C., Weeks, K.L., Pretorius, L., and McMullen, J.R. (2010). Pharmacology & Therapeutics Molecular distinction between physiological and pathological cardiac hypertrophy: Experimental findings and therapeutic strategies. *Pharmacol. Ther.* *128*, 191–227.

Bleumink, G.S., Knetsch, A.M., Sturkenboom, M.C.J.M., Straus, S.M.J.M., Hofman, A., Deckers, J.W., Wittman, J.C.M., and Stricker, B.H.C. (2004). Quantifying the heart failure epidemic: Prevalence, incidence rate, lifetime risk and prognosis of heart failure - The Rotterdam Study. *Eur. Heart J.* *25*, 1614–1619.

Boucas, J., Fritz, C., Schmitt, A., Riabinska, A., Thelen, L., Peifer, M., Leeser, U., Nuernberg, P., Altmueller, J., Gaestel, M., et al. (2015). Label-free protein-RNA interactome analysis identifies khsrp signaling downstream of the p38/Mk2 kinase complex as a critical modulator of cell cycle progression. *PLoS One* *10*, 1–19.

Breckenridge, R. (2010). Heart failure and mouse models. *DMM Dis. Model. Mech.* *3*, 138–143.

Bridges, C.R., Tan, M.C., Premarathne, S., Nanayakkara, D., Bellette, B., Zencak, D., Domingo, D., Gecz, J., Murtaza, M., Jolly, L.A., et al. (2017). USP9X deubiquitylating enzyme maintains RAPTOR protein levels, mTORC1 signalling and proliferation in neural progenitors. *Sci. Rep.* *7*, 1–15.

De Bruin, R.G., Rabelink, T.J., Van Zonneveld, A.J., and Van Der Veer, E.P. (2017). Emerging roles for RNA-binding proteins as effectors and regulators of cardiovascular disease. *Eur. Heart J.* *38*, 1380–1388.

Bueno, O.F., Windt, L.J. De, Tymitz, K.M., Witt, S.A., Kimball, T.R., Klevitsky, R., Hewett, T.E., Jones, S.P., Lefer, D.J., Peng, C., et al. (2000). The MEK1 ± ERK1 / 2 signaling pathway promotes compensated cardiac hypertrophy in transgenic mice. *J. Biol. Chem.* *275*, 6341–6350.

Calderone, V., Gallego, J., Fernandez-Miranda, G., Garcia-Pras, E., Maillo, C., Berzigotti, A., Mejias, M., Bava, F.-A., Angulo-Urarte, A., Graupera, M., et al. (2016). Sequential Functions of CPEB1 and CPEB4 Regulate Pathologic Expression of Vascular Endothelial Growth Factor and Angiogenesis in Chronic Liver Disease. *Gastroenterology* *150*, 982-997.e30.

Carrier, L., Knöll, R., Vignier, N., Keller, D.I., Bausero, P., Prudhon, B., Isnard, R., Ambroisine, M.L., Fiszman, M., Ross, J., et al. (2004). Asymmetric septal hypertrophy in heterozygous cMyBP-C null mice. *Cardiovasc. Res.* *63*, 293–304.

- Castello, A., Fischer, B., Eichelbaum, K., Horos, R., Beckmann, B.M., Strein, C., Davey, N.E., Humphreys, D.T., Preiss, T., Steinmetz, L.M., et al. (2012). Insights into RNA Biology from an Atlas of Mammalian mRNA-Binding Proteins. *Cell* *149*, 1393–1406.
- Castello, A., Horos, R., Strein, C., Fischer, B., Eichelbaum, K., Steinmetz, L.M., Krijgsveld, J., and Hentze, M.W. (2013). System-wide identification of RNA-binding proteins by interactome capture. *Nat. Protoc.* *8*, 491–500.
- Castello, A., Fischer, B., Hentze, M.W., and Preiss, T. (2013). RNA-binding proteins in Mendelian disease. *Trends Genet.* *29*, 318–327.
- Castello, A., Hentze, M.W., and Preiss, T. (2015). Metabolic Enzymes Enjoying New Partnerships as RNA-Binding Proteins. *Trends Endocrinol. Metab.* *26*, 746–757.
- Chaugule, V.K., and Walden, H. (2016). Specificity and disease in the ubiquitin system. *Biochem. Soc. Trans.* *44*, 212–227.
- Chien, K.R., Zhu, H., Knowlton, K.U., Brien, T.X.O., and Evans, M. (1993). *Development.* *77–95.*
- Chong-Kopera, H., Inoki, K., Li, Y., Zhu, T., Garcia-Gonzalo, F.R., Rosa, J.L., and Guan, K.L. (2006). TSC1 stabilizes TSC2 by inhibiting the interaction between TSC2 and the HERC1 ubiquitin ligase. *J. Biol. Chem.* *281*, 8313–8316.
- Chothani, S., Schäfer, S., Adami, E., Viswanathan, S., Widjaja, A.A., Langley, S.R., Tan, J., Wang, M., Quaife, N.M., Jian Pua, C., et al. (2019). Widespread Translational Control of Fibrosis in the Human Heart by RNA-Binding Proteins. *Circulation* *140*, 937–951.
- Ciechanover, A. (2005). Proteolysis from the lysosome to. *Mol. Cell Biol.* *6*, 9.
- Cohn, J.N., Ferrari, R., and Sharpe, N. (2000). Cardiac remodeling-concepts and clinical implications: A consensus paper from an International Forum on Cardiac Remodeling. *J. Am. Coll. Cardiol.* *35*, 569–582.
- Davis, J., Salomonis, N., Ghearing, N., Lin, S.C.J., Kwong, J.Q., Mohan, A., Swanson, M.S., and Molkenin, J.D. (2015). MBNL1-mediated regulation of differentiation RNAs promotes myofibroblast transformation and the fibrotic response. *Nat. Commun.* *6*, 1–14.
- Day, D.A., and Tuite, M.F. (1998). Post-transcriptional gene regulatory mechanisms in eukaryotes: An overview. *J. Endocrinol.* *157*, 361–371.
- Daya, S., and Berns, K.I. (2008). Gene therapy using adeno-associated virus vectors. *Clin. Microbiol. Rev.* *21*, 583–593.

- deAlmeida, A.C., van Oort, R.J., and Wehrens, X.H.T. (2010). Transverse aortic constriction in mice. *J. Vis. Exp.* 7–9.
- Depre, C., Wang, Q., Yan, L., Hedhli, N., Peter, P., Chen, L., Hong, C., Hittinger, L., Ghaleh, B., Sadoshima, J., et al. (2006). Activation of the cardiac proteasome during pressure overload promotes ventricular hypertrophy. *Circulation* *114*, 1821–1828.
- Dickhuth, H.-H., Röcker, K., Mayer, F., König, D., and Korsten-Reck, U. (2004). Ausdauersport und kardiale Adaptation (Sporthertz). *Herz* *29*, 373–380.
- Dorn, G.W., and Force, T. (2005). Protein kinase cascades in the regulation of cardiac hypertrophy. *J. Clin. Invest.* *115*, 527–537.
- Doroudgar, S., Hofmann, C., Boileau, E., Malone, B., Riechert, E., Gorska, A.A., Jakobi, T., Sandmann, C., Jürgensen, L., Kmietczyk, V., et al. (2019). Monitoring cell-Type-specific gene expression using ribosome profiling in vivo during cardiac hemodynamic stress. *Circ. Res.* *125*, 431–448.
- Evangelista, F.S., Brum, P.C., and Krieger, J.E. (2003). Duration-controlled swimming exercise training induces cardiac hypertrophy in mice. *Brazilian J. Med. Biol. Res.* *36*, 1751–1759.
- Finn, R.D., Mistry, J., Tate, J., Coghill, P., Heger, A., Pollington, J.E., Gavin, O.L., Gunasekaran, P., Ceric, G., Forslund, K., et al. (2009). The Pfam protein families database. *Nucleic Acids Res.* *38*, 211–222.
- Fonseca, B.D., Smith, E.M., Lee, V.H.Y., MacKintosh, C., and Proud, C.G. (2007). PRAS40 is a target for mammalian target of rapamycin complex 1 and is required for signaling downstream of this complex. *J. Biol. Chem.* *282*, 24514–24524.
- Franken, H., Mathieson, T., Childs, D., Sweetman, G.M.A., Werner, T., Tögel, I., Doce, C., Gade, S., Bantscheff, M., Drewes, G., et al. (2015). Thermal proteome profiling for unbiased identification of direct and indirect drug targets using multiplexed quantitative mass spectrometry. *Nat. Protoc.* *10*, 1567–1593.
- Gadicherla, A.K., Stowe, D.F., Antholine, W.E., Yang, M., and Camara, A.K.S. (2012). Damage to mitochondrial complex I during cardiac ischemia reperfusion injury is reduced indirectly by anti-anginal drug ranolazine. *Biochim. Biophys. Acta* *1817*, 419–429.
- Gao, D., Inuzuka, H., Tan, M.K.M., Fukushima, H., Locasale, J.W., Liu, P., Wan, L., Zhai, B., Chin, Y.R., Shaik, S., et al. (2011). mTOR drives its own activation via SCF β TrCP-dependent degradation of the mTOR inhibitor DEPTOR. *Mol. Cell* *44*, 290–303.

- Garcia-Moreno, M., Noerenberg, M., Ni, S., Järvelin, A.I., González-Almela, E., Lenz, C.E., Bach-Pages, M., Cox, V., Avolio, R., Davis, T., et al. (2019). System-wide Profiling of RNA-Binding Proteins Uncovers Key Regulators of Virus Infection. *Mol. Cell* *74*, 196-211.e11.
- Ginestet, C. (2011). ggplot2: Elegant Graphics for Data Analysis. *J. R. Stat. Soc. Ser. A Statistics Soc.* *174*, 245–246.
- Goldberg, R.J., Ciampa, J., Lessard, D., Meyer, T.E., and Spencer, F.A. (2007). Long-term Survival After Heart Failure: A Contemporary Population-Based Perspective. *Arch. Intern. Med.* *167*, 490–496.
- Guillén-Boixet, J., Buzon, V., Salvatella, X., and Méndez, R. (2016). CPEB4 is regulated during cell cycle by ERK2/Cdk1-mediated phosphorylation and its assembly into liquid-like droplets. *Elife* *5*, 1–29.
- Haar, E. Vander, Lee, S. il, Bandhakavi, S., Griffin, T.J., and Kim, D.H. (2007). Insulin signalling to mTOR mediated by the Akt/PKB substrate PRAS40. *Nat. Cell Biol.* *9*, 316–323.
- Han, M.L., Zhao, Y.F., Tan, C.H., Xiong, Y.J., Wang, W.J., Wu, F., Fei, Y., Wang, L., and Liang, Z.Q. (2016). Cathepsin L upregulation-induced EMT phenotype is associated with the acquisition of cisplatin or paclitaxel resistance in A549 cells. *Acta Pharmacol. Sin.* *37*, 1606–1622.
- Havel, J.J., Li, Z., Cheng, D., Peng, J., and Fu, H. (2015). Nuclear PRAS40 couples the Akt/mTORC1 signaling axis to the RPL11-HDM2-p53 nucleolar stress response pathway. *Oncogene* *34*, 1487–1498.
- He, C., Sidoli, S., Warneford-Thomson, R., Tatomer, D.C., Wilusz, J.E., Garcia, B.A., and Bonasio, R. (2016). High-Resolution Mapping of RNA-Binding Regions in the Nuclear Proteome of Embryonic Stem Cells. *Mol. Cell* *64*, 416–430.
- van Heesch, S., Witte, F., Schneider-Lunitz, V., Schulz, J.F., Adami, E., Faber, A.B., Kirchner, M., Maatz, H., Blachut, S., Sandmann, C.-L., et al. (2019). The Translational Landscape of the Human Heart. *Cell* *178*, 242-260.e29.
- Heineke, J., and Molkenin, J.D. (2006). Regulation of cardiac hypertrophy by intracellular signalling pathways. *Nat. Rev. Mol. Cell Biol.* *7*, 589–600.
- Henning, R.H., and Brundel, B.J.J.M. (2017). Proteostasis in cardiac health and disease. *Nat. Rev. Cardiol.* *14*, 637–653.

- Hentze, M.W., Castello, A., Schwarzl, T., and Preiss, T. (2018). A brave new world of RNA-binding proteins. *Nat. Rev. Mol. Cell Biol.* *19*, 327–341.
- Holz, M.K., Ballif, B.A., Gygi, S.P., and Blenis, J. (2005). mTOR and S6K1 Mediate Assembly of the Translation Preinitiation Complex through Dynamic Protein Interchange and Ordered Phosphorylation Events. *123*, 569–580.
- Huang, L., Nakai, Y., Kuwahara, I., and Matsumoto, K. (2012). PRAS40 is a functionally critical target for EWS repression in Ewing sarcoma. *Cancer Res.* *72*, 1260–1269.
- Hughes, C.S., Foehr, S., Garfield, D.A., Furlong, E.E., Steinmetz, L.M., and Krijgsveld, J. (2014). Ultrasensitive proteome analysis using paramagnetic bead technology. *Mol. Syst. Biol.* *10*, 757.
- Hughes, C.S., Moggridge, S., Müller, T., Sorensen, P.H., Morin, G.B., and Krijgsveld, J. (2019). Single-pot, solid-phase-enhanced sample preparation for proteomics experiments. *Nat. Protoc.* *14*, 68–85.
- Hughes, D.C., Turner, D.C., Baehr, L.M., Seaborne, R.A., Viggars, M., Jarvis, J.C., Gorski, P.P., Stewart, C.E., Owens, D.J., Bodine, S.C., et al. (2020). Knockdown of the E3 Ubiquitin ligase UBR5 and its role in skeletal muscle anabolism. *Am. J. Physiol. Physiol.* 45–56.
- Humphreys, D.T., Hynes, C.J., Patel, H.R., Wei, G.H., Cannon, L., Fatkin, D., Suter, C.M., Clancy, J.L., and Preiss, T. (2012). Complexity of murine cardiomyocyte miRNA biogenesis, sequence variant expression and function. *PLoS One* *7*.
- Iaccarino, G., Tomhave, E.D., Lefkowitz, R.J., Koch, W.J. (1998). Reciprocal in vivo regulation of myocardial G protein-coupled receptor kinase expression by β -adrenergic receptor stimulation and blockade. *Circulation.* *98*, 1783-1789.
- Ignatiadis, N., Klaus, B., Zaugg, J.B., and Huber, W. (2016). Data-driven hypothesis weighting increases detection power in genome-scale multiple testing. *Nat. Methods* *13*, 577–580.
- Ingolia, N.T. (2010). *Genome-Wide Translational Profiling by Ribosome Footprinting* (Elsevier Inc.).
- Jovanovic, M., Rooney, M.S., Mertins, P., Przybylski, D., Chevrier, N., Satija, R., Rodriguez, E.H., Fields, A.P., Schwartz, S., Raychowdhury, R., et al. (2015) Dynamic profiling of the protein life cycle in response to pathogens. 347

- Justice, M.J., and Bode, V.C. (1988). Three ENU-induced alleles of the murine quaking locus are recessive embryonic lethal mutations. *Genet. Res.* *51*, 95–102.
- Kan, M.-C., Oruganty-Das, A., Cooper-Morgan, A., Jin, G., Swanger, S.A., Bassell, G.J., Florman, H., van Leyen, K., and Richter, J.D. (2010). CPEB4 Is a Cell Survival Protein Retained in the Nucleus upon Ischemia or Endoplasmic Reticulum Calcium Depletion. *Mol. Cell. Biol.* *30*, 5658–5671.
- Kaplan, E.L., and Meier, P. (1958). Nonparametric Estimation from Incomplete Observations. *J. Am. Stat. Assoc.* *53*, 457–481.
- Kemi, O.J., Loennechen, J.P., Wisløff, U., and Ellingsen, Y. (2002). Intensity-controlled treadmill running in mice: Cardiac and skeletal muscle hypertrophy. *J. Appl. Physiol.* *93*, 1301–1309.
- Kim, L.C., Cook, R.S., and Chen, J. (2017). mTORC1 and mTORC2 in cancer and the tumor microenvironment. *Oncogene* *36*, 2191–2201.
- Klaips, C.L., Jayaraj, G.G., and Hartl, F.U. (2018). Pathways of cellular proteostasis in aging and disease. *J. Cell Biol.* *217*, 51–63.
- Kmieczyk, V., Riechert, E., Kalinski, L., Boileau, E., Malovrh, E., Malone, B., Gorska, A., Hofmann, C., Varma, E., Jürgensen, L., et al. (2019). m6A-mRNA methylation regulates cardiac gene expression and cellular growth. *Life Sci. Alliance* *2*, 1–12.
- Kovacina, K.S., Park, G.Y., Bae, S.S., Guzzetta, A.W., Schaefer, E., Birnbaum, M.J., and Roth, R.A. (2003). Identification of a proline-rich Akt substrate as a 14-3-3 binding partner. *J. Biol. Chem.* *278*, 10189–10194.
- Kwon, S.C., Yi, H., Eichelbaum, K., Föhr, S., Fischer, B., You, K.T., Castello, A., Krijgsveld, J., Hentze, M.W., and Kim, V.N. (2013). The RNA-binding protein repertoire of embryonic stem cells. *Nat. Struct. Mol. Biol.* *20*, 1122–1130.
- Lamech, L.T., and Haynes, C.M. (2015). The unpredictability of prolonged activation of stress response pathways. *J. Cell Biol.* *209*, 781–787.
- Laplante, M., and Sabatini, D.M. (2012). mTOR signaling in growth control and disease. *Cell* *149*, 274–293.
- Le, N.-T., Takei, Y., Shishido, T., Woo, C.-H., Chang, E., Heo, K.-S., Lee, H., Lu, Y., Morrell, C., Oikawa, M., et al. (2012). p90RSK targets the ERK5-CHIP ubiquitin E3 ligase activity in diabetic hearts and promotes cardiac apoptosis and dysfunction. *Circ. Res.* *110*, 536–550.

- Lehmann, W., Mossmann, D., Kleemann, J., Mock, K., Meisinger, C., Brummer, T., Herr, R., Brabletz, S., Stemmler, M.P., and Brabletz, T. (2016). ZEB1 turns into a transcriptional activator by interacting with YAP1 in aggressive cancer types. *Nat. Commun.* 7.
- Levy, D., Kenchaiah, S., Glarson, M., Benjamin, E.J., J.kupka, M., Ho, K.K.L., Murabito, J.M., and Vasan, R.S. (2002). Long-term trends in the incidence of and survival with heart failure. *N. Engl. J. Med.* 347, 1397–1402.
- Li, J., Powell, S.R., and Wang, X. (2011). Enhancement of proteasome function by PA28 α overexpression protects against oxidative stress. *FASEB J.* 25, 883–893.
- Liao, Y., Castello, A., Krijgsveld, J., Matthias, W., Preiss, T., Frese, C.K., and Ragan, C. (2016). The Cardiomyocyte RNA-Binding Proteome: Links to Intermediary Metabolism and Heart Disease Resource The Cardiomyocyte RNA-Binding Proteome: Links to Intermediary Metabolism and Heart Disease. 1456–1469.
- Liepelt, A., Naarmann-De Vries, I.S., Simons, N., Eichelbaum, K., Föhr, S., Archer, S.K., Castello, A., Usadel, B., Krijgsveld, J., Preiss, T., et al. (2016). Identification of RNA-binding proteins in macrophages by interactome capture. *Mol. Cell. Proteomics* 15, 2699–2714
- Lilienbaum, A. (2013). Relationship between the proteasomal system and autophagy. *Int. J. Biochem. Mol. Biol.* 4, 1–26.
- Liu, C., and Lin, J. (2016). Long noncoding RNA ZEB1-AZS1 acts as an oncogene in osteosarcoma by epigenetically activating ZEB1. *Am. J. Transl. Res.* 8, 4095–4105.
- Liu, W., Huang, Y.J., Liu, C., Yang, Y.Y., Liu, H., Cui, J.G., Cheng, Y., Gao, F., Cai, J.M., and Li, B.L. (2014). Inhibition of TBK1 attenuates radiation-induced epithelial-mesenchymal transition of A549 human lung cancer cells via activation of GSK-3 β and repression of ZEB1. *Lab. Investig.* 94, 362–370.
- Liu, Y., and Aebersold, R. (2016). and Protein Abundance: New Data – New Complexities. 1–2.
- Lukong, K.E., Chang, K. wei, Khandjian, E.W., and Richard, S. (2008). RNA-binding proteins in human genetic disease. *Trends Genet.* 24, 416–425.

- Luo, T., Chen, B., and Wang, X. (2015). 4-PBA prevents pressure overload-induced myocardial hypertrophy and interstitial fibrosis by attenuating endoplasmic reticulum stress. *Chem. Biol. Interact.* *242*, 99–106.
- Lv, D., Guo, L., Zhang, T., and Huang, L. (2017). PRAS40 signaling in tumor. *Oncotarget* *8*, 69076–69085.
- Madhunapantula, S.R. V., Sharma, A., and Robertson, G.P. (2007). PRAS40 deregulates apoptosis in malignant melanoma. *Cancer Res.* *67*, 3626–3636.
- Mao, J.-H., Kim, I.-J., Wu, D., Climent, J., Kang, H.C., DelRosario, R., and Balmain, A. (2008). FBXW7 Targets mTOR for Degradation and Cooperates with PTEN in Tumor Suppression. *Science* (80-.). *321*, 1499 LP – 1502.
- Marin, T.M., Keith, K., Davies, B., Conner, D. a, Guha, P., Kalaitzidis, D., Wu, X., Lauriol, J., Wang, B., Bauer, M., et al. (2011). Dbsejpnzpqbuiz Jo B Npvtf Npefm. *J Clin Invest* *121*.
- McAlister, G.C., Nusinow, D.P., Jedrychowski, M.P., Wühr, M., Huttlin, E.L., Erickson, B.K., Rad, R., Haas, W., and Gygi, S.P. (2014). MultiNotch MS3 enables accurate, sensitive, and multiplexed detection of differential expression across cancer cell line proteomes. *Anal. Chem.* *86*, 7150–7158.
- McKee, A.E., Minet, E., Stern, C., Riahi, S., Stiles, C.D., and Silver, P.A. (2005). A genome-wide in situ hybridization map of RNA-binding proteins reveals anatomically restricted expression in the developing mouse brain. *BMC Dev. Biol.* *5*, 1–9.
- McMullen, J.R., Sherwood, M.C., Tarnavski, O., Zhang, L., Dorfman, A.L., Shioi, T., and Izumo, S. (2004). Inhibition of mTOR signaling with rapamycin regresses established cardiac hypertrophy induced by pressure overload. *Circulation* *109*, 3050–3055.
- Mearini, G., Schlossarek, S., Willis, M.S., and Carrier, L. (2008). Biochimica et Biophysica Acta The ubiquitin – proteasome system in cardiac dysfunction. *BBA - Mol. Basis Dis.* *1782*, 749–763.
- Nascimento, E.B.M., Fodor, M., Van Der Zon, G.C.M., Jazet, I.M., Meinders, A.E., Voshol, P.J., Vlasblom, R., Baan, B., Eckel, J., Maassen, J.A., et al. (2006). Insulin-mediated phosphorylation of the proline-rich Akt substrate PRAS40 is impaired in insulin target tissues of high-fat diet-fed rats. *Diabetes* *55*, 3221–3228.
- Nathans, D. (1964). Inhibition of Protein Synthesis By Puromycin. *Fed. Proc.* *23*, 9

- Nithianandarajah-Jones, G.N., Wilm, B., Goldring, C.E.P., Müller, J., and Cross, M.J. (2012). ERK5: Structure, regulation and function. *Cell. Signal.* *24*, 2187–2196.
- Oliveira, C., Faoro, H., Alves, L.R., and Goldenberg, S. (2017). RNA-binding proteins and their role in the regulation of gene expression in *trypanosoma cruzi* and *saccharomyces cerevisiae*. *Genet. Mol. Biol.* *40*, 22–30.
- Opie LH, Hasenfuss G and Mann DL. Heart failure. In: RO Bonow, DL Mann, DP Zipes and P Libby, Braunwald's heart disease: a textbook of cardiovascular medicine. 9. edition. Philadelphia/PA, USA Elsevier Saunders; 2012: 459-504.
- Ortiz-Zapater, E., Pineda, D., Martínez-Bosch, N., Fernández-Miranda, G., Iglesias, M., Alameda, F., Moreno, M., Eliscovich, C., Eyra, E., Real, F.X., et al. (2012). Key contribution of CPEB4-mediated translational control to cancer progression. *Nat. Med.* *18*, 83–90.
- Oshiro, N., Takahashi, R., Yoshino, K.I., Tanimura, K., Nakashima, A., Eguchi, S., Miyamoto, T., Hara, K., Takehana, K., Avruch, J., et al. (2007). The proline-rich Akt substrate of 40 kDa (PRAS40) is a physiological substrate of mammalian target of rapamycin complex 1. *J. Biol. Chem.* *282*, 20329–20339.
- Pacak, C.A., and Byrne, B.J. (2011). AAV vectors for cardiac gene transfer: Experimental tools and clinical opportunities. *Mol. Ther.* *19*, 1582–1590.
- Pallares-Cartes, C., Cakan-Akdogan, G., and Teleman, A.A. (2012). Tissue-Specific Coupling between Insulin/IGF and TORC1 Signaling via PRAS40 in *Drosophila*. *Dev. Cell* *22*, 172–182.
- Perez-Perri, J.I., Rogell, B., Schwarzl, T., Stein, F., Zhou, Y., Rettel, M., Brosig, A., and Hentze, M.W. (2018). Discovery of RNA-binding proteins and characterization of their dynamic responses by enhanced RNA interactome capture. *Nat. Commun.* *9*.
- Peterson, T.R., Laplante, M., Thoreen, C.C., Sancak, Y., Kang, S.A., Kuehl, W.M., Gray, N.S., and Sabatini, D.M. (2009). DEPTOR Is an mTOR Inhibitor Frequently Overexpressed in Multiple Myeloma Cells and Required for Their Survival. *Cell* *137*, 873–886.
- Piper HM, Daut J, Dessen A, Brandes R, Busse R. Herz und Kreislauf. In: RF Schmidt, F Lang, M Heckmann Physiologie des Menschen Mit Pathophysiologie. 31. edition. Heidelberg: Springer Medizin Verlag; 2010: 517-626.

- Piqué, M., López, J.M., Foissac, S., Guigó, R., and Méndez, R. (2008). A Combinatorial Code for CPE-Mediated Translational Control. *Cell* 132, 434–448.
- Rabanal-Ruiz, Y., Otten, E.G., and Korolchuk, V.I. (2017). MTORC1 as the main gateway to autophagy. *Essays Biochem.* 61, 565–584.
- Radhakrishnan, S.K., Lee, C.S., Young, P., Beskow, A., Chan, J.Y., and Deshaies, R.J. (2010). Transcription Factor Nrf1 Mediates the Proteasome Recovery Pathway after Proteasome Inhibition in Mammalian Cells. *Mol. Cell* 38, 17–28.
- Ram, R., Mickelsen, D.M., Theodoropoulos, C., and Blaxall, B.C. (2011). New approaches in small animal echocardiography: Imaging the sounds of silence. *Am. J. Physiol. - Hear. Circ. Physiol.* 301.
- Redfield, M.M., Jacobsen, S.J., Burnett Jr, J.C., Mahoney, D.W., Bailey, K.R., and Rodeheffer, R.J. (2003). Burden of Systolic and Diastolic Ventricular Dysfunction in the Community: Appreciating the Scope of the Heart Failure Epidemic. *JAMA* 289, 194–202.
- Reichel, M., Liao, Y., Rettel, M., Ragan, C., Evers, M., Alleaume, A.M., Horos, R., Hentze, M.W., Preiss, T., and Millar, A.A. (2016). In planta determination of the mRNA-binding proteome of arabidopsis etiolated seedlings. *Plant Cell* 28, 2435–2452.
- Riechert, E., Stein, F., Schwarzl T., Sekaran, T., Jürgensen, L., Kamuf-Schenk, V., Varma, E., Hofmann, C., Rettel, M., Martin, J., Ramirez-Pedraza, M., Fernandez, M., Mendez, R., Katus, H.A., Hentze, M.W., Völkers, M. (2020). Identification of Dynamic RNA-Binding Proteins Uncovers a Cpeb4-Controlled Regulatory Cascade During Pathological Cell Growth of Cardiomyocytes. Available at SSRN: <https://ssrn.com/abstract=3647257> or <http://dx.doi.org/10.2139/ssrn.3647257>
- Rockman, H.A., Ross, R.S., Harris, A.N., Knowlton, K.U., Steinhilper, M.E., Field, L.J., Ross, J., and Chien, K.R. (1991). Segregation of atrial-specific and inducible expression of an atrial natriuretic factor transgene in an in vivo murine model of cardiac hypertrophy. *Proc. Natl. Acad. Sci. U. S. A.* 88, 8277–8281.
- Roth, D.M., Hutt, D.M., Tong, J., Bouhccareilh, M., Wang, N., Seeley, T., Dekkers, J.F., Beekman, J.M., Garza, D., Drew, L., et al. (2014). Modulation of the Maladaptive Stress Response to Manage Diseases of Protein Folding. *PLoS Biol.* 12, 12–14.
- Rousseau, A., and Bertolotti, A. (2016). An evolutionarily conserved pathway controls proteasome homeostasis. *Nature* 536, 184–189.

Sancak, Y., Thoreen, C.C., Peterson, T.R., Lindquist, R. a., Kang, S. a., Spooner, E., Carr, S. a., and Sabatini, D.M. (2007). PRAS40 Is an Insulin-Regulated Inhibitor of the mTORC1 Protein Kinase. *Mol. Cell* 25, 903–915.

Sanz, E., Bean, J.C., Carey, D.P., Quintana, A., and McKnight, G.S. (2019). RiboTag: Ribosomal Tagging Strategy to Analyze Cell-Type-Specific mRNA Expression In Vivo. *Curr. Protoc. Neurosci.* 88, e77.

Sarkar, S., Chawla-Sarkar, M., Young, D., Nishiyama, K., Rayborn, M.E., Hollyfield, J.G., and Sen, S. (2004). Myocardial cell death and regeneration during progression of cardiac hypertrophy to heart failure. *J. Biol. Chem.* 279, 52630–52642.

Saxton, R.A., and Sabatini, D.M. (2017). mTOR Signaling in Growth, Metabolism, and Disease. *Cell* 168, 960–976.

Schrimpf, S.P., Weiss, M., Reiter, L., Ahrens, C.H., Jovanovic, M., Malmström, J., Brunner, E., Mohanty, S., Lercher, M.J., Hunziker, P.E., et al. (2009). Comparative functional analysis of the *Caenorhabditis elegans* and *Drosophila melanogaster* proteomes. *PLoS Biol.* 7, 0616–0627.

Schwanhüsser, B., Busse, D., Li, N., Dittmar, G., Schuchhardt, J., Wolf, J., Chen, W., and Selbach, M. (2011). Global quantification of mammalian gene expression control. *Nature* 473, 337–342.

Sciarretta, S., Volpe, M., and Sadoshima, J. (2014). Mammalian target of rapamycin signaling in cardiac physiology and disease. *Circ. Res.* 114, 549–564.

Shepherd, P.R., and Kahn, B.B. (1999). Review Articles Mechanisms of Disease. *N. Engl. J. Med.* July 1999.

Shimizu, I., and Minamino, T. (2016). Physiological and pathological cardiac hypertrophy. *J. Mol. Cell. Cardiol.* 97, 245–262.

Shioi, T., McMullen, J.R., Tarnavski, O., Converso, K., Sherwood, M.C., Manning, W.J., and Izumo, S. (2003). Rapamycin attenuates load-induced cardiac hypertrophy in mice. *Circulation* 107, 1664–1670.

Siles, L., Ninfali, C., Cortés, M., Darling, D.S., and Postigo, A. (2019). ZEB1 protects skeletal muscle from damage and is required for its regeneration. *Nat. Commun.* 10, 1–18.

Simpson, P. (1985). Stimulation of hypertrophy of cultured neonatal rat heart cells through an α 1-adrenergic receptor and induction of beating through an α 1- and β 1-

adrenergic receptor interaction. Evidence for independent regulation of growth and beating. *Circ. Res.* 56, 884–894.

Steffen, J., Seeger, M., Koch, A., and Krüger, E. (2010). Proteasomal degradation is transcriptionally controlled by TCF11 via an ERAD-dependent feedback loop. *Mol. Cell* 40, 147–158.

Sysoev, V.O., Fischer, B., Frese, C.K., Gupta, I., Krijgsveld, J., Hentze, M.W., Castello, A., and Ephrussi, A. (2016). Global changes of the RNA-bound proteome during the maternal-to-zygotic transition in *Drosophila*. *Nat. Commun.* 7.

Taegtmeyer, H., Sen, S., and Vela, D. (2010). Return to the fetal gene program: A suggested metabolic link to gene expression in the heart. *Ann. N. Y. Acad. Sci.* 1188, 191–198.

Taubeneck, U. (1967). J. D. Watson: *Molecular Biology of the Gene*. 494 S., 195 Abb., 24 Tab. New York 1965: W. A. Benjamin, Inc. \$ 11.00. *Z. Allg. Mikrobiol.* 7, 171.

Vogel, C., and Marcotte, E.M. (2013). Insights into regulation of protein abundance from proteomics and transcriptomics analyses. Vogel, C. & Marcotte, E. M. Insights into regulation of protein abundance from proteomics and transcriptomics analyses. *Nat. Rev. Genet.* 13, 227–232 (2013). *Nat. Rev. Genet.* 13, 227–232.

Volkers, M., Toko, H., Doroudgar, S., Din, S., Quijada, P., Joyo, A.Y., Ornelas, L., Joyo, E., Thuerlauf, D.J., Konstandin, M.H., et al. (2013). Pathological hypertrophy amelioration by PRAS40-mediated inhibition of mTORC1. *Proc. Natl. Acad. Sci.* 110, 12661–12666.

Wang, L., Harris, T.E., Roth, R.A., and Lawrence, J.C. (2007). PRAS40 regulates mTORC1 kinase activity by functioning as a direct inhibitor of substrate binding. *J. Biol. Chem.* 282, 20036–20044.

Wang, Y.-H., and Huang, M.-L. (2009). Reduction of Lobe leads to TORC hypoactivation that induces ectopic Jak/STAT signaling to impair *Drosophila* eye development. *Mech. Dev.* 126, 781–790.

Weiss, M., Schrimpf, S., Hengartner, M.O., Lercher, M.J., and von Mering, C. (2010). Shotgun proteomics data from multiple organisms reveals remarkable quantitative conservation of the eukaryotic core proteome. *Proteomics* 10, 1297–1306.

- Werner, T., Sweetman, G., Savitski, M.F., Mathieson, T., Bantscheff, M., and Savitski, M.M. (2014). Ion Coalescence of Neutron Encoded TMT 10-Plex Reporter Ions. *Anal. Chem.* *86*, 3594–3601.
- WHO (2019). Cardiovascular Diseases Key Facts. *World Heal. Organ.* 1–6.
- Wienholds, E., and Plasterk, R.H.A. (2005). MicroRNA function in animal development. *FEBS Lett.* *579*, 5911–5922.
- Wilhelm, M., Schlegl, J., Hahne, H., Gholami, A.M., Lieberenz, M., Savitski, M.M., Ziegler, E., Butzmann, L., Gessulat, S., Marx, H., et al. (2014). Mass-spectrometry-based draft of the human proteome. *Nature* *509*, 582–587.
- Wiza, C., Herzfeld De Wiza, D., Nascimento, E.B.M., Lehr, S., Al-Hasani, H., and Ouwens, D.M. (2013). Knockdown of PRAS40 inhibits insulin action via proteasome-mediated degradation of IRS1 in primary human skeletal muscle cells. *Diabetologia* *56*, 1118–1128.
- Wiza, C., Chadt, A., Blumensatt, M., Kanzleiter, T., Herzfeld De Wiza, D., Horrigs, A., Mueller, H., Nascimento, E.B.M., Schürmann, A., Al-Hasani, H., et al. (2014). Over-expression of PRAS40 enhances insulin sensitivity in skeletal muscle. *Arch. Physiol. Biochem.* *120*, 64–72.
- Xue, Y., Zhang, L., Zhu, Y., Ke, X., Wang, Q., and Min, H. (2019). Regulation of proliferation and epithelial-to-mesenchymal transition (EMT) of gastric cancer by ZEB1 via modulating Wnt5a and related mechanisms. *Med. Sci. Monit.* *25*, 1663–1670.
- Xiong, X., Xie, R., Zhang, H., Gu, L., Xie, W., Cheng, M., Jian, Z., Kovacina, K., and Zhao, H. (2014). PRAS40 plays a pivotal role in protecting against stroke by linking the Akt and mTOR pathways. *Neurobiol. Dis.* *66*, 43–52.
- Yang, H., Jiang, X., Li, B., Yang, H.J., Miller, M., Yang, A., Dhar, A., and Pavletich, N.P. (2017). Mechanisms of mTORC1 activation by RHEB and inhibition by PRAS40. *Nature* *552*, 368–373.
- Yun, Y.S., Kim, K.H., Tschida, B., Sachs, Z., Noble-Orcutt, K.E., Moriarity, B.S., Ai, T., Ding, R., Williams, J., Chen, L., et al. (2016). mTORC1 Coordinates Protein Synthesis and Immunoproteasome Formation via PRAS40 to Prevent Accumulation of Protein Stress. *Mol. Cell* *61*, 625–639.

Zhang, K.S., Schecker, J., Krull, A., Riechert, E., Jürgensen, L., Kamuf-Schenk, V., Burghaus, J., Kiper, L., Cao Ho, T., Wöltje, K., et al. (2019). PRAS40 suppresses atherogenesis through inhibition of mTORC1-dependent pro-inflammatory signaling in endothelial cells. *Sci. Rep.* 9, 1–13.

Zhang, Y., Nicholatos, J., Dreier, J.R., Ricoult, S.J.H., Widenmaier, S.B., Hotamisligil, G.S., Kwiatkowski, D.J., and Manning, B.D. (2014). Coordinated regulation of protein synthesis and degradation by mTORC1. *Nature* 513, 440.

Zhao, J., Zhai, B., Gygi, S.P., and Goldberg, A.L. (2015). MTOR inhibition activates overall protein degradation by the ubiquitin proteasome system as well as by autophagy. *Proc. Natl. Acad. Sci. U. S. A.* 112, 15790–15797.

Zhao, Y., Xiong, X., and Sun, Y. (2011). DEPTOR, an mTOR Inhibitor, is a physiological substrate of SCF β TrCP E3 ubiquitin ligase and regulates survival and autophagy. *Mol. Cell* 44, 304–316.

Zhu, G., Qi, Q., Havel, J.J., Li, Z., Du, Y., Zhang, X., and Fu, H. (2017). PRAS40 promotes NF- κ B transcriptional activity through association with p65. *Oncogenesis* 6, e381–e381.

Zhou, H.L., Mangelsdorf, M., Liu, J.H., Zhu, L., and Wu, J.Y. (2014). RNA-binding proteins in neurological diseases. *Sci. China Life Sci.* 57, 432–444.

Zimmer, H.G. (1997). Catecholamine-induced cardiac hypertrophy: Significance of proto-oncogene expression. *J. Mol. Med.* 75, 849–859.

VI. SUPPLEMENTAL FIGURES

Supplemental figure 1

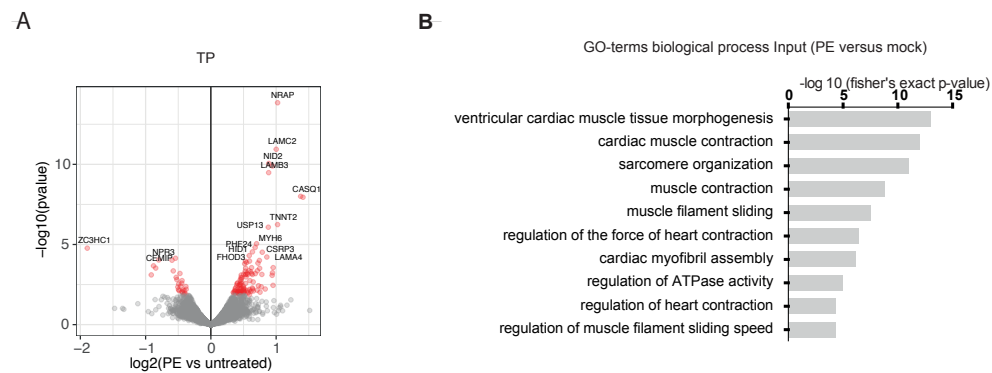


Figure S1: PE treatment of NRVCs for dynamic RBPome. (A) Volcano plot of PE-treated versus untreated TP. Plot by Frank Stein, EMBL Heidelberg. (B) GO terms “Biological process” for PE- versus untreated total proteome.

Supplemental figure 2

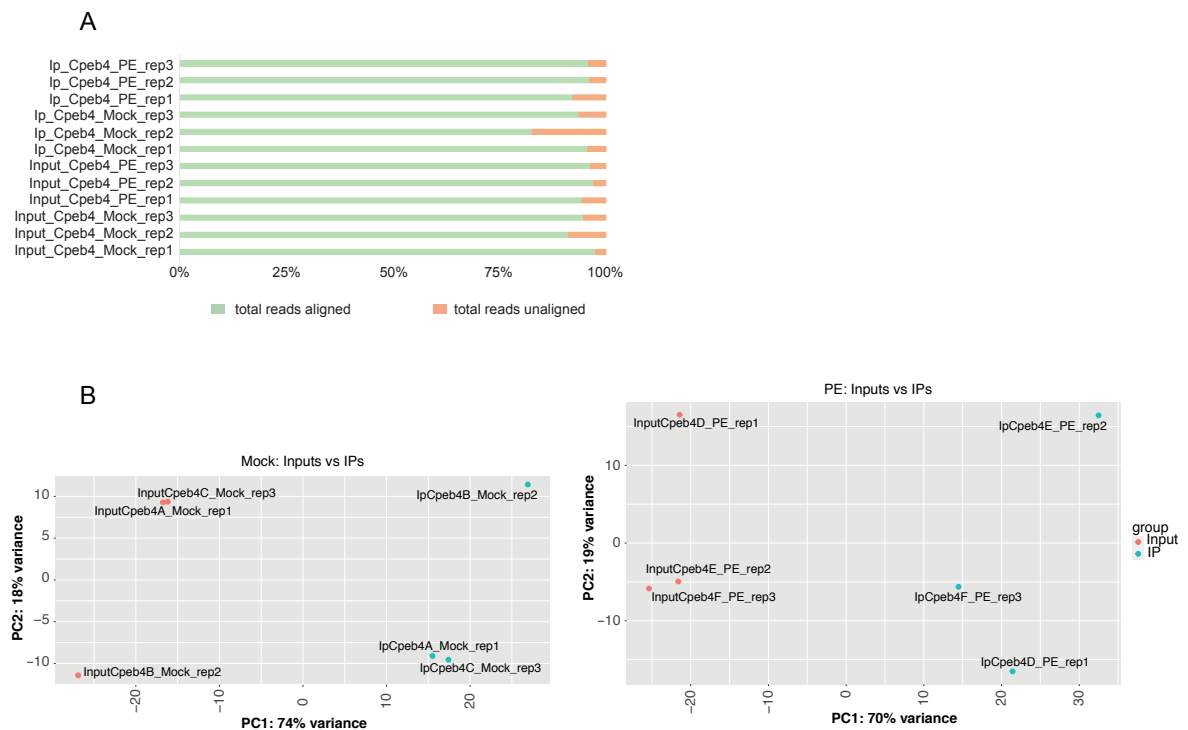


Figure S2: RIP-Seq of PE-treated versus control (mock) NRVCs. (A) Percentage of alignments of RipSeq samples of RIP-IP and Input samples. (B) Principal component analysis of Mock (left panel) and PE treatment (right panel) RIP Seq replicates. Raw data analysis and quality control by Thileepan Sekaran.

Supplemental figure 3

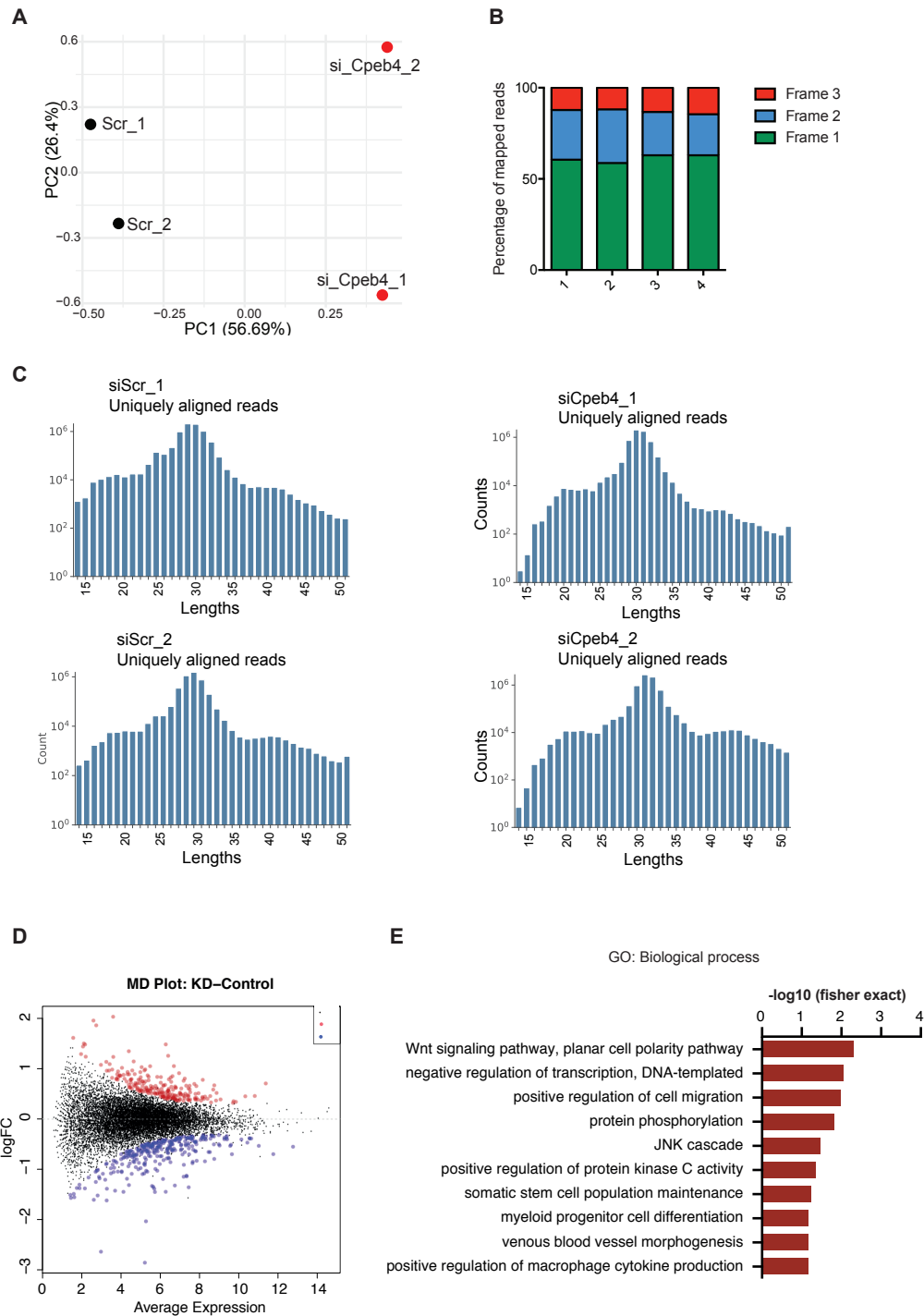


Figure S3: Ribo-Seq of Cpeb4 KD versus control NRVCMs. (A) Principal component analysis of biological replicates of RibSeq. (B) Percentage of mapped reads for each reading frame (C) Read length distribution of aligned reads for each replicate of RibSeq. (D) MD plot with average expression and logFC of regulated genes between KD and control. A-D Preprocessing and quality control by Christoph Hofmann and Etienne Boileau. (E) GO terms “Biological process” of DEGs (Cpeb4 KD versus scr), logFC >0,5, FDR <0,01.

Supplemental figure 4

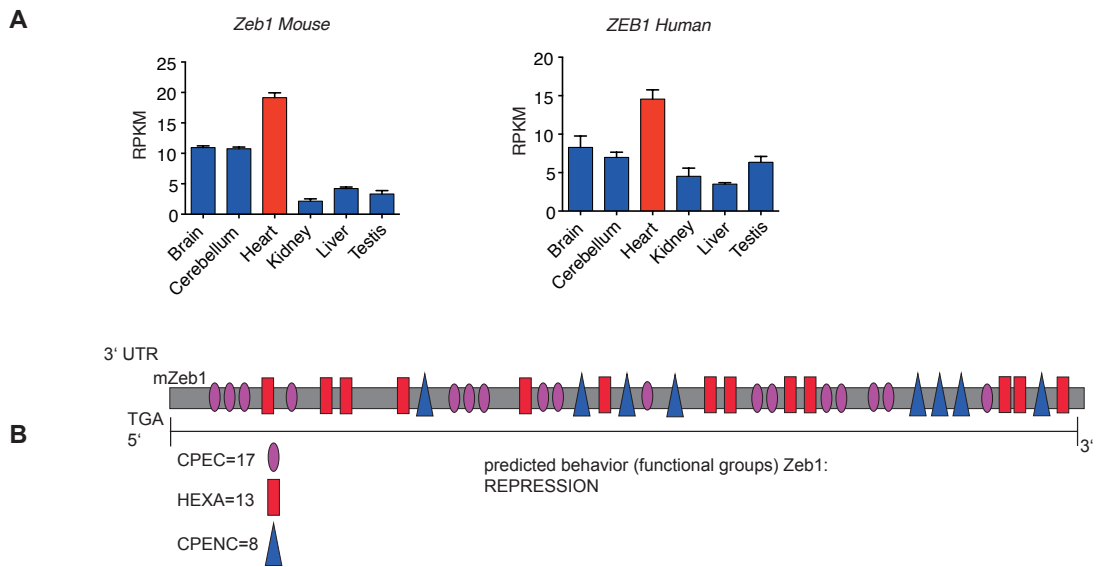


Figure S4: Cpeb4 target Zeb1. (A) Levels of Zeb1 in human and mouse in different organs, taken from (Cardoso-Moreira, 2019). (B) Prediction of suppressive function of Cpeb4 onto Zeb1 by number and position of functional units CPEC, HEXA and CPENC according to (Piqué et al., 2008). Figure by Mirko Völkers.

Supplemental figure 5

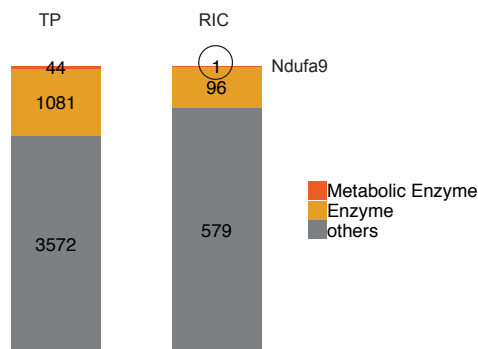


Figure S5: Enzymes and metabolic enzymes in basal cardiac RBPome. Number of enzymes and metabolic enzymes that we determined by RNA-interactome capture. Enzymes and metabolic enzymes were defined as previously published by Castello et al. (2015) by Thomas Schwarzl, EMBL Heidelberg.

Supplemental figure 6

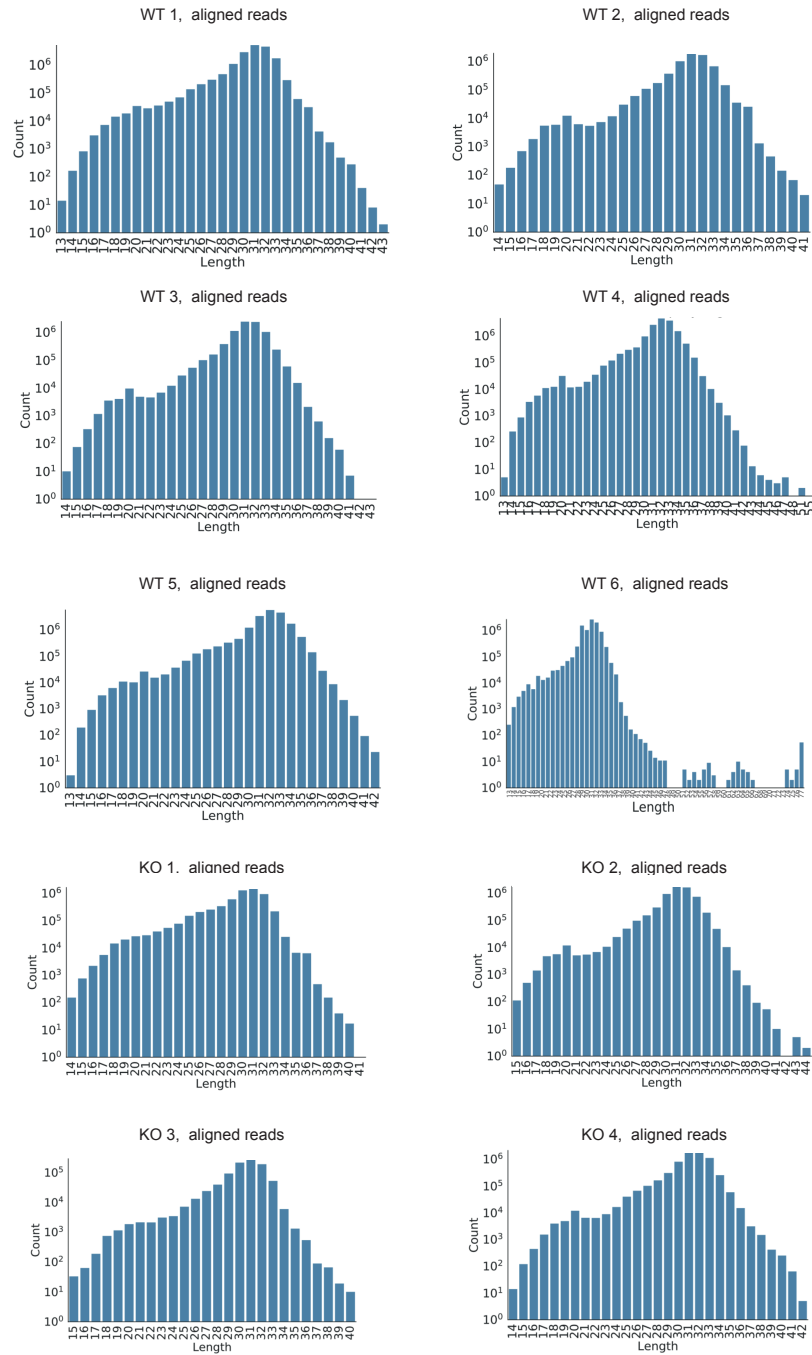


Figure S6: Quality control of RiboSeq libraries of Pras40 KO versus WT hearts. Read length distribution of aligned reads for each replicate of RiboSeq. Preprocessing of data by Etienne Boileau.

Supplemental figure 7

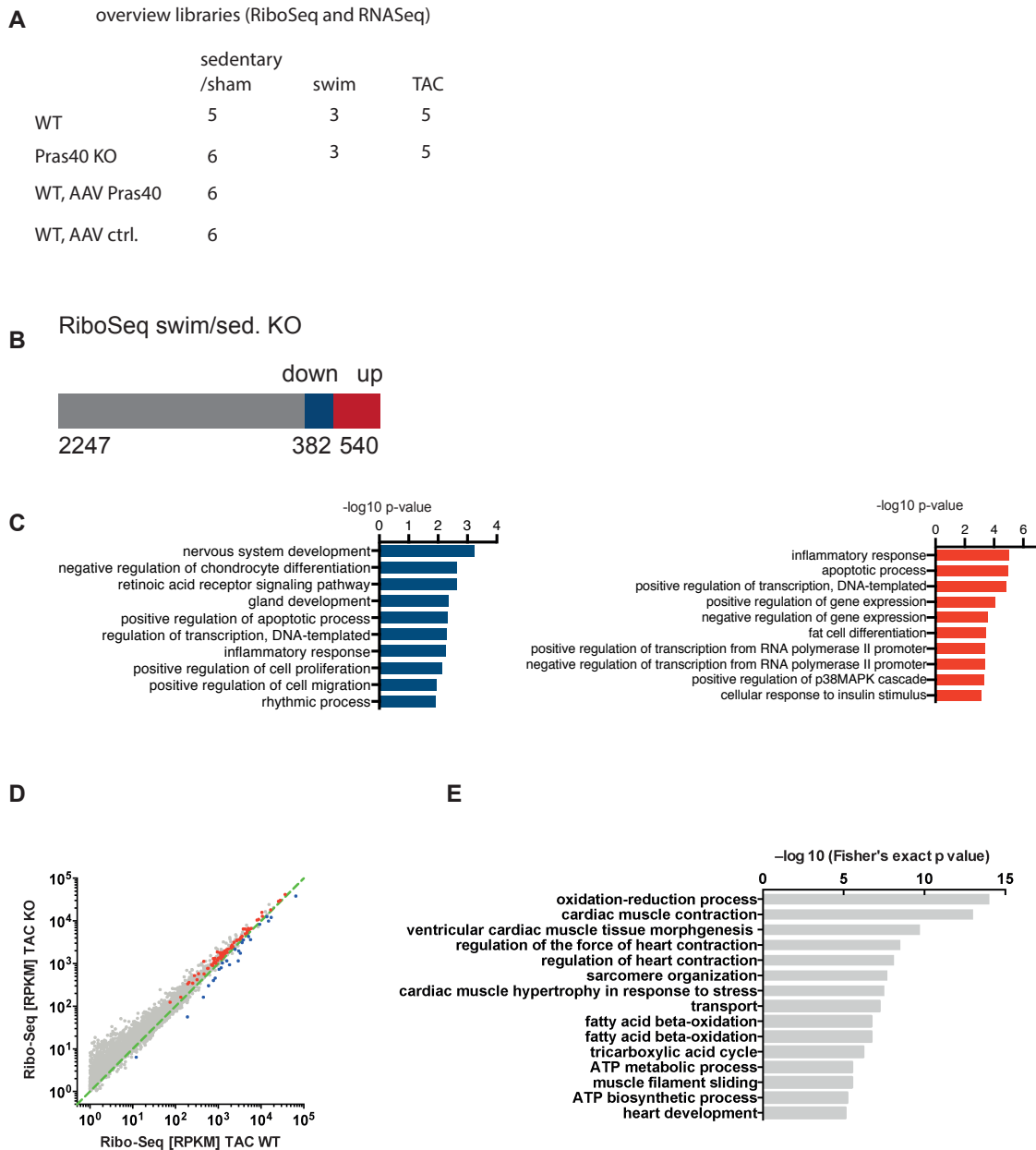


Figure S7: Overview and first analysis of RiboSeq and RNASeq libraries. (A) Overview of samples, that were used for the generation of RiboSeq and RNASeq libraries. (B) Distribution of differentially regulated genes (FDR<0.1; log FC>0.5) in RiboSeq analysis of KO mice that underwent swimming versus sedentary animals. (C) Unsupervised clustering and GO analysis of downregulated genes (blue) and unregulated genes (red) from (B). (D) Scatter plot of RiboSeq comparing KO TAC with WT TAC. (E) GO of (D).

Supplemental figure 8

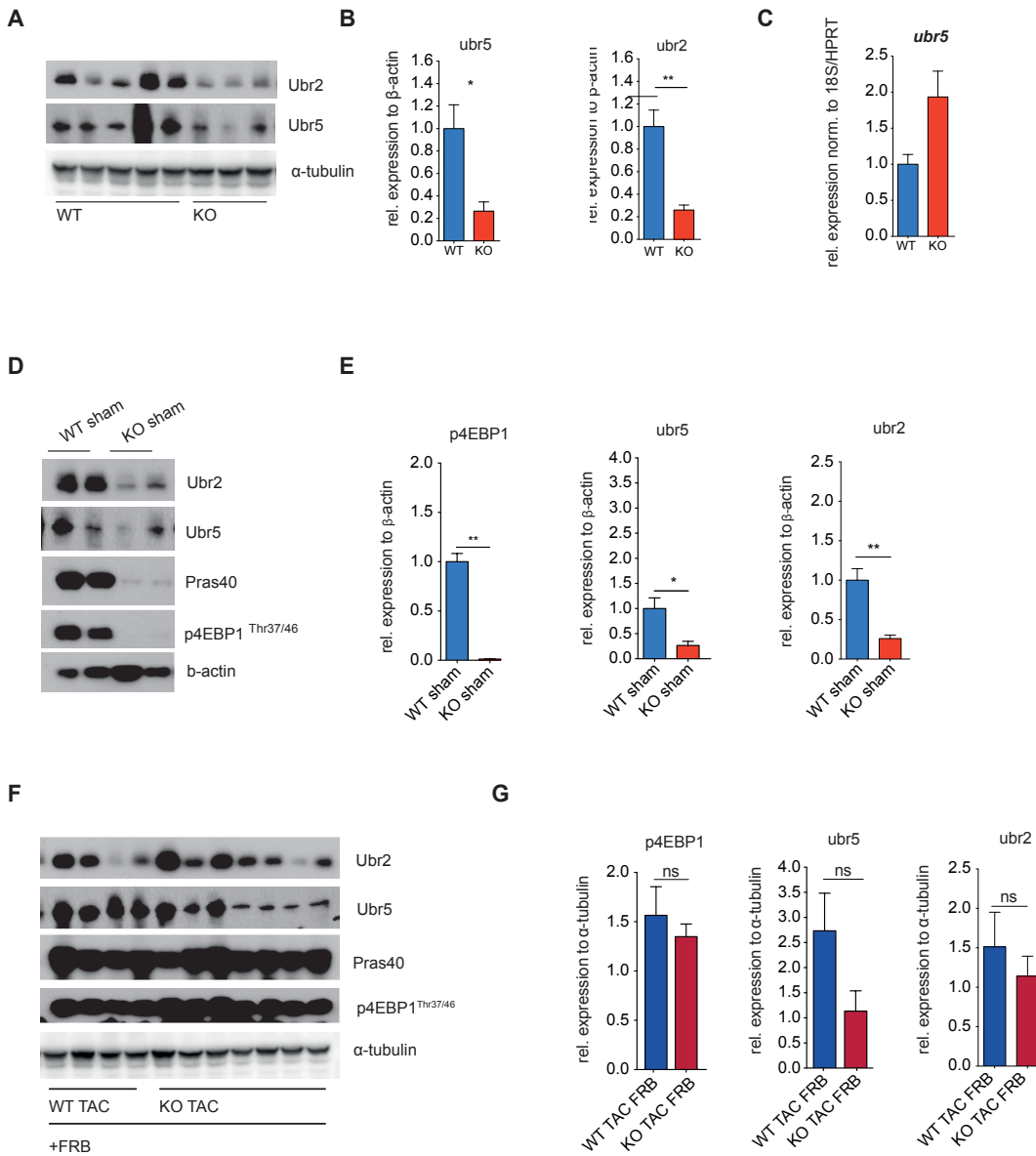


Figure S8: Signaling in FRB-overexpressing WT and Pras40 KO mice after TAC. (A) Western blot of WT versus KO mice (B) Quantification of (A). (C) qPCR analysis of qDNA from WT versus KO left ventricular lysates. (D) Western blot of WT and KO sham controls of experiment of Figure 6.18 (E) Quantification of (D). (F) Western blot analysis of WT and KO TAC mice treated with FRB virus. (G) Quantification of F.

VII. PUBLICATIONS

First-authored:

Identification of Dynamic RNA-Binding Proteins Uncovers a Cpeb4-Controlled Regulatory Cascade During Pathological Cell Growth of Cardiomyocytes

Eva Riechert; Frank Stein; Thomas Schwarzl; Thileepan Sekaran; Lonny Jürgensen; Verena Kamuf-Schenk; Eshita Varma; Christoph Hofmann; Mandy Rettel; Judit Martin; Marta Ramirez-Pedraza; Mercedes Fernandez; Raul Mendez; Hugo A Katus; Matthias W Hentze; Mirko Völkers

Cell Reports, *under revision* and published as Cell Press Sneak Peek at DOI: <http://dx.doi.org/10.2139/ssrn.3647257>

m6A-mRNA methylation regulates cardiac gene expression and cellular growth

Vivien Kmietczyk*, **Eva Riechert***, Laura Kalinski, Etienne Boileau, Ellen Malovrh, Brandon Malone, Agnieszka Gorska, Christoph Hofmann, Eshita Varma, Lonny Jürgensen, Verena Kamuf-Schenk, Janine Altmüller, Rewati Tappu, Martin Busch, Patrick Most, Hugo Katus, Christoph Dieterich, and Mirko Völkers

Life Science Alliance Apr 2019, 2 (2) e201800233; DOI: 10.26508/lsa.201800233.

* *contributed equally*

mTOR-proteasomal dysfunction upon deletion of Pras40 inhibits cardiac growth but results in cardiac failure

Eva Riechert, Christoph Hofmann, Etienne Boileau, Lonny Jürgensen, Verena Kamuf-Schenk, Kira Gür, Moritz H. Kern, Claudia Stroh, Thanh Cao Ho, Carolyn Schneider, Hugo A. Katus, Christoph Dieterich, Mirko Völkers

in preparation

Others:

A multi-network comparative analysis of transcriptome and translome identifies novel hub genes in cardiac remodeling

Etienne Boileau, Shirin Doroudgar, **Eva Riechert**, Lonny Jürgensen, Thanh Cao Ho, Hugo Albert Katus, Mirko Völkers and Christoph Dieterich

Frontiers in Genetics 2020. 11:583124. DOI: 10.3389/fgene.2020.583124

Saraf-dependent activation of mTORC1 regulates cardiac growth.

Sanli alp, A.*, Schumacher, D.*, Kiper, L.*, Varma, E., **Riechert, E.**, Ho, T.C., Hofmann, C., Kmietczyk, V., Zimmermann, F., Dlugosz, S., Angela Wirth, Agnieszka A. Gorska, Jana Burghaus, Juan E. Camacho Londoño, Hugo A. Katus, Shirin Doroudgar, Marc Freichel, Mirko Völkers

Journal of Molecular and Cellular Cardiology 2020; 141, 30–42. DOI: 10.1016/j.yjmcc.2020.03.004

* *contributed equally*

CITED4 Protects Against Adverse Remodeling in Response to Physiological and Pathological Stress.

Lerchenmüller C, Rabolli CP, Yeri AS, Kitchen R, Salvador AM, Liu LX, Ziegler O, Danielson KM, Platt C, Shah R, Damilano F, Kundu P, **Riechert E**, Katus HA, Saffitz JE, Keshishian H, Carr S, Bezzerides VJ, Das S, Rosenzweig A.

Circulation Research 2020; DOI: 10.1161/CIRCRESAHA.119.315881.

Monitoring cell type-specific gene expression using ribosomal sequencing in vivo during cardiac hemodynamic stress

Shirin Doroudgar, Christoph Hofmann, Etienne Boileau, Brandon Malone, **Eva Riechert**, Aga Gorska, Tobias Jakobi, Clara Sandmann, Lonny Juergensen, Vivien Kmietczyk, Ellen Malovrh, Jana Burghaus, Fereshteh Younesi, Ulrike Friedrich, Johannes Backs, Günter Kramer, Hugo Katus, Christoph Dieterich, and Mirko Völkens

Circulation Research. 2019; 125:431–448 DOI: 10.1161/CIRCRESAHA.119.314817.

PRAS40 suppresses atherogenesis through inhibition of mTORC1-dependent pro-inflammatory signaling in endothelial cells.

Zhang, K.S., Schecker, J., Krull, A., **Riechert, E.**, Jürgensen, L., Kamuf-Schenk, V., Burghaus, J., Kiper, L., Cao Ho, T., Wöltje, K., Verena Stangl, Hugo A. Katus, Karl Stangl, Mirko Völkens & Till F. Althof

Nature Scientific Reports 2019; 9, 1–13. 2019; 9:16787 DOI: 10.1038/s41598-019-53098-1

TIP30 counteracts cardiac hypertrophy and failure by inhibiting translational elongation

Andrea Grund, Malgorzata Szaroszyk, Mortimer Korf–Klingebiel, Mona Malek Mohammadi, Felix A Trogisch, Ulrike Schrameck, Anna Gigina, Christopher Tiedje, Matthias Gaestel, Theresia Kraft, Jan Hegermann, Sandor Batkai, Thomas Thum, Andreas Perrot, Cris dos Remedios, **Eva Riechert**, Mirko Völkens, Shirin Doroudgar, Andreas Jungmann, Ralf Bauer, Xiaoke Yin, Manuel Mayr, Kai C Wollert, Andreas Pich, Hua Xiao, Hugo A Katus, Johann Bauersachs, Oliver J Müller, Joerg Heineke

EMBO Molecular Medicine 2019 DOI: 10.15252/emmm.201810018.

Genomic structural variations lead to dysregulation of important coding and non-coding RNA species in dilated cardiomyopathy

Jan Haas, Stefan Mester, Alan Lai, Karen S Frese, Farbod Sedaghat–Hamedani, Elham Kayvanpour, Tobias Rausch, Rouven Nietsch, Jes–Niels Boeckel, Avisha Carstensen, Mirko Völkens, Carsten Dietrich, Dietmar Pils, Ali Amr, Daniel B Holzer, Diana Martins Bordalo, Daniel Oehler, Tanja Weis, Derliz Mereles, Sebastian Buss, **Eva Riechert**, Emil Wirsz, Maximilian Wuerstle, Jan O Korbel, Andreas Keller, Hugo A Katus, Andreas E Posch, Benjamin Meder

EMBO Molecular Medicine 2017; 10(1):107–120. DOI:10.15252/emmm.201707838

Cand2 links pathological mTORC1 signaling to adverse cardiac remodeling by regulating Grk5 expression

Agnieszka A. Gorska*, Clara Sandmann*, **Eva Riechert**, Christoph Hofmann, Ellen Malovrh, Eshita Varma, Vivien Kmietczyk, Lonny Jürgensen, Verena Kamuf-Schenk, Claudia Stroh, Jennifer Furkel, Carsten Sticht, Etienne Boileau, Christoph Dieterich Hugo A. Katus, Shirin Doroudgar and Mirko Völkers

** contributed equally*

under revision

VIII. CONTRIBUTIONS

Technical support was given as followed: By Kira Gür and Lonny Jürgensen for immunofluorescence stainings and cell size determination, by Claudia Stroh for select qPCRs, by Verena Kamuf-Schenk for generation of virus, for select Western blots and immunoprecipitations and by Lonny Jürgensen for staining of histological sections, for the generation of Cpeb4 KD RiboSeq libraries and for select proteasome assays. Teil vein injections of AAV9 were performed by Ulrike Gärtner from the IBF Heidelberg.

IX. ACKNOWLEDGMENTS

I would like to thank Mirko Völkers for supervising this thesis. Thank you for entrusting me with these two great projects, that I have greatly enjoyed working on, for valuable scientific discussions and for supporting the progress of the projects.

I would further like to thank the members of my thesis advisory committee, Prof. Georg Stoecklin and Prof. Aurelio Teleman for your helpful advice, and your supportive feedback during the TAC meetings. Thank you to Prof. Stephan Frings for being part of the defense committee.

Further I would like to thank all members of the Völkers lab, for the great working atmosphere. Thank you Thanh, Christoph, Clara, Eshita, Aga and Moritz for great scientific collaborations, and thank you Maja for proof-reading my thesis. Thank you Lonny, Verena, Kira and Claudi for your great technical assistance and organizing the lab routine.

Thank you Lonny, for your great support in bench work and everything else it takes to finish a PhD, and especially for being such a great friend. Sharing the daily lab life with you was a great pleasure.

I would also like to thank my collaborators Frank, Tom and Thileepan for the very fruitful and enjoyable collaboration in the RIC project, that was clearly a favorite part of my PhD. Thank you Etienne for many analyzed RiboSeq libraries and your helpfulness.

Thank you Carolin for your continuous support and mentorship and for always having an open door for me.

Thank you Shirin for your mentorship, sharing your enthusiasm for science and introducing me to your scientific community.

To all the friends that I made during the time in Analysezentrum 3, it was a great pleasure working here, and I have rarely had a working environment with so many friendly and helpful people around.

I would also like to thank the friends that have supported me in Heidelberg during the time of my PhD! Luana, Katrin, Axel, Linda and Staffan, your friendship has made the Heidelberg years unforgettable and so very special.

My heartfelt thank you goes to my family: To my parents, for supporting me not only in the course of this PhD, but in life! Dad, for sharing your scientific enthusiasm with me- for sure one of the reasons to start a career in science- and for discussing science even between fields.

To my aunt Christiane, who is always there and has given me regular weekend treats whenever needed during the course of my PhD. And to my grandmother, who has always supported and cheered me. I wish we could share this moment now! To my parents-in-law Anne and Raimund, for always having an open ear, and for supporting us in everything we do.

Most importantly, my heartfelt gratitude goes to you Hanno, for standing by my side in all I do, and for your love!